ҚАЗАҚСТАН РЕСПУБЛИКАСЫ
ҒЫЛЫМ ЖӘНЕ ЖОҒАРЫ БІЛІМ МИНИСТРЛІГІ
SATBAYEV UNIVERSITY
МЕТАЛЛУРГИЯ ЖӘНЕ КЕН БАЙЫТУ ИНСТИТУТЫ

ISSN 2616-6445 (Online)
ISSN 2224-5243 (Print)
DOI 10.31643/2018/166445

Минералдық **ш**икізаттарды **к**ешенді **п**айдалану

3**(346)**

Комплексное **И**спользование **М**инерального **С**ырья

Complex **U**se of **M**ineral **R**esources

ШІЛДЕ-ҚЫРКҮЙЕК 2028
JULY-SEPTEMBER 2028
ИЮЛЬ-СЕНТЯБРЬ 2028

ЖЫЛЫНА 4 РЕТ ШЫҒАДЫ
QUARTERLY JOURNAL
ВЫХОДИТ 4 РАЗА В ГОД

ЖУРНАЛ 1978 ЖЫЛДАН БАСТАП ШЫҒАДЫ
JOURNAL HAS BEEN PUBLISHING SINCE 1978
ЖУРНАЛ ИЗДАЕТСЯ С 1978 ГОДА

АЛМАТЫ - 2028

Редакция мекен жайы:
«Металлургия және кен байыту институты» АҚ
050010, Қазақстан Республикасы, Алматы қ., Шевченко к-сі, Уәлиханов к-нің қиылысы, 29/133,
Fax. +7 (727) 298-45-03, Tel. +7-(727) 298-45-02, +7 (727) 298-45-19
E mail: journal@kims-imio.kz, product-service@kims-imio.kz
http://kims-imio.com/index.php/main

«Минералдық шикізаттарды кешенді пайдалану» журналы ғылыми жұмыстардың негізгі нәтижелерін жариялау үшін Қазақстан Республикасы Білім және ғылым министірлігінің Білім және ғылым сапасын қамтамасыз ету комитеті ұсынған ғылыми басылымдар тізіміне енгізілген.
Меншік иесі: «Металлургия және кен байыту институты» АҚ

Журнал Қазақстан Республикасының Ақпарат және коммуникация министрлігінің Байланыс, ақпараттандыру және бұқаралық ақпарат құралдары саласындағы мемлекеттік бақылау комитетінде қайта тіркелген

2016 ж. 18 қазандағы № 16180-Ж Куәлігі

Address:
"Institute of Metallurgy and Ore Beneficiation" JSC
29/133 Shevchenko Street, corner of Ch. Valikhanov Street, Almaty, 050010, Kazakhstan
Fax. +7 (727) 298-45-03, Tel. +7-(727) 298-45-02, +7 (727) 298-45-19
E mail: journal@kims-imio.kz, product-service@kims-imio.kz
http://kims-imio.com/index.php/main

The Journal "Complex Use of Mineral Resources" is included in the List of publications recommended by the Committee for Control in the Sphere of Education and Science of the Ministry of Education and Science of the Republic of Kazakhstan for the publication of the main results of scientific activities.
Owner: "Institute of Metallurgy and Ore Beneficiation" JSC

The Journal was re-registered by the Committee for State Control in the Sphere of Communication, Information and Mass Media of the Ministry of Information and Communication of the Republic of Kazakhstan.

Certificate № 16180-Ж since October 18, 2016

Адрес редакции:
АО «Институт металлургии и обогащения»
050010, Республика Казахстан, г. Алматы, ул. Шевченко, уг. ул. Валиханова, 29/133,
Fax. +7 (727) 298-45-03, Tel. +7 (727) 298-45-02, +7 (727) 298-45-19
E mail: journal@kims-imio.kz, product-service@kims-imio.kz
http://kims-imio.com/index.php/main

Журнал «Комплексное использование минерального сырья» включен в Перечень изданий, рекомендуемых Комитетом по контролю в сфере образования и науки Министерства образования и науки Республики Казахстан для публикации основных результатов научной деятельности.
Собственник: АО «Институт металлургии и обогащения»

Журнал перерегистрирован в Комитете государственного контроля в области связи, информатизации и средств массовой информации
Министерства информации и коммуникации Республики Казахстан
Свидетельство № 16180-Ж от 18 октября 2016 г.

Crossref
DOI: 10.31643/2028/6445.24
Earth and Planetary Sciences: Earth-Surface Processes

Application of bank protection structures for regulation of channel processes in the lower reaches of the Shu River

[1*] Yerzhanova N.K., [2]Mussin Zh.A., [1]Altynbekova A.D.

[1]L.N. Gumilyov Eurasian National University, Astana, Kazakhstan
[2]Kazakh Scientific Research Institute of Water Economy, Taraz, Kazakhstan

** Corresponding author email: nur66gidro@mail.ru*

Received: *March 27, 2026*
Peer-reviewed: *May 16, 2026*
Accepted: *July 10, 2026*

ABSTRACT
The article presents the application of bank protection structures for regulating channel processes in the lower reaches of the Shu River under conditions of high hydrological variability. The analysis is based on long-term hydrological observations conducted at the Tashutkul (Tasotkel) hydrological station over the period 1967–2022. A statistical assessment of annual maximum and mean discharges, including measures of variability, skewness, and exceedance probability, revealed the occurrence of rare but extreme flood events that significantly influence channel deformation and bank erosion in reaches composed of sandy–gravel alluvial deposits. A probabilistic hydrological analysis was applied to justify the design hydraulic loads acting on river training structures. Based on the identified hydrological and morphological risks, an improved prefabricated modular floating bank protection spur was developed for river engineering and channel regulation. The proposed structure provides adjustable permeability, promotes flow energy dissipation, and reduces local scour intensity under different flow conditions. The obtained results may be applied in the design and operation of adaptive bank protection structures for the lower reaches of the Shu River and other rivers characterized by pronounced channel instability and hydrological variability.

Keywords: bank protection spur; erosion protection; river channel regulation; polyethylene beams; hydraulic structure; prefabricated modular structure; flood regulation; hydrological variability; discharge exceedance probability.

Information about authors:
Yerzhanova Nurliza Kiyakbayevna — *Master of Agricultural Sciences, Senior Lecturer, L.N. Gumilyov Eurasian National University, 010000, Satbaev st., 2, Astana, Kazakhstan. Email: nur66gidro@mail.ru; ORCID ID: https://orcid.org/0000-0002-0671-945X*

Mussin Zhasulanbai Akkairovich — *Candidate of Technical Sciences, Kazakh Scientific Research Institute of Water Economy, 080016, Taraz, Kazakhstan. Email: musin_jasulan@mail.ru; ORCID ID: https://orcid.org/0000-0002-8727-5749*

Altynbekova Aliya Doszhankyzy — *PhD, Senior Lecturer, L.N. Gumilyov Eurasian National University, Satbaev st., 2, 010000, Astana, Kazakhstan. Email: kleo-14@mail.ru; ORCID ID: https://orcid.org/0000-0003-1010-9328*

Introduction

Erosion of riverbanks and changes in river channels under the influence of natural and anthropogenic factors represent one of the pressing issues in hydraulic engineering and environmental protection [[1], [2]]. Bank washout, soil collapse, and alterations in river course pose threats to infrastructure, agricultural lands, settlements, and aquatic ecosystems [3]. Under conditions of floods, high water events, and sudden water level fluctuations, traditional bank protection structures, such as levees, embankments, and concrete constructions, often prove insufficiently effective, and their construction requires significant time, financial, and material resources [[4], [5]].

The relevance of this research is driven by the high variability of runoff in Central Asia, frequent floods, and anthropogenic river regulation, which create significant risks to the safety of hydraulic structures and the stability of riverbank zones [[1], [3], [5], [6]]. Modern approaches to the design and construction of bank protection structures include the use of modular and permeable constructions capable of adapting to changing hydrological conditions, reducing flow velocity in the near-bank zone, and decreasing the intensity of erosion [[7], [8], [9]].

When addressing the durability and reliability of hydraulic and land-reclamation structures, particular attention is paid to improving design, implementing new, more environmentally friendly

and cost-effective bank protection technology structures, and developing methods for their hydraulic justification [[10], [11]]. Such structures are characterized by good construction qualities, relative simplicity of installation, and cost efficiency; they integrate harmoniously into the bank zone of any water body and reliably protect it from negative natural and anthropogenic impacts. They can be used both for permanent bank protection and for emergency interventions in critical situations [[8], [12]].

The Zhambyl region is classified as a medium-risk area due to the potential occurrence of floods in the region. A preliminary assessment of flood-prone areas in the country is based on data from RSE «Kazhydromet», including snow reserves, precipitation, autumn soil moisture, soil freezing depth, and river ice conditions. In the event of floods, water may pose a threat to settlements in the Moyynkum, Sarysu, Zhambyl, Shu, Merken, Talas, Korday, Ryskulov, Baizak, and Zhualyn districts. Flooding during the flood-prone period and in the residential area of Tekturmas in Taraz is characteristic [2].

Some flood-related emergencies in the Zhambyl region, reported on regional websites of the Republic of Kazakhstan, in chronological order, include:

- March 27, 2017: Due to increased snowmelt in the mountainous area and higher inflow into the Ters-Ashybulaq Reservoir, there was a risk of washout of the roadway of the «Western Europe–Western China» highway in the Zhambyl district. Additionally, 15 dacha plots and 1 residential house in a dacha settlement, as well as areas in the village of Baiterek, were at risk of flooding. Water levels rose up to 25 centimeters.

- April 2017: In the Talas district, flooding from Lake Akkol caused inundation of the local «Akkol–Usharal» road.

- February 2018: Heavy rainfall, rapid snowmelt, and half-meter soil freezing led to the formation of hillside runoff, resulting in the flooding of 30 yards in three settlements in the Turar Ryskulov district.

- May 20, 2021: Due to heavy rainfall, yard areas in the villages of Ornek, Mamai-Kayindy, and Akyrtobe of the Ryskulov district were flooded. In total, 11 yard areas were flooded, with water levels ranging from 10 to 30 centimeters. Additionally, a local automobile bridge at the entrance to the village of Salimbay in the Ornek rural district was partially damaged.

- February 2023: Due to a sudden warming in the region and its foothill areas, intense snowmelt caused flooding in 11 settlements across four rural districts and in Taraz. Emergency response efforts to combat flooding in the villages of Merken, Tyskulov, Shu, and Zhualyn districts continued for four days.

- July 7, 2024: In the city of Zhanatas, Sarysu district, heavy rainfall caused the formation and passage of hillside runoff along Bayseitova, Ayapova, Yeseeva, Kurmangazy, and Klochkova streets. According to the akimat, more than 200 yard areas and 21 houses located in the foothill area were flooded as a result of the emergency.

The flood period can be complicated by a sudden rise in air temperature, which, in turn, can lead to intensive snowmelt in mountainous areas. The examples considered illustrate the types of natural disasters and enormous losses caused by spring floods on rivers. The only solution is timely preparation to prevent natural catastrophes and mitigate their consequences.

During potential flood periods, particular attention should be paid to existing hydraulic structures in the region (Figure 1). In the Zhambyl region, there are 142 hydraulic structures in operation: 84 reservoirs, 2 dams, 11 hydroelectric complexes, and 44 ponds. These structures are owned by the state, municipal authorities, and private entities.

Figure 1 - Tashutkul Dam with the Right-Bank and Left-Bank Regulators

Analysis shows that hydraulic structures in the region require special attention during the flood-prone period. In the Zhambyl region, there are 142 hydraulic structures in operation: 84 reservoirs, 2 dams, 11 hydraulic complexes, and 44 ponds, which are owned by the state, municipal authorities, and private entities [[1], [3]]. Thus, the relevance of this study lies in the need for a comprehensive assessment of hydrological conditions affecting river channels and bank erosion, as well as in the justification for the use of adaptive bank protection structures capable of effectively regulating channel processes and safeguarding coastal areas.

Experimental part

The methodological basis of this study is a comprehensive statistical analysis of long-term series of annual maximum discharges of the Shu River at the «Tashutkul» hydrological station for the period 1967–2022. The primary aim of the analysis is to determine the statistical characteristics of runoff distribution, assess its variability, identify extreme values, and construct theoretical and empirical exceedance probability curves, which are essential for the design of hydraulic structures and water resources planning.

The calculation of runoff module coefficients, reflecting the ratio of the actual annual discharge to the long-term mean discharge, is expressed as:

$$k_i = Q_i/Q_{mean} \quad (1)$$

The empirical exceedance probability for each discharge value in the ranked series of observations is determined as:

$$\mathrm{P} = \frac{m}{n+1} * 100\% \quad (2)$$

The correctness of the calculations is verified using the following conditions:

$\sum K_i \approx n; \sum(K_i - 1) \approx 0$, with a maximum allowable error of 0.3–0.5%.

Based on the obtained values, the biased coefficients of variation $(\tilde{C}_v)$ and skewness $(\tilde{C}_s)$ are calculated:

$$\tilde{C}_v = \sqrt{\frac{\sum_{i=1}^{n}(K_i-1)}{n-1}} \quad (3)$$

$$\tilde{\mathrm{C}}_\mathrm{s} = \frac{\mathrm{n}\cdot\sum_{\mathrm{i}=1}^{\mathrm{n}}(\mathrm{K_i}-1)^3}{(\mathrm{n}-1)\cdot(\mathrm{n}-2)\cdot\tilde{\mathrm{C}}_\mathrm{v}^3} \quad (4)$$

The adequacy of the observation series is assessed using relative errors:

$$\varepsilon_Q = \frac{C_v}{\sqrt{n}} \cdot 100\% \quad (5)$$

$$\varepsilon_{\mathrm{C_v}} = \sqrt{\frac{1+\mathrm{C_v^1}}{2\cdot\mathrm{n}}} \cdot 100\% \quad (6)$$

The length of the observation series is considered sufficient for the determination of the mean annual discharge Q_{mean} and the biased coefficient of variation $\tilde{C}_v$, if $\varepsilon_Q \leq 5-10\%$, and $\varepsilon_{C_v} \leq 10-15\%$. hus, the observation series for the period 1967–2022 is regarded as sufficient for estimating the mean annual runoff Q_{mean} and the coefficient of variation.

To construct theoretical exceedance probability curves, the calculated coefficients of variation and skewness for the three-parameter gamma distribution and the binomial distribution are used, with coefficients a_1, …, a_6 and b_1, …, b_6 selected in accordance with the ratio $C_s/C_v=2$ and the lag-1 autocorrelation coefficient $r(1)=0.4$. The autocorrelation between adjacent terms of the series is calculated using the following formula:

$$r(1) = \frac{\sum_{i=1}^{n-1}(Q_i-\bar{Q}_1)\cdot(Q_{i+1}-\bar{Q}_2)}{\sqrt{\sum_{i=1}^{n}(Q_i-\bar{Q}_1)^2\cdot\sum_{i=1}^{n-1}(Q_{i+1}-\bar{Q}_2)^2}} \quad (7)$$

Results and Discussion

The results of the study are structured to consistently link the hydrological conditions of the Shu River with the engineering measures aimed at regulating channel processes and protecting riverbanks from erosion. First, the results of the statistical analysis of maximum river discharges are presented, which characterize the hydrological loads governing channel deformation and bank erosion in the lower reaches of the river. Second, based on the identified hydrological and channel-forming conditions, the applicability of a modular floating permeable groyne is substantiated as an adaptive bank protection structure.

1. Statistical Processing and Hydrological Assessment of Maximum Discharges. Analysis of the chronological series of maximum annual discharges of the Shu River at the Tashutkul hydrological station for the period 1967–2022 reveals significant fluctuations in runoff, indicating a high variability of the hydrological regime (Figure 2). During the analyzed period, the minimum maximum discharge was recorded in 1992 at 102 m³/s, while the

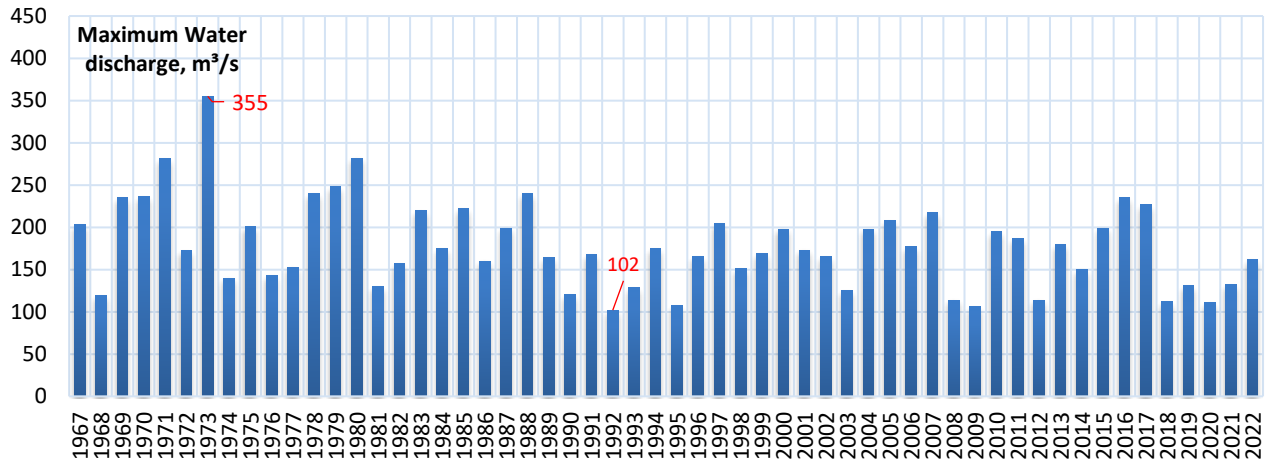

Figure 2 - Chronological series of annual maximum discharges of the Shu River at Tashutkul (1967–2022)

maximum occurred in 1973, reaching 355 m³/s, which is almost four times higher than the minimum value. This extreme reflects the impact of an exceptionally wet year and highlights the significant instability of runoff in the lower reaches of the river. Between 1967 and 1981, maximum discharges showed a stable increasing trend: starting at 203 m³/s in 1967, the values rose to 355 m³/s in 1973. From 1974 to 1981, relatively moderate and fluctuating values were observed (130–282 m³/s), which may be associated with alternating dry and wet periods.

Between 1982 and 1994, maximum discharges decreased, peaking at 240 m³/s in 1988 and reaching a minimum of 102 m³/s in 1992, indicating a prolonged dry period at the end of the 20th century. From 1995 to 2001, maximum discharges increased again, reaching 132 m³/s in 2005; after 2002, maximum discharge values remained high but exhibited pronounced variability (68–287 m³/s), reflecting changing climatic conditions and the influence of anthropogenic factors on the river's flow regime.

The high interannual variability of maximum discharges of the Shu River has important practical implications: it must be considered in the design and operation of hydraulic structures, planning of irrigation systems, flood preparedness, and water resource management. Analysis of extreme values allows for the assessment of the probability of rare but potentially hazardous hydrological events and enhances the reliability of engineering solutions.

To assess the homogeneity of the maximum annual discharges of the Shu River at the Tashutkul hydrological station for the period 1967–1994, the t and F statistical tests were applied. The series of maximum discharges was examined for systematic differences and stability of variance between data subseries.

The t-test showed that the calculated value of t was 1.4109, while the critical tabular value at a significance level of 0.05 is ±2.006. Since the calculated value falls within the critical interval ($-2.006 < 1.4109 < 2.006$), the hypothesis of equality of means is not rejected. This indicates that there are no statistically significant differences in the average maximum discharges between the subseries of the dataset.

The F-test allows for the assessment of equality of variances between two subseries. The calculated F value was 1.523, which is less than the tabular value F = 1.96 at a 0.05 significance level. This confirms that the variances of the subseries do not differ statistically.

The results of both statistical tests indicate the homogeneity of the series of maximum discharges of the Shu River at the Tashutkul hydrological station for the analyzed period. The practical significance of this homogeneity lies in the possibility of using the series for further hydrological analysis, construction of exceedance probability curves, calculation of extreme discharges, and the design of hydraulic structures without the need for adjustments. Stability of the statistical characteristics of the series ensures the reliability of engineering calculations and water management planning.

Based on long-term observations of maximum annual discharges of the Shu River at the Tashutkul hydrological station for 1967–2022, statistical processing was performed using the method of moments. The objective of the analysis is to assess the distribution of extreme discharges, construct the exceedance probability curve, and determine design values for various water management tasks.

The series of maximum discharges exhibits high interannual variability. The calculated parameters are as follows: mean maximum discharge Q_{mean} =179.5 m³/s, coefficient of variation $\tilde{C}_v = 0.4$, reflecting substantial year-to-year fluctuations in maximum runoff; skewness coefficient $\tilde{C}_s = 0.9$, indicating a right-skewed distribution, i.e., the presence of individual years with extremely high discharges. The analysis shows that the river is subject to rare but powerful floods, with several high extreme years (e.g., 1973 - 355 m³/s, 1971 - 281 m³/s, 1980 - 280 m³/s) significantly influencing the mean value and shape of the distribution.

Using the module coefficients k_i , an empirical exceedance probability curve of maximum discharges was constructed. The curve was approximated using a three-parameter gamma distribution, allowing for the assessment of the hydrological reliability of extreme discharges. Comparison of the empirical and theoretical curves showed good agreement, confirming the reliability of the original observations, the correctness of the selected distribution model, and the suitability of the data for engineering design and water management planning.

Based on the constructed exceedance probability curve, design values of maximum discharge were determined for different exceedance probabilities: rare extreme events P ≤ 1 %): $Q_{0.1}$=415 m³/s; Q_1=332.6 m³/s; average conditions (P = 50%): Q_{50}=146 m³/s; minimum guaranteed extremes (P ≥ 95%): Q_{95}=68.97 m³/s. These values allow a quantitative assessment of the range of extreme maximum discharges and can be used for: the design of dams, reservoirs, and hydro complexes; calculation of channel and spillway capacities; and forecasting flood and high-water risks.

Assessment of interannual dependence of maximum discharges revealed a positive first-order autocorrelation *r(1)=0.4* in Figure 3. This indicates the inertia of the hydrological regime, where high or low maximum discharges tend to recur over several consecutive years. This feature is particularly important for long-term water management planning and forecasting of extreme floods. The method of moments confirmed the statistical reliability of the maximum discharge series: the variation and skewness indicators agree with empirical data, and the constructed theoretical exceedance probability curve allows the determination of design discharges for a wide range of probabilities.

After constructing the empirical exceedance probability curve of maximum discharges of the Shu River at the Tashutkul hydrological station, its correspondence with the theoretical curve was verified. The analysis showed that the empirical points generally agree well with the theoretical values, confirming the correctness of the calculated coefficients of variation and skewness of the series, as well as the reliability of the constructed empirical curve. This agreement demonstrates a strong correlation between observed and calculated discharges, providing a basis for water resources analysis, irrigation system planning, and assessment of risks associated with floods or water scarcity.

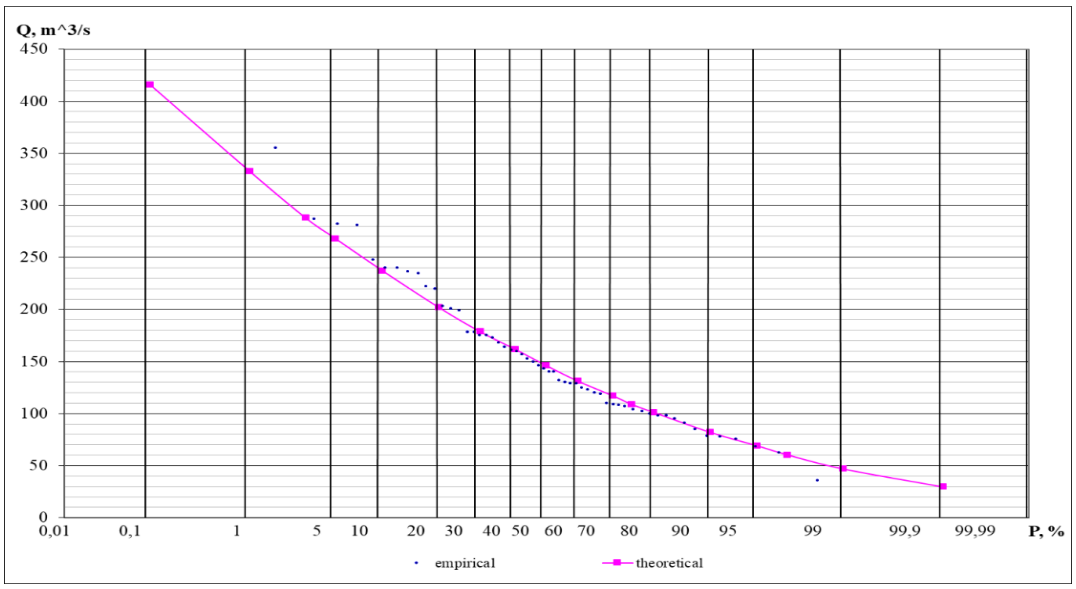

Figure 3 - Exceedance probability curve of annual maximum discharges of the Shu River

Table 1 - Theoretical exceedance probability curve values $C_v = 0.4$ and $C_s=2C_v$

Exceedance probability, *P* (%)	0.1	1	3	5	10	20	30	40	50
Modular coefficient, K_p	2.700	2.160	1.870	1.740	1.540	1.310	1.160	1.050	0.948
River discharge Q_p, m^3/s	415.7	332.6	287.9	267.9	237.1	201.7	178.6	161.7	146.0
Exceedance probability, *P* (%)	60	70	75	80	90	95	97	99	99.9
Modular coefficient, K_p	0.852	0.760	0.708	0.656	0.532	0.448	0.392	0.304	0.192
River discharge Q_p, m^3/s	131.17	117.01	109.00	101.00	81.91	68.97	60.35	46.80	29.56

The calculated ordinates of the exceedance probability curve and the corresponding maximum discharges for different exceedance probabilities are presented in Table 1.

The analysis of the hydrological regime of the Shu River confirms a pronounced interannual variability and significant asymmetry of maximum annual discharges, which indicates the presence of rare but powerful flood events exerting substantial influence on the statistical characteristics of runoff. Similar patterns have been identified for other river systems of Central Asia, where climate change and anthropogenic regulation intensify hydrological extremes and increase uncertainty in the estimation of design discharges [[1], [2], [3]]. Long-term observation series therefore remain a key prerequisite for reliable flood-frequency analysis and assessment of hydraulic structure reliability.

The obtained results demonstrate that, despite noticeable interannual fluctuations, the series of maximum annual discharges remains statistically homogeneous, which is consistent with conclusions reported in hydrological studies emphasizing the importance of multi-decadal datasets for engineering applications [[6], [7]]. The detected positive lag-1 autocorrelation indicates inertia in the hydrological regime, meaning that high-flow and low-flow conditions tend to persist over several consecutive years. Such behavior has been widely discussed in the context of flood risk assessment and should be explicitly considered when evaluating the safety margins of hydraulic engineering structures [[4], [10]]. The application of the method of moments and probabilistic exceedance curves based on the three-parameter gamma distribution proved effective for describing the distribution of extreme discharges. A good agreement between empirical and theoretical curves confirms the adequacy of the selected statistical model and supports its applicability for determining design discharges of various exceedance probabilities [13]. Similar probabilistic approaches have been successfully applied in climate impact assessments for river basins in Kazakhstan, demonstrating their robustness under conditions of increasing hydrological variability [[5], [14]].

The obtained design discharges for low exceedance probabilities (P ≤ 1–5%) indicate that hydraulic loads during extreme flood years may significantly exceed the design parameters of existing hydraulic structures, many of which were constructed based on outdated hydrological norms. This conclusion is consistent with recent studies highlighting increased flood risks and the need to revise design criteria for hydraulic structures under changing climatic conditions [[1], [4], [11]].

2. Improved Prefabricated Modular Floating Bank Protection Spur. An effective method for diverting floodwaters and providing flood protection is the rapid construction of prefabricated, demountable river-regulating structures. Such structures are widely used not only in emergency response situations but also as permanent regulators of local channel deformations. The application of a system of permeable spurs makes it possible to modify the river flow regime, reduce unit discharge, and decrease near-bank flow velocities, thereby transforming a wandering channel into a stable meandering one [8].

The permeable bank protection spur proposed by V.D. Shuminsky [9] is known to reduce erosion of riverbanks and improve flow energy dissipation efficiency through regulation of the structure's porosity coefficient. In hydraulic engineering practice, the «Movable Bank Protection Spur» [15] is also used, maintaining its operational performance under varying hydrological conditions. Traditionally, such structures are installed from the riverbank at a specific angle to the flow and consist of an abutment (root), a main body, and a head section, which is subjected to the most intensive erosive forces. However, rigid fixed structures have several disadvantages: during ice drift, they reduce the effective ice passage width and act as partial dams [[16], [17]]; moreover, under variable water levels and flow velocities, they require excessive height

and material consumption, being designed based on extreme maximum hydrological conditions [[8], [12]].

A more advanced type is the floating bank protection spur [18], which is capable of operating in both solid and permeable flow regimes. Its structural disadvantages include the need for preparatory works involving the placement of reinforced concrete blocks in the lower part of the structure, the complexity of installing stoppers and embedded components, which reduces the speed of assembly, as well as the circular surface of the pipes used, which increases flow slip and reduces transverse roughness [[9], [16]].

Based on an analysis of existing river-regulating and bank protection structures, as well as prefabricated floating bank protection spur systems, this paper presents the development of an improved prefabricated floating bank protection spur design that eliminates the identified shortcomings.

This is achieved through an improved prefabricated floating bank protection spur design, in which the upper part consists of hollow polyethylene beams with a cross-sectional size of 20 × 15 cm, hermetically sealed at the ends. The lower part of each beam is equipped with mounting holes through which the elements are installed onto a cable; one end of the cable is fixed to a driven metal stake using a fastening clamp or anchored, while the other end is secured to the bank after installation is completed. When operating in a permeable spur mode, polyethylene spacer bushings with the required degree of porosity are installed between the beams along the axis. The upper free part of the beams remains in a floating condition.

As a result of the improvement of the prefabricated floating bank protection spur, the upper part is replaced with polyethylene beams, while the lower part is freely mounted on a cable without a foundation base, which allows the structure's configuration to be adjusted depending on hydrological conditions and operating regimes.

An important advantage of the proposed spur is the ability to regulate its permeability through replaceable spacing elements. This enables flexible control of flow velocity, energy dissipation, and sediment transport downstream of the structure, ensuring effective performance under extreme flood events, medium discharges, and low-flow periods. Such adaptability significantly distinguishes the proposed design from traditional spurs and enhances its reliability under conditions of hydrological uncertainty [[15], [17]].

Overall, the integration of long-term flow analysis with adaptive engineering solutions provides a comprehensive approach to improving the reliability and safety of hydraulic structures. For transboundary river systems such as the Shu River, where climatic variability, upstream flow regulation, and increasing water resource demands jointly affect the hydrological regime, the combined application of probabilistic hydrological assessment and flexible bank protection structures is particularly well justified [[2], [11], [16], [18], [19], [20]].

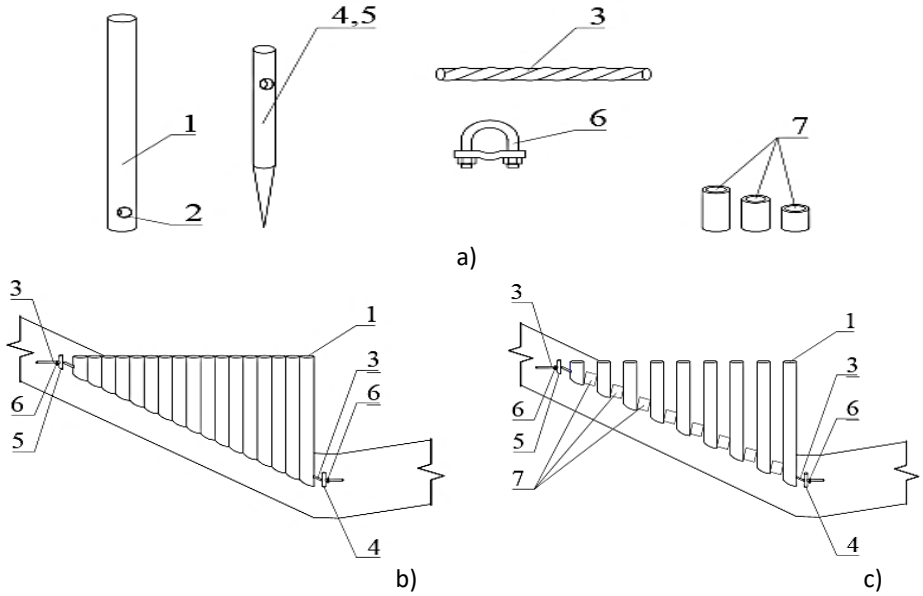

a – Prefabricated elements of the improved modular floating bank protection spur: 1 – polyethylene beams, 2 – mounting holes, 3 – cable, 4,5 – metal stake, 6 – fastening clamp, 7 – polyethylene spacer bushings; b, c – assembled solid and through versions of the improved modular floating bank protection spur.

Figure 4 - Improved modular floating bank protection spur

For the practical implementation of the proposed spur and the evaluation of its hydraulic performance, it is necessary to determine the principal structural and hydraulic parameters governing the interaction between the structure and the flow. The definition of the permeability coefficient follows the calculation methodology for combined permeable river training structures [21]. Owing to the different geometry of the proposed design, the original calculation relationships were adapted for a system of horizontally oriented polyethylene beams and adjustable spacer bushings.

The fundamental design parameter is the permeability (porosity) coefficient of the structure (P), defined as the ratio of the open (permeable) area of the structure to the total area of its frontal projection:

$$P = \frac{\omega_c}{\omega} = \frac{\omega_c}{\omega_b + \omega_c} \quad (8)$$

where:

$$\omega_c = (d_1 + d_2 + \cdots + d_m) \cdot H \quad (9)$$

$$\omega_b = (s_1 + s_2 + \cdots + s_n) \cdot H \quad (10)$$

Here: $\omega_b, \omega_c, \omega$ - the areas occupied by the beams, the inter-beam openings, and the total frontal area of the structure, respectively, m²; $s_1, s_2, \cdots, s_n$ - the frontal widths of the beams, m; $d_1, d_2, \cdots, d_m$ - the widths of the openings between the beams, which are adjustable through the length of the spacer bushings, m; n - the number of beams; m is the number of inter-beam openings ($m = n - 1$); H - the design flow depth, m.

For a structure with uniformly spaced beams of equal width (s) and openings of equal width (d), Equation (8) can be simplified as follows:

$$P = \frac{d}{s+d} \quad (11)$$

The permeability coefficient is related to the channel blockage coefficient by the following relationship:

$$P = 1 - P_b \quad (12)$$

Adaptation of the proposed structure to different hydrological conditions is achieved by varying the length of the spacer bushings. For a polyethylene beam with a frontal width of $s = 0.20$ m, an opening width of d=0.20 m is adopted under mean-flow conditions ($Q_{50\%}$), corresponding to a permeability coefficient of P=0.50. Under extreme flood conditions ($Q_{1\%}$), the opening width is increased to d=0.30 m, resulting in a permeability coefficient of P=0.60 and a corresponding reduction in the hydrodynamic load acting on the retaining cable.

The flow velocity immediately downstream of the proposed permeable spur (V_p) is determined using the velocity coefficient φ, based on the analytical relationships reported in [22] and their subsequent nonlinear approximation using experimental datasets presented in [21]:

$$V_p = \varphi \cdot V_1 = [1{,}2 \cdot P^{0,4} \cdot (1 - P)^{0,1}] \cdot V_1 \quad (13)$$

where: φ - the dimensionless velocity coefficient of the permeable barrier accounting for turbulent head losses; P - the dimensionless permeability (porosity) coefficient of the spur flow section, determined by the length of the spacer bushings; V_1 - the approach flow velocity of the Shu River during the design flood corresponding to $Q_{1\%}$, m/s. The permeability coefficient P is related to the structural blockage coefficient P_b by the relationship $P_b = 1 - P$.

The kinematic structure of flow deformation downstream of permeable elements has been comprehensively investigated in the monograph [21]. Based on the experimental jet-contraction curves and the relationships between the geometric characteristics of the deformation zones, the channel blockage ratio (n), and the installation angle of the structure (α) presented therein, the authors of the present study performed an analytical approximation of the experimental datasets using the least-squares method in Microsoft Excel. The resulting regression equation (13) represents a local empirical model and is applicable within the investigated permeability range of $0.2 \leq P \leq 0.6$, which, according to the experimental conditions reported in [21] and the relationship between the coefficients, corresponds to blockage coefficients of $0.4 \leq P_b \leq 0.8$.

Statistical analysis of the long-term observational series (1967–2022) at the reference Tashutkul hydrological station showed that, under extreme conditions corresponding to the centennial flood discharge $Q_{1\%}$, the design mean flow depth is H= 2.5 m, while the mean approach velocity is V_1 = 1.8 m/s. Under these conditions, the proposed floating structure provides controlled flow velocity reduction downstream of the barrier. In the baseline operating mode at a permeability coefficient P=0.50

(blockage coefficient P_b = 0.50), the flow velocity downstream of the structure V_p decreases to 1.55 m/s (a reduction of 14%), while the kinetic energy of the flow is dissipated by up to 26%. In the extreme flood operating mode (P = 0.60, corresponding to P_b = 0.40), the velocity downstream of the spur is 1.61 m/s (a reduction of 11%), and the kinetic energy of the surface flow layer is effectively dissipated by 20%, which minimizes the risk of bank deformation in reaches composed of sandy–gravel deposits with particle sizes d_i= 1.0÷2.5 mm.

Based on experimental studies presented in [21], it has been substantiated that the velocity distribution in the zone of intense turbulent mixing follows the universal self-similar Schlichting–Abramovich law. The classical physical foundations of this relationship for channel flows are described in detail in [23]:

$$\frac{u-u_*}{u_{max}-u_*} = (1-\eta^{1.5})^2 \qquad (14)$$

where: u - the local longitudinal flow velocity at the considered point in the downstream reach, m/s; u_* - the velocity of the co-flow penetrating through the permeable gaps of the bushings, m/s; u_{max} - the maximum velocity at the boundary of the core of the main (transit) flow; η - the dimensionless relative vertical coordinate of the investigated cross-section.

This theoretical justification enables the application of the classical velocity distribution law for numerical assessment of flow kinematics downstream of the proposed spur, thereby preventing the formation of hazardous secondary (reverse and unstable) flow structures.

Based on the maximum hydrodynamic loading during the extreme flood event $Q_{1\%}$ at the Tashutkul hydrological station, the peak longitudinal tensile force (T) acting on the supporting cable system was determined. In accordance with the requirements of the regulatory document SP RK 3.04-107-2014 [24], the longitudinal component of the flow force (N_w, kN) was adapted to the geometry of the permeable barrier of the proposed floating structural model:

$$T = N_w = 0.59 \cdot (b \cdot h_1) \cdot {V_1}^2 \cdot P_b \qquad (15)$$

where: T - the distributed hydrodynamic load on the supporting steel cable, kN/m; N_w - the distributed longitudinal component of the flow force acting on the structure, kN/m; 0.59 - the hydrodynamic coefficient according to SP RK 3.04-107-2014 [24]; b - the frontal width of the polyethylene beam (0.20 m); h_1 - the design flood depth at the Tashutkul hydrological station cross-section (2.5 m); V_1 - the approach flood-flow velocity (1.8 m/s), which governs the loading on the cable as it is induced by the incoming flow; P_b - the dimensionless blockage (channel constriction) coefficient of the spur formed by the beams according to [21].

Substitution of field hydrological parameters of the Shu River under emergency extreme flood conditions (V_1 = 1.8 m/s), with a frontal projection area of the beam ($b \cdot h_1$) = 0.5 m², and a blockage coefficient in extreme conditions P_b = 0.40 (corresponding to a permeability coefficient P = 0.60), yields a peak distributed load on the supporting cable of T = 0.382 kN/m (or 382.3 N/m). The obtained hydrodynamic load characterizes the force exerted by the flow on the supporting system of the structure and may be used for subsequent structural design and selection of the retaining cable parameters.

The quantitative design assessment of the static and dynamic stability of the floating element in the river flow was performed based on the balance of vertical forces. The distributed buoyant force (F_A), N/m, was determined using the following expression:

$$F_A = \rho_v \cdot g \cdot (a \cdot b) \qquad (16)$$

where: ρ_v - the water density (1000 kg/m³); g - the gravitational acceleration (9.81 m/s²); a and b - the geometric dimensions of the cross-section of the polyethylene beam (0.15 × 0.20 m). Substitution of the structural parameters yields a buoyant force under full submergence of F_A = 294.3 N/m. Considering the distributed self-weight load of the polyethylene beams together with the supporting cable (F_b = 65.0 N/m), the net static buoyancy reserve of the structure amounts to 229.3 N/m.

To assess the dynamic stability of the proposed structure under flood conditions, the associated vertical (downward) hydrodynamic force (Q_w), arising from the pressure difference and tending to press the floating barrier toward the riverbed, was calculated. The computation was performed in accordance with the regulatory provisions of SP RK 3.04-107-2014 [24] using the following expression:

$$Q_w = 0.59 \cdot A_1 \cdot {V_1}^2 \cdot P_b \qquad (17)$$

where: A_1 - the lateral submerged projected area (sail area) of the submerged element per unit length of the structure, taken as $a \cdot 1$ = 0.15 m²; V_1 -

the approach flood-flow velocity of the Shu River at the design discharge $Q_{1\%}$, (1.8 m/s); P_b - the dimensionless blockage coefficient of the spur.

The obtained value of the hydrodynamic submerging force under the design permeability of the structure (P = 0.50, corresponding to a blockage coefficient P_b = 0.50) is:

$Q_w = 0.59 \cdot 0.15 \cdot (1.8)^2 \cdot (1 - 0.50) = 0.143$ kN/m or (143,4) N/m

A comparison between the dynamic submerging force and the net static buoyancy reserve shows that the restoring Archimedes forces exceed the destabilizing hydrodynamic forces by a factor of 1.6 (229.3/143.4 ≈ 1.6). This result indicates sufficient stability of the floating barrier and the maintenance of its stable operating position at the water surface even during the passage of a critical centennial flood with a 1% exceedance probability at the Tashutkul hydrometric station cross-section.

For a quantitative assessment of erosional channel processes beneath the proposed structure, the relationship of I.I. Levi for permeable systems was used to estimate the limiting depth of local scour H_{p} [[21], [25]]:

$$H_p = h_1 \cdot \left(\frac{V_p}{V_n}\right)^{1.2} \cdot {P_b}^{0,5} \qquad (18)$$

where: h_1 - the design flood depth at the Tashutkul hydrological station cross-section, m; V_p - the flow velocity immediately downstream of the permeable spur, m/s; V_n - the critical non-scouring velocity of the flow for the riverbed soils of the Shu River, m/s; P_b - the dimensionless blockage (constriction) coefficient of the structure formed by the beams.

The physical meaning of equation (18) lies in the modification of the classical erosional framework proposed by I.I. Levi through the introduction of a reducing dimensionless factor (${P_b}^{0,5}$). This coefficient accounts for the jet-like structure of the flow in the downstream reach and the reduction in unit discharge due to partial filtration of water through the regulated gaps between the spacer bushings of the proposed structure.

Downstream of the Tashutkul hydrological station, the riverbed of the Shu River consists of sandy–gravel alluvial deposits with a mean weighted sediment diameter of (d_i = 1.0–2.5) mm. For this type of soil and a flood depth of 2.5 m, the mean cross-sectional non-scouring velocity ranges from 0.85÷1.20 m/s. However, in the present study, the critical near-bed velocity corresponding to the initiation of sediment motion, equal to 0.55 m/s according to a verified methodology, was adopted as the design value of (V_n) in equation (18). Partial conveyance of flood discharge through the body of the proposed floating spur leads to a reduction in the calculated depth of the local scour hole at the structure head by 15–37% compared with solid prototype structures.

As shown in numerical hydrodynamic studies [26], localized flow velocities at the head of permeable spurs decrease due to nonlinear filtration processes. The proposed structure allows maintaining the permeability coefficient within the optimal range P = 0.50÷0.60 (corresponding to a blockage coefficient P_b = 0.50÷0.40). This ensures the «flattening» (spreading) of the near-bed vortex zone downstream of the barrier and increases the effective length of the protected riverbank to 4–10 times the length of the structure itself.

The sedimentation regime analysis within the spur cells was performed according to the regional methodology of «KRSU» for piedmont–plain conditions of the Shu River. The critical near-bed velocity at which transported sediments begin to deposit in the inter-spur space ($V_{i.s.}$, m/s) is determined using the relationship proposed by V.F. Talmaza [27], which has been thoroughly validated in studies of the Shu River [28]:

$$V_{i.s.} = 1{,}4 \cdot \frac{m-1{,}5}{m+1} \cdot \left(\frac{H_i}{d_i}\right)^{\frac{1}{m}} \cdot \sqrt{\frac{\gamma_n - \gamma_v}{\gamma_n} \cdot g \cdot d_i} \qquad (19)$$

where: m = 4 is the exponent describing the vertical velocity distribution for the considered reach; H - the design flood depth (2.5 m); d_i - the mean weighted diameter of sandy–gravel sediments (1.0–2.5 mm); γ_n and γ_v - the unit weights of bed sediments (26.5 kN/m³) and river water (10.0 kN/m³), respectively; g - the gravitational acceleration (9.81 m/s²).

Adjustment of the permeability of the proposed floating spur to the optimal range of 0.50÷0.60 (achieved through the selection of polyethylene spacer bushings) artificially reduces the local near-bank flood velocity V_p within the inter-spur zone to a level satisfying the sedimentation condition $V_p \leq V_{i.s.}$. This ensures stable and controlled accumulation of sandy–gravel material within the spur cells, prevents the formation of hazardous impinging flow conditions, and promotes natural aggradation and widening of the protected riverbank zone on the Kazakhstan side of the transboundary Shu River.

For an objective assessment of technical advancement and to substantiate the novelty of the

Table 2 – Comparative Assessment of the Hydraulic Performance of the Proposed and Prototype Bank Protection Spurs

Hydraulic and Structural Parameter	Floating Prototype (Rigid Sealed Pipes)	Proposed Modular Permeable Spur	Quantitative Assessment of Technical Advancement Based on Verification
Regulation of permeability (P)	Fixed ($P \leq 0.15$)	Adjustable (P = 0.20÷0.60)	Adaptation to flood variability ranging from 50% to 1% exceedance probability in the Shu River
Flow velocity reduction coefficient (V_p/V_1)	Uncontrolled flow impingement and attachment	Reduction of flow velocity immediately downstream of the spur by 11–14%	Transformation of near-bank flow into a safe non-erosive regime ($V_p \leq V_{i.s.}$)
Degree of flow kinetic energy dissipation (E_k)	Intense local vortex formation at the head	Internal friction of split jets (energy dissipation of 20–45%)	Effective dissipation of kinetic energy within the permeable body of the spur
Local scour depth beneath the structure (H_p)	High (1,3 ÷1,5h_1)	Minimized (reduction of calculated scour depth by 32–37%)	Reduced risk of structural undermining; expansion of the protection zone up to 4–10 spur lengths (according to validated methodology [25])
Installation complexity and deployment rate	High (on-site welding and installation of heavy bed anchors required)	Low (modular assembly on a bank-mounted cable without heavy machinery)	High operational efficiency for emergency flood response conditions

claimed utility model, a comparative analysis of its characteristics with a baseline floating prototype made of rigid sealed pipes was conducted. The comparative evaluation, verified using external sources, is summarized in Table 2.

The implementation of the proposed engineering solution enables a transition from passive resistance to the dynamic impact of the river flow to active and controlled regulation of channel deformation processes. This makes the developed floating structure particularly suitable for bank protection in transboundary river basins (notably the Shu River), which are characterized by high variability of flood discharge and intensive anthropogenic flow regulation.

Conclusions

The study of channel processes in the lower reaches of the Shu River revealed pronounced interannual variability of river discharge, which intensifies bank erosion during extreme flood events. Based on long-term hydrological observations, design discharges corresponding to different exceedance probabilities were determined and used to justify the hydraulic loads acting on bank protection structures in accordance with the fundamental principles of hydrodynamics [23]. As an adaptive engineering solution, an improved prefabricated modular floating bank protection spur with adjustable permeability is proposed. Computational and theoretical analyses, together with a comparison with a conventional rigid prototype, confirmed its advantages in terms of structural stability, ease of installation, and overall hydraulic performance.

Based on the hydraulic justification of the structural parameters for the proposed spur at the Tashutkul hydrological station cross-section of the Shu River, the following conclusions were drawn:

1. It was established that varying the length of the polyethylene spacer bushings from 0.20 to 0.30 m allows the permeability coefficient of the structure to be adjusted within the range $0.50 \leq P \leq 0.60$, which, according to the relationship ($P_b = 1 - P$), corresponds to channel blockage coefficients of $0.40 \leq P_b \leq 0.50$. This enables the spur to adapt to both mean annual flow conditions ($Q_{50\%}$ = 146.0 m³/s) and extreme flood discharges ($Q_{1\%}$ = 332.6 m³/s).

Quantitative evaluation of the hydraulic performance showed that, at the baseline permeability coefficient P = 0.50, the proposed structure reduces the approach flood-flow velocity by 14% (from 1.80 to 1.55 m/s) and dissipates up to 26% of the flow kinetic energy. Under the extreme operating condition (P = 0.60), the flow velocity immediately downstream of the spur is reduced to 1.61 m/s, corresponding to a 20% reduction in the kinetic energy of the surface flow layer.

Partial conveyance of flood discharge through the permeable body of the spur reduces the intensity of local scour at the spur head by 15–37% compared with impermeable prototype structures. Redistribution of the flow structure increases the effective length of the protected riverbank to

approximately 4–10 times the length of the structure itself.

Reducing the local near-bank velocity within the inter-spur zone to the condition ($V_p \leq V_{i.s.}$) creates favorable hydraulic conditions for the stable deposition of sandy–gravel sediments, prevents the formation of hazardous bank-attached currents, and promotes the natural accretion of the protected riverbank.

The calculated peak distributed hydrodynamic load acting on the supporting system is T = 382.3 N/m. At the same time, the net static buoyancy reserve of the polyethylene beams (229.3 N/m) exceeds the dynamic submerging force of the flow (143.4 N/m) by a factor of 1.6, thereby ensuring the stability of the floating structure. The calculated hydrodynamic load characterizes the force exerted by the flow on the supporting system and may be used for the subsequent structural design and selection of the retaining steel cable.

The obtained results confirm the potential of the proposed improved prefabricated modular floating permeable bank protection spur for river engineering applications, including bank protection and channel regulation in rivers characterized by high hydrological variability and intensive anthropogenic flow regulation.

Conflicts of interest. On behalf of all authors, the corresponding author states that there is no conflict of interest.

CRediT author statement: **N. Yerzhanova**: Conceptualization, Data curation, Writing draft preparation, Supervision, Visualization and Investigation; **Zh. Mussin**: Supervision, Methodology; **A. Altynbekova**: Software, Validation, Reviewing and Editing.

Cite this article as: Yerzhanova NK, Mussin ZhA, Altynbekova AD. Application of bank protection structures for regulation of channel processes in the lower reaches of the Shu River. Kompleksnoe Ispolzovanie Mineralnogo Syra = Complex Use of Mineral Resources. 2028; 346(3):5-18. https://doi.org/10.31643/2028/6445.24

Шу өзенінің төменгі ағысындағы арналық процестерді реттеу үшін жағалауды қорғау құрылымдарын қолдану

[1]Ержанова Н.К., [2]Мусин Ж.А., [1]Алтынбекова А.Д.

[1]Л.Н. Гумилев атындағы Еуразия ұлттық университеті, Астана, Қазақстан
[2]Қазақ су шаруашылығы ғылыми-зерттеу институты, Тараз, Қазақстан

Мақала келді: *27 наурыз 2026*
Сараптамадан өтті: *16 мамыр 2026*
Қабылданды: *10 шілде 2026*

ТҮЙІНДЕМЕ

Мақалада гидрологиялық режимнің жоғары өзгергіштігі жағдайында Шу өзенінің төменгі ағысындағы арналық процестерді реттеу үшін жағалауды қорғау құрылыстарын қолдану мәселелері қарастырылған. Зерттеу 1967–2022 жылдар аралығында Ташуткөл (Тасөткел) гидробекетінде жүргізілген көпжылдық гидрологиялық бақылаулар деректеріне негізделген. Жылдық ең жоғары және орташа су шығындарына, олардың өзгергіштігіне, асимметриясына және қамтамасыз етілуіне жүргізілген статистикалық талдау сирек кездесетін, бірақ арнаның деформациясы мен құмды-қиыршықтасты шөгінділерден құралған жағалаулардың шайылуына елеулі әсер ететін экстремалды су тасқыны оқиғаларының бар екенін көрсетті. Арнаны реттейтін құрылыстарға әсер ететін есептік гидравликалық жүктемелерді негіздеу үшін ағындының ықтималдық талдауы қолданылды. Анықталған гидрологиялық және морфологиялық қауіптер негізінде инженерлік қорғау мен арналық процестерді реттеуге арналған жетілдірілген құрастырмалы-жиналмалы қалқымалы жағалауды қорғау шпорасының конструкциясы ұсынылды. Ұсынылған конструкция өткізгіштік дәрежесін реттеуге, ағын энергиясын бәсеңдетуге және әртүрлі ағыс режимдерінде жергілікті шайылу қарқындылығын төмендетуге мүмкіндік береді. Алынған нәтижелер Шу өзенінің төменгі ағысында және арналық процестері мен гидрологиялық режимі айқын тұрақсыз өзге де өзендерде бейімделгіш жағалауды қорғау құрылыстарын жобалау мен пайдалануда қолданылуы мүмкін.

Түйін сөздер: жағалауды қорғау шпорасы, шайылудан қорғау, арнаны реттеу, полиэтилен арқалықтары, гидротехникалық құрылыс, құрастырмалы-жиналмалы конструкциясы, су тасқынын реттеу, гидрологиялық өзгермелілік, су шығынының қамтамасыз етілуі.

Авторлар туралы ақпарат:

Ержанова Нурлиза Киякбаевна — *Ауыл шаруашылығы ғылымдарының магистрі, аға оқытушы, Л.Н. Гумилев атындағы Еуразия ұлттық университеті, Сәтбаев к-сі, 2, 010000, Астана, Қазақстан. Email: nur66gidro@mail.ru; ORCID ID: https://orcid.org/0000-0002-0671-945X*

Мусин Жасуланбай Аккаирович — *Техника ғылымдарының кандидаты, Қазақ су шаруашылығы ғылыми-зерттеу институты, 080016, Тараз, Қазақстан. Email: musin_jasulan@mail.ru; ORCID ID: https://orcid.org/0000-0002-8727-5749*

Алтынбекова Алия Досжанкызы	*PhD докторы, аға оқытушы, Л.Н. Гумилев атындағы Еуразия ұлттық университеті, Сәтбаев к-сі, 2, 010000, Астана, Қазақстан. Email: kleo-14@mail.ru; ORCID ID: https://orcid.org/0000-0003-1010-9328*

Применение берегозащитных сооружений для регулирования русловых процессов реки Шу в нижнем течении

[1]Ержанова Н.К., [2]Мусин Ж.А., [1]Алтынбекова А.Д.

[1] Евразийский национальный университет им. Л.Н. Гумилева, Астана, Казахстан
[2] Казахский научно-исследовательский институт водного хозяйства, Тараз, Казахстан

Поступила: *27 марта 2026*
Рецензирование: *16 мая 2026*
Принята в печать: *10 июля 2026*

АННОТАЦИЯ

В статье рассмотрено применение берегозащитных сооружений для регулирования русловых процессов в нижнем течении реки Шу в условиях высокой изменчивости гидрологического режима. Анализ выполнен на основе многолетних гидрологических наблюдений на гидропосту Ташуткуль (Тасоткель) за период 1967–2022 гг. Статистическая оценка максимальных и средних годовых расходов воды, включая показатели изменчивости, асимметрии и обеспеченности, выявила наличие редких, но экстремальных паводковых событий, существенно влияющих на деформацию русла и размыв берегов, сложенных песчано-гравелистыми отложениями. Для обоснования расчетных гидравлических нагрузок, действующих на руслорегулирующие сооружения, применен вероятностный анализ стока. На основе выявленных гидрологических и морфологических рисков предложена усовершенствованная сборно-разборная конструкция плавающей берегозащитной шпоры, предназначенная для инженерной защиты и регулирования русловых процессов. Конструкция позволяет регулировать проницаемость, обеспечивать рассеивание энергии потока и снижать интенсивность размыва при различных режимах течения. Полученные результаты могут быть использованы при проектировании и эксплуатации адаптивных берегозащитных сооружений в нижнем течении реки Шу и на аналогичных реках с выраженной русловой и гидрологической нестабильностью.

Ключевые слова: берегозащитная шпора, защита от размыва, регулирование русел, полиэтиленовые брусья, гидротехническое сооружение, сборно-разборная конструкция, регулирование паводков, гидрологическая изменчивость, обеспеченность расходов.

Информация об авторах:

Ержанова Нурлиза Киякбаевна — *Магистр сельскохозяйственных наук, старший преподаватель, Евразийский национальный университет им. Л.Н. Гумилева, Астана, Казахстан, ул. Сатпаева, 2, 010000, Астана, Казахстан. Email: nur66gidro@mail.ru; ORCID ID: https://orcid.org/0000-0002-0671-945X*

Мусин Жасуланбай Аккаирович — *Кандидат технических наук, Казахский научно-исследовательский институт водного хозяйства, 080016, Тараз, Казахстан. Email: musin_jasulan@mail.ru; ORCID ID: https://orcid.org/0000-0002-8727-5749*

Алтынбекова Алия Досжанкызы — *Доктор PhD, старший преподаватель, Евразийский национальный университет им. Л.Н. Гумилева, Астана, Казахстан, ул. Сатпаева, 2, 010000, Астана, Казахстан. Email: kleo-14@mail.ru; ORCID ID: https://orcid.org/0000-0003-1010-9328*

References

[1] Didovets I, Lobanova A, Krysanova V, Menz C, Babagalieva Z, Nurbatsina A, Hattermann F. Central Asian Rivers under Climate Change: Impacts assessment in eight representative catchments. Journal of Hydrology: Regional Studies. 2021; 34:100779. https://doi.org/10.1016/j.ejrh.2021.100779

[2] Kaliyeva K, Punys P, Zhaparkulova Y. The impact of climate change on hydrological regime of the transboundary River Shu Basin (Kazakhstan–Kyrgyzstan): forecast for 2050. Water. 2021; 13(20):2800. https://doi.org/10.3390/w13202800

[3] Issaldayeva S, Alimkulov S, Raimbekova Z, Bekseitova R, Karatayev M. The climatic and river runoff trends in Central Asia: The case of Zhetysu Alatau region, the south-eastern part of Kazakhstan. Heliyon. 2023; 9(7):e17897. https://doi.org/10.1016/j.heliyon.2023.e17897

[4] Kundzewicz ZW, Kanae S, Seneviratne SI. Flood risk and climate change: global and regional perspectives. Hydrological Sciences Journal. 2014; 59(1):1-28. https://doi.org/10.1080/02626667.2013.857411

[5] Chen F, Yuan Y, Trouet V, Büntgen U, Esper J, Chen F, Zhang H. Ecological and societal effects of Central Asian streamflow variation over the past eight centuries. Climate and Atmospheric Science. 2022; 5(1):27. https://doi.org/10.1038/s41612-022-00239-5

[6] Yue S, Pilon P, Phinney BOB. Canadian streamflow trend detection: impacts of serial and cross-correlation. Hydrological Sciences Journal. 2003;48(1):51-63. https://doi.org/10.1623/hysj.48.1.51.43478

[7] Hamed KH. Trend detection in hydrologic data: The Mann–Kendall trend test under the scaling hypothesis. Journal of hydrology. 2008;349(3-4):350-363. https://doi.org/10.1016/j.jhydrol.2007.11.009

[8] Giupponi C, Gain AK. Integrated water resources management (IWRM) for climate change adaptation. Regional

Environmental Change. 2017;17(7):1865-1867. https://doi.org/10.1007/s10113-017-1173-x

[9] SU1070257A1 Russia. Skvozna beregozashchitna shpora [Permeable bank protection spur]. Shuminsky VD. Patent of the USSR. 1982. (in Russ.).

[10] Rakhimova M, Liu T, Bissenbayeva S, Mukanov Y, Gafforov KS, Bekpergenova Z, Gulakhmadov A. Assessment of the Impacts of Climate Change and Human Activities on Runoff Using Climate Elasticity Method and General Circulation Model (GCM) in the Buqtyrma River Basin, Kazakhstan. Sustainability. 2020; 12(12):4968. https://doi.org/10.3390/su12124968

[11] Tazhiyev S, Murtazin Y, Rakhimova V, Rakhmetov I, Adenova D, Koshpanova K, Sotnikov Y, Abdizhalel M, Akylbayeva A, Yerezhep D. Applied Hydrogeological Assessment and GIS-Based Modeling of Transboundary Aquifers in the Shu River Basin. Water. 2025; 17(16):2476. https://doi.org/10.3390/w17162476

[12] Yapiyev V, Ongdas N, Saidaliyeva Z, Zhiyenbek A, Smogulova T, Baigaliyeva M, Prikaziuk E. Baseline information and regionalization of the large river basins of Kazakhstan. Frontiers in Water. 2025; 7:1601671. https://doi.org/10.3389/frwa.2025.1601671

[13] Bolatova A, Krysanova V, Lobanova A, Bolatov K. Assessment of climate change impacts for two tributary basins of the Irtysh River in Kazakhstan. Climate Research. 2023; 91:159-174. https://doi.org/10.3354/cr01726

[14] Tursunova A, Nurbatsina A, Salavatova Z, Huthoff F. Sustainability Challenges in Kazakhstan's River Systems: Assessing Climate-Induced Hydrological Changes. Sustainability. 2025; 17(8):3405. https://doi.org/10.3390/su17083405

[15] RU2730607C1 Russia. Podvizhnaya beregozashchitnaya shpora [Movable bank protection spur]. Kupchikova NV. Patent of the Russian Federation. 2020. (in Russ.).

[16] Yerzhanova NK, Sennikov MN, Transgranichnoe sotrudnichestvo v sfere upravleniya riskami pavodkov [Transboundary Cooperation in Flood Risk Management], Mezhdunarodnaya nauchno-prakticheskaya konferentsiya «Teoreticheskie i prikladnie problemi geografii» [International Scientific and Practical Conference «Theoretical and Applied Problems of Geography»], Astana, 20 May. L.N. Gumilyov Eurasian National University. 2024, 244-248. (in Russ.).

[17] US20240279892A1 USA. River training structure, system comprising river training structure, and method for training a river. Jan SR. US international patent application. 2021.

[18] KZ27570 Kazakhstan. Sborno-razbornaya konstruktsiya plavayushchei beregozashchitnoi shpori [Prefabricated modular floating bank protection spur]. Bakbergenov NN, Musin Zh. Patent of the Kazakhstan. 2013. (in Russ.).

[19] Sennikov MN, Yerzhanova NK, Sovershenstvovanie upravleniya transgranichnimi vodnimi resursami po Shu-Talasskomu basseinu Respubliki Kazakhstan [Improving the management of transboundary water resources in the Shu-Talas basin of the Republic of Kazakhstan], Materiali Mezhdunarodnoi konferentsii SVO VEKTsA «Problemi upravleniya rechnimi basseinami v usloviyakh izmeneniya klimata» [Proceedings of the International Conference of the North-Eastern European Central Asian Region «Problems of River Basin Management in the Context of Climate Change»], Tashkent, 18-19 May, 2017. NITs MKVK. 2017, 208. (in Russ.).

[20] Sennikov MN, Yerzhanova NK, Prognoznoe povishenie vodoobespechennosti po regulirovaniyu vodnimi resursami Zhambilskoi oblasti [Projected Increase in Water Availability for Water Resources Regulation in Zhambyl Oblast], Mezhdunarodnaya nauchno-prakticheskaya konferentsiya Innovatsionnie i prakticheskie resheniya uskorennogo vosstanovleniya produktivnosti degradirovannikh oroshaemikh zemel KazNIIVKh [International Scientific and Practical Conference Innovative and Practical Solutions for Accelerated Restoration of Degraded Irrigated Land Productivity], Taraz, 20 May, 2022. KazNIIVH. 2022, 68-72. (in Russ.).

[21] Khalimbetov AB, Bakiev MR, Khudaiberganov HA, Sovershenstvovanie konstrukcii i metodov rascheta kombinirovanny`x damb na predgorny`x uchastkax rekax [Improvement of the design and calculation methods of combined dams on foothill river sections]: monograph. Tashkent: NIU TIIIMSKH. 2022, 100. (in Russian).

[22] Ambartsumyan GA, K voprosu gidromekhanicheskogo rascheta skvoznoi shpory s gidravlicheskim barerom [On the problem of hydromechanical design of a permeable spur with a hydraulic barrier] Izvestiya Akademii nauk Armyanskoi SSR. Seriya tekhnicheskikh nauk. Gidravlika, gidrotekhnika. – 1968. – T. XXI, № 5. – p. 32–37 (in Russ.).

[23] Levi II, Dinamika ruslovykh potokov [Dynamics of channel flows]. 2-e izd., pererab. i dop. Leningrad: Gosenergoizdat. 1957, 223.

[24] SP RK 3.04-107-2014, Nagruzki i vozdeistviya na gidrotekhnicheskie sooruzheniya (volnovye, ledovye i ot sudov) [Loads and impacts on hydraulic structures (wave, ice and ship loads). Astana: Committee for Construction]. Astana: Komitet po delam stroitel'stva, ZHKKh i upravleniya zemel'nymi resursami MNE RK. 2015.

[25] Levi I I. Dvizheniya rechnykh potokov v nizhnikh biefakh gidrotekhnicheskikh sooruzheniy [Movements of river flows in downstream reaches of hydraulic structures]. M.-L.: Gosenergoizdat. 1955, 256.

[26] Mikhasek AA, Malyugin NR. Vliyanie fil'tratsii v tele aktivnogo beregozaschitnogo sooruzheniya na kharakteristiki obtekayushchego potoka [Influence of filtration through the body of an active bank protection structure on the characteristics of the surrounding flow]. Gradostroitel'stvo i arkhitektura. 2019; 9(3):92–98. https://doi.org/10.17673/Vestnik.2019.03.12

[27] Talmaza V F. Nekotorye osobennosti dvizheniya vlekomykh nanosov na rekakh gorno-predgornoi zony [ome features of bedload sediment transport in rivers of mountainous and foothill regions]. Dinamika i termika rek. Moscow: Stroiizdat. 1973.

[28] Rustembek uulu Abdinazar, Meyman uulu Bektur. Rezul'taty model'nykh issledovanii regulyatsionnykh sooruzhenii na uchastke reki Chu [Results of physical model studies of river training structures on the Shu River reach]. Vestnik KRSU. 2018; 18(8):134–137.

Crossref
DOI: 10.31643/2028/6445.25
Earth and Planetary Sciences: Earth-Surface Processes

Geochemical Partitioning and Correlation of Rare Earth Elements, Thorium, and Uranium in Ion-Adsorption Clays from the Gemang Area, West Kelantan, Malaysia

Chang S.C., Fendy N.A., Shoparwe N.F., *Yusoff A.H.

Universiti Malaysia Kelantan, Malaysia

** Corresponding author email: hafidz.y@umk.edu.my*

Received: *November 1, 2025*
Peer-reviewed: *November 30, 2025*
Accepted: *July 13, 2026*

ABSTRACT

This study aimed to determine the geochemical partitioning of total rare earth elements (ΣREE), thorium (Th), and uranium (U) in ion-adsorption clays (IACs) from the Gemang area, West Kelantan, Malaysia, and to evaluate how this partitioning may influence selective REE recovery with limited radionuclide mobilisation. An eight-step sequential extraction procedure was applied to representative saprolitic IAC samples, and the extracted fractions were analysed by ICP-OES. Pearson correlation analysis and principal component analysis (PCA) were further used to examine associations among ΣREE, Th, U, and selected major elements. The sequential extraction results showed that ΣREE were concentrated mainly in the ion-exchangeable fraction (average 22.0%), with additional contributions from the residual fraction (15.3%) and a notably high proportion in the primary sulphide step (53.4%). In contrast, Th and U were concentrated mainly in the primary sulphide fraction (54.4% and 41.3%, respectively) and the residual fraction (26.2% and 45.0%, respectively). Major elements such as Al, Fe, Mn, Ca, and Na showed distributions consistent with clay, oxide, and refractory mineral hosts. Statistical analysis indicated a positive association between ΣREE and Ca-Na, whereas Th and U were more closely associated with Fe-Mn-bearing fractions, indicating different host controls and different mobilisation behaviour. These results suggest that a recoverable REE pool is present in the exchangeable fraction, while most Th and U remain in less labile phases under the tested operational scheme. The study therefore provides geochemical evidence that mild ammonium-salt leaching may favour selective REE recovery from Gemang IACs while limiting the release of naturally occurring radioactive materials, although further mineralogical validation and dynamic leaching tests are still required.

Keywords: rare earth elements, thorium, uranium, sequential extraction, Ion-adsorption clay, west Kelantan, correlation analysis.

Information about authors:

Chang S.C. *PhD Student at the Faculty of Bioengineering and Technology, and graduate research assistant at Gold, Rare Earth and Material Technopreneurship Centre, Universiti Malaysia Kelantan 17600 Jeli, Kelantan, Malaysia. Email: chang.shenchang@yahoo.com*

Fendy N.A. *Graduate research assistant at Gold, Rare Earth and Material Technopreneurship Centre, Universiti Malaysia Kelantan, 17600 Jeli, Kelantan, Malaysia. Email: nurafikahfendy@gmail.com*

Shoparwe N.F. *Associate Professor at the Faculty of Bioengineering and Technology, and Director at Gold, Rare Earth and Material Technopreneurship Centre (GREAT), Universiti Malaysia Kelantan, 17600 Jeli, Kelantan, Malaysia. Email: fazliani.s@umk.edu.my*

Yusoff A.H. *Associate Professor at the Faculty of Bioengineering and Technology and technical advisor at Gold, Rare Earth and Material Technopreneurship Centre (GREAT), Universiti Malaysia Kelantan, 17600, Kelantan, Malaysia. Email: hafidz.y@umk.edu.my*

Introduction

Ion-adsorption clay (IAC) deposits are an important class of secondary REE resources—particularly in subtropical and tropical weathering profiles—because they host a significant fraction of REEs as adsorbed ions on clay mineral surfaces, making low-impact extraction by ammonium-salt leaching feasible [1]. However, the co-occurrence of naturally occurring radioactive materials (NORMs) such as Th and U can complicate environmental management and product quality [[2], [3]]. This study addresses the partitioning of ΣREE, Th and U among operationally defined geochemical fractions in IACs from the Gemang area (West Kelantan, Malaysia), and the statistical relationships between these trace elements and major matrix components (Al, Fe, Mn, Ca, Na). The goal is to demonstrate mineralogical and chemical controls on element mobility and to provide evidence-based recommendations for selective in-situ leaching strategies that minimize Th/U mobilisation.

Recent studies emphasise the importance of mineralogical controls and quantitative validation (DXRD/XRD, SEM–EDS, and multivariate statistics) for interpreting sequential extraction results [[4, [5], [6]]. Building on this work, a dataset of partitioning and correlation analyses was presented using Agilent 51100 SVDV ICP-OES data, and it includes robust methodological details and QA/QC to strengthen reproducibility.

Experimental part

Sampling and Study Area

The study samples were collected from drill core G3 (Gemang area, West Kelantan) at depths of 7.5–10.0 m, from the B horizons of a weathered granitic saprolite profile developed under humid tropical conditions. Representative intervals (7.5, 8.0, 8.5, 9.0, 9.5, 10.0 m) were sampled. Samples were air-dried, gently crushed, and sieved to <63 µm.

Table 1 - Sequential Extraction Steps

Step	Target	Reagent	Time (h)	Temperature (℃)
1	Water Soluble, Free Ion	Deionized Water	1	Room
2	Ion-exchangeable	0.5 M ammonium sulphate	2	Room
3	Weak Acid Dissociable	0.5 M acetic acid	2	Room
4	Associate with Fe (III) oxyhydroxides and Mn oxides	0.2 M oxalic acid	1	Room (dark, no light)
5	Associate with Fe (III) oxides	0.2 M oxalic acid	2	80 (water bath)
6	Organics and supergene sulphides	35% hydrogen peroxide	1	80 (water bath)
7	Primary sulphides	$KClO_3$ + HCl + 4 M HNO_3	4	150
8	Residual	HF + HNO_3 + $HClO_4$	12	185

Sequential extraction procedure

An eight-step sequential extraction, as shown in Table 1, modified from Dold (2003) and Shi et al. (2014) to suit the mineralogical and analytical conditions of the present IAC samples [[7], [8]], was applied to each sample. The solid-to-liquid ratio was 1:50 (w/v). Extraction steps and conditions were: (1) water-soluble (deionized water, 1 h, RT, 1:50); (2) ion-exchangeable (0.5 M $(NH_4)_2SO_4$, 2 h, RT); (3) acetic acid (0.5 M CH_3COOH, pH~4.5, 2 h, RT); (4) oxalic acid dark (0.2 M $H_2C_2O_4$, pH~3.0, 1 h, RT, protected from light); (5) oxalic acid heated (0.2 M $H_2C_2O_4$, 80 °C, 2 h); (6) 35% H_2O_2 (80 °C, 1 h) for organics and supergene sulphides; (7) $KClO_3$ + HCl oxidation followed by 4 M HNO_3 boil for primary sulphides; and (8) residual digestion (HF–HNO_3–$HClO_4$) for silicate-bound elements. After each step, samples were centrifuged (3000 rpm, 10 min), the supernatants filtered (0.45 µm), and the filtrates stored for analysis. The total digestion values were used as the reference basis for normalising sequential extraction recoveries and evaluating cumulative mass balance.

Analytical methods and QA/QC

Elemental analyses were conducted by ICP-OES (Agilent 51100 SVDV operating in SVDV mode) [[9], [10]]. Calibration used multi-element standards (0.1, 0.25, 0.5, 1, 2.5, 5, 10, 25, 50, 100 ppm). Method detection limits (MDLs) for the REEs and actinides were determined from replicate blanks (n = 8). Certified reference material (CRM) digests (SY-5) and laboratory spikes (n = 3) were included to monitor recovery [11]; mean recoveries for REEs were 92–106% and for Th/U 88–102%. Duplicate extractions (n = 10) returned relative standard deviations (RSD) <7% for major elements and <12% for low-abundance REEs. Blanks and procedural controls confirmed that no systematic contamination occurred.

Data processing and statistical analysis

Element concentrations from sequential steps were normalised to total digestion (complete HF-HNO_3-HCl-HClO4 digestion) and expressed as a percentage of the total [12]. Pearson correlation coefficients were calculated between phase percentages of ΣREE, Th, U, and selected major elements (Al, Fe, Mn, Ca, Na). Principal component analysis (PCA) was performed on the centred and scaled phase percentage matrix to identify major modes of covariance. All statistics were conducted in R (v4.2), using the packages stats and FactoMineR.

The overall analytical workflow comprised sample collection and preparation, sequential extraction, ICP-OES determination, normalisation to

total digestion, and statistical interpretation using Pearson correlation and PCA.

Results and Discussion

Distribution of Thorium, Uranium, and Total REE Across Extraction Phases

Sequential extraction results of the B horizon of Gemang (G3) ion-adsorption clay profile are shown in Table 2 and Figure 1. Thorium (Th), uranium (U), and total rare earth elements (ΣREEs) exhibit distinct geochemical partitioning, i.e., they are distributed in different mineral phases in different proportions. In terms of method validity and analytical precision, the total sequential recovery of each element across all samples (7.5–10 m) is at 100 ± 10%.

Thorium in the collected soil samples was mainly of the primary sulphide and residual phases at 80.6%; followed by iron (III), Fe^{3+} bound phase at 16.1%; iron-manganese oxide, Fe-Mn oxides bound phase at 1.4%; and organic and supergene phases at 1.1%, whereas the ion-exchangeable phases were 0.1%, which is almost negligible. This collectively suggests that Th is primarily associated with refractory accessory minerals such as thorite, monazite, and xenotime. These minerals are most probably bound within crystalline Fe-oxyhydroxides or phosphate phases, which can only be dissolved by strong acid [[13], [14]]. Thorium thus cannot be desorbed from the surface by ion exchange.

Uranium has a similar phase partitioning pattern where U is embedded in the primary sulphide and residual phases at 86.3%; followed by Fe^{3+} bound phase at 7.6%; Fe-Mn oxides bound phase at 2.4%, and weakly acid-dissociable at 1.7%. No U has been found in the ion-exchange, organic, and supergene phases. This together suggests that uranium is also mainly associated with refractory accessory minerals such as uraninite, apatite, allanite and zircon [[15], [16]]. Only a small portion of U is liberated in the water-soluble phase as uranium (VI), U^{6+}, at 1.9%. Uranium in the form of the tetravalent ion, U^{4+}, as in the Fe-Mn oxides, primary sulphide and residual phases, is less soluble and thus immobile in the ion exchange phase. The mobility of uranium depends strongly on redox conditions and is thus convertible.

The large sulphide-association of Th (54.4%) and U (41.3%) suggests that Th and U are mainly hosted or included in the hypogene sulphide phase. Essentially, a low exchangeable fraction Th and U (<0.1%) indicates that they are not easily mobilised by simple changes in the surrounding water's ionic composition. This is a key finding for operational safety in the conventional use of ammonium sulphate, as the release of radioactive elements is thus limited and poses a low risk of immediate widespread contamination. Despite their stability in the raw soil exchangeable fraction, Th and U can be co-precipitated during processing and concentrated as beneficiation proceeds from intermediate products to tailings [17].

In contrast, the total rare earth distribution, ΣREE, was more mobile and readily leached by ammonium sulphate. 25.5% of ΣREE is of ion-exchangeable and weak-acid leachable phases. It is somewhat consistent with the ion-adsorption type lateritic clays of southern China and Malaysia [[18], [19]]. The ΣREE in the ion-exchangeable fraction at 22% affirms that the Gemang IACs are ion-adsorption systems with a significant recoverable REE pool by mild salt leaching. The residual ΣREE fraction at 15.3% likely reflects structural incorporation in aluminosilicate lattices, e.g., phyllosilicate interlayers or REE-bearing accessory minerals such as monazite/ xenotime in fine fractions [20]. The small contribution of oxalate-extractable fractions indicates limited binding to poorly crystalline Fe-oxyhydroxides [21].

The unusually high proportion of ΣREE in the sulphide fraction at 53.4% contrasts with typical IAC behaviour, where REEs are predominantly exchangeable. This suggests that REE-bearing sulphides may be present in specific samples, potentially as unique or localized mineral phases or sulphidic micro-inclusions [[22], [23]]; incomplete selectivity of the sulphide extraction step using $KClO_3$ + HCl oxidation then HNO_3 (operational overlap) may partially leach non-sulphide REE hosts e.g., poorly crystalline Fe-oxides, or loosely bound REE complexes, artificially inflating REE in the sulphide fraction or co-precipitation of REE with sulphide/Fe–Mn phases during weathering.

Table 2- Average phase distribution (%) of REE, Th, U and major elements from sequential extraction (n=6)

Element	Water-soluble	Ion-exchangeable	Acetic acid	Oxalic acid (dark)	Oxalic acid (80°C)	H_2O_2	Primary Sulphide	Residual
REE	0.2	22.0	3.5	0.9	4.3	0.4	53.4	15.3
Th	0.1	0.1	0.6	1.4	16.1	1.1	54.4	26.2
U	1.9	0.0	1.7	2.4	7.6	0.0	41.3	45.0
Al	0.0	0.3	0.0	0.6	3.1	0.3	13.3	82.5
Fe	0.0	0.0	0.0	0.1	11.7	1.0	53.5	33.7
Mn	0.0	1.9	0.5	2.6	24.6	2.0	44.9	23.5
Ca	14.4	60.9	6.9	3.0	0.7	0.1	4.7	9.3
Na	1.6	20.2	40.4	2.0	3.0	1.4	12.6	19.9

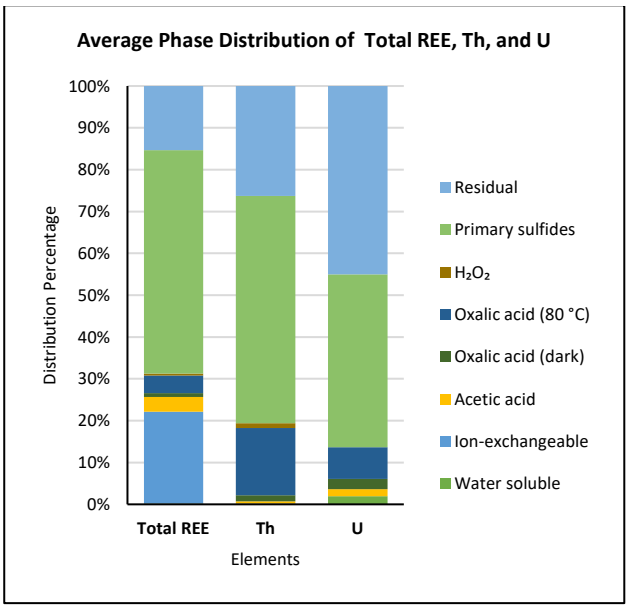

Figure 1 - Phase Distribution of Total REE, Th and U of average G3 soil profile(n=7)

Correlation Between Th, U, REE and Major Elements

Pearson correlation coefficients rounded to one decimal place (Table 3), and PCA results (Figure 2) reveal two principal geochemical associations distinct from the earlier hypothesis. Thorium and uranium are very strongly correlated (r = +0.90), confirming their common mineralogical host and co-behaviour during weathering. Both Th and U exhibit negative correlations with Fe, Mn, Ca, and Na (r≈−0.5 to −0.6), indicating that these actinides are not controlled by secondary oxide or exchangeable carbonate phases, but are instead retained in refractory mineral lattices such as monazite–xenotime or thorite-type phosphates [24]. Their weak to moderate positive correlation with Al (r ≈ +0.5 to +0.6) suggests partial structural substitution or mechanical entrapment within aluminosilicate residues [25]. Th and U remain structurally sequestered within stable mineral phases, reducing their mobility during in-situ leaching operations.

Table 3- Pearson correlation matrix (phase percentages)

Element	Th	U	∑REE	Al	Fe	Mn	Ca	Na
Th	1.0							
U	0.9	1.0						
∑REE	0.1	0.3	1.0					
Al	0.6	0.5	0.2	1.0				
Fe	-0.5	-0.6	-0.4	0.1	1.0			
Mn	-0.4	-0.3	0.2	0.1	0.7	1.0		
Ca	-0.6	-0.6	-0.5	-0.4	0.6	0.3	1.0	
Na	-0.4	-0.6	-0.3	-0.5	-0.1	-0.3	-0.2	1.0

In contrast, the ΣREE group shows a weak positive correlation with Al (r=+0.2) but a mild negative relationship with Fe (r=-0.4) and Ca (r=-0.5). This trend implies that REEs in the Gemang ion-adsorption clay are not strongly bound to Fe–Mn oxides or carbonates, but are instead associated with clay mineral surfaces through outer-sphere cation exchange. The absence of a positive ΣREE–Ca/Na correlation contradicts the behaviour observed in some South China IACs [26], highlighting local mineralogical control in which kaolinite-dominated matrices limit alkaline exchange buffering.

However, given the limited sample size (n=6), the correlation coefficients should be interpreted as indicative rather than definitive. However, the magnitude of some correlations (r > 0.7) is high enough to suggest real covariant behaviour deserving further mineralogical corroboration.

Principal Component Analysis (PCA)

Principal component analysis (PCA), as shown in Figure 2 of the phase-percentage matrix (Table 2), extracted two components that explained 70.0% of the total variance (PC1: 45.4%; PC2: 24.7%).

PC1 separates phases associated with exchangeable /leachable pools from lithogenic /oxidative pools, i.e., strong positive loadings on Ion-exchangeable and Water-soluble contrast with negative loadings on Primary sulphide, Residual, H_2O_2, and Oxalic acid at 80 °C. PC2 contrasts Residual (positive) with H_2O_2 and Oxalic acid at 80 °C (negative), distinguishing more refractory host control from oxide- and organic-bound contributions.

In score space, Ca and Na plot toward the Ion-exchangeable /Water-soluble quadrant, consistent with the readily leachable REE association, while Th, Fe and Mn align with Primary sulphide and oxidative phases, and Al is aligned toward Residual, reflecting its clay-framework affinity. REE and U sit intermediate but trend toward Ion-exchangeable vs Residual, respectively, supporting the selective exchangeability of REE under mild ammonium leaching with limited co-mobilisation of Th/U.

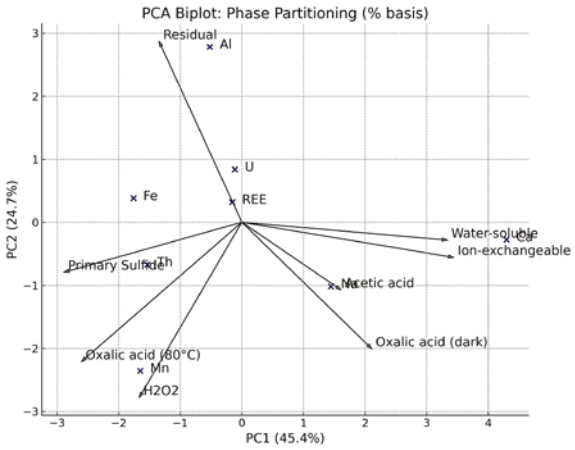

Figure 2- PCA Biplot of Phase Partitioning

Samples at 8.0 - 9.0 m depth plot as shown in Figure 3, toward the REE-enriched quadrant, reflecting zones of higher weathering and greater ion-exchange potential, whereas deeper samples (≥9.5 m) cluster in Th-U-Fe-rich domains, suggesting lithogenic enrichment and incomplete alteration. The PCA plot demonstrates that the 8.0–9.0 m depth is the most favourable for REE leaching using ion-exchange ammonium sulphate, as a high proportion of the ion-exchangeable phase characterises this zone. In contrast, in the deeper depths, particularly those ≥ 9.5 m, REE recovery is less favourable. This is because the REEs in these depths are more strongly associated with refractory phases, i.e., residual or primary sulphide phases. Stronger acids are needed to break down and release the REEs if these phases are intended for extraction. This geochemical differentiation illustrates the natural zonation of the soil profile, which can be utilised as a selective in-situ leaching strategy. The processing zone can thus be divided into two: the shallow zones using milder, more cost-effective, and environmentally friendlier leaching agents, while the deeper zones use stronger, more potent acid–complexant combinations to mobilise the refractory-bound REEs [[26], [27]].

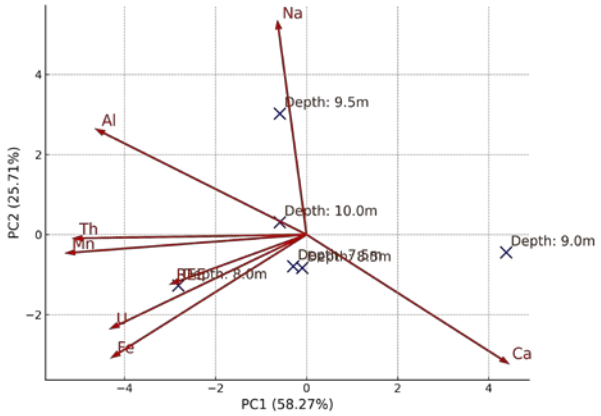

Figure 3- PCA Biplot of Elements Partitioning in Depths

Implications for the process design of selective in-situ leaching

The clear geochemical separation between exchangeable ΣREE and refractory Th/U implies that mild ammonium-salt leaching can preferentially mobilise REEs while leaving Th and U immobile, provided leaching remains non-oxidative and pH is controlled above 4. To reduce the risk of releasing Th/U due to sulphide/oxide dissolution, the leaching solution should not contain strong oxidants and should be maintained near-neutral to mildly acidic conditions.

The natural zonation and vertical variation in exchangeable ΣREE and major element concentrations, as indicated by PCA sample spread, suggest that in-situ leaching designs should also consider stratigraphic variability. Early-stage exploration should prioritise mapping vertical heterogeneity within the exchangeable fraction of the deposit to delineate the high-value zones accurately. This spatial understanding enables the application of selective leaching techniques, such as targeted well placement or confined percolation, to preferentially recover exchangeable rare earth elements (REEs). This targeted approach optimises efficiency by minimising overall reagent consumption, thereby reducing the operation's environmental footprint.

A robust monitoring strategy is also important during leaching operations. Dissolved iron (Fe) and manganese (Mn) concentrations, and the redox potential, should be included as key monitoring parameters. These measures serve as critical indicators of incipient sulphide oxidation, an event that could lead to the unintended mobilisation of thorium (Th) and uranium (U) into the leachate pool.

Limitations and recommendations for future research

Data derived from sequential extraction procedures have some inherent limitations. The methods are operationally defined to ensure accuracy and repeatability. However, the results are consequently dependent on the specific extraction procedure and matrix. Furthermore, in this study, only a small sample size was used (n=6), which limits statistical power and thus does not reflect regional conditions.

To overcome the limitations and enhance understanding of the deposits, more samples from the spatial lateral and vertical profiles should be collected and data included to produce a more statistically significant data set [28].

Other mineralogical and geochemical methods should also be included to minimise ambiguities. X-ray diffraction (XRD) can be used to analyse the removal or persistence of mineral phases before and after leaching [29]. Scanning electron microscopy with energy-dispersive X-ray spectrometry (SEM-EDS) and Laser Ablation Inductively Coupled Plasma Mass Spectrometry (LA–ICP–MS) can be employed to visually identify the elements hosted in the mineral matrix [30].

To bridge the gap from laboratory data to operational reality, pilot leach tests, such as small columns, are needed to simulate in-situ conditions and thus allow further optimisation.

Conclusions

The sequential extraction results show that rare earth elements (ΣREE), thorium (Th), and uranium (U) in the Gemang ion-adsorption clay do not share the same geochemical behaviour. ΣREE display a meaningful exchangeable component, with an average of 22.0% occurring in the ion-exchangeable fraction, confirming that part of the REE inventory remains potentially recoverable by mild ammonium-salt leaching. In contrast, Th and U are concentrated mainly in the primary sulphide and residual fractions, indicating stronger retention in less labile phases and lower susceptibility to release under simple ion-exchange conditions.

The correlation and PCA results support this distinction. ΣREE show closer association with Ca and Na, consistent with exchangeable or weakly bound occurrence, whereas Th and U are more closely associated with Fe- and Mn-bearing phases and refractory mineral hosts. This separation in geochemical behaviour suggests that selective mobilisation of REEs is more feasible than co-mobilisation of radionuclides under mild leaching conditions. However, the unusually high ΣREE proportion in the primary sulphide step indicates that some overlap between operational fractions remains possible, and that the extraction sequence should be interpreted as an operational partitioning tool rather than a direct mineralogical determination.

From a process perspective, the results support the view that ammonium-sulphate leaching can preferentially target the exchangeable REE pool while limiting Th and U release, provided that the leaching system remains non-oxidative and chemically controlled. This is important for the design of safer and more selective REE recovery routes from Malaysian ion-adsorption clays, where minimising radionuclide mobilisation is a key environmental and operational requirement.

At the same time, the present work should be treated as a geochemical and operational baseline rather than a complete process validation. Future work should include direct mineralogical verification of host phases by XRD, SEM-EDS, and LA-ICP-MS, together with dynamic column or pilot leaching tests to confirm whether the selective behaviour inferred from sequential extraction is maintained under realistic in-situ leaching conditions.

Conflicts of interest. On behalf of all authors, the corresponding author states that there is no conflict of interest.

CRediT author statement.

S. Chang: Conceptualization, Methodology, Investigation, Formal analysis, Data curation, Visualization, Writing – original draft. **N. Fendy:** Investigation, Validation, Writing – review&editing; **N. Shoparwe:** Supervision, Project administration, Resources; **A. Yusoff**: Conceptualization, Supervision, Project administration, Writing– review&editing.

Acknowledgement

This research is funded by Industrial Matching Grant (IMAP) Ministry of Higher Education (MOHE) Malaysia (Grant Code: R/IMAP/A1300/01684A/014 /2025/01452), supported also by Matching Grant between Universiti Malaysia Kelantan (UMK) and Al Balqa Applied University (BAU) Jordan (Grant Code: R/MATCH/A1300/01684A/017/2025/01512).

Cite this article as: Chang SC, Fendy NA, Shoparwe NF, Yusoff AH. Geochemical Partitioning and Correlation of Rare Earth Elements, Thorium, and Uranium in Ion-Adsorption Clays from the Gemang Area, West Kelantan, Malaysia. Kompleksnoe Ispolzovanie Mineralnogo Syra = Complex Use of Mineral Resources. 2028; 346(3):19-27. https://doi.org/10.31643/2028/6445.25

Геманг аймағы, Батыс Келантан, Малайзиядағы ион-адсорбциялық саздардағы сирек жер элементтерінің, торий мен уранның геохимиялық бөлінуі және корреляциясы

Chang S.C., Fendy N.A., Shoparwe N.F., Yusoff A.H.

Келантан Малайзия университеті, Малайзия

Мақала келді: *1 қараша 2025*
Сараптамадан өтті: *30 қараша 2025*
Қабылданды: *13 шілде 2026*

ТҮЙІНДЕМЕ

Бұл зерттеу Малайзияның Батыс Келантан қаласындағы Геманг аймағынан алынған иондық-адсорбциялық саздардағы (ИАС) жалпы сирек кездесетін жер элементтерінің (ΣREE), торийдің (Th) және уранның (U) геохимиялық бөлінуін анықтауға және бұл бөлінудің шектеулі радионуклидті мобилизациямен ИАС-ты селективті қалпына келтіруге қалай әсер етуі мүмкін екенін бағалауға бағытталған. Өкілетті сапролиттік ИАС үлгілеріне сегіз сатылы тізбекті экстракция процедурасы қолданылды, ал алынған фракциялар ICP-OES арқылы талданды. Пирсон корреляциялық талдауы және негізгі компоненттік талдау (PCA) ΣREE, Th, U және таңдалған негізгі элементтер арасындағы байланысты зерттеу үшін қолданылды. Тізбекті экстракция нәтижелері ΣREE негізінен ион алмастырылатын фракцияда (орташа 22,0%) шоғырланғанын, қалдық фракциядан (15,3%) қосымша үлестер қосылғанын және бастапқы сульфид сатысында айтарлықтай жоғары үлеске ие болғанын (53,4%) көрсетті. Керісінше, Th және U негізінен бастапқы сульфид фракциясында (сәйкесінше 54,4% және 41,3%) және қалдық фракцияда (сәйкесінше 26,2% және 45,0%) шоғырланған. Al, Fe, Mn, Ca және Na сияқты негізгі элементтер саз, оксид және отқа төзімді минералды иелермен сәйкес таралуды көрсетті. Статистикалық талдау ΣREE және Ca-Na арасындағы оң байланысты көрсетті, ал Th және U Fe-Mn бар фракциялармен тығыз байланысты болды, бұл әртүрлі ие бақылаулары мен әртүрлі мобилизация мінез-құлқын көрсетеді. Бұл нәтижелер алмасатын фракцияда қалпына келтірілетін сирек кездесетін жердегі элменттер пулының бар екенін, ал Th және U-ның көпшілігі тексерілген пайдалану схемасы бойынша онша тұрақсыз фазаларда қалатынын көрсетеді. Сондықтан зерттеу аммоний-тұзды жұмсақ шаймалау табиғи радиоактивті материалдардың шығарылуын шектей отырып, Геманг ИАС-тан сирек кездесетін жердегі элменттерді селективті түрде қалпына келтіруге ықпал етуі мүмкін екендігінің геохимиялық дәлелдерін ұсынады, дегенмен минералогиялық валидация және динамикалық шаймалау сынақтары әлі де қажет.

Түйін сөздер: сирек кездесетін жер элементтері, торий, уран, тізбектей экстракция, ион-адсорбциялық саз, батыс Келантан, корреляциялық талдау.

Авторлар туралы ақпарат:

Chang S.C. *PhD докторант, ғылыми қызметкер, Биоинженерия және технология факультеті, Алтын, сирек жер және материалдық технологиялар орталығы, Келантан Малайзия университеті, 17600 Джели, Келантан, Малайзия. Email: chang.shenchang@yahoo.com*

Fendy N.A. *Ғылыми қызметкер, Алтын, сирек жер және материалдар технологиялары орталығы, Малайзия университеті Келантан, 17600 Джели, Келантан, Малайзия. Email: nurafikahfendy@gmail.com*

Shoparwe N.F. *Доцент, директор, Биоинженерия және технологиялар факультеті, Алтын, сирек жер және материалдық технологиялар орталығы, Малайзия университеті Келантан, 17600 Джели, Келантан, Малайзия. Email: fazliani.s@umk.edu.my*

Yusoff A.H. *Доцент, техникалық кеңесші, Биоинженерия және технология факультеті, Алтын, сирек жер және материалдық технологиялар орталығы, Келантан Малайзия университеті, 17600 Джели, Келантан, Малайзия. Email: hafidz.y@umk.edu.my*

Геохимическое распределение и корреляция редкоземельных элементов, тория и урана в ионно-адсорбционных глинах района Геманг, Западный Келантан, Малайзия

Chang S.C., Fendy N.A., Shoparwe N.F., Yusoff A.H.

Университет Малайзии Келантан, Малайзия

Поступила: *1 ноября 2025*
Рецензирование: *30 ноября 2025*
Принята в печать: *13 июля 2026*

АННОТАЦИЯ

Целью данного исследования было определение геохимического распределения общего количества редкоземельных элементов (ΣREE), тория (Th) и урана (U) в ионно-адсорбционных глинах (ИАГ) из района Геманг, Западный Келантан, Малайзия, а также оценка того, как это распределение может влиять на селективное извлечение РЗЭ при ограниченной мобилизации радионуклидов. К репрезентативным образцам сапролитовых ИАГ была применена восьмиступенчатая процедура последовательной экстракции, а извлеченные фракции были проанализированы методом ICP-OES. Для изучения взаимосвязей между ΣREE, Th, U и некоторыми основными элементами были дополнительно использованы корреляционный анализ Пирсона и анализ главных компонентов (PCA). Результаты последовательной экстракции показали, что ΣREE в основном сконцентрированы в ионообменной фракции (в среднем 22,0%), с дополнительным вкладом остаточной фракции (15,3%) и заметно высокой долей в первичной сульфидной стадии (53,4%). Напротив, Th и U были сконцентрированы в основном в первичной сульфидной фракции (54,4% и 41,3% соответственно) и остаточной фракции (26,2% и 45,0% соответственно). Основные элементы, такие как Al, Fe, Mn, Ca и Na, показали распределение, соответствующее глинистым, оксидным и тугоплавким минеральным вмещающим породам. Статистический анализ показал положительную корреляцию между ΣREE и Ca-Na,

	тогда как Th и U были более тесно связаны с Fe-Mn-содержащими фракциями, что указывает на различные факторы, влияющие на вмещающую породу, и различное поведение при мобилизации. Эти результаты предполагают, что в обменной фракции присутствует восстанавливаемый пул REE, в то время как большая часть Th и U остается в менее лабильных фазах при протестированной схеме эксплуатации. Таким образом, исследование предоставляет геохимические доказательства того, что мягкое выщелачивание аммонийными солями может способствовать селективному извлечению REE из рудных месторождений Геманг, ограничивая при этом выброс природных радиоактивных материалов, хотя для подтверждения этого необходимы дальнейшие минералогические исследования и динамические испытания на выщелачивание.
	Ключевые слова: редкоземельные элементы, торий, уран, последовательная экстракция, ионно-адсорбционная глина, Западный Келантан, корреляционный анализ.
Chang S.C.	***Информация об авторах:*** *Аспирант факультета биоинженерии и технологий и аспирант-исследователь Центра технопредпринимательства по золоту, редкоземельным металлам и материалам Университета Малайзии Келантан 17600 Джели, Келантан, Малайзия. Email: chang.shenchang@yahoo.com*
Fendy N.A.	*Аспирант-исследователь Центра технологического предпринимательства по золоту, редкоземельным металлам и материалам, Университет Малайзии, Келантан, 17600 Джели, Келантан, Малайзия. Email: nurafikahfendy@gmail.com*
Shoparwe N.F.	*Доцент факультета биоинженерии и технологий и директор Центра технологического предпринимательства в области золота, редких земель и материалов (GREAT), Университет Малайзии Келантан, 17600 Джели, Келантан, Малайзия. Email: fazliani.s@umk.edu.my*
Yusoff A.H.	*Доцент факультета биоинженерии и технологий и технический консультант Центра технологического предпринимательства в области золота, редких земель и материалов (GREAT), Университет Малайзии Келантан, 17600, Келантан, Малайзия. Email: hafidz.y@umk.edu.my*

References

[1] Liu S-L, Fan H-R, Liu X, Meng J, Butcher AR, Yann L, et al. Global rare earth elements projects: New developments and supply chains. Ore Geology Reviews. 2023; 157:105428.

[2] Agency IAE. Radiation protection and NORM residue management in the production of rare earths from thorium containing minerals: International Atomic Energy Agency. 2011.

[3] Manyoba N, Olukotun SF, John SO, Mathuthu M. Health Impact Assessment of Naturally Occurring Radioactive Materials (NORMs) from a Gold Mine Tailing in Mpumalanga Province, South Africa. Polytechnica. 2025; 8(1):3.

[4] Denys A, Janots E, Auzende A-L, Lanson M, Findling N, Trcera N. Evaluation of selectivity of sequential extraction procedure applied to REE speciation in laterite. Chemical Geology. 2021; 559:119954.

[5] Rukayah, Marzani N, Saud A, Jabit N, editors. Physicochemical analysis and sequential extraction of rare earth elements from Malaysian ion-adsorption clays. IOP Conference Series: Earth and Environmental Science; 2024: IOP Publishing.

[6] Wu P, Li X, Liang X, Lin X, Zhu J. Optimized quantitative analysis of rare earth elements associated with typical secondary minerals in regolith-hosted deposits. Chemical Geology. 2025, 122942.

[7] Dold B. Speciation of the most soluble phases in a sequential extraction procedure adapted for geochemical studies of copper sulfide mine waste. Journal of Geochemical Exploration. 2003; 80(1):55-68.

[8] Shi Y, Li X, Yang Z, Fu W. Application of inductively coupled plasma-mass spectrometry to the speciation analysis of rare earth elements in ion-adsorption rare earth ore. Metall Anal. 2014; 34:14-9.

[9] Nóbrega J, Schiavo D, Amaral C, Barros J, Mogueira AR, Virgilio A, et al. Determination of rare earth elements in geological and agricultural samples by ICP-OES. 2017.

[10] Amaral CD, Machado RC, Barros JA, Virgilio A, Schiavo D, Nogueira ARA, et al. Determination of rare earth elements in geological samples using the Agilent SVDV ICP-OES. Agilent Technologies: Santa Clara, CA, USA. 2016, 1-6.

[11] Scott JL, Maureen E. SY-5: Certified Reference Material for a Syenite. CanmetMINING (NRCan). 2022.

[12] USEPA. Method 3050B acid digestion of sediments, sludges, and soils 1.0 scope and application. Washington, DC, USA. 1996.

[13] Martín D, Fernández-Caliani JC, Romero-Baena A, Delgado J, González I. Geological constraints on the distribution of naturally occurring uranium and thorium in soils of southwestern Spain. Journal of Iberian Geology. 2025, 1-17.

[14] Sanusi M, Ramli A, Basri N, Heryanshah A, Said M, Lee M, et al. Thorium distribution in the soils of Peninsular Malaysia and its implications for Th resource estimation. Ore Geology Reviews. 2017; 80:522-35.

[15] Ong YH, Sallehhuddin M. Promising uranium prospects in the central Belt area, Peninsular Malaysia. Uranium deposits in Asia and the Pacific: Geology and exploration. 1988, 97-107.

[16] Seow SQ, Mohan Viswanathan P, Dodge-Wan D. Distribution of natural radioactivity in different geological formations and their environmental risk assessment in Malaysia. Environmental Science and Pollution Research. 2024; 31(30):43292-308.

[17] Al Wafi T, Kurniawan K, Ichlas Z, Tampubolon A, Mubarok M. Leaching Characteristics of Rare-Earth Elements from Indonesian Ion-Adsorption Clay-Type Weathered Granite Ore Deposit. Journal of Sustainable Metallurgy. 2025, 1-14.

[18] Borst AM, Smith MP, Finch AA, Estrade G, Villanova-de-Benavent C, Nason P, et al. Adsorption of rare earth elements in regolith-hosted clay deposits. Nature communications. 2020; 11(1):4386.

[19] Ibad SM, Tsegab H, Siddiqui NA, Adam M, Mishra S, Ridha S, et al. The upstream rare earth resources of Malaysia: Insight into geology, geochemistry, and hydrometallurgical approaches. Geoscience Frontiers. 2024; 15(6):101899.

[20] Sobri NAM, Harun N, Yunus MYM. A review of the ion exchange leaching method for extracting rare earth elements from ion adsorption clay. Chemical Engineering Research and Design. 2024; 208:94-114.

[21] Cao X, Chen Y, Wang X, Deng X. Effects of redox potential and pH value on the release of rare earth elements from soil. Chemosphere. 2001; 44(4):655-61.

[22] Gieré R. Transport and deposition of REE in H2S-rich fluids: evidence from accessory mineral assemblages. Chemical Geology. 1993; 110(1-3):251-68.

[23] Ayupova N, Melekestseva I, Maslennikov V, Sadykov S. Mineralogy and geochemistry of clastic sulfide ores from the Talgan VHMS deposit, South Urals, Russia: Signatures of diagenetic alteration. Ore Geology Reviews. 2022; 144:104839.

[24] Hazen RM, Ewing RC, Sverjensky DA. Evolution of uranium and thorium minerals. American Mineralogist. 2009; 94(10):1293-311.

[25] Gray TR, Hanley JJ, Dostal J, Guillong M. Magmatic enrichment of uranium, thorium, and rare earth elements in Late Paleozoic rhyolites of southern New Brunswick, Canada: evidence from silicate melt inclusions. Economic Geology. 2011; 106(1):127-43.

[26] Zhou W, Chen Z, Yan H, Wang H, Chen Z. Probing the geochemical characteristics of rare earth elements in the weathering profile of yttrium-rich heavy rare earth mine. Science of The Total Environment. 2024; 931:172906.

[27] Pan J, Zhao L, Li Z, Huang X, Feng Z, Chen J. Occurrence and vertical distribution of aluminum and rare earths in weathered crust elution-deposited rare earth ore: Effect of soil solution pH and clay minerals. Journal of Rare Earths. 2024; 42(7):1394-402.

[28] Bourdeau JE, Zhang SE, Nwaila GT, Ghorbani Y. Data generation for exploration geochemistry: Past, present and future. Applied Geochemistry. 2024; 172:106124.

[29] Pinskii D, Minkina T, Bauer T, Nevidomskaya D, Shuvaeva V, Mandzhieva S, et al. Identification of heavy metal compounds in technogenically transformed soils using sequential fractionation, XAFS spectroscopy, and XRD powder diffraction. Eurasian Soil Science. 2022; 55(5):613-26.

[30] Saputra HA, Aji D, Ali BTI, Asranudin. Emerging Analytical Techniques for Rare Earth Element Study: Basic Principles and Cutting-Edge Developments. Analytica. 2025; 6(3):35.

Crossref
DOI: 10.31643/2028/6445.26
Earth and Planetary Sciences: Earth-Surface Processes

Mineralogical characteristics of oxidized copper-porphyry ores at the Koktaszhal deposit

[1]Toleubek K.E., [1*]Kopobayeva A.N., [1]Amangeldikyzy A., [1]Askarova N.S., [2]Zengin E., [1]Zhunusbekova G.Ye., [1]Mazakh B., [1]Battalova A.S.

[1]*Abylkas Saginov Karaganda Technical University, Karaganda, Kazakhstan*
[2]*Istanbul Technical University (ITU), Istanbul, Turkey*

**Corresponding author email: a.n.kopobayeva@gmail.com*

Received: *April 27, 2026*
Peer-reviewed: *May 21, 2026*
Accepted: *July 24, 2026*

ABSTRACT

This paper presents the results of a comprehensive mineralogical study of oxidized copper-porphyry ore from the Koktashal deposit. Optical microscopy, silicate analysis, and quantitative phase analysis were used to characterize the mineral composition and forms of copper occurrence in the oxidation zone. The ore contains 0.735% total copper, of which 89.8% occurs in oxidized form, 6.39% in primary sulfides, 2.72% in secondary sulfides, and 1.09% in water-soluble form. The principal ore minerals are malachite (1.5–2.0%) and azurite (0.3–0.4%), accompanied by hematite with magnetite (0.5%), goethite (0.2%), and pyrite (0.2%), whereas copper sulfides and native copper occur only in trace amounts. The integration of classical mineralogical methods with quantitative phase analysis provides new insights into the distribution of copper occurrence forms and their relationship to oxidation processes. Malachite and azurite occur as well-crystallized vein and nest aggregates as well as colloform earthy masses developed along microcracks in association with iron hydroxides. Their close association with iron hydroxides and the near absence of copper sulfides represent a diagnostic feature of the oxidation zone in copper-porphyry systems. These findings improve the assessment of supergene alteration during exploration and support the classification of oxidation-zone ores as a distinct geological and industrial type for reserve estimation, ore body delineation, and processing scheme selection.

Keywords: Koktaszhal, copper-porphyry deposits, oxidized ores, phase analysis of copper, malachite, azurite, forms of gold, material composition.

Information about authors:

Toleubek Kymbat Esmakhaikyzy — *PhD student at the Geology and Exploration MD Department of Abylkas Saginov Karaganda Technical University, 100027, Ave. Nursultan Nazarbayev, 56, Karaganda, Kazakhstan. E-mail: toleubekkymbat69@gmail.com; ORCID ID: https://orcid.org/0000-0003-2126-8084*

Kopobayeva Aiman Nygmetovna — *PhD, associate professor of the Geology and Exploration MD Department of Abylkas Saginov Karaganda Technical University, 100027, Ave. Nursultan Nazarbayev, 56, Karaganda, Kazakhstan. E-mail: a.n.kopobayeva@gmail.com; ORCID ID: https://orcid.org/0000-0002-0601-9365*

Amangeldikyzy Altynay — *PhD, associate professor of the Geology and Exploration MD Department of Abylkas Saginov Karaganda Technical University, 100027, Ave. Nursultan Nazarbayev, 56, Karaganda, Kazakhstan. E-mail: a.amangeldykyzy@ktu.edu.kz; ORCID ID: https://orcid.org/0000-0002-6665-8804*

Askarova Nazym Srazhadinkyzy — *PhD, associate professor of the Geology and Exploration MD Department of Abylkas Saginov Karaganda Technical University, 100027, Ave. Nursultan Nazarbayev, 56, Karaganda, Kazakhstan. E-mail: n.askarova@ktu.edu.kz; ORCID ID: https://orcid.org/0000-0002-2103-6198*

Zengin Enes — *PhD, Associate Professor, Department of Geological Engineering, Faculty of Mines, Istanbul Technical University (ITU), Ayazağa Campus, 34469 Maslak, Istanbul, Turkey. E-mail: eneszengin@itu.edu.tr; ORCID ID: https://orcid.org/0000-0002-5740-7763*

Zhunusbekova Gulden Yermukhanovna — *Senior Lecturer of the Geology and Exploration MD Department of Abylkas Saginov Karaganda Technical University, 100027, Ave. Nursultan Nazarbayev, 56, Karaganda, Kazakhstan. E-mail: zh.gulden@ktu.edu.kz; ORCID ID: https://orcid.org/0000-0002-6578-5959*

Mazakh Bakytzhan — *PhD student at the Geology and Exploration MD Department of Abylkas Saginov Karaganda Technical University, 100027, Ave. Nursultan Nazarbayev, 56, Karaganda, Kazakhstan. E-mail: 06.06.2005@mail.ru; ORCID ID: https://orcid.org/0009-0007-5390-298X*

Battalova Arai Sayakhatovna — *Master's student of the Geology and Exploration MD Department of Abylkas Saginov Karaganda Technical University, 100027, Ave. Nursultan Nazarbayev, 56, Karaganda, Kazakhstan. E-mail: a84207553@gmail.com; ORCID ID: https://orcid.org/0009-0009-3192-1367*

Introduction

The importance of copper globally is determined not only by its wide range of industrial applications, but also by the steady increase in demand for the metal over time. According to the International Copper Association (ICA) [1], approximately 28 million tons of copper are consumed annually

worldwide, with nearly 70% used in electrical and communication applications, which directly relates to the metal's excellent electrical properties. At the same time, the International Copper Study Group (ICSG) [2] reports that global consumption of refined copper has increased more than threefold over the last 50 years, reflecting a long-term trend in growing demand from energy, construction, mechanical engineering, transportation, and electronics industries.

In these conditions, copper deposits with large reserves and resources, capable of providing a stable long-term raw material base, are particularly important. Among them, porphyry copper deposits play a leading role, considered the world's largest source of copper and an important source of molybdenum, gold, and silver [[3], [4]]. Their industrial value stems from the combination of enormous ore masses, significant total reserves, the possibility of open-pit mining, and integrated extraction of several valuable components. Even with relatively low copper grades, these deposits form the basis of the modern global copper mining industry [[3], [4]].

A key feature of porphyry copper deposits is the combination of relatively low average metal grades with extremely large ore systems. The United States Geological Survey (USGS) [3] emphasizes that the average copper content in porphyry deposits was approximately 0.44% in 2008, but their economic significance remains exceptionally high due to the large scale of mineralization, which is often measured in hundreds of millions and even billions of tons of ore [1]. It is this combination of low content and gigantic volumes that makes porphyry copper a unique type of mineral resource and determines its special role in global metallurgy [[1], [3]].

In modern conditions, interest in porphyry copper systems is growing due to the energy transition and the rising demand for copper as a key metal for electrification. According to the International Energy Agency (IEA) [[5], [6]], total copper demand may rise from 25.855 million tons in 2023 to 36.379 million tons by 2040, with the need for clean energy technologies growing particularly rapidly [[5], [6]]. In this context, porphyry copper deposits are considered among the most promising types of mineralization capable of significantly increasing copper reserves. This area is particularly important for the Republic of Kazakhstan, which has high potential for porphyritic copper mineralization [[7],[8],[9],[10],[11]] within the Central Asian fold belt. Moreover, a significant portion of known deposits is in mature stages of exploitation, making detailed study urgent and the identification of new deposits, including hidden and deep ore bodies, a priority [[12],[13],[14]]. State policy in the field of subsoil use focuses on addressing these problems. Geologists face a range of interrelated scientific and applied issues in developing geological and genetic models for porphyry systems, identifying criteria for predicting concealed mineralization, and integrating geophysical and geochemical techniques into detailed exploration of the geological characteristics of porphyritic copper mineralization [[2],[5]]. These trends underscore the importance of both searching for new porphyritic deposits and conducting in-depth exploration of known ones, including their mineral composition, mineralogical properties, and the forms of occurrence of valuable components. Accordingly, this work aims to conduct a detailed mineralogical study of oxidized copper-porphyry ores from the Koktaszhal deposit, determining their material composition, the forms of copper occurrence, and the ratios among oxidized, secondary, and primary forms.

Geological settings

The Koktaszhal deposit is located in the Egindybulak district of the Karaganda region (Fig. 1), 30 km northwest of the district center of Eginbulak [[15],[16]]. In regional-geological terms, it is confined to the eastern part of the Spassky anticlinorium. It is associated with an anticlinal fold composed of andesite-basalt porphyrites and their tuffs, with interlayers and lenses of rhyolite, dacite, siliceous tuffite, sandstone, siltstone, and limestone from the Middle Devonian period. The aforementioned volcanogenic-sedimentary formations have been universally cataclased, sheared, and propylitised, indicating significant tectonic reworkings and hydrothermal-metasomatic transformations of rocks [[15], [16]].

Intrusive magmatism is represented by the granitoids of the Koktaszhal Massif, which belong to the tonalite-granodiorite-plagiogranite suite and exhibit a three-phase structure. The first phase consists of gabbro and diorite; the second includes quartz diorites, tonalites, and granodiorites, which make up the main part of the massif; and the third comprises additional intrusions of plagiogranitic and granitic porphyries.

Ore-bearing structures are sill-like apophyses of the Koktaszhal Massif, formed by third-phase plagiogranitic porphyries and traced over about 1.300 meters (see Fig. 2).

Figure 1 – Location of the Koktaszhal Copper-Porphyry Deposit

Mineralization in the volcanic rocks is predominantly found at contact zones, indicating a close spatial relationship between ore mineralization and late-stage porphyritic intrusions.

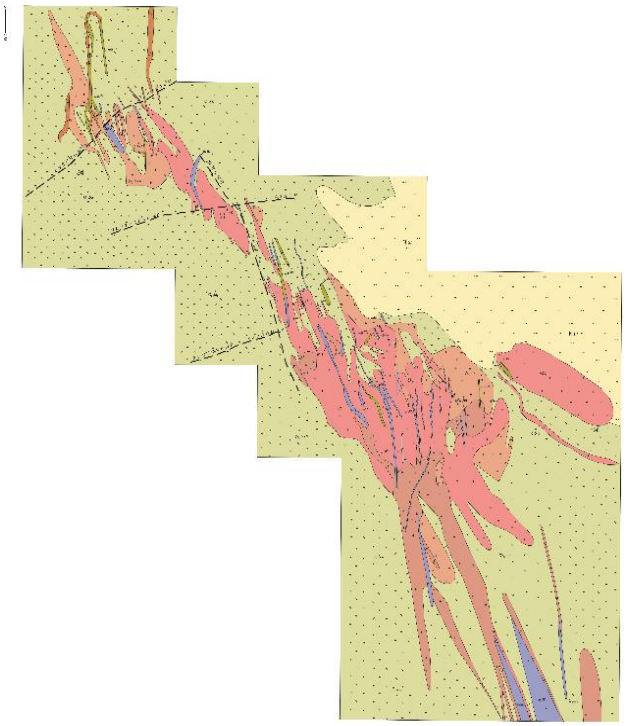

1 – weakly brownish bladed clays; 2 – quartzites over porphyrites and their tuffs; 3 – plagiogranit porphyry and granodiorite porphyry; 4 – secondary quartzite over porphyrite; 5 – albitophyres; 6 – secondary quartzite over plagiogranit porphyry; 7 – diorite porphyry; 8 – diabase porphyrite; 9 – tectonic faults

Figure 2 – Geological map of Koktaszhal Deposit [7]

The structural control of mineralization is evident in the development of a quartz-sulfide stockwork, which is concentrated primarily in the hanging wall of an apophysis. This stockwork is accompanied by intense quartzization, resulting in the formation of monocrystalline quartz rocks. Quartz veins are located along schistose planes and sometimes constitute up to 60-80% of rock volume, with the spaces between them filled with chlorite-sericite aggregates. The main ore mineralization associated with this vein system is represented by quartz-chalcopyrite and quartz-chalcopirite-bornite veins [15]. Thus, the Koktaszhal ore field is characterized by distinctly expressed vein-disseminated and stockwork-type mineralization that is structurally controlled by schistification zones and contact zones of intrusive bodies.

An essential feature of the deposit is the extensive development of the oxidation zone, which can be clearly traced to a depth of 20-50 meters. Malachite, azurite, chrysocolla, native copper, and goethite are found within this zone. At the same time, the leaching zone and the zone of secondary sulfide enrichment are virtually absent, with only occasional grains of covellite and chalcopyrite being observed up to a depth of about 90-95 meters [[15],[16],[17],[18],[19]]. This characteristic of the structure of the upper portion of the ore body suggests that the predominant processes involved are oxidative transformation of copper mineralization without formation of a distinct horizon of secondary sulphide enrichment [[18],[19]].

According to mineralogical and petrographic studies, ore-bearing rocks are represented by silicified acidic intrusive rocks, monocrystalline quartz formations, and layered schistose quartz-mica-chloritic rocks, often with interlayers of injected intrusive rock [[18],[19]].

Rock-forming minerals include quartz (43-45%), acidic plagioclase (31-33%), chlorite (9-11%), hydrophlogite (8-10%), and dolomite (2-3%). In some varieties of rock, intense fracturing is noted, with the development of microfractures, sericite, and impregnation with iron hydroxide, with fine inclusions of ore minerals and free gold grains [18]. This allows us to consider microfracturing and schistosity as the most significant structural and textural characteristics that control the distribution of mineralization within the deposit [[19],[20]].

In general, the geological and structural features of Koktaszhal are determined by a combination of the anticlinal position of the ore field, mineralization associated with silicate apophyses of the Koktaszhal massif, widespread development of quartz-sulfide veins and intense processes of calcification, schistosity and propylitisation of host rocks [15]. This combination reflects the complex structure of the

ore-magma system and creates structural and lithological conditions for the formation of vein-interspaced and oxidised copper-gold mineralisation at the Koktaszhal deposit.

Research methodology

For a more detailed study of the mineralogical features of the oxidized copper-gold ores from the Koktaszhal deposit, results of laboratory studies on representative technological samples of ore and mining material were used.

Samples were taken from central parts of ore bodies - Center-1 and Center-2 sites from upper horizons of the oxidation zone within the 2nd layer at 694m. A total of 8 samples of oxidized ore weighing up to 100 kg, including 6.4 kg, were sent to the FLSmidth Dawson Metallurgical Laboratories for analysis. The research involved sample preparation, mineralogical description, chemical, phase, and spectral analyses.

These studies included sample preparation, mineralogical descriptions, chemical, phase, rational, and spectral analyses. Main factual data were obtained during research carried out by the State Scientific and Production Association of Industrial Ecology "Kazmekhanobr" (Subsidiary State Enterprise SSAPIE "Kazmekhanobr"), Kazzink LLP, East Research Mining and Metallurgical Institute of Nonferrous Metals "VNIITSVETMET", and FLSmidt Dawson Metallurgical Laboratories.

Sample preparation for analysis involved mixing the source material, reducing it by quartering, crushing, screening, and separating it into subsamples for individual analysis methods. Loose samples and a medium-sized sample were collected for mineralogical study. Individual subsamples were sent for chemical, fire assay, phase analysis, and mineralogy analysis.

The mineralogical study of ores was conducted using optical-mineralogical methods on transparent and polished thin sections, immersed in liquids, and on polished artificial briquettes made from a medium sample and its heavy fraction. This approach allowed us to determine the composition of the ore and rock-forming minerals as well as the morphological features of malachite and azurite.

The mined material was studied using an Olympus BX51 Pol microscope, a Simagis 2P-2C video camera and SIAMS Mineral C7 software for oxidized primary and secondary copper sulfide deposits in polished sections. Additional information about finely dispersed phases and spatial relationships between copper-bearing minerals and host rock was provided by FLSmidth mineralogical data, including optical microscopy, backscatter electron microscopy, and QEMSCAN analysis.

The chemical and material characteristics of the ores were refined based on the results of semi-quantitative atomic emission spectral analysis, chemical analysis, and phase analysis of copper. Phase analysis was used to determine the ratio of water-soluble, oxidized, secondary, and primary forms of copper, which made it possible to determine the degree of oxidation of the ore and characterize it as an oxidized type of ore. Rational analysis was used to assess the forms of gold and silver, revealing free forms, aggregates with sulfides, rock grains coated with iron hydroxide films, as well as difficult-to-extract forms associated with rock.

Results and Discussion

To characterize the Koktaszhal ore sample, a chemical analysis was performed to determine the main useful components. The results are presented in Table 1. As can be seen from the presented data, the original ore contains 1.0% Cu, 0.8 g/t Au, and 2.0 g/t Ag, making it a porphyry copper deposit with significant commercial copper and precious metal content. Lead and zinc are present in low concentrations, and iron at 1.51% indicates that these elements play a subordinate role in the overall composition of the ore.

Table 1 – Chemical composition of the ore sample from the Koktaszhal deposit

Name	Content, %					g/t	
	lead	zinc	copper	iron	S_{pyr}	gold	silver
Ore	0.07	0.02	1.0	1.51	0	0.8	2.0

According to Table 1, copper is the leading mineral component of the ore, with associated gold and silver. Combined with subsequent mineralogical and phase data, this allows us to consider the sample as oxidized copper porphyry ore.

To characterize the host mineral mass, a silicate analysis of the sample for rock-forming elements was performed. The results are presented in Table 2. The table shows that silicon dioxide (SiO_2) predominates in the ore composition at 69.82%, with a subordinate aluminum oxide (Al_2O_3) content of 12.78%. The contents of the remaining components are significantly lower: Fe_2O_3 – 2.08%, BaO – 1.63%, MgO – 1.35%, and CaO – 0.66%.

Table 2 shows that the ore is dominated by siliceous and aluminosilicate components. The elevated SiO_2 content indicates a significant proportion of siliceous material in the ore structure and may indicate increased strength of the host rocks, while the Al_2O_3 content reflects the presence of aluminosilicate [[20],[21]]. This establishes the significant role of silicate material in the structure of the ore mass, which is important for characterizing its composition and interpreting the properties of the host rocks.

Table 2 – Chemical analysis of the ore sample from the Koktaszhal deposit for rock-forming elements

Name	Content, %					
	BaO	Fe_2O_3	CaO	MgO	Al_2O_3	SiO_2
Ore	1.63	2.08	0.66	1.35	12.78	69.82

To clarify the elemental composition of the studied process sample and assess the role of rare and trace components, a semi-quantitative atomic emission spectral analysis was performed. The results are presented in Table 3. These analysis data allow us to characterize the general geochemical background of the ore and clarify the composition of the host mineral mass.

As can be seen from Table 3 and Fig. 3, the sample is dominated by silicon, aluminum, calcium, magnesium, iron, and sodium, confirming the significant role of the quartz-plagioclase and aluminosilicate host mass. Among the minor components, titanium, barium, and strontium are characterized by relatively elevated contents. Most rare and trace elements are present at low concentrations or below the detection limit.

To determine the mineral composition of the sample, a quantitative mineralogical analysis was performed. Microscopic examination was conducted on the original sample, its heavy fraction, and crushed material. The observation results were compared with data from previous analytical studies, which allowed us to refine the sample's mineral composition and the quantitative ratios of individual minerals.

The results are presented in Table 4 and additionally presented as a histogram (Fig. 4). Analysis of the table and histogram data shows that the main industrially valuable minerals are malachite and azurite, while associated and minor minerals include hematite, magnetite, goethite, pyrite, and limited copper sulfides.

Table 3 – Results of semi-quantitative atomic emission spectral analysis of the sample

Elements	Concentration, %	Elements	Concentration, %
Au	<0.00005	Cd	<0.0005
Cu	<1.0	Ni	0.005
Ag	0.001	Co	0.002
Si	>>1.0	Cr	0.007
Fe	>1.0	Sr	0.1
Ca	>1.0	Sn	0.0003
Al	>>1.0	Ti	0.5
Mg	>1.0	Bi	<0.0002
Pb	0.01	Y	0.003
Zn	0.01	Ge	<0.0002
Na	≥1.0	Tl	<0.0005
Mo	0.0007	Te	<0.003
Hg	<0.003	As	<0.01
Ba	0.15	Be	0.0001
Ga	0.004	W	<0.003
Ta	<0.01	Yb	0.00025
Se	<0.1	Nb	0.001
Re	<0.0003	Sc	0.002

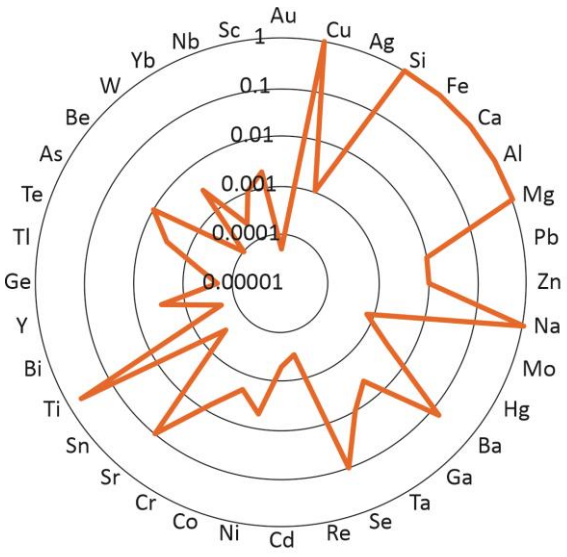

Figure 3 – Element distribution in the sample based on semi-quantitative atomic emission spectral analysis

The rock-forming component is represented primarily by quartz, plagioclase, chlorite, mica, and dolomite.

The described features of the distribution and morphology of copper minerals are clarified by the results of microscopic studies shown in Figures 5 and 6. Microscopic examination of a sample of copper oxide ore allowed us to establish the forms of separation of malachite and azurite, the nature of their distribution in the ore mass, and the features of accretion with rock-forming minerals. It was established that malachites and azurites are represented by two main morphological differences. The first difference is expressed by well-crystallized translucent and transparent formations observed in the form of nests, 1-5 mm in size; veins, 1-3 mm thick; as well as secretions along microcracks and between grains of rock-forming mineral. The second difference is represented by earthy, slightly crystallized collomorphic formations forming inclusions, 0.07-0.2 μm or more, which form cracks and sometimes form accretions with iron hydroxide.

Malachite is characterized by the development of radially fibrous aggregates and kidney-shaped forms.

Table 4 – Mineral Composition of the Ore Sample

Product	Mineral Composition, Mass Fraction, %											
	Ore							Rock-Forming Materials				
Sample	Malachite	Azurite	Gold*	Hematite, Magnetite	Goethite	Sulfides Cu, Cu itself	Pyrite	Quartz	Plagioclase	Chlorite	Mica	Dolomite
	1.5-2.0	0.3-0.4	*SCE*	0.5	0.2	*SCE*	0.2	43-45	31-33	9-11	8-10	2-3

*Note: * – content of gold, copper sulfides, and native copper – SCE (significant concentrations not established). These minerals are present in the sample in quantities below the detection limit; therefore, their mass fraction cannot be quantitatively determined. The absence of significant concentrations of copper sulfides confirms that the sample belongs to the oxidation zone, where primary sulfide minerals are completely replaced by secondary copper oxides and carbonates (malachite, azurite) [[18], [19]].*

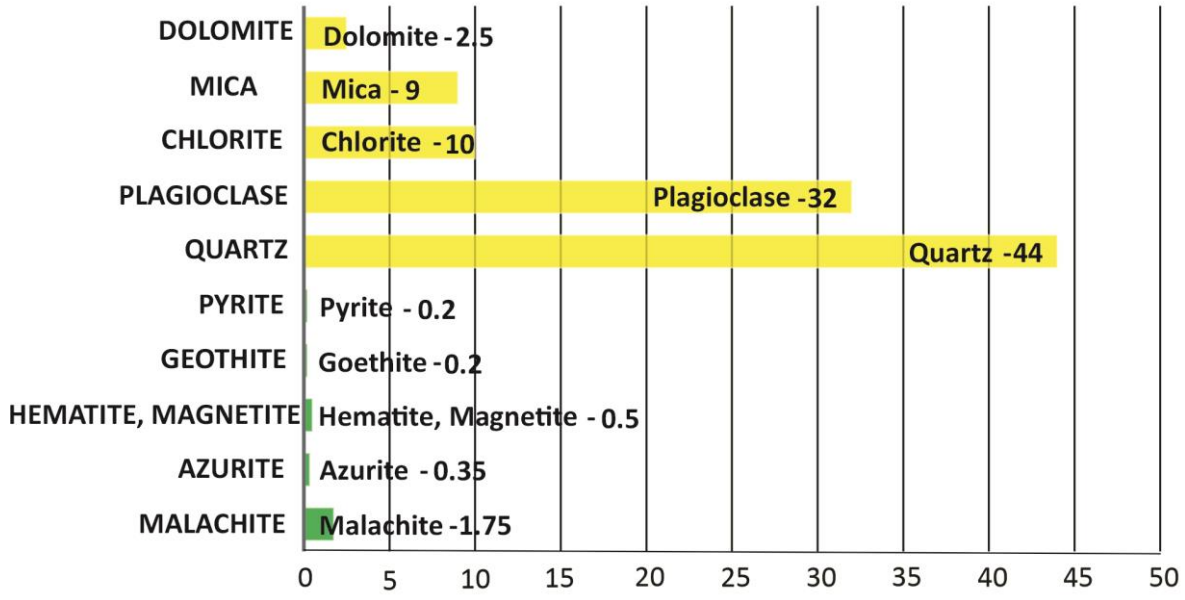

Figure 4 – Distribution of Ore and Rock-Forming Minerals in the Koktaszhal Deposit Ore

The results of rational analysis presented in Table 5 were used to characterize copper species in a sample. Based on phase analysis, copper was found to be extremely unevenly distributed among various compound forms in the Koktashal deposit sample. The total copper content was 0.735%, with the vast majority concentrated in the oxidized form – 0.66% or 89.8% of the total content. Primary copper content was found at 0.047% (6.39%) and secondary copper at 0.2% (2.72%). Water-soluble copper was also found at a concentration of 0.8%.

The predominance of the oxidized form of copper indicates a significant degree of transformation of the original ore mineralization in the hypergenesis zone [22]. According to modern concepts, the formation of powerful oxidation zones in porphyry copper systems requires long-term exposure to oxidation processes in a semi-arid climate and tectonic uplift, resulting in a lowering of the groundwater level [[22],[23]]. The low content of primary and secondary sulfides (around 9% in total) indicates that they are largely destroyed and replaced by oxidation products. Similar processes have been described for hypergenesis zones in the Southern Urals and Lesser Caucasus, where oxidized ores form full-profile zonal patterns with subzones of oxidation, leaching, and secondary sulfide enrichment [[24], [25]]. This allows us to interpret the studied ore samples as material formed under conditions of intense hypergenic oxidation and copper redistribution [[22], [24], [25]].

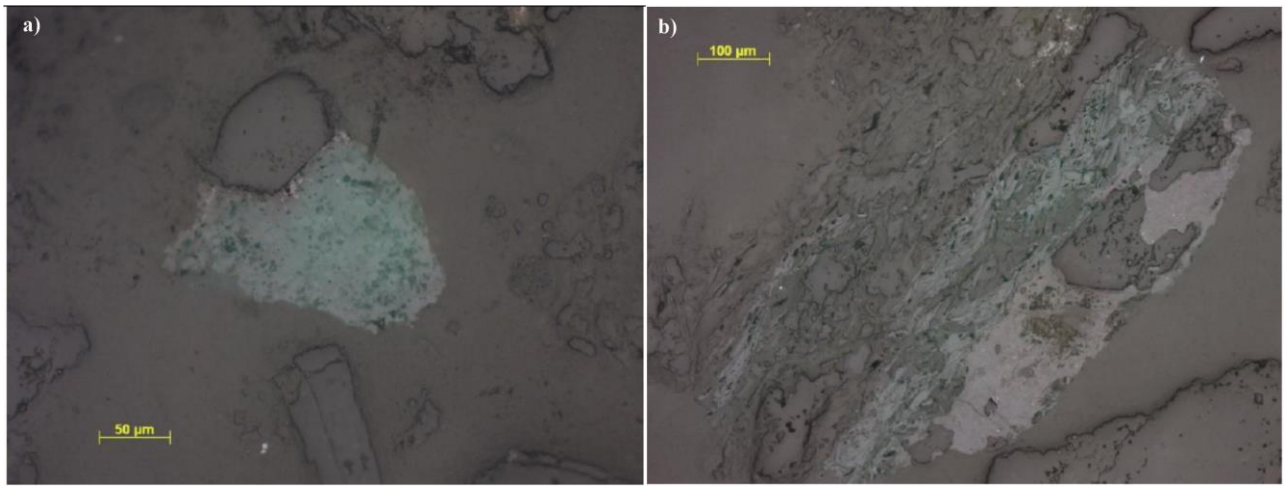

Figure 5 – Optical microscopy images of Cu oxide ore sample: turquoise – malachite /azurite

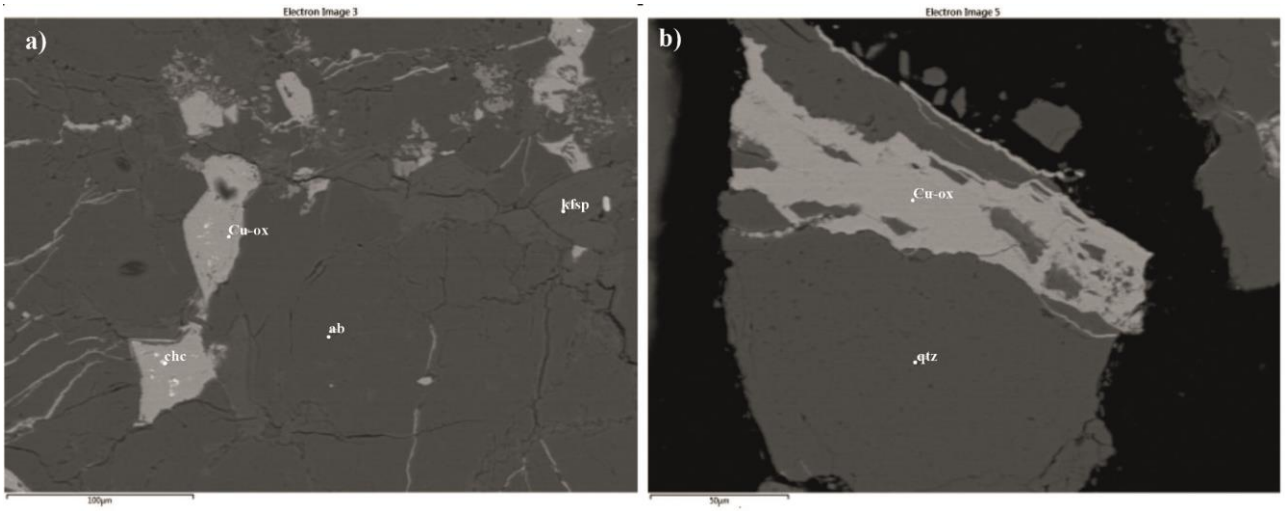

Figure 6 – Electron backscatter microscopy images of a Cu oxide ore sample: Cu-ox = malachite/azurite, chc = chalcocite, ab = albite, kfsp = K-feldspar, qtz = quartz

The results of copper phase analysis in the sample were further visualized as a histogram (Fig.7). This representation allows for a more visual assessment of the ratio of primary, secondary, oxidized, and water-soluble forms of copper, as well as identification of its dominant type in ore. Analysis of the data presented in Table 5 and the resulting histogram (Fig.7) shows that the sample belongs to the oxidized ore type.

Table 5 – Phase analysis of an ore sample from the Koktaszhal deposit (copper)

Minerals	Compounds	Content, %	
		abs.	rel.
Copper	Primary	0.047	6.39
	Secondary	0.02	2.72
	Oxidized	0.66	89.80
	Water-soluble	0.008	1.09
	Total	0.735	100

This is entirely consistent with its mineralogical characteristics, according to which the main ore minerals are malachite and azurite, while primary sulfide forms of copper are subordinate. Determining the oxidized type of ore is of significant scientific and practical importance. On the one hand, this confirms the significant role of hypergenic processes in the transformation of primary copper mineralization [[25], [26]]. On the other hand, it allows us to predict technological features of ore processing, since the predominance of oxidized copper minerals determines specifics of its enrichment and extraction of valuable components [[27], [28]].

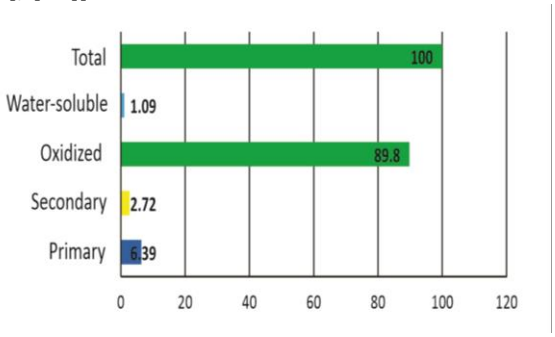

Figure 7 – Phase analysis of ore from the Koktaszhal deposit (copper)

The obtained analytical data indicate that the Koktaszhal ore belongs to the oxidized copper porphyry type with a well-developed supergene alteration zone. Copper is predominantly represented by secondary minerals such as malachite and azurite, which determines favorable conditions for hydrometallurgical processing. The high silica content reflects a strong quartz–aluminosilicate host matrix, which may increase ore hardness and influence comminution characteristics. At the same time, low contents of carbonate components suggest reduced acid consumption during leaching. The presence of finely disseminated copper mineralization and its association with iron hydroxides may negatively affect metal recovery and should be taken into account when selecting processing technology. Overall, the ore is characterized by a favorable composition in terms of valuable components and relatively low concentrations of harmful impurities, making it a promising object for further technological evaluation.

Conclusions

The study revealed that the oxidized copper porphyry ores of the Koktaszhal deposit are characterized by a complex composition and pronounced mineralogical heterogeneity. The main ore minerals in the studied samples were malachite and azurite, while primary and secondary copper sulfides were present in subordinate amounts. The host mineral mass is predominantly siliceous-aluminosilicate in nature and consists primarily of quartz, plagioclase, chlorite, and mica, reflecting the significant role of the silicate matrix in the structure of the ore strata.

It was found that malachite and azurite exhibit significant morphological diversity and are represented by both well-crystallized veinlet-nested formations and colloform earthy aggregates. Their development along microcracks, between grains of rock-forming minerals, and in association with iron hydroxides indicates a significant role for hypergene processes in the transformation of the original copper mineralization. At the same time, the presence of preserved sulfide forms of copper indicates signs of an earlier stage of mineral formation.

The phase composition of copper confirms that the studied ores belong to the oxidized type, as the majority of the metal is associated with oxidized forms.

Therefore, the oxidized ores of the Koktaszhal deposit represent a mineralogically complex product of the processing of a copper-porphyry system under conditions of intense hypergenesis. The combined data obtained allow Koktaszhal to be considered a representative object for the study of the mineral composition, morphology of secondary copper minerals, and the forms of copper occurrence in oxidized copper-porphyry ores.

Conflicts of interest. The authors declare that they have no conflicts of interest regarding the publication of this paper.

CRediT author statement: **K.Toleubek:** Conceptualization, Investigation, Data curation, Writing – original draft; **A. Kopobayeva:** Supervision, Methodology, Validation, Writing – review & editing; **A. Amangeldikyzy:** Investigation, Formal analysis, Data curation; **N. Askarova:** Laboratory analyses, Validation, Data interpretation; **E. Zengin:** Methodology, Software, Formal analysis; **G. Zhunusbekova:** Visualization, Data processing, Writing – review; **B. Mazakh:** Validation, Data curation, Investigation; **A. Battalova:** Resources, Project administration.

Cite this article as: Toleubek KE, Kopobayeva AN, Amangeldikyzy A, Askarova NS, Zengin E, Zhunusbekova GYe, Mazakh B, Battalova AS. Mineralogical Characteristics of Oxidized Copper-Porphyry Ores at the Koktaszhal Deposit. Kompleksnoe Ispolzovanie Mineralnogo Syra = Complex Use of Mineral Resources. 2028; 346(3):28-39. https://doi.org/10.31643/2028/6445.26

Көктасжал кен орнының тотыққан мыс-порфирлі кендерінің минералогиялық ерекшеліктері

[1] Төлеубек К.Е., [1*]Копобаева А.Н., [1]Амангелдіқызы А., [1]Асқарова Н.С., [2]Zengin E., [1]Жунусбекова Г.Е., [1]Мазах Б., [1]Батталова А.С.

[1]Әбілқас Сағынов атындағы Қарағанды техникалық университеті, Қарағанды, Қазақстан
[2]Ыстанбұл техникалық университеті (ITU), Ыстанбұл, Түркия

Мақала келді: *27 сәуір 2026*
Сараптамадан өтті: *21 мамыр 2026*
Қабылданды: *24 шілде 2026*

ТҮЙІНДЕМЕ

Мақалада Көктасжал кен орнының тотыққан мыс порфир кендерін егжей-тегжейлі зерттеу нәтижелері ұсынылған. Оптикалық микроскопияны, силикатты және фазалық талдауды кешенді қолдану негізінде тотығу аймағының негізгі минералогиялық ерекшеліктері анықталды. Кендердің материалдық құрамы анықталды: мыстың жалпы мөлшері 0,735% құрайды, оның ішінде 0,66% (89,8%) тотыққан түрінде, 0,047% (6,39%) бастапқы, 0,02% (2,72%) екінші реттік және суда еритін 0,008% (1,09%) болды. Анықталған жетекші кен минералдары малахит (1,5-2,0%) және азурит (0,3-0,4%), сондай-ақ қосымша минералдар: магнетит қосылған гематит (0,5%), гетит (0,2%) және пирит (0,2%) бар; мыс сульфидтері және табиғи мыс анықтау шегінен төмен мөлшерде кездеседі. Бұл жұмыстың ғылыми жаңалығы классикалық минералогиялық зерттеулердің сандық фазалық талдау деректерімен үйлесімінен туындайды, бұл бізге кендердің минералды құрамы туралы ақпаратты жүйелеуге ғана емес, сонымен қатар мыстың пайда болуының әртүрлі формалары арасындағы байланысты анықтауға мүмкіндік берді. Малахит пен азуриттің морфологиялық ерекшеліктері сипатталады: олар жақсы кристалданған тамырлы ұялы түзілімдермен және темір гидроксидтерімен байланысты микрожарықтар бойымен дамыған коллоформды жер агрегаттарымен ұсынылған. Алынған нәтижелерді ұқсас объектілерді болжау және іздеу кезінде пайдалануға болады, себебі мыс сульфидтері болмаған кезде малахит пен азуриттің темір гидроксидтерімен байланысы мыс-порфирлік жүйелердің тотығу аймағының диагностикалық ерекшелігі болып табылады, ал мыстың пайда болу формалары туралы сандық деректер бір жағынан барлаудың алғашқы кезеңдерінде кендерді гипергенмен өңдеу тереңдігін бағалауға, ал екінші жағынан, тотығу аймағының кендерін тәуелсіз геологиялық және өнеркәсіптік түрге бөлуге мүмкіндік береді, бұл қорларды есептеуде, кен денелерін анықтауда және өңдеу схемасын таңдауда маңызды болып табылады.

Түйін сөздер: Көктасжал, мыс-порфир кен орындары, тотыққан кендер, мыстың фазалық талдауы, малахит, азурит, алтынның пайда болу формалары, заттық құрамы.

Авторлар туралы ақпарат:

Төлеубек Қымбат Есмахайқызы
Әбілқас Сағынов атындағы Қарағанды техникалық университетінің Геология және пайдалы қазбалар кен орындарын барлау кафедрасының докторанты, 100027, Нұрсұлтан Назарбаев даңғ. 56, Қарағанды, Қазақстан. E-mail: toleubekkymbat69@gmail.com; ORCID ID: https://orcid.org/0000-0003-2126-8084

Копобаева Айман Ныгметовна
PhD, Әбілқас Сағынов атындағы Қарағанды техникалық университетінің Геология және пайдалы қазбалар кен орындарын барлау кафедрасының қауымдастырылған профессоры, 100027, Нұрсұлтан Назарбаев даңғ. 56, Қарағанды, Қазақстан. E-mail: a.n.kopobayeva@gmail.com; ORCID ID: https://orcid.org/0000-0002-0601-9365

Амангелдіқызы Алтынай
PhD, Әбілқас Сағынов атындағы Қарағанды техникалық университетінің Геология және пайдалы қазбалар кен орындарын барлау кафедрасының қауымдастырылған профессоры, 100027, Нұрсұлтан Назарбаев даңғ. 56, Қарағанды, Қазақстан. E-mail: a.amangeldykyzy@ktu.edu.kz; ORCID ID: https://orcid.org/0000-0002-6665-8804

Асқарова Назым Сражадинқызы	*PhD, Әбілқас Сағынов атындағы Қарағанды техникалық университетінің Геология және пайдалы қазбалар кен орындарын барлау кафедрасының қауымдастырылған профессоры (доценті), 100027, Нұрсұлтан Назарбаев даңғ. 56, Қарағанды, Қазақстан. E-mail: n.askarova@ktu.edu.kz; ORCID ID: https://orcid.org/0000-0002-2103-6198*
Zengin Enes	*PhD, Ыстанбұл техникалық университетінің (ITU) Тау-кен факультетінің Геологиялық инженерия кафедрасының қауымдастырылған профессоры, Аязаға кампусы, 34469, Маслак, Ыстанбұл, Түркия. E-mail: eneszengin@itu.edu.tr; ORCID ID: https://orcid.org/0000-0002-5740-7763*
Жунусбекова Гулден Ермухановна	*Әбілқас Сағынов атындағы Қарағанды техникалық университетінің Геология және пайдалы қазбалар кен орындарын барлау кафедрасының аға оқытушысы, 100027, Нұрсұлтан Назарбаев даңғ. 56, Қарағанды, Қазақстан. E-mail: zh.gulden@ktu.edu.kz; ORCID ID: https://orcid.org/0000-0002-6578-5959*
Мазах Бакытжан	*Әбілқас Сағынов атындағы Қарағанды техникалық университетінің Геология және пайдалы қазбалар кен орындарын барлау кафедрасының докторанты, 100027, Қарағанды, Қазақстан. E-mail: 06.06.2005@mail.ru; ORCID ID: https://orcid.org/0009-0007-5390-298X*
Батталова Арай Саяхатовна	*Әбілқас Сағынов атындағы Қарағанды техникалық университетінің Геология және пайдалы қазбалар кен орындарын барлау кафедрасының магистранты, 100027, Нұрсұлтан Назарбаев даңғ. 56, Қарағанды, Қазақстан. E-mail: a84207553@gmail.com; ORCID ID: https://orcid.org/0009-0009-3192-1367*

Минералогические особенности окисленных медно-порфировых руд месторождения Коктасжал

[1]Төлеубек К.Е., [1*]Копобаева А.Н., [1]Амангелдіқызы А., [1]Асқарова Н.С., [2]Zengin E., [1]Жунусбекова Г.Е., [1]Мазах Б., [1]Батталова А.С.

[1]Карагандинский технический университет имени Абылкаса Сагинова, Караганда, Казахстан
[2]Стамбульский технический университет (ITU), Стамбул, Турция

Поступила: *27 апреля 2026*
Рецензирование: *21 мая 2026*
Принята в печать: *24 июля 2026*

АННОТАЦИЯ

В статье представлены результаты детального изучения окисленных медно-порфировых руд месторождения Коктасжал. На основе комплексного применения методов оптической микроскопии, силикатного и фазового анализов выявлены ключевые минералогические особенности зоны окисления. Установлен вещественный состав руд: общее содержание меди составляет 0,735%, из которых 0,66% (89,8%) приходится на окисленную форму, 0,047% (6,39%) – на первичную, 0,02% (2,72%) – на вторичную и 0,008% (1,09%) – на водорастворимую. Идентифицированы ведущие рудные минералы: малахит (1,5-2,0%) и азурит (0,3-0,4%), а также второстепенные: гематит с магнетитом (0,5%), гетит (0,2%) и пирит (0,2%); сульфиды меди и самородная медь присутствуют в количествах ниже предела обнаружения. Научная новизна работы обусловлена сочетанием классического минералогического изучения с количественными данными фазового анализа, что позволило не только систематизировать сведения о минеральном составе руд, но и уточнить соотношение различных форм нахождения меди. Охарактеризованы морфологические особенности малахита и азурита: они представлены как хорошо окристаллизованными прожилково-гнездовыми образованиями, так и колломорфными землистыми агрегатами, развитыми по микротрещинам в ассоциации с гидрооксидами железа. Полученные результаты могут быть использованы при прогнозировании и поисках аналогичных объектов, поскольку установленная ассоциация малахита и азурита с гидрооксидами железа при отсутствии сульфидов меди является диагностическим признаком зоны окисления медно-порфировых систем, а количественные данные о формах нахождения меди позволяют, с одной стороны, оценивать глубину гипергенной переработки руд на ранних стадиях разведки, а с другой – выделить руды зоны окисления в самостоятельный геолого-промышленный тип, что важно при подсчёте запасов, оконтуривании рудных тел и выборе технологической схемы переработки.

Ключевые слова: Коктасжал, медно-порфировые месторождения, окисленные руды, фазовый анализ меди, малахит, азурит, формы нахождения золота, вещественный состав.

Толеубек Кымбат Есмахайкызы	***Информация об авторах:*** *Докторант кафедры Геология и разведка месторождений полезных ископаемых Карагандинского технического университета имени Абылкаса Сагинова, 100027, пр. Нурсултана Назарбаева, 56, Караганда, Казахстан. E-mail: toleubekkymbat69@gmail.com; ORCID ID: https://orcid.org/0000-0003-2126-8084*
Копобаева Айман Ныгметовна	*Доктор PhD, ассоциированный профессор кафедры Геология и разведка МПИ, Карагандинский технический университет имени Абылкаса Сагинова, 100027, пр. Нурсултана Назарбаева, 56, Караганда, Казахстан. E-mail: a.n.kopobayeva@gmail.com; ORCID ID: https://orcid.org/0000-0002-0601-9365*

Амангелдіқызы Алтынай	*Доктор PhD, ассоциированный профессор кафедры Геология и разведка МПИ, Карагандинский технический университет имени Абылкаса Сагинова, 100027, пр. Нурсултана Назарбаева, 56, Караганда, Казахстан. E-mail: a.amangeldykyzy@ktu.edu.kz; ORCID ID: https://orcid.org/0000-0002-6665-8804*
Аскарова Назым Сраджадиновна	*Доктор PhD, ассоциированный профессор (доцент) кафедры Геология и разведка МПИ, Карагандинский технический университет имени Абылкаса Сагинова, 100027, пр. Нурсултана Назарбаева, 56, Караганда, Казахстан. E-mail: n.askarova@ktu.edu.kz; ORCID ID: https://orcid.org/0000-0002-2103-6198*
Zengin Enes	*PhD, ассоциированный профессор кафедры геологической инженерии горного факультета Стамбульского технического университета (ITU), кампус Аязага, 34469, Маслак, Стамбул, Турция; E-mail: eneszengin@itu.edu.tr; ORCID ID: https://orcid.org/0000-0002-5740-7763*
Жунусбекова Гулден Ермухановна	*Старший преподаватель кафедры Геология и разведка кафедры МПИ, Карагандинский технический университет имени Абылкаса Сагинова, 100027, пр. Нурсултана Назарбаева, 56, Караганда, Казахстан. E-mail: zh.gulden@ktu.edu.kz; ORCID ID: https://orcid.org/0000-0002-6578-5959*
Мазах Бакытжан	*Докторант кафедры Геология и разведка месторождений полезных ископаемых Карагандинского технического университета имени Абылкаса Сагинова, 100027, пр. Нурсултана Назарбаева, 56, Караганда, Казахстан. E-mail: 06.06.2005@mail.ru; ORCID ID: https://orcid.org/0009-0007-5390-298X*
Батталова Арай Саяхатовна	*Магистрант кафедры Геология и разведка месторождений полезных ископаемых, Карагандинский технический университет имени Абылкаса Сагинова, 100027, пр. Нурсултана Назарбаева, 56, Караганда, Казахстан. E-mail: a84207553@gmail.com; ORCID ID: https://orcid.org/0009-0009-3192-1367*

References

[1] International Copper Association. Copper Environmental Profile. URL: https://copperalliance.org/wp-content/uploads/2021/08/ICA-EnvironmentalProfileHESD-201803-FINAL-LOWRES-1.pdf

[2] International Copper Study Group. The World Copper Factbook 2024. Lisbon: International Copper Study Group, 2024. URL: https://icsg.org/download/2024-09-23-the-world-copper-factbook-2024/

[3] Ayuso RA, Barton MD, Blakely RJ, Bodnar RJ, Dilles JH, Gray F, Graybeal FT, Mars JL, McPhee D, Seal RR, Taylor RD, Vikre P. Porphyry copper deposit model. Reston, VA: U.S. Geological Survey. Scientific Investigations Report 2010-5070-B. 2010, 169. https://doi.org/10.3133/sir20105070B

[4] Sillitoe RH. Porphyry copper systems. Economic Geology. 2010; 105(1):3-41. https://doi.org/10.2113/gsecongeo.105.1.3

[5] International Energy Agency. Global Critical Minerals Outlook 2024. Paris: IEA. 2024.

[6] International Energy Agency. Copper. Paris: IEA. 2024.

[7] Li C, Shen P, Seltmann R, Zhang D, Pan H, Seitmuratova E. Quartz textures, trace elements, fluid inclusions, and in situ oxygen isotopes from Aktogai porphyry Cu deposit, Kazakhstan. American Mineralogist. 2025; 110(2):272–292. https://doi.org/10.2138/am-2023-8931

[8] Serikbayeva E, Togizov K, Talgarbayeva D, Orynbassarova E, Sydyk N, Bermukhanova A. Application of Multispectral Data in Detecting Porphyry Copper Deposits: The Case of Aidarly Deposit, Eastern Kazakhstan. Minerals. 2025; 15:938. https://doi.org/10.3390/min15090938

[9] Ragdanova A, Mataibayeva I, Frolova O, Agaliyeva B, Dolgopolova A, Togizov K. Structural-formational zones with porphyry copper mineralization – A promising mineral resource base for copper in Eastern Kazakhstan. Min. Miner. Depos. 2025; 19:107-120. https://doi.org/10.33271/mining19.01.107

[10] Baibatsha A, Vikentyev I, Muratkhanov D, Bulegenov K. New Porphyry Copper-Molybdenum Ore Occurrence in Arganaty Granites of the Eastern Balkhash (Kazakhstan): Geology, Geochemistry, and Mineralogy. Geosciences. 2024; 14:237. https://doi.org/10.3390/geosciences14090237

[11] Kopobayeva AN, Zharylgapov YeYe, Ulgibayeva BS, Amangeldikyzy A, Askarova NS, Kabyken AB. A study of the geochemical features of the Nurkazgan copper-porphyry deposit. Kompleksnoe Ispolzovanie Mineralnogo Syra = Complex Use of Mineral Resources. 2027; 340(1):67-76. https://doi.org/10.31643/2027/6445.07

[12] Kopobayeva A, Musabayeva M, Amangeldikyzy A, Askarova N, Issatayeva F, Toleubek K, & Mazakh B. Study of geochemical characteristics of the Bakyrchik ore zone. Kompleksnoe Ispolzovanie Mineralnogo Syra = Complex Use of Mineral Resources. 2026; 338(3):81–91. https://doi.org/10.31643/2026/6445.31

[13] Shah Z, Bayramov E, Neafie J, Seltmann R, Rahnama Z. Determination of geospatial criteria and prediction of potential areas for porphyry copper deposits in Kazakhstan. Sec. Geoinformatics. 2025; 13. https://doi.org/10.3389/feart.2025.1489969

[14] Feng H, Seltmann R, Shen P, Chu X, Suo Q, Seitmuratova E, Shatov V. Hydrothermal rutile chemistry and U-Pb age fingerprinting of the formation of the giant Nurkazgan porphyry Cu-Au deposit, Central Kazakhstan. Ore Geology Reviews. 2024, 174. https://doi.org/10.1016/j.oregeorev.2024.106293

[15] Bolatbekuly S, Umirova G, Zakariya M, Temirkhanova R, Togizov K. Formation of prospecting criteria for copper-porphyry deposits based on the construction of reference models. Nauk. Visnyk Natsionalnoho Hirnychoho Universytetu. 2024; 2:19-24. https://doi.org/10.33271/nvngu/2024-2/019

[16] Kopobayeva AN, Toleubek KE, Amangeldikyzy A, Askarova NS. Mineral and geochemical features of the porphyry copper ores at Koktaszhal deposit, central Kazakhstan. Naukovyi Visnyk Natsionalnoho Hirnychoho Universytetu. 2025; 5:23-31. https://doi.org/10.33271/nvngu/2025-5/023

[17] Duzhnikova EV, Kryazheva TV, Kenzhin B M. Mineralnyy sostav rud i usloviya ikh obrazovaniya na mestorozhdenii Koktaszhal [Mineral composition of ores and conditions of their formation at the Koktaszhal deposit]. Vestnik VKGTU im. D. Serikbayeva. 2019; 1(83):3-8. (in Russ.).

[18] Duzhnikova Ye V, Kryazheva TV, Toleubek KYe. Koktaszhal ore field (Central Kazakhstan) research results. Naukovyi Visnyk Natsionalnoho Hirnychoho Universytetu. 2020; 3:5-12. https://doi.org/10.33271/nvngu/2020-3/005

[19] Otchet po rezultatam laboratornykh issledovaniy na obogatimost proby rudy mestorozhdeniya Koktaszhal [Report on the results of laboratory tests on the enrichment of ore samples from the Koktaszhal deposit]. Zyryanovsk. 2011. (in Russ.).

[20] Izucheniye prichin poter medi pri flotatsii okislennoy rudy na OF TKB i razrabotka rezhima povysheniya izvlecheniya eye iz srednikh klassov krupnosti (-0.125+0.04 mm): otchet o nauchno-issledovatelskoy rabote [Investigation of the causes of copper losses during flotation of oxidized ore at the Office of the TCB and the development of a mode for increasing its extraction from medium grades of fineness (-0.125+0.04 mm): research report] Ust-Kamenogorsk: VNIItsvetmet. 2017. (in Russ.).

[21] Pękala A. The Influence of Siliceous Mineral Phases on the Mechanical Properties of Transitional Rocks in the Belchatow Lignite Deposit. E3S Web of Conferences. 2015; 8:01018. https://doi.org/10.1051/e3sconf/20150801018.

[22] Sillitoe RH. Supergene oxidized and enriched porphyry copper and related deposits. Economic Geology 100th Anniversary Volume. 2005, 723-768. https://doi.org/10.5382/AV100.22.

[23] Sillitoe RH, McKee EH. Age of supergene oxidation and enrichment in the Chilean porphyry copper province. Economic Geology. 1996; 91(1):164-179. https://doi.org/10.2113/gsecongeo.91.1.164

[24] Belogub EV, Novoselov KA. Gipergenez sulfidnykh mestorozhdeniy Yuzhnogo Urala: novyye dannyye po stroyeniyu. mineralogii i izotopnomu sostavu sery i ugleroda. Rudogenez [Hypergenesis of sulfide deposits in the Southern Urals: new structural data. mineralogy and isotopic composition of sulfur and carbon]. 2020. (in Russ.).

[25] Azadaliyev DzhA. Guseynova EB. Mineralogo-geneticheskiye osobennosti zony gipergeneza Garadagskogo mestorozhdeniya medno-porfirovykh rud (Gyadabeyskiy rudnyy rayon Malogo Kavkaza, Azerbaydzhan) [Mineralogical and genetic features of the hypergenesis zone of the Garadagh deposit of copper porphyry ores (Gadabeysky ore district of the Lesser Caucasus. Azerbaijan)]. ANAS Transactions. Earth Sciences. (in Russ.).

[26] Atapour H, Aftabi A. The geochemistry of gossans associated with Sarcheshmeh porphyry copper deposit, Rafsanjan, Kerman, Iran: Implications for exploration and the environment. Journal of Geochemical Exploration. 2007; 93(1):47-65. https://doi.org/10.1016/j.gexplo.2006.07.007

[27] Chavez WX. Supergene oxidation of copper deposits: Zoning and distribution of copper oxide minerals. SEG Discovery. 2000; 41:1-21. https://doi.org/10.5382/SEGnews.2000-41.fea

[28] Feng Q, Yang W, Wen S, Wang H, Zhao W, Han G. Flotation of copper oxide minerals: A review. International Journal of Mining Science and Technology. 2022; 32(6):1351-1364. https://doi.org/10.1016/j.ijmst.2022.09.011.

Crossref
DOI: 10.31643/2028/6445.27
Earth and Planetary Sciences: Earth-Surface Processes

Radioactivity as a prospecting indicator of rare earth, gold and polymetal deposits in eastern Kazakhstan and an indicator of increased radioecological hazard during their development

[1] Berkinbayev G.D., [1] Kayukov P.G., [1] Fedorov G.V., [1] Askarov S.A., [1] Nazyrova D.R., [2] Gavrilenko O.D., [2, 3] Temirbekov N.M., [2, 3] Temirbekov A.N., [2, 4*] Mustafina Z.A., [4] Zimanovskaya N.A.

[1] Ecoservice-S LLP, Almaty, Kazakhstan
[2]ROO National Engineering Academy of RK, Almaty, Kazakhstan
[3] Al-Farabi Kazakh National University, Almaty, Kazakhstan
[4] D. Serikbayev East Kazakhstan Technical University, Ust-Kamenogorsk, Kazakhstan

** Corresponding author email: zinurrka86@gmail.com*

Received: *March 22, 2026*
Peer-reviewed: *May 18, 2026*
Accepted: *July 30, 2026*

ABSTRACT
This study evaluates the role of natural radioactivity as an exploration indicator for rare-metal, gold, and polymetallic mineralization in Eastern Kazakhstan, as well as its significance as a factor of radioecological hazard. The analysis is based on the results of regional radiohydrolithochemical surveys conducted at a scale of 1:1,000,000, including bottom sediment sampling within microbasins. The study focuses on key natural radionuclides (U-238, Ra-226, Th-232, Ra-228, K-40) and their spatial distribution. Factor analysis was applied to identify anomalous geochemical associations and to assess their relationship with metallogenic structures. As a result, 80 potentially radioecologically hazardous zones were identified across Kazakhstan, including 5 zones within Eastern Kazakhstan. Within the study area, 12 anomalous sites were distinguished, characterized by 3–5 factors with cumulative explained variance ranging from 62.8% to 83.6%. The identified anomalies show spatial correspondence with major metallogenic zones, particularly the Rudny Altai and Kalba-Narym regions, which are associated with polymetallic and rare-metal mineralization. The results demonstrate that natural radioactivity can serve both as an effective exploration indicator and as an important factor of environmental risk. The study highlights the potential of integrating radioactivity parameters into exploration criteria and emphasizes the need to consider radiation safety in geological exploration and mining activities.

Keywords: radioactivity, prospecting indicator, gamma spectrometry, uranium, thorium, ore deposits.

Information about authors:

Berkinbayev Galym Dzhumanazarovich	*Candidate of Biological Sciences, Advisor to the Director, ECOSERVICE-S LLP, 050009, Tole Bi str., 202A, Almaty, Kazakhstan. Email: berkinbayev.g@ecoservice.kz; ORCID ID: https://orcid.org/0000-0003-0039-6909*
Kayukov Pavlin Gerasimovich	*Deputy Head of the Department of Radiometric Research Methods, ECOSERVICE-S LLP, Tole Bi St., 202A, 050009, Almaty, Kazakhstan. Email: kayukov.p@ecoservice.kz; ORCID ID: https://orcid.org/0000-0003-0567-7961*
Fedorov German Vasilyevich	*Academician of IANEB, Deputy Director of the Strategic Directorate, ECOSERVICE-S LLP, 050009, Tole Bi St., 202A, Almaty, Kazakhstan. Email: gvfyodorov@gmail.com; ORCID ID: https://orcid.org/0000-0003-0033-2657*
Askarov Seilkhan Akkazinovich	*PhD candidate, Director of the Strategic Directorate, ECOSERVICE-S LLP, 050009, Tole Bi str., 202A, Almaty, Kazakhstan. Email: askarov.s@ecoservice.kz; ORCID ID: https://orcid.org/0009-0009-1293-9334*
Nazyrova Dilyara Rivkatovna	*PhD candidate, GIS specialist, ECOSERVICE-S LLP, 050009, Tole Bi St., 202A, Almaty, Kazakhstan. Email: nazyrovadilyara@gmail.com; ORCID ID: https://orcid.org/0000-0002-1148-4480*
Gavrilenko Oleg Dmitrievich	*Candidate of Geological and Mineralogical Sciences, Leading Researcher, National Engineering Academy of the Republic of Kazakhstan (NEA RK), 050060, 67 Khodzhanova St., Almaty, Kazakhstan. Email: ogavrilenko8@gmail.com; ORCID ID: https://orcid.org/0000-0003-4227-1098*
Temirbekov Nurlan Mukhanovich	*Doctor of physical and mathematical sciences, professor, Al-Farabi Kazakh National University; Vice President of the National Engineering Academy of the Republic of Kazakhstan (NEA RK), 050060, 67 Khodzhanova St., Almaty, Kazakhstan. Email: ntemirbekov314@gmail.com; ORCID ID: https://orcid.org/0000-0001-7542-3778*
Temirbekov Almaz Nurlanovich	*PhD, Associate professor, Al-Farabi Kazakh National University; Leading Researcher, National Engineering Academy of the Republic of Kazakhstan (NEA RK), 050060, 67 Khodzhanova St., Almaty, Kazakhstan. Email: almastemir86@gmail.com; ORCID ID: https://orcid.org/0000-0002-4157-2799*

Mustafina Zinura Agzamovna	*PhD candidate, D. Serikbayev East Kazakhstan Technical University, Ust-Kamenogorsk, Kazakhstan; Researcher, National Engineering Academy of the Republic of Kazakhstan (NEA RK), 050060, 67 Khodzhanova St., Almaty, Kazakhstan. Email: zinurrka86@gmail.com; ORCID ID: https://orcid.org/0009-0001-6233-2479*
Zimanovskaya Nataliya Aleksandrovna	*PhD, associate professor, D. Serikbayev East Kazakhstan Technical University, 070004, Serikbayev str., 19, Ust-Kamenogorsk, Kazakhstan. Email: nzimanovskaya@edu.ektu.kz; ORCID ID: https://orcid.org/0000-0002-9881-690X*

Introduction

Uranium and thorium are often genetically unrelated to many ore-forming elements; however, they serve as parent nuclides of radioactive decay series that include isotopes with physical and chemical properties similar to those of other elements. Many of these isotopes exhibit elevated gamma activity, making it possible to indirectly detect the presence of associated chemical elements [[1], [2]]. During migration through structurally weakened zones, such as fault systems, oxidation zones, and weathering crusts, these isotopes form dispersion haloes that are commonly associated with ore-related elements. The identification and interpretation of such haloes can facilitate the recognition of their source zones and, ultimately, concealed ore bodies [2]. Combined with a comprehensive assessment of ore body characteristics, this approach may provide a basis for the future application of artificial intelligence technologies in solid mineral exploration.

Drawing on extensive geological exploration experience, JSC Volkovgeology maintained a specialized geological team that collaborated with various scientific and industrial organizations. The primary objective of this team was to provide scientific support for uranium prospecting throughout its area of operation.

In addition, a regional prospecting team was responsible for collecting and analyzing current information on uranium occurrences, supervising prospecting activities, evaluating the quality of exploration work, and providing technical support. Similar prospecting groups operated within individual expeditions, carrying out equivalent tasks within their designated territories. These exploration teams constituted the primary operational units of uranium prospecting. Comparable thematic teams and groups were also involved in the exploration of other mineral resources. At the same time, petroleum geologists and hydrogeologists conducted their activities independently from other geological services in Kazakhstan. Collectively, these efforts contributed to the establishment of a mineral resource base that has supported the country's needs for decades. However, further expansion and reassessment of this resource base have now become increasingly important.

The activities of thematic exploration teams were organized according to the standard stages of geological investigation, including reconnaissance, prospecting, evaluation, and detailed exploration. Each stage involved a specific set of tasks, such as geological surveying, compilation and analysis of previous exploration results, resource assessment, and planning of subsequent exploration activities.

Field teams prepared exploration programs and work plans, carried out field investigations, and produced technical reports, geological maps, and resource and reserve estimates. All activities were conducted in accordance with the requirements of the corresponding exploration stage. Recent developments in digital technologies and artificial intelligence have created a need for the systematic formalization and digitization of accumulated geological and related datasets. This includes the processing of digital information, the development of analytical algorithms, and the creation of decision-support systems capable of translating complex digital data into interpretable geological knowledge [[3], [4]].

This study aims to evaluate the role of natural radioactivity as an exploration indicator for rare-metal, gold, and polymetallic mineralization in Eastern Kazakhstan and to assess its significance as a source of potential radioecological hazards.

The objectives of the study include analyzing the distribution of radionuclides in bottom sediments, identifying anomalous zones through factor analysis, and evaluating their relationship with regional metallogenic structures.

In addition, the study considers the potential application of modern digital and analytical methods for processing geological and radiometric data as a promising direction for future research [5].

Materials and Methods

Data source. The present study is based on the results of regional radiohydrolithogeo-chemical surveys conducted across Kazakhstan

at a scale of 1:1,000,000. In Eastern Kazakhstan, field sampling and laboratory analyses were carried out between 1991 and 1994.

Although the surveys were originally designed to assess the radioecological state of the environment, the resulting dataset contains information not only on radionuclides but also on ore-related chemical elements. Consequently, these data can be effectively applied to geological and metallogenic investigations.

To date, a national geochemical database has been established, comprising approximately 18,000 sampling sites and analytical results for an average of 25 chemical components per sample. Based on these data, a series of digital maps depicting the distribution of radioactive and geochemical contaminants in bottom sediments and natural waters has been developed for all regions of Kazakhstan.

The surveys were conducted within the framework of the State Program 011, “Ensuring Radiation Safety,” which was aimed at evaluating the radiation situation throughout the territory of the Republic of Kazakhstan [[6], [7]].

Sampling design. The survey was conducted using a microbasin-based approach, whereby each sampling site reflects the integrated geochemical signature of its corresponding drainage basin [8].

Sampling was primarily carried out at the mouths of small rivers and streams. The average area of the investigated microbasins was approximately 120 km², with individual basin areas ranging from 80 to 150 km². In regions characterized by well-developed endorheic drainage systems, bottom sediment samples were collected from lakes. In dry stream channels, samples were taken from the lowest sections of the channel beds, where fine-grained material tends to accumulate.

In low-relief terrain, composite samples were collected from 10 × 10 m plots. Each composite sample consisted of five subsamples obtained from the four corners and the center of the sampling area. Quality-control samples accounted for approximately 5% of the total number of collected samples.

Field observations included the description of sediment grain size, color, and the presence of organic matter.

Sample preparation and analytical methods. Bottom sediment samples were air-dried and prepared according to standard laboratory procedures. From each initial sample weighing 5–6 kg, a representative subsample of approximately 0.7–0.8 kg (particle size fraction < 3 mm) was selected for analytical determination.

Gamma-ray spectrometric measurements were performed to determine the activities of Ra-226, Ra-228, Th-232, and K-40 using a Canberra gamma spectrometer equipped with a high-purity germanium detector [9]. The relative analytical uncertainty at background activity levels was approximately 30%. The corresponding detection limits were as follows:

- Ra-226: 20 Bq/kg
- Ra-228: 40 Bq/kg
- Th-232: 40 Bq/kg
- K-40: 100 Bq/kg

The concentrations of uranium, thorium, Pb, As, and Se were additionally determined by X-ray fluorescence analysis using an ARF-6 spectrometer. The detection limits were:

- U: 0.4 mg/kg (approximately 4.0 Bq/kg)
- Th: 1.0 mg/kg (approximately 4.1 Bq/kg)
- Pb: 0.001%
- Se: 0.001%
- As: 0.002%

Although more advanced analytical techniques, such as inductively coupled plasma mass spectrometry (ICP–MS), are currently available, the present study is based on archived datasets obtained using the analytical methods described above.

Data selection. For the present study, only bottom sediment samples were considered. Five naturally occurring radionuclides were selected as the primary indicators: U-238, Ra-226, Th-232, Ra-228, and K-40.

These radionuclides were used as geochemical indicators of geological processes and ore-forming environments. Their distribution patterns provide valuable information on the migration and accumulation of radioactive elements and may reflect the influence of lithological, structural, and metallogenic factors.

Data processing and interpretation. The analysis was based on factor analysis using the principal component method applied to radionuclide and associated geochemical datasets [[10], [11]]. Factor analysis was employed to:

- identify anomalous geochemical associations;
- reduce the dimensionality of the dataset;
- reveal spatial patterns in radionuclide distribution.

The extracted factors were interpreted in terms of geological processes and subsequently compared with the distribution of known metallogenic zones.

Spatial analysis included the comparison of identified anomalous areas with major ore-bearing regions of Eastern Kazakhstan, particularly the Rudny Altai and Kalba–Narym metallogenic zones.

The study focuses on regional-scale interpretation and the assessment of spatial relationships between radionuclide anomalies and mineralization patterns rather than on the re-evaluation of primary analytical data.

Results

The boundaries of the identified radiogeochemical zones and the locations of major radioactive sites at a scale of 1:1,000,000 are presented on regional radiation intensity maps. The radiological characteristics of individual radioactive sites and radiogeochemical zones are documented in the radiation-hygienic passports of the corresponding oblasts. These datasets provide an important basis for the development of a national radiation monitoring system in the Republic of Kazakhstan.

In addition to their application in radiation safety assessment, radiohydrolithogeochemical survey data can also be used for the exploration of non-radioactive solid mineral resources.

Within the study area, several radiogeochemical anomalies were identified in the Kalba–Narym and Rudny Altai regions. These anomalies are associated with elevated concentrations of Ra-226 in bottom sediments, as well as with radioactive waste dumps and natural radon sources [7].

The average annual effective radiation doses for the population were estimated as follows:

• Kalba–Narym region: 3.6 mSv/year (Ulan site), 4.1 mSv/year (Bukhtarma site), and 4.5 mSv/year (Kurchum site);

• Rudny Altai region: more than 6.7 mSv/year (Leninogorsk site) and 3.7 mSv/year (Rakhmanovskie Klyuchi site).

Studies of indoor radon exposure in residential areas yielded the following average annual effective doses:

• 2.4 mSv/year in Ust-Kamenogorsk;
• 6.3 mSv/year in Ulansky District;
• 5.0 mSv/year in Kokpektinsky District;
• 4.1 mSv/year in Kurchumsky District.

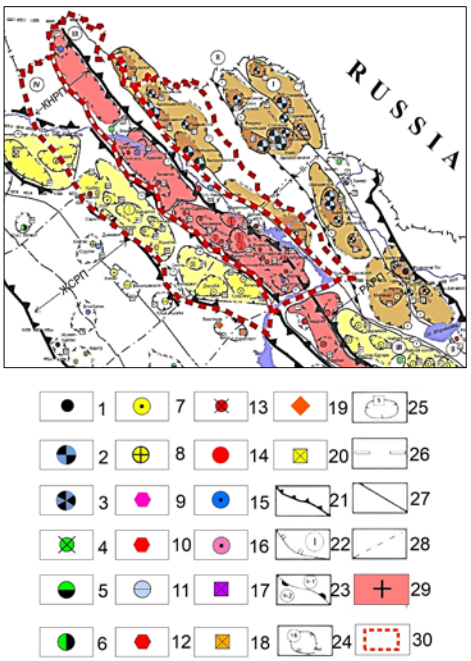

Figure 1 - Scheme of zoning of ore belts and metallogenic zones of the Greater Altai [12]. Geological and industrial types of deposits: 1 - hematite-magnetite volcanogenic-sedimentary (Kholzunsky); 2-copper-coal (ore-altai); 3-lead-zinc (South- Altai); 4-copper-pyrrhotite (Karchiginsky); 5-copper-porphyry (Kyzylkainsky); 6-copper-nickel sulfide (Maksutsky); 7-gold-quartz (Kuludzhunsky); 8-gold-myshyakovite-carboniferous (Bakyrchiksky); 9-epimagmatic niobium-zirconium-rare earth (Upper Espinsky); 10-pegmatitic rare-metal (Kalbinsky); 11-skarnovo-greisen-tungsten; 12-albitite-greisen tin-tantalum (Karasu type); 13-greisen-quartz-quartz vein stockwork tin (Cherdoyak type); 14-greisen-quartz-quartz vein tin; 15- tungsten and 16- molybdenum; 17-silicate cobalt-nickel (Gornostayevsky); 18- zircon-ilmenite weathering crust (Karaotkel type); 19- alluvial (Satpayevsky); 20-gold-alluvial (Suzdal); 21-boundaries of ore belts: Rudno-Altaisky (RARP), Kalba-Narymsky (KNRP), Zapadno-Kalbinsky (ZKRP), Zharma-Saursky (ZhSRP); 22-boundaries of metallogenic zones and their numbers: I - Beloubinsko-Sarymsaktinskaya, III - Rudnoaltayskaya, IIIII - Irtyshskaya, IV - Kalba-Narymskaya, V - Zapadno-Kalbinskaya, VII - Charskaya, VII - Zharma-Saurskaya, VIII - Sirektas-Sarzanskaya; 23 - boundaries of metallogenic subzones and their numbers: III-1-Leninogorsk-Zyryanovskaya, III-2-Priirtyshskaya; 24- known and potential (dotted) ore districts, their numbers; 25- known and potential ore nodules, their numbers; 26- deep latitudinal faults of ancient emplacement; 27-deep north-western faults limiting metallogenic zones; 28-northeastern block and cliff faults; 29-granitoids of Kalba-Narym pluton (Kalbinsky complex, $P_{1)}$; 30-contours of ore subzones included in the 2025 Scientific Research Program. (The map is presented at a regional scale corresponding to 1:1,000,000).

These results indicate generally higher radiation exposure levels in rural areas than in urban environments.

A comparison of the factor-analysis results with the geotectonic and metallogenic zoning pattern of the Greater Altai reveals a spatial relationship between radiogeochemical anomalies and major ore-bearing structures [12].

According to the metallogenic zoning scheme of the Greater Altai (Fig. 1), twenty geological-industrial deposit types have been identified. Among them, three principal groups are of particular economic importance:

• polymetallic (Cu–Pb–Zn), iron-polymetallic, and copper-gold deposits;

• gold-quartz and related gold-bearing deposits;

• rare-metal deposits.

Pyrite polymetallic type. The pyrite-polymetallic type of mineralization, which is widespread throughout the Rudny Altai metallogenic zones (I–III), is commonly associated with gold, silver, and various rare metals [13].

Secondary geochemical dispersion haloes of uranium and thorium have been identified in association with these ore deposits (Figs. 2 and 3).

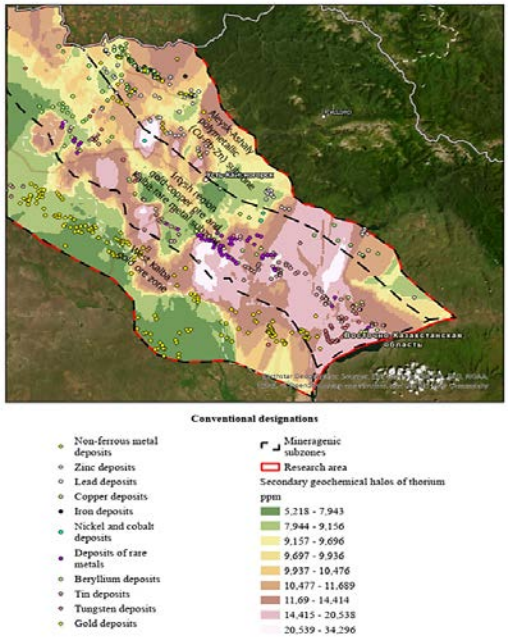

Figure 2 - Secondary geochemical halos of thorium. Spatial distribution of thorium (ppm) in bottom sediments. Color gradations represent concentration ranges, while symbols indicate mineral deposits of various types. The red boundary outlines the study area, and mineralogenic subzones are shown. The map reflects the regional survey scale of 1:1,000,000 used in the study.

Based on their gold and silver contents, the deposits can be classified into three groups:

• high-gold (1–5 g/t) and moderate-silver (20–85 g/t) deposits;

• moderate-gold (0.3–1.3 g/t) and relatively silver-rich (35–120 g/t) deposits;

• deposits characterized by low concentrations of both gold and silver.

Factor analysis of the bottom sediment dataset identified twelve anomalous sites characterized by three to five significant factors, with cumulative explained variance ranging from 62.8% to 83.6%. These values indicate that the adopted factor model adequately represents the structure of the dataset and provides a reliable basis for interpreting the spatial distribution of radionuclides and associated geochemical elements.

The first two anomalous sites (Fig. 4) are located within the Rudny Altai region and coincide with known uranium-bearing zones.

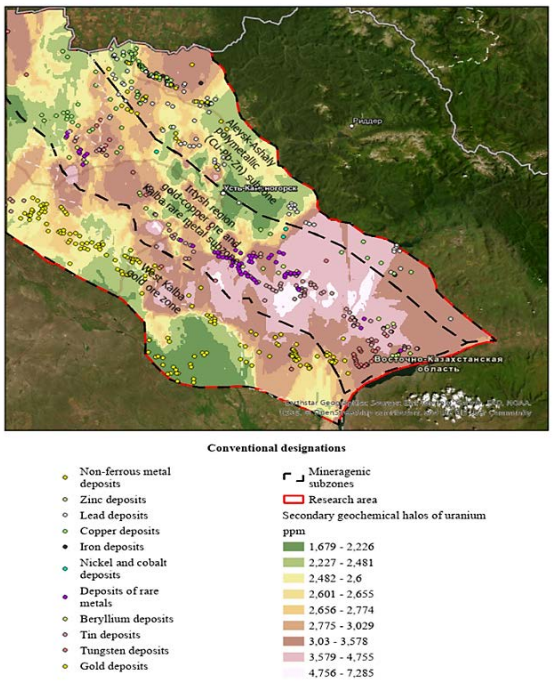

Figure 3 - Secondary geochemical halos of uranium. The map shows the spatial distribution of uranium concentrations (ppm) in bottom sediments, classified by intensity. Color gradations represent concentration ranges, while symbols indicate mineral deposits of various types. The red boundary outlines the study area, and mineralogenic subzones are shown. The map reflects the regional survey scale of 1:1,000,000 used in the study.

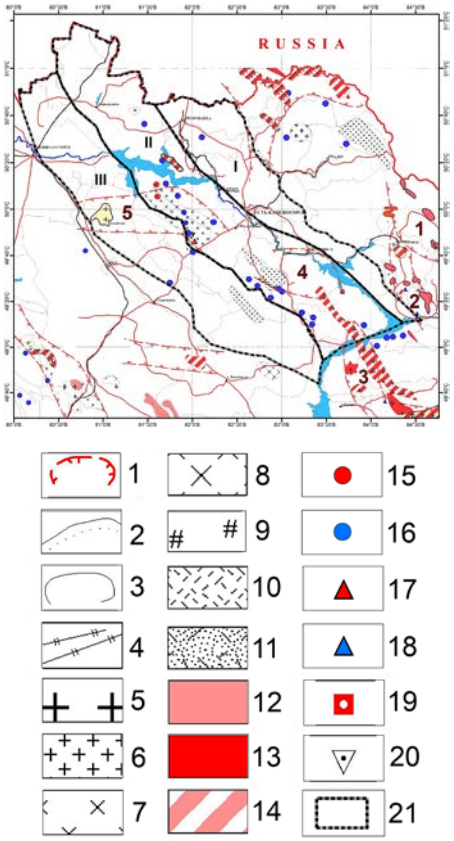

Figure 4 - Anomalous radiogeochemical sites identified by factor analysis in the microbasins of bottom sediments of Eastern Kazakhstan. Sites 1–2 are located within the Rudny Altai zone, while sites 3–5 correspond to the Kalba-Narym rare-metal zone. The map includes geological boundaries, mineral occurrences, and anomalous zones of uranium and thorium distribution. The inset shows the location of the study area within Kazakhstan. The map reflects the regional survey scale of 1:1,000,000 used in the study [6].

Gold type. Gold mineralization is widely distributed in the western and southeastern parts of the Kalba–Narym metallogenic zone. The distribution patterns and geological characteristics of gold deposits in Eastern Kazakhstan have been comprehensively described in regional geological studies and reference publications [20].

Within the gold-bearing zones, reduced activities of uranium and thorium are generally observed, whereas the activities of Ra-226 and Ra-228 remain close to regional background levels. This observation is consistent with the absence of significant uranium and thorium anomalies within these areas.

At the same time, elevated levels of natural radioactivity may occur due to the contribution of other radionuclides, particularly K-40.

Although gold and uranium are not generally considered genetically related, correlation analysis between gold concentrations and radionuclide activities may enhance the effectiveness of gamma-spectrometric methods in mineral exploration.

This relationship is supported by studies conducted at the Malomyrskoye deposit, where statistically significant correlations between radioactivity parameters and gold concentrations were identified.

To evaluate these relationships, correlation analysis [14] was performed between gold content and the activities of several radionuclides, including potassium-40 (40K), cesium-137 (137Cs), radium isotopes (226Ra, 228Ra, and 224Ra), radon (222Rn), and thorium-232 (232Th).

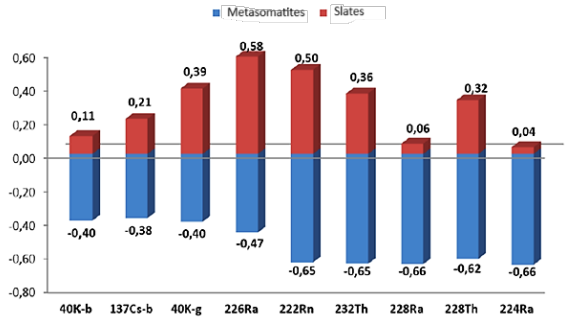

Figure 5 - Correlation coefficients (R) between gold content and radioisotope activity (40K, 137Cs, 226Ra, 222Rn, 232Th, 228Ra, 224Ra). Positive and negative correlations are shown.
Significant values at $p < 0.05$ are indicated

Rare metal type. The Kalba–Narym rare-metal metallogenic zone is characterized by granitoid magmatism and associated mineralization, including Sn, W, Ta, and Nb deposits [15].

The results of factor analysis (Table 1) indicate that anomalous sites 3, 4, and 5 spatially coincide with this metallogenic zone. This spatial relationship suggests a possible association between radionuclide distribution patterns and rare-metal mineralization.

Table 1 presents the results of factor analysis for radionuclides and associated chemical elements in bottom sediments. The obtained factor structure reflects the relationships between radionuclides and geochemical elements within the sedimentary environment.

Positive factor loadings indicate the co-occurrence and accumulation of elements controlled by common geochemical processes. In contrast, negative loadings may reflect contrasting behavior, including element separation, migration, or depletion under conditions of oxidation, weathering, and transport.

The identified factor associations allow the recognition of geochemical patterns characteristic of ore-forming environments and provide a basis for interpreting anomalous sites in relation to potential mineralization processes.

Table 1 - Results of factor analysis of radionuclides and associated chemical elements in bottom sediments of Eastern Kazakhstan

Anomalous site number	Parameters of factors	Factor 1		Factor 2		Factor 3		Factor 4		Factor 5	
		Positive correlation	Negative correlation	Positive correlation	Negative correlation	Positive correlation	Negative correlation	Positive correlation	Negative correlation	Positive correlation	Negative correlation
1 RA		K40 U238 Th232 Pb	Ra228 Cs137	Ra228 Th232 Pb	As Cs137 K40 Se	Se	As K40 Cs137 Ra226	Ra226 Th232	As Pb Se Cs137	Cs137	As U238 Se Ra228
	% of variance	26.1		16.6		14.8		13.5		12.6	
	cumulative %	26.1		42.7		57.5		71.0		83.7	
2 RA		U238 Cs137	Se Ra228 Ra226	K40 Ra226 Ra228 U238	Pb	Th232 Pb Ra226	Ra228 K40 U238		Th232		
	% of variance	24.3		20.0		19.6		16.7			
	cumulative %	24.3		44.3		63.9		80.6			
3 KN		Th232 Pb Ra228 U238	Cs137	Ra226 Cs137 U238	K40 Se Th232	Se Ra228	K40 U238 Cs137	As Pb Se	Ra228 Ra226		
	% d of variance	27.0		21.4		13.1		12.9			
	cumulative %	27.0		48.4		61.5		74.4			
4 KN		Ra228 Th232 Pb Ra226	As Cs137	As Ra226	Cs137 Ra228	Cs137 K40 Ra226	Se Th232 As U238				
	% of variance	26.1		18.8		18.7					
	cumulative %	26.1		45.0		63.7					
5 KN		Th232 U238 Pb	As Se Cs137 K40	Ra228 Se	Ra226 Th232 As	K40 Pb	U238 Ra226 Ra228 Cs137	Cs137 Pb As	Ra226 U238 K40 Se	Ra226 As	Th232 K40 Se Ra228
	% of variance	20.5		17.8		15.4		15.1		14.5	
	cumulative %	20.5		38.3		53.6		68.7		83.2	

Rare earth type. Rare earth element exploration in Kazakhstan is currently receiving increasing attention due to the implementation of the Concept for the Development of the Geological Industry of the Republic of Kazakhstan for 2023–2027 and the Comprehensive Plan for the Development of the Rare and Rare-Earth Metals Industry for 2024–2028.

According to recent geological assessments, at least 15 rare earth element occurrences and deposits have been identified in different regions of Kazakhstan [20]. The revealed patterns of radionuclide distribution and their associations with ore-related chemical elements may contribute to the identification of new prospective areas and improve approaches for rare earth element exploration.

Discussion

The obtained results demonstrate that natural radioactivity can be considered not only as an indicator of environmental conditions but also as a valuable exploration criterion for various types of mineralization in Eastern Kazakhstan [16].

The identified anomalous zones, established through radiohydrolithogeochemical surveys and factor analysis, show a clear spatial association with major metallogenic structures of the Greater Altai region [13]. In particular, polymetallic mineralization of the Rudny Altai and rare-metal mineralization of the Kalba–Narym zone are characterized by elevated concentrations of uranium and thorium and the presence of their secondary geochemical dispersion haloes.

In the Rudny Altai region, the association between polymetallic mineralization and radioactive elements may be related to ore-forming processes involving volcanogenic-sedimentary sequences and granitoid complexes. The occurrence of uranium-bearing zones and uranium–thorium geochemical anomalies supports the use of radioactive elements as indicators of ore-forming environments [17].

In contrast, gold-bearing zones are characterized by reduced uranium and thorium activities, whereas radium isotopes generally remain at background levels. This suggests that gold mineralization is not directly genetically associated with uranium; however, indirect relationships may occur through common geological and geochemical processes. The analysis of correlations between radionuclide activities, including K-40, and gold concentrations may improve the efficiency of gamma-spectrometric approaches in mineral exploration.

This interpretation is supported by investigations of the Malomyr gold deposit, where statistically significant relationships between radioactivity parameters and gold content were identified. Such relationships may contribute to a more reliable assessment of the mineral potential of geological sections.

For the Kalba–Narym rare-metal zone, the spatial coincidence of radiogeochemical anomalies with granitoid complexes and rare-metal mineralization (Sn, W, Ta, Nb, and rare earth elements) indicates a close relationship between thorium-enriched geological environments and rare-metal mineralization. This association can be explained by the similar geochemical behavior of thorium and rare earth elements, including comparable ionic characteristics and their distribution during magmatic and hydrothermal processes. This interpretation is consistent with studies of rare-metal and rare-earth mineralization related to alkaline granitoid systems [18].

The results highlight the dual significance of natural radioactivity. On the one hand, radioactive anomalies provide important information on ore-forming processes and can be applied in the exploration of rare-metal, noble-metal, and polymetallic deposits. On the other hand, elevated radioactivity levels may represent a potential environmental and health risk that should be considered during exploration and mining activities.

It should be noted that this study is based on archived regional datasets; therefore, further investigations using modern analytical techniques and digital approaches are required to refine the identified relationships. The integration of radiohydrolithogeochemical data with geographic information systems (GIS) and advanced data-processing methods may significantly improve the efficiency of mineral prospecting and resource assessment [19].

Conclusions

The major geological-industrial types of mineral deposits in Eastern Kazakhstan associated with elevated radioactivity demonstrate spatial relationships with the Rudny Altai and Kalba–Narym linear structures, as well as with the Irtysh suture zone.

Granite complexes related to these tectonic structures, particularly within the Kalba–Narym rare-metal zone and partly within the Rudny Altai and Irtysh zones, are characterized by increased levels of natural radioactivity.

Uranium-thorium mineralization is mainly associated with acidic intrusive complexes of subalkaline to alkaline composition of Permian,

Triassic age, whereas rare-earth mineralization is commonly related to alkaline granite complexes.

Gold deposits of the Mukur, Bakyrchik, and Kuludzhun ore districts are characterized by relatively low uranium and thorium contents and elevated Ra-226 activities compared with regional background values.

Deep-seated faults play an important ore-controlling role, reflecting the influence of hydrothermal processes and acting as potential pathways for the migration of ore-forming fluids. The application of modern analytical methods, including spectral, chemical, X-ray, mass spectrometric, and X-ray fluorescence techniques, expands the capabilities for mineral deposit investigation and improves the reliability of geochemical interpretation.

The incorporation of radioactivity parameters and natural isotope associations into exploration criteria can enhance the efficiency of prospecting for rare-metal, gold, and polymetallic deposits. At the same time, elevated radioactivity associated with rare-metal, rare-earth, and uranium mineralization highlights the importance of radiation safety considerations during exploration and mining activities, including the protection of personnel and the environment.

Conflict of interest: The authors declare that they have no known competing financial interests or personal relationships that could have appeared to influence the work reported in this paper

Author contributions: All authors contributed equally to this work.

CRediT Author Statement: **P.Kayukov:** Conceptualization, Methodology, Investigation, Data curation, Writing – original draft, Supervision; **G.Fedorov:** Conceptualization, Methodology, Investigation, Writing – original draft, Supervision; **G.Berkinbayev:** Conceptualization, Writing – review & editing, Visualization; **S.Askarov:** Conceptualization, Methodology, Investigation, Writing – original draft, Supervision; **D.Nazyrova:** Conceptualization, Writing – review & editing, Visualization; **O.Gavrilenko:** Conceptualization, Methodology, Investigation, Writing – original draft, Supervision; **N.Temirbekov:** Resources, Funding acquisition; **A.Temirbekov:** Resources; **Z.Mustafina:** Conceptualization, Data curation, Writing – review & editing, Visualization, Project administration; **N.Zimanovskaya:** Conceptualization, Writing – review & editing, Visualization.

Funding information: This research was funded by the Committee of Science of the Ministry of Science and Higher Education of the Republic of Kazakhstan (No. BR 27100483 “Development of predictive exploration technologies for identifying ore-prospective areas based on data analysis from the unified subsurface user platform Minerals.gov.kz using artificial intelligence and remote sensing methods”).

Cite this article as: Berkinbayev GD, Kayukov PG, Fedorov GV, Askarov SA, Nazyrova DR, Gavrilenko OD, Temirbekov NM, Temirbekov AN, Mustafina ZA, Zimanovskaya NA. Radioactivity as a prospecting indicator of rare earth, gold and polymetal deposits in eastern Kazakhstan and an indicator of increased radioecological hazard during their development. Kompleksnoe Ispolzovanie Mineralnogo Syra = Complex Use of Mineral Resources. 2028; 346(3):40-51. https://doi.org/10.31643/2028/6445.27

Шығыс Қазақстандағы сирек жер элементтері, алтын және полиметалл кен орындарын іздеудің белгісі ретінде радиоактивтілік және осы кен орындарын игеру кезінде радиациялық-экологиялық қауіптің жоғары деңгейінің индикаторы

[1] Беркинбаев Г.Д., [1]Каюков П.Г., [1]Федоров Г.В., [1]Аскаров С.А., [1]Назырова Д.Р., [2]Гавриленко О.Д., [2,3]Темирбеков Н.М., [2,3]Темирбеков А.Н., [2,4]Мустафина З.А., [4]Зимановская Н.А.

[1]ЖШС ECOSERVICE-S, Алматы, Қазақстан
[2]Қазақстан Республикасының Ұлттық инженерлік академиясы (ҚР ҰИА), Алматы, Қазақстан
[3] Әл-Фараби атындағы Қазақ ұлттық университеті, Алматы, Қазақстан
[4]Д. Серікбаев атындағы Шығыс Қазақстан техникалық университеті, Өскемен, Қазақстан

ТҮЙІНДЕМЕ

Бұл зерттеу Шығыс Қазақстандағы сирек металды, алтын және полиметалл минералдануы үшін табиғи радиоактивтіліктің іздеу белгісі ретіндегі рөлін, сондай-ақ оның радиоэкологиялық қауіп факторы ретіндегі маңызын бағалауға бағытталған. Талдау 1:1 000

Мақала келді: *22 наурыз 2026*
Сараптамадан өтті: *18 мамыр 2026*
Қабылданды: *30 шілде 2026*

000 масштабында жүргізілген аймақтық радиогидролитохимиялық түсірілімдердің нәтижелеріне негізделген және микробассейндер шегінде түптік шөгінділерден сынама алуды қамтиды. Зерттеу негізгі табиғи радионуклидтерге (U-238, Ra-226, Th-232, Ra-228, K-40) және олардың кеңістіктік таралуына бағытталған. Аномальды геохимиялық ассоциацияларды анықтау және олардың металлогендік құрылымдармен байланысын бағалау үшін факторлық талдау қолданылды. Нәтижесінде Қазақстан аумағында 80 әлеуетті радиоэкологиялық қауіпті аймақ анықталды, оның ішінде 5 аймақ Шығыс Қазақстанда орналасқан. Зерттелген аумақта 12 аномальды учаске белгіленді, олар 3–5 фактормен сипатталады, ал жиынтық түсіндірілген дисперсия 62,8%-дан 83,6%-ға дейін өзгереді. Анықталған аномалиялар негізгі металлогендік аймақтармен, әсіресе полиметалл және сирек металды минералданумен байланысты Рудный Алтай және Калба-Нарым өңірлерімен кеңістіктік сәйкестік көрсетеді. Нәтижелер табиғи радиоактивтіліктің тиімді іздеу белгісі әрі экологиялық қауіп факторы бола алатынын дәлелдейді. Зерттеу радиоактивтілік параметрлерін іздеу критерийлеріне енгізудің әлеуетін көрсетеді және геологиялық барлау мен тау-кен жұмыстарын жүргізу кезінде радиациялық қауіпсіздікті ескеру қажеттігін атап өтеді.

Түйін сөздер: радиоактивтілік, іздеу белгісі, гамма-спектрометрия, уран, торий, кен орындары.

Авторлар туралы ақпарат:

Беркинбаев Галым Джуманазарович — *Биология ғылымдарының кандидаты, директордың кеңесшісі, ECOSERVICE-S ЖШС, 050009, Төле би көшесі, 202А, Алматы, Қазақстан. Email: berkinbayev.g@ecoservice.kz; ORCID ID: https://orcid.org/0000-0003-0039-6909*

Каюков Павлин Герасимович — *Радиометриялық зерттеу әдістері бөлім бастығының орынбасары, ECOSERVICE-S ЖШС, 050009, Төле би көшесі, 202А, Алматы, Қазақстан. Email: kayukov.p@ecoservice.kz; ORCID ID: https://orcid.org/0000-0003-0567-7961*

Федоров Герман Васильевич — *МАНЭБ академигі, стратегиялық дирекция директорының орынбасары, ECOSERVICE-S ЖШС, 050009, Төле би көшесі, 202А, Алматы, Қазақстан. Email: gvfyodorov@gmail.com; ORCID ID: https://orcid.org/0000-0003-0033-2657*

Аскаров Сейлхан Акказинович — *Стратегиялық дирекция директоры, ECOSERVICE-S ЖШС, 050009, Төле би көшесі, 202А, Алматы, Қазақстан. Email: askarov.s@ecoservice.kz; ORCID ID: https://orcid.org/0009-0009-1293-9334*

Назырова Диляра Ривкатовна — *PhD докторанты, ГАЖ маманы, ECOSERVICE-S ЖШС, 050009, Төле би көшесі, 202А, Алматы, Қазақстан. Email: nazyrovadilyara@gmail.com; ORCID ID: https://orcid.org/0000-0002-1148-4480*

Гавриленко Олег Дмитриевич — *Геология-минералогия ғылымдарының кандидаты, жетекші ғылыми қызметкер, Қазақстан Республикасының Ұлттық инженерлік академиясы (ҚР ҰИА), 050060, Ходжанов көшесі, 67, 6-қабат, Алматы, Қазақстан. Email: ogavrilenko8@gmail.com; ORCID ID: https://orcid.org/0000-0003-4227-1098*

Темирбеков Нурлан Муханович — *Физика-математика ғылымдарының докторы, профессор, Әл-Фараби атындағы Қазақ ұлттық университеті; Вице-президент, Қазақстан Республикасының Ұлттық инженерлік академиясы (ҚР ҰИА), 050060, Ходжанов көшесі, 67, Алматы, Қазақстан. Email: ntemirbekov314@gmail.com; ORCID ID: https://orcid.org/0000-0001-7542-3778*

Темирбеков Алмаз Нурланович — *Қауымдастырылған профессор, PhD, Әл-Фараби атындағы Қазақ ұлттық университеті; жетекші ғылыми қызметкер, Қазақстан Республикасының Ұлттық инженерлік академиясы (ҚР ҰИА), 050060, Ходжанов көшесі, 67, Алматы, Қазақстан. Email: almastemir86@gmail.com; ORCID ID: https://orcid.org/0000-0002-4157-2799*

Мустафина Зинура Агзамовна — *PhD докторанты, Д. Серікбаев атындағы Шығыс Қазақстан техникалық университеті, Өскемен, Қазақстан; ғылыми қызметкер, Қазақстан Республикасының Ұлттық инженерлік академиясы (ҚР ҰИА), 050060, Ходжанов көшесі, 67, Алматы, Қазақстан. Email: zinurrka86@gmail.com; ORCID ID: https://orcid.org/0009-0001-6233-2479*

Зимановская Наталья Александровна — *PhD, қауымдастырылған профессор, Д. Серікбаев атындағы Шығыс Қазақстан техникалық университеті, Серікбаев көшесі, 19, Өскемен, Қазақстан. Email: nzimanovskaya@edu.ektu.kz; ORCID ID: https://orcid.org/0000-0002-9881-690X*

Радиоактивность как поисковый признак месторождений редких земель, золота и полиметаллов Восточного Казахстана и индикатор повышенного уровня радиоэкологической опасности при разработке этих месторождений

[1] Беркинбаев Г.Д., [1] Каюков П.Г., [1] Федоров Г.В., [1] Аскаров С.А., [1] Назырова Д.Р., [2] Гавриленко О.Д., [2, 3] Темирбеков Н.М., [2, 3] Темирбеков А.Н., [2, 4] Мустафина З.А., [4] Зимановская Н.А.

[1] ТОО Экосервис – С, Алматы, Казахстан
[2] РОО Национальная инженерная Академия Республики Казахстан, Алматы, Казахстан
[3] Казахский национальный университет имени аль-Фараби, Алматы, Казахстан
[4] Восточно-Казахстанский технический университет имени Д. Серикбаева, Усть-Каменогорск, Казахстан

Поступила: *22 марта 2026*
Рецензирование: *18 мая 2026*
Принята в печать: *30 июля 2026*

АННОТАЦИЯ

Данное исследование направлено на оценку роли естественной радиоактивности как поискового признака редкометальной, золоторудной и полиметаллической минерализации Восточного Казахстана, а также её значения как фактора радиоэкологической опасности. Анализ основан на результатах региональных радиогидролитохимических съёмок, выполненных в масштабе 1:1 000 000, включая отбор проб донных отложений в пределах микробассейнов. Основное внимание уделено ключевым природным радионуклидам (U-238, Ra-226, Th-232, Ra-228, K-40) и их пространственному распределению. Для выявления аномальных геохимических ассоциаций и оценки их связи с металлогеническими структурами был применён факторный анализ. В результате на территории Казахстана было выделено 80 потенциально радиоэкологически опасных зон, из которых 5 расположены в Восточном Казахстане. В пределах исследуемой территории выявлено 12 аномальных участков, характеризующихся 3–5 факторами с суммарной объяснённой дисперсией от 62,8% до 83,6%. Выявленные аномалии демонстрируют пространственное соответствие основным металлогеническим зонам, прежде всего Рудного Алтая и Калба-Нарымского региона, ассоциированных с полиметаллической и редкометальной минерализацией. Полученные результаты показывают, что естественная радиоактивность может служить как эффективным поисковым признаком, так и важным фактором экологического риска. В работе показан потенциал включения параметров радиоактивности в систему поисковых критериев, а также подчёркивается необходимость учёта радиационной безопасности при проведении геологоразведочных и горных работ.

Ключевые слова: радиоактивность, поисковый признак, гамма-спектрометрия, уран, торий, рудные месторождения

Информация об авторах:

Беркинбаев Галым Джуманазарович — *Кандидат биологических наук, советник директора, ТОО ЭКОСЕРВИС-С, 050009, ул. Толе Би, 202А, Алматы, Казахстан. Email: berkinbayev.g@ecoservice.kz; ORCID ID: https://orcid.org/0000-0003-0039-6909*

Каюков Павлин Герасимович — *Заместитель начальника отдела радиометрических методов исследований, ТОО ЭКОСЕРВИС-С, ул. Толе Би, 202А, 050009, Алматы, Казахстан. Email: kayukov.p@ecoservice.kz; ORCID ID: https://orcid.org/0000-0003-0567-7961*

Федоров Герман Васильевич — *Академик МАНЭБ, заместитель директора стратегической дирекции, ТОО ЭКОСЕРВИС-С, 050009, ул. Толе Би, 202А, Алматы, Казахстан. Email: gvfyodorov@gmail.com; ORCID ID: https://orcid.org/0000-0003-0033-2657*

Аскаров Сейлхан Акказинович — *Директор стратегической дирекции, ТОО ЭКОСЕРВИС-С, ул. Толе Би, 202А, 050009, Алматы, Казахстан. Email: askarov.s@ecoservice.kz; ORCID ID: https://orcid.org/0009-0009-1293-9334*

Назырова Диляра Ривкатовна — *Докторант (PhD), ГИС-специалист, ТОО ЭКОСЕРВИС-С, 050009, ул. Толе Би, 202А, Алматы, Казахстан. Email: nazyrovadilyara@gmail.com; ORCID ID: https://orcid.org/0000-0002-1148-4480*

Гавриленко Олег Дмитриевич — *Кандидат геолого-минералогических наук, ведущий научный сотрудник, Национальная инженерная академия Республики Казахстан (НИА РК), 050060, ул. Ходжанова, 67, 6 этаж, Алматы, Казахстан. Email: ogavrilenko8@gmail.com; ORCID ID: https://orcid.org/0000-0003-4227-1098*

Темирбеков Нурлан Муханович — *Доктор физико-математических наук., профессор, Казахский национальный университет имени Аль-Фараби; Вице-Президент, Национальная инженерная академия Республики Казахстан (НИА РК), 050060, ул. Ходжанова, 67, Алматы, Казахстан. Email: ntemirbekov314@gmail.com; ORCID ID: https://orcid.org/0000-0001-7542-3778*

Темирбеков Алмаз Нурланович — *Ассоциированный профессор, PhD Казахский национальный университет имени аль-Фараби, Алматы, Казахстан; ведущий научный сотрудник, Национальная инженерная академия Республики Казахстан (НИА РК), 050060, ул. Ходжанова, 67, Алматы, Казахстан. Email: almastemir86@gmail.com; ORCID ID: https://orcid.org/0000-0002-4157-2799*

Мустафина Зинура Агзамовна — *PhD докторант, Восточно-Казахстанский технический университет имени Д. Серикбаева, Усть-Каменогорск, Казахстан; Научный сотрудник, Национальная инженерная академия Республики Казахстан (НИА РК), 050060, ул. Ходжанова, 67, Алматы, Казахстан. Email: zinurrka86@gmail.com; ORCID ID: https://orcid.org/0009-0001-6233-2479*

Зимановская Наталья Александровна — *PhD, ассоциированный профессор, Восточно-Казахстанский технический университет имени Д. Серикбаева, 070004, ул. Серикбаева, 19, Усть-Каменогорск, Казахстан. Email: nzimanovskaya@edu.ektu.kz; ORCID ID: https://orcid.org/0000-0002-9881-690X*

References

[1] Dickson BL, Scott KM. Interpretation of aerial gamma-ray surveys – adding the geochemical factors. AGSO Journal of Australian Geology and Geophysics. 1997; 17(2):187–200. https://doi.org/10.1080/08120099708728317

[2] Maden N, Akaryalı E. Gamma ray spectrometry for recognition of hydrothermal alteration zones related to a low sulfidation epithermal gold mineralization (eastern Pontides, NE Türkiye). Journal of Applied Geophysics. 2015; 122:74–85. https://doi.org/10.1016/j.jappgeo.2015.09.003

[3] Mou N, Carranza EJM, Xue J, Zhang S, Wang G, Song H, Ren X. Interpretable machine learning for mineral prospectivity mapping in the Qulong–Jiama district, Tibet, China. Ore Geology Reviews. 2025; 182:106659. https://doi.org/10.1016/j.oregeorev.2025.106659

[4] Sun K, Chen Y, Geng G, Lu Z, Zhang W, Song Z, Zhang Z. A review of mineral prospectivity mapping using deep learning. Minerals. 2024; 14(10):1021. https://doi.org/10.3390/min14101021

[5] Taha AMM, Liu G, Chen Q, Fan W, Cui Z, Wu X, Fang H. Toward data-driven mineral prospectivity mapping from remote sensing data using deep forest predictive model. Natural Resources Research. 2024; 33(6):2407–2431. https://doi.org/10.1007/s11053-024-10387-5

[6] Kayukov PG, Efremov GF, Berikbolov BR, et al. Report on the activity Study of Radiation Situation on the Territory of the Republic of Kazakhstan under the budget program 011 Ensuring Radiation Safety (results of work for the period 2004–2008). Almaty. 2008.

[7] Kayukov PG, Shishkov IA, Pasysaev VA, Dubinchin PP, Bobylev AI. Radiation situation of the territory of the Republic of Kazakhstan on the results of implementation of the state budget program 011 Ensuring Radiation Safety in 2004–2008. Almaty. 2008.

[8] Reimann C, de Caritat P. Establishing geochemical background variation and threshold values for 59 elements in Australian surface soil. Science of the Total Environment. 2017; 578:633–648. https://doi.org/10.1016/j.scitotenv.2016.11.010

[9] IAEA. Guidelines for radioelement mapping using gamma ray spectrometry data. IAEA-TECDOC-1363. Vienna. 2003.

[10] Grunsky EC. The interpretation of geochemical survey data using multivariate methods. Journal of Geochemical Exploration. 2010; 107(2):117–130. https://doi.org/10.1144/1467-7873/09-210

[11] Zuo R. Geodata science-based mineral prospectivity mapping: A review. Natural Resources Research. 2020; 29(6):3415–3424. https://doi.org/10.1007/s11053-020-09700-9

[12] Dyachkov BA, Chernenko ZI, Mataibaeva IE, Frolova OV. Zoning and types of deposits of East Kazakhstan. Bulletin of KazNTU. 2005; 4:101–109.

[13] Pyatkova AP. Features of geologic structure and ore formation patterns of gold-silver-coal deposits of ore-altai type on the example of Maleevskoye and Artemyevskoye deposits. PhD dissertation. D. Serikbayev East Kazakhstan State Technical University. 2023.

[14] Moiseenko NV, Sinyakova NI, Safina NM. Specific activity of radioisotopes of different types of rocks of Malomyrsky gold deposit and its correlation with gold content in them. International Journal of Humanities and Natural Sciences. 2023; 11-3(86):129-134.

[15] Laumulin TM, Gubaidulin FG, Sheptura VI, Akylbekov SA, Darbadaev AB, Baimuldin BA, Gulyaeva NY, Dyachkov BA, Radenko NL. Deposits of rare metals and rare earths in Kazakhstan. Almaty. 1998.

[16] Carranza EJM. Geochemical anomaly and mineral prospectivity mapping in GIS. Elsevier. 2008.

[17] IAEA. Airborne gamma ray spectrometry. IAEA Nuclear Energy Series. Vienna. 2010.

[18] Černý P, Ercit TS. The classification of granitic pegmatites revisited. The Canadian Mineralogist. 2005; 43(6):2005–2026. https://doi.org/10.2113/gscanmin.43.6.2005

[19] Cracknell MJ, Reading AM. Geological mapping using remote sensing data: a comparison of five machine learning algorithms, their response to variations in the spatial distribution of training data and the use of explicit spatial information. Computers & Geosciences. 2014; 63:22–33. https://doi.org/10.1016/j.cageo.2013.10.008

[20] Poezzhaev I, Nigmatov D, Imangalieva M, Gavrilenko O, Temirbekov N, Mustafina Z, & Zimanovskaya N. Placer formation processes in the cenozoic of Northern and Eastern Kazakhstan. Kompleksnoe Ispolzovanie Mineralnogo Syra = Complex Use of Mineral Resources. 2026; 345(2):52–71. https://doi.org/10.31643/2028/6445.16

Crossref
DOI: 10.31643/2028/6445.28
Mining & Mineral Processing

Physicochemical and commercial properties of a microelement-containing nitrogen fertilizer based on ammonium nitrate and spent lithium-ion batteries

[1]Fazilova M.Kh., [1]Khasanov Sh.B., [2]Alimov U.K., [3*]Ruzmetova A.Sh., [4]Numonov B.O., [5]Khoshimov A.A., [6]Kholmurodov J.E., [7]Qosimov D.M., [7]Tojimamatova M.Y.

[1] Khorezm Mamun Academy, Khiva, Uzbekistan
[2] Institute of General and Inorganic Chemistry, Academy of Sciences of the Republic of Uzbekistan, Tashkent, Uzbekistan
[3] Urgench State University named after Abu Rayhon Beruni, Urgench, Uzbekistan
[4]Kokand State University, Kokand, Uzbekistan
[5]The International Institute of Food Technology and Engineering, Fergana, Uzbekistan
[6]Namangan State Technical University, Namangan, Uzbekistan
[7] Fergana State Technical University, Fergana, Uzbekistan

** Corresponding author email: aida0330@list.ru*

Received: *January 26, 2026*
Peer-reviewed: *February 5, 2026*
Accepted: *August 4, 2026*

ABSTRACT

The results of a comprehensive study of the physicochemical and commercial properties (hygroscopic point, sorption kinetics, sorption moisture capacity) of trace-containing nitrogen fertilizers based on ammonium nitrate (AN) melt and cathode powder from used lithium-ion batteries are presented. The use of cathode powder as a polymicroelement additive (PMA) is shown, and they were introduced into the saltpeter melt at various mass ratios of NA: PMA from 100 (0.5-3.0). The prepared samples of fertilizers with a granule size of 2-3 mm were tested to determine the hygroscopic point, sorption kinetics, and sorption moisture capacity at relative air humidity of 60, 70, 85, and 100%. The samples of fertilizers were studied at a relative humidity of 60%, and it was proved that at such a relative humidity, the samples do not get moistened, but rather dry out. The results of the study of samples with a 4-hour exposure are given and it is found that fertilizer granules have a low hygroscopic point from 50 to 60% and a high moisture absorption rate in the order of 1.860; 5.920 and 6.710; 2.052; 6.790 and 9.451, as well as 3.481; 6.954 and 9.906 mg/(g min) at relative air humidity of 70, 85 and 100%, respectively. Due to the fact that the process of sorption of the investigated granules of products lasts up to 30 days (or 720 hours), they have a hygroscopic point of 60 to 70%, related to hygroscopic substances. Appropriate conclusions are drawn due to the properties of the studied fertilizers: they have a low moisture capacity, and their physical properties begin to deteriorate sharply only at a moisture content of about 2%. The resulting fertilizers are not inferior to known fertilizers in their characteristics. Recommendations are given for packaging the finished product in plastic bags for storage and transportation over long distances.

Keywords: ammonium nitrate, melt, microelement, hygroscopicity, absorption rate, sorption kinetics, moisture capacity.

Information about authors:

Fazilova Mukaddas Khalillaevna — *Basic doctoral student, Mamun Khorezm Academy, Khiva, Uzbekistan. Email: mukaddasfazilova09@gmail.com; ORCID ID: https://orcid.org/0009-0007-1998-0554*

Khasanov Shodlik Bekpulatovich — *Candidate of Chemical Sciences, Senior Researcher, Deputy Chairman for Research, Mamun Khorezm Academy, Khiva, Uzbekistan. Email: shadlik@mail.ru; ORCID ID: https://orcid.org/0000-0002-0334-6977*

Alimov Umarbek Kadyrbergenovich — *Senior Researcher, Doctor of Technical Sciences (DSc), Leading Researcher, Phosphorus Fertilizers Laboratory, Institute of General and Inorganic Chemistry, Academy of Sciences of the Republic of Uzbekistan. Email: umaralihonalimov@mail.ru; ORCID ID: https://orcid.org/0000-0001-5608-5304*

Ruzmetova Aida Shonazarovna — *Doctor of Philosophy in Technical Sciences (PhD), Associate Professor of the Department of Chemical Technologies, Urgench State University, Urgench, Uzbekistan. Email: aida0330@list.ru; ORCID ID: https://orcid.org/0000-0002-9637-4503*

Numonov Bakhtiyorjon Omonjonovich — *Doctor of Philosophy in Technical Sciences (PhD), Associate Professor of the Department of Chemistry and Ecology, Kokand State University, Kokand, Uzbekistan. Email: kimyogar_1985@mail.ru; ORCID ID: https://orcid.org/0009-0004-0110-8002*

Khoshimov Akhrorjon Akhadovich — *Vice-Rector for Scientific Affairs and Innovations of the International Institute of Food Technology and Engineering, Fergana, Uzbekistan. Email: axrorhoshimov1989@gmail.com; ORCID ID: https://orcid.org/0009-0003-4276-5538*

Kholmurodov Jamshidbek Erkinovich — *Doctor of Philosophy in Technical Sciences, Doctoral student, Namangan State Technical University, Namangan, Uzbekistan. Email: erkinovichjamshid@mail.ru; ORCID ID: https://orcid.org/0009-0004-3413-8144*

Qosimov Dilshodjon Mamurjon o'g'li	*Doctor of Philosophy in Technical Sciences, Senior Lecturer, Fergana State Technical University, Fergana, Uzbekistan. Email: d.qosimov.m@gmail.com; ORCID ID: https://orcid.org/0009-0000-6698-5293*
Tojimamatova Muqaddam Yormaxammatovna	*Senior Lecturer, Fergana State Technical University, Fergana, Uzbekistan. Email: m_tojimamatova@mail.ru; ORCID ID: https://orcid.org/0000-0003-0038-895x*

Introduction

Ammonium nitrate (AN) is an efficient and versatile nitrogen fertilizer used for all types of crops and soils. AN rapidly responds to crop growth and development, promoting high yields even within a short vegetation period. The consumption of AN (100% nutrient component—N) required to obtain an additional 1 ton of yield is 80 kg for cereals, 141 kg for cotton, 142 kg for flax, 10.3 kg for sugar beet, 157 kg for sunflower, 13.8 kg for potatoes, and 8.1 kg for vegetables [1]. Therefore, global production of nitrogen fertilizers continues to increase, reaching up to 127 million tons per year by 2020 in terms of 100% nutrient content [2]. According to information from the International Fertilizer Association (IFA), global production of ammonium nitrate increased from 41.18 to 50.6 million tons (as 100% N) between 2009 and 2020, whereas prior annual production had been approximately 43 million tons [3]. The largest ammonium nitrate production capacities are located in the United States and Russia, whose combined share of global capacity is estimated at slightly over 13% [4]. In contrast, the share of Uzbekistan's chemical industry enterprises—such as JSC "Maksam-Chirchik," "Navoiyazot," and "Ferganaazot"—accounts for about 2%. Despite the high level of production and consumption of ammonium nitrate, it has two major drawbacks, namely increased explosion hazard and a strong tendency to cake during storage [5].

Caking is the adhesion of ammonium nitrate granules to one another under the combined effects of external load and ambient temperature, resulting in the formation of a monolithic mass. This, in turn, causes difficulties during the transportation and storage of ammonium nitrate over long distances, as well as during its application on agricultural land.

The main factors affecting caking are associated with the high solubility, hygroscopicity, and low mechanical strength of ammonium nitrate granules. In addition, polymorphic transformations of ammonium nitrate within the temperature range from −17 to 169.6 °C, accompanied by various structural changes, also contribute to caking [[6], [7]]. This phenomenon can be explained by the transformation mechanism of ammonium nitrate involving the dissolution of one phase and the crystallization of another within its structure [[8], [9]]. Commercial ammonium nitrate containing 26% and 33% nitrogen is produced through industrial manufacturing processes [10].

To this end, it is necessary to reduce the solubility and hygroscopicity while increasing the mechanical strength of ammonium nitrate granules through the use of special additives. Such additives are mainly carbonate-, sulfate-, and phosphate-based compounds, as well as aluminosilicates (kaolin, bentonite, vermiculite, etc.).

In parallel, mineral and hybrid additives derived from natural and technogenic raw materials have been widely studied in cementitious systems, where such additives are known to regulate physicochemical interactions, moisture-related properties, and microstructural development of composite materials. These studies demonstrate that multicomponent mineral additives can improve material stability without critically compromising functional properties, highlighting the potential for cross-sectoral application of mineral additives in nitrogen fertilizer systems [[11], [12], [13]].

However, after the addition of these types of additives, one of the key commercial properties—the hygroscopic point of the product—decreases sharply from the initial 63% for ammonium nitrate to about 30%. Moreover, not all of the above-mentioned mineral additives provide a useful functional benefit. In this regard, the use of microelement additives can be proposed, which are simultaneously applied to crops at sufficient levels due to the high rates of nitrogen fertilization. In our view, cathode materials from lithium-ion batteries (LIBs) can be considered as promising microelement additives. This is because the production of lithium salts is steadily increasing, and various methods for their recovery are being developed [14]. However, the issue of recycling spent lithium-ion batteries remains highly relevant.

In this regard, the scientific and practical objective of this work is to investigate the physicochemical and commercial properties (hygroscopic point, kinetics of water vapor sorption, sorption moisture capacity, and dissolution temperature) of ammonium nitrate containing microelements of 3d metals derived from spent lithium-ion batteries (LIBs).

The calcination temperature of 700 °C was selected on the basis of preliminary experiments to ensure decomposition of residual organic compounds and stabilization of the cathode material structure. Experimental measurements were repeated three times, and the experimental error did not exceed ±3%.

Experimental part

The experimental part of this study describes the research methodology and analytical methods applied.

Laboratory experiments were carried out in accordance with Ref. [12] using cathode powder extracted from a branded mobile phone battery. The extraction of the cathode material was performed by ultrasonic treatment using a GT SONIC ultrasonic device (China). After ultrasonic separation, the recovered cathode powder was calcined at 700 °C for 3 h in a SNOL muffle furnace (Russia). The calcined material was subsequently cooled in a desiccator at 25 °C and ground to a particle size of 0.25 mm.

Additional analytical control confirmed the absence of significant concentrations of Pb and Cd impurities within the detection limits of the method. For chemical composition analysis, the calcined and ground material was dissolved in aqua regia, prepared as a mixture of concentrated nitric acid (HNO_3) and hydrochloric acid (HCl) in a volume ratio of 1:3. The resulting nitric–hydrochloric acid extract was cooled, filtered, and subjected to elemental analysis using a Shimadzu ICPE - 9000 instrument (Japan). The analysis was conducted by inductively coupled argon plasma optical emission spectrometry (ICP-OES) in the wavelength range of λ = 179–769 nm.

The elemental composition of the investigated LIB material is presented in Table 1. It should be noted that elements with contents not exceeding 0.02% are not included in the table. The tabulated data show that the LIB material consists mainly of lithium, cobalt, manganese, and nickel; therefore, it can be conditionally classified as a polymetallic microelement additive (PMD).

The process of incorporating PMD into ammonium nitrate is as follows:

Ammonium nitrate of grade “Ch” was melted at 170 °C in a metal reactor on an electric hot plate. Then PMD was introduced into the melt at a mass ratio of AN: PMD = 100: (0.5–3.0), ensuring that the nitrogen content did not exceed 34% (to obtain non-caking AN) and that the content of microelements was 0.08–0.3% (this refers to the application of microelements at 0.5–2.0 kg per hectare together with 200 kg N, 150 kg P_2O_5, and 80 kg K_2O during the cultivation of raw cotton) [[13], [14]]. The hygroscopic point of microelement-containing nitrogen fertilizers with particle sizes of 2–3 mm was determined by the desiccator method [[15], [16]] at a temperature of 25 °C over a period of 30 days. The composition of the studied products is presented in Table 2 [17].

Table 1 - Chemical composition of calcined spent LIB cathode powder

Chemical composition, %				Total Li + Co + Mn + Ni %	Other elements with low content (less than 0.02%)
Li	Co	Mn	Ni		
2.47	13.80	10.31	2.38	28.96	71.04

Table 2 - Chemical composition of microelement-containing ammonium nitrate fertilizer granules

Sample №	Mass ratio AN: PMD	pH of a 10% solution	Component content, wt.%					Strength, MPa	Moisture content, %
			N	Li	Co	Mn	Ni		
1	2	3	4	5	6	7	8	9	10
1	100: 0.5	6.02	34.62	0.0094	0.0561	0.0387	0.0112	4.62	0.396
2	100: 1.0	6.04	34.40	0.0193	0.109	0.091	0.0189	5.16	0.087
3	100: 1.5	6.08	34.28	0.0342	0.185	0.1355	0.0164	5.49	0.214
4	100: 2.0	6.15	34.09	0.0432	0.248	0.1925	0.0244	5.85	0.208
5	100: 3.0	6.42	33.87	0.0527	0.2395	0.2860	0.0387	6.13	0.289

Granules with a diameter of 2–3 mm were obtained by laboratory granulation followed by thermal drying at 80–90 °C.

The obtained experimental data were statistically processed using Microsoft Excel 2019. Average values obtained from parallel experiments were used for graphical dependences and regression analysis.

Results and Discussion

According to the results presented in Table 2, the initial moisture content of the first sample obtained at a mass ratio of AN: PMD = 100:0.5 is 0.396%. The moisture contents of the remaining samples are as follows: the second sample—0.087%, the third—0.214%, the fourth—0.208%, and the fifth—0.289%, corresponding to mass ratios of AN: PMD = 100:1.0, 100:1.5, 100:2.0, and 100:3.0, respectively. For the investigation of physicochemical and commercial properties, samples № 1, №. 3, №. 4, and №. 5 were selected.

First, a study was conducted to determine the hygroscopic point (h) of the samples. For this purpose, according to the procedure described in [[15], [16]], the selected samples were kept in desiccators at 25 °C for 4 hours. To artificially create relative air humidities of 50, 60, 70, 85, and 100%, sulfuric acid solutions of appropriate concentrations were placed in the desiccators. After a 4-hour exposure, the samples were weighed on analytical balances with a division of no more than 0.1 mg (i.e., 0.0001 g).

During the weighing procedure, it was found that at a relative air humidity of 50% the samples lost moisture, while at 60% they practically did not absorb it. At higher relative air humidities of 70, 85, and 100%, significant moisture uptake by the samples was observed. Based on the analytical data, the moisture absorption rate, Q, was calculated [18]. The resulting data were graphically presented in Figure 1 as the dependence Q = f(h). The mathematical relationships of the equations and the correlation coefficient (R^2) were processed using Excel 2019. The figure shows that all samples have a hygroscopic point above 50%. For the first sample, at a relative air humidity of 50%, moisture is initially released in the amount of −0.0495 g, i.e., moisture is absorbed at a rate of −0.201 mg/(g·min). At a relative air humidity of 60%, the product practically does not absorb moisture (Q ≈ 0). At relative air humidities of 70, 85, and 100%, the absorption rates are 1.635, 5.890, and 6.359 mg/(g·min), respectively, indicating a high Q value for the latter two conditions. The hygroscopic point of the first sample was determined to be 59.01%.

A similar pattern was observed for the other samples of microelement-containing ammonium nitrate (№. 3, №. 4, and №. 5). It was found that for samples 3, 4, and 5, the moisture absorption rate Q at a relative air humidity of 60% varies from −0.204 to 0.62, from −0.410 to 1.246, and from 0.206 to 1.235 mg/(g·min), respectively. These samples are more hygroscopic, with determined hygroscopic points of 56.50% (sample 3), 56.08% (sample 4), and 54.02% (sample 5). They also exhibit relatively high moisture absorption rates Q of 1.860, 5.920, and 6.710; 2.052, 6.790, and 9.451; as well as 3.481, 6.954, and 9.906 mg/(g·min) at relative air humidities of 70, 85, and 100%, respectively.

According to Pestov's scale, a substance with a hygroscopic point below 50% is classified as very strongly hygroscopic; from 50 to 60% as strongly hygroscopic; from 60 to 70% as hygroscopic; from 70 to 80% as weakly hygroscopic; from 80 to 85% as almost non-hygroscopic; and above 85% as practically non-hygroscopic [[15], [16], [18]]. In this case, the fertilizer samples belong to the group of strongly hygroscopic substances.

The decrease in the hygroscopic point may additionally indicate the formation of mixed nitrate phases containing cobalt, manganese, nickel, and lithium ions. However, the determined hygroscopic points of the samples are relatively lower compared with pure ammonium nitrate (62%), which can be explained by the action of Raoult's law. According to this law, the total concentration of salts in a saturated mixed solution is higher, and consequently the vapor pressure of water is lower [18]. In addition, physicochemical principles indicate that a mixture of salts is more hygroscopic than its individual components [19]. It is also inevitable that the decrease in the hygroscopic point is closely associated with the formation of cobalt, manganese, nickel, and lithium nitrates and their crystalline hydrates [[20], [21], [22], [23], [24]]. The latter are more hygroscopic, and their formation intensifies with an increase in the mass fraction of PMD relative to ammonium nitrate (Table 2). Since moisture

absorption continues in the studied samples, it became necessary to investigate the kinetics of water vapor sorption in these materials. The observed sorption behaviour is generally characteristic of diffusion-controlled processes occurring in granular nitrogen fertilizers.

Therefore, it is expedient to study the kinetics of water sorption by fertilizers over a prolonged period. This, in turn, will provide a set of statistical and kinetic data and allow an assessment of the process rate. Consequently, it will be possible to determine the hygroscopicity of the samples in more detail based on the dependence of the sorption moisture capacity of the samples on relative air humidity.

The latter will be established after completion of the kinetic studies. Granules with a diameter of 2–3 mm were obtained by laboratory granulation followed by thermal drying at 80–90 °C.

In this regard, the kinetics of water vapor sorption by fertilizer granules of samples 1, 3, 4, and 5 with granule diameters of 2–3 mm were studied under isothermal conditions at 25 °C and relative air humidities of 60, 70, and 85% over a period of 30 days (Figs. 2–5). The numbering of the figures corresponds to the fertilizer sample numbers listed in Table 2.

As follows from the results, samples 1, 3, 4, and 5 undergo only minor changes in water vapor sorption at a relative air humidity of 60%. For example, sample 1 does not absorb moisture throughout the entire study period but, on the contrary, loses it from 0.1482 to 0.099%. Sample 3 absorbs only a small amount of moisture, from 0.0498 to 0.1987%, but by the end of the 30th day it instead releases moisture down to −0.397%. Sample 4, with an initial moisture content of 0.214%, absorbs moisture during the first day of testing from 0.2990 to 0.2990%, after which it gradually releases it down to −0.2505%.

As for sample 5, moisture absorption occurs with an increase in moisture content from the initial 0.289 to 0.293%. As can be seen, the granules of all fertilizer samples maintain equilibrium, remain dry, retain their initial moisture content, and exhibit 100% free-flowing properties.

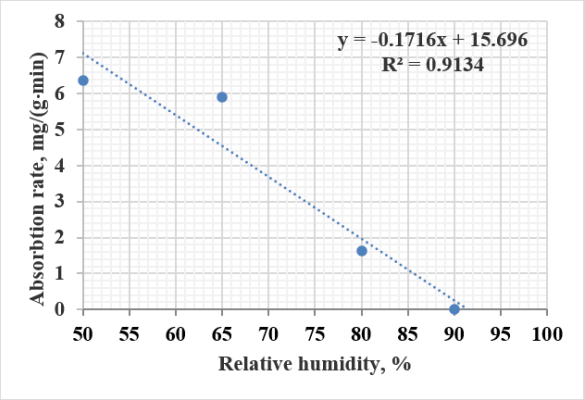

1)

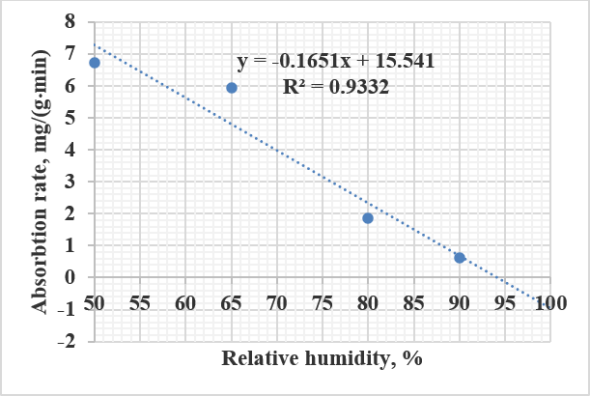

2)

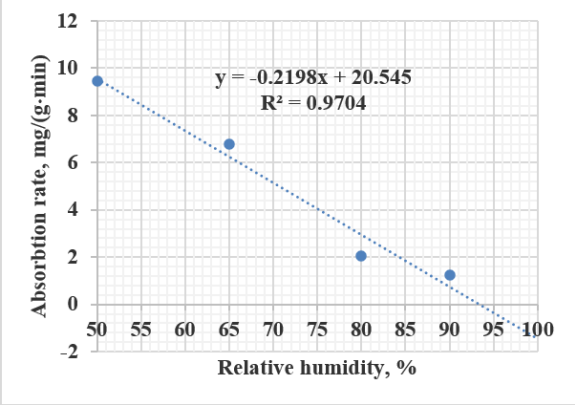

3)

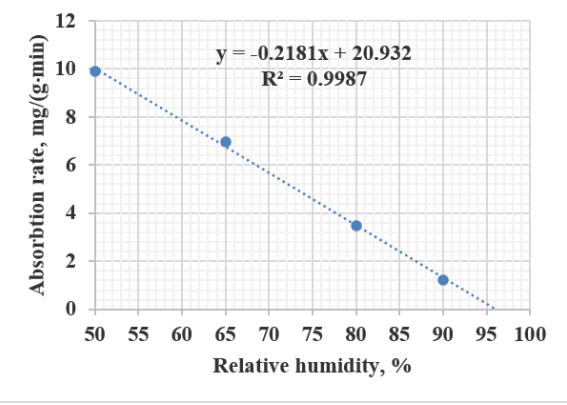

4)

Figure 1 - Dependence of the moisture absorption rate (Q) on relative air humidity (h) for samples of microelement-containing ammonium nitrate (samples 1, 3, 4, and 5) obtained at the following AN: PMD mass ratios: (1) 100:0.5; (2) 100:1.5; (3) 100:2.0; and (4) 100:3.0

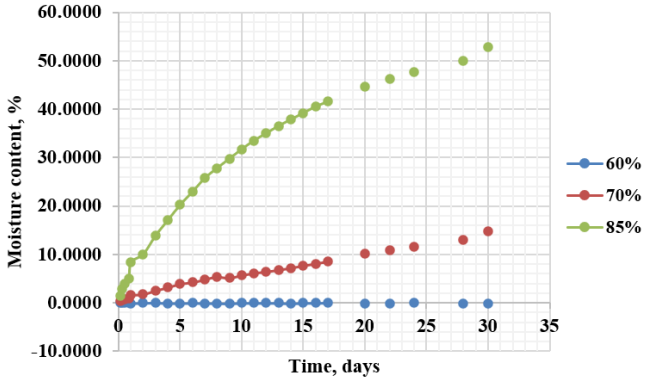

Figure 2 - Kinetics of water vapor sorption for sample 1 obtained at an AN: PMD mass ratio of 100:0.5 under relative air humidities of: (1) 60%, (2) 70%, and (3) 85%

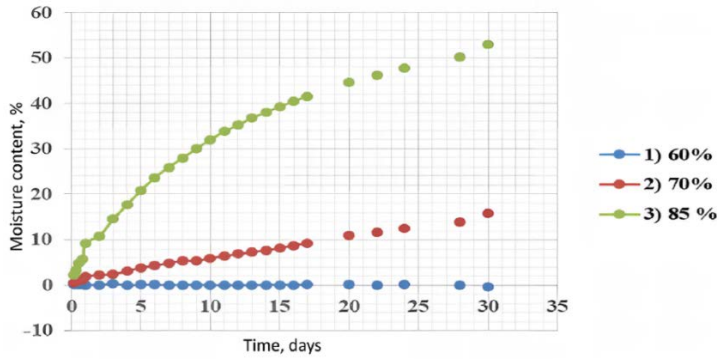

Figure 3 - Kinetics of water vapor sorption for sample 3 obtained at an AN:PMD mass ratio of 100:1.5 under relative air humidities of: (1) 60%, (2) 70%, and (3) 85%

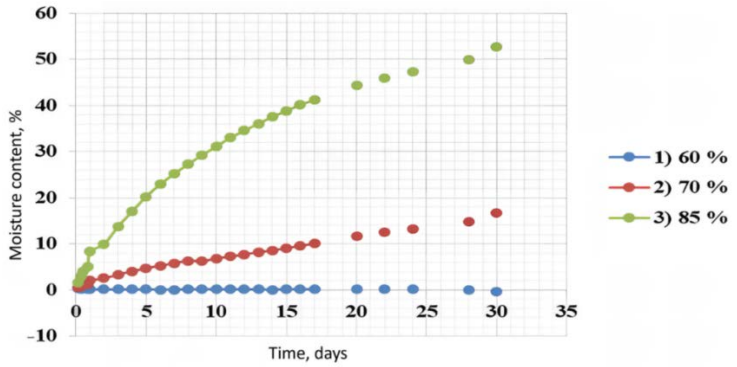

Figure 4 - Kinetics of water vapor sorption for sample 4 obtained at an AN: PMD mass ratio of 100:2.0 under relative air humidities of: (1) 60%, (2) 70%, and (3) 85%

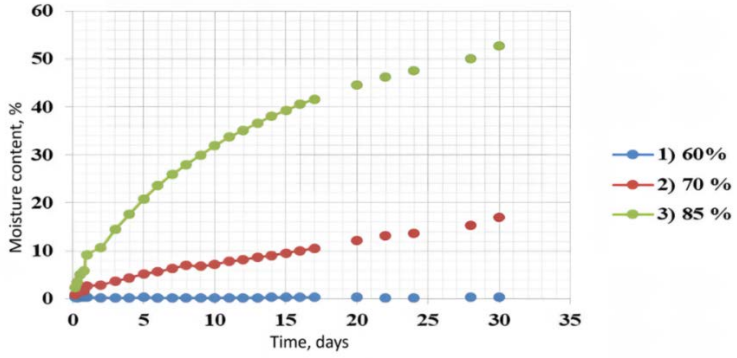

Figure 5 - Kinetics of water vapor sorption for sample 5 obtained at an AN: PMD mass ratio of 100:3.0 under relative air humidities of: (1) 60%, (2) 70%, and (3) 85%.

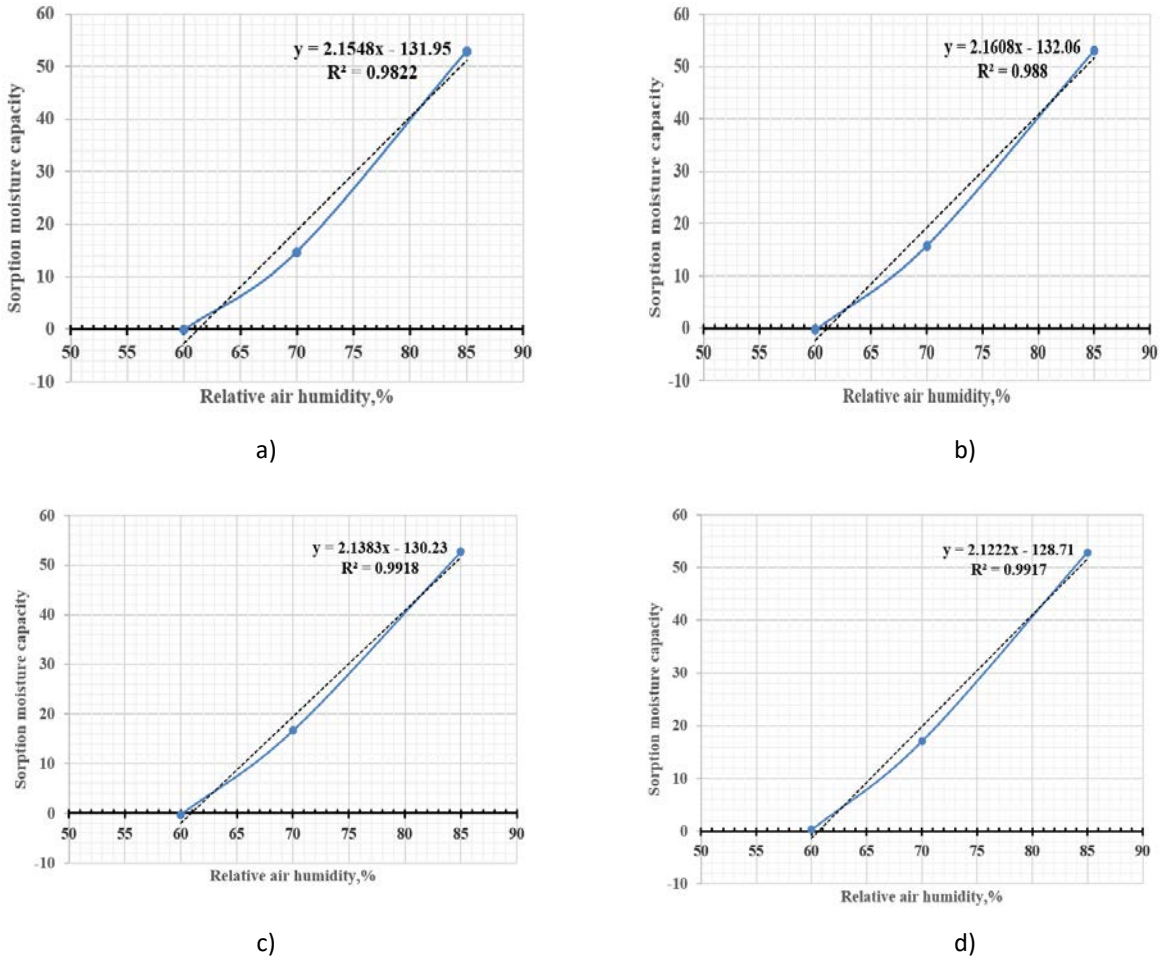

Figure 6 - Dependence of the sorption moisture capacity of fertilizer samples (a) №. 1, №. 3, №. 4, and №. 5 on relative air humidity

At the other relative air humidities of 70 and 85%, equilibrium is not established for all the investigated fertilizer samples throughout the entire test period. At a relative air humidity of 70%, samples 1, 3, and 4 absorb moisture in amounts of 0.8789, 1.1840, and 1.2708%, respectively, over 16 hours while retaining their free-flowing properties and sieve ability. However, sample 5 begins to cake at this time, absorbing 1.7510% moisture. A similar phenomenon is observed for samples 1, 3, and 4 already on the second day of testing, with absorbed moisture contents of 1.7900, 2.1973, and 2.5567%, respectively, whereas the granules of sample 5, after absorbing 2.9313% moisture, become immobile and lose their ability to be sieved. An analogous state for samples 1, 3, and 4 is observed on the fourth day of testing, when their moisture contents reach 3.1950, 3.0963, and 4.0836%, respectively.

After 7 days, the granules of sample 5 absorb moisture up to 6.3080% and begin to wet, forming water droplets on the walls of the weighing bottle. With moisture uptake of 5.1402, 5.3850, and 6.2645%, the granules of samples №. 1, 3, and 4, respectively, begin to wet after 9 days of testing. At this stage, all granules adhere to each other and start to lose their original shape.

Only after 20 days do the granules of all samples 1, 3, 4, and 5, having sorbed moisture up to 10.1372, 10.8986, 11.7133, and 12.1357%, respectively, begin to disintegrate and flow.

For the investigated fertilizer samples at a relative air humidity of 85%, the processes of caking, wetting, and complete melting occur over a much shorter test period. When the total moisture uptake of samples №. 1, №. 3, №. 4, and №. 5 reaches 2.8183, 2.9383, 3.3429, and 3.5012%, respectively, they begin to cake and adhere to each other after 8 hours. After 4 days, samples №. 1, №. 3, №. 4, and №. 5 absorb 17.0469, 17.0441, 17.7570, and 17.6422% moisture, respectively, at which point they disintegrate and spread, forming a barely noticeable layer of solution above the granules.

Subsequently, a study was carried out to determine the sorption moisture capacity, obtained from the results of maximum moisture uptake at the end of the test period (30 days). The data are

presented in Figure 6 (the numbering of the curves in the figure corresponds to the sample numbering in Table 2). The mathematical relationships of the equations and the correlation coefficient (R^2) were processed using Excel 2019.

The research results show that the sorption moisture capacity curves for fertilizer granule samples №. 1, №. 3, №. 4, and №. 5 at a relative air humidity of 60% naturally indicate no moisture absorption, and the samples fully retain their appearance and free-flowing properties.

At a relative air humidity of 70%, fertilizer granule samples №. 1, №. 3, №. 4, and №. 5 sorb moisture in amounts of 14.7059, 15.7693, 16.6323, and 17.0431%, respectively. At a relative air humidity of 85%, the moisture uptake of all fertilizer granule samples is almost the same and amounts to 52.8857, 52.6439, 52.9849, and 52.7921% for samples №. 1, №. 3, №. 4, and №. 5, respectively. This indicates that, upon absorbing such amounts of moisture, the fertilizer granules reach dynamic equilibrium. Naturally, at this moisture content, the granules spread and transition into a liquid state by the 30th day of testing.

According to the definition, the hygroscopic point corresponds to the relative air humidity at which a substance neither becomes wetted nor dries out. In the present case, sample №. 1 has a hygroscopic point of 63.14%, sample №. 3—61.49%, sample №. 4—61.23%, and sample №. 5—60.97%. These values are 1.07, 1.08, 1.09, and 1.13 times higher, respectively, than the hygroscopic points determined after 4 hours of exposure (№. 1—59.01%; №. 3—56.50%; №. 4—56.08%; and №. 5—54.02%). This circumstance is explained by the fact that sorption in the fertilizer granule samples did not reach its maximum level under the shorter exposure conditions.

No signs of spontaneous decomposition or thermal instability of the investigated fertilizer samples were visually observed during laboratory storage.

Considering climatic characteristics, relative air humidity in Uzbekistan is characterized by an average monthly minimum of 46% and an average monthly maximum of 74%, while the annual average is about 60%. Therefore, the obtained products are classified as hygroscopic materials and should be packaged in polyethylene bags.

Further studies should include ecotoxicological evaluation, thermal stability analysis, and field agrochemical testing to assess the industrial applicability of the developed fertilizers.

Conclusions

Thus, a detailed study was carried out to determine the physicochemical and commercial properties (hygroscopic point, sorption kinetics, and sorption moisture capacity) of microelement-containing nitrogen fertilizers based on ammonium nitrate melt and cathode powder. The results show that the presence of microelement-containing components in the fertilizer granules leads to a decrease in the hygroscopic point and to a high rate of moisture absorption. The obtained data were experimentally confirmed by establishing the dependence of changes in sorption kinetics on exposure time (days) and by determining the relationship between sorption moisture capacity and relative air humidity. It was found that all granule samples studied at a relative air humidity of 60% do not become wetted but, on the contrary, tend to dry.

It was also revealed that the discrepancy between the hygroscopic points of the granule samples studied over 30 days (or 720 hours) is greater than that observed after a 4-hour exposure. Fertilizers with a hygroscopicity range of 60–70% are classified as hygroscopic substances, which necessitates their packaging in polyethylene bags for transportation and storage.

Conflicts of interest. On behalf of all authors, the corresponding author states that there is no conflict of interest.

CRediT author statement: **M. Fazilova**: Conceptualization, Methodology, Software, Data curation, Writing draft preparation; **Sh. Khasanov, D. Qosimov, M. Tojimamatova**: Visualization, Investigation; **U. Alimov**: Supervision, Software, Validation; **A. Ruzmetova, B. Numonov, J. Kholmurodov, A. Khoshimov**: Reviewing and Editing.

Acknowledgements. We express our sincere gratitude to the leading researchers of the Khorezm Mamun Academy and the Research Laboratory and Testing Center of the Institute of General and Inorganic Chemistry of the Academy of Sciences of the Republic of Uzbekistan for their practical assistance in conducting the experiments. We also extend our sincere appreciation to ***Khadzhiev Azamat Shamuratovich*** for his support in translation and language-related matters, as well as to the co-authors for their contributions to the writing and editing of the article.

Formatting of funding sources. This research did not receive any specific grant from funding agencies in the public, commercial, or not-for-profit sectors.

Cite this article as: Fazilova MKh, Khasanov ShB, Alimov UK, Ruzmetova ASh, Numonov BO, Khoshimov AA, Kholmurodov JE, Qosimov DM, Tojimamatova MY. Physicochemical and commercial properties of a microelement-containing nitrogen fertilizer based on ammonium nitrate and spent lithium-ion batteries. Kompleksnoe Ispolzovanie Mineralnogo Syra = Complex Use of Mineral Resources. 2028; 346(3):52-63. https://doi.org/10.31643/2028/6445.28

Аммоний нитраты мен пайдаланылған литий-ионды батареялар негізіндегі микроэлементтермен байытылған азотты тыңайтқыштың физика-химиялық және тауарлық қасиеттері

[1]Фазилова М.Қ., [1]Хасанов Ш.Б., [2]Әлімов Ұ.Қ., [3]Рузметова А.Ш., [4]Нумонов Б.О., [5]Хошимов А.А., [6]Холмуродов Ж.Э., [7]Қосимов Д.М., [7]Тожимаматова М.Ю.

[1] Хорезм Мамун академиясы, Хива, Өзбекстан
[2] Өзбекстан Республикасы Ғылым академиясының Жалпы және бейорганикалық химия институты, Ташкент, Өзбекстан
[3] Әбу Райхон Беруни атындағы Ургенч мемлекеттік университеті, Ургенч, Өзбекстан
[4]Қоқан мемлекеттік университеті, Қоқан, Өзбекстан
[5]Халықаралық азық-түлік технологиялары және инженерия институты, Ферғана, Өзбекстан
[6]Наманган мемлекеттік техникалық университеті, Наманган, Өзбекстан [7]Ферғана мемлекеттік техникалық университеті, Ферғана, Өзбекстан

Мақала келді: *26 қаңтар 2026*
Сараптамадан өтті: *5 ақпан 2026*
Қабылданды: *4 тамыз 2026*

ТҮЙІНДЕМЕ

Аммоний нитраты (АН) балқымасы мен пайдаланылған литий-ионды батареялардың катодтық ұнтағы негізінде алынған микроэлементтермен байытылған азотты тыңайтқыштардың физика-химиялық және тауарлық қасиеттерін (гигроскопиялық нүкте, сорбция кинетикасы, сорбциялық ылғал сыйымдылығы) кешенді зерттеу нәтижелері келтірілген. Катодтық ұнтақты полимикроэлементті қоспа (ПМА) ретінде пайдалану мүмкіндігі көрсетіліп, ол селитра балқымасына АН:ПМА = 100:(0,5–3,0) массалық қатынастарында енгізілді. Гранула өлшемі 2–3 мм болатын дайын тыңайтқыш үлгілері гигроскопиялық нүктені, сорбция кинетикасын және сорбциялық ылғал сыйымдылығын анықтау үшін ауаның салыстырмалы ылғалдылығы 60; 70; 85 және 100% жағдайында зерттелді. Ауаның салыстырмалы ылғалдылығы 60% болғанда тыңайтқыш үлгілері ылғалданбай, керісінше, кебетіні дәлелденді. 4 сағаттық экспозиция нәтижелері бойынша тыңайтқыш гранулаларының гигроскопиялық нүктесі 50–60% аралығында екені және ауаның салыстырмалы ылғалдылығы 70, 85 және 100% болғанда ылғалды сіңіру жылдамдығы тиісінше 1,860; 5,920 және 6,710; 2,052; 6,790 және 9,451, сондай-ақ 3,481; 6,954 және 9,906 мг/(г·мин) мәндеріне жететіні анықталды. Зерттелген өнім гранулаларында сорбция процесі 30 тәулікке (немесе 720 сағатқа) дейін жалғасатындықтан, олардың гигроскопиялық нүктесі 60–70% аралығында болып, гигроскопиялық заттарға жататыны көрсетілді. Зерттелген тыңайтқыштардың қасиеттеріне байланысты олардың ылғал сыйымдылығы төмен екені, ал физикалық қасиеттерінің күрт нашарлауы шамамен 2% ылғалдылық деңгейінде басталатыны анықталды. Алынған тыңайтқыштар өз сипаттамалары бойынша белгілі тыңайтқыштардан кем түспейді. Ұзақ қашықтыққа тасымалдау және сақтау үшін дайын өнімді полиэтилен қаптарға орау бойынша ұсынымдар берілді.

Түйін сөздер: аммоний нитраты, балқыма, микроэлемент, гигроскопиялық қасиет, сіңіру жылдамдығы, сорбция кинетикасы, ылғал сыйымдылығы.

Авторлар туралы ақпарат:

Фазилова Мұқаддас Халиллаевна — *Негізгі докторант, Хорезм Мамун академиясы, Хива, Өзбекстан. Email: mukaddasfazilova09@gmail.com; ORCID ID: https://orcid.org/0009-0007-1998-0554*

Хасанов Шодлик Бекпулатұлы — *Химия ғылымдарының кандидаты, аға ғылыми қызметкер, ғылым жөніндегі төраға орынбасары, Хорезм Мамун академиясы, Хива, Өзбекстан. Email: shadlik@mail.ru; ORCID ID: https://orcid.org/0000-0002-0334-6977*

Әлімов Умарбек Қадырбергенұлы — *Аға ғылыми қызметкер, техника ғылымдарының докторы (DSc), жетекші ғылыми қызметкер, Фосфорлы тыңайтқыштар зертханасы, Өзбекстан Республикасы Ғылым академиясының Жалпы және бейорганикалық химия институты, Ташкент, Өзбекстан. Email: umaralihonalimov@mail.ru; ORCID ID: https://orcid.org/0000-0001-5608-5304*

Рузметова Аида Шоназарқызы — *Техника ғылымдары бойынша философия докторы (PhD), Химиялық технологиялар кафедрасының доценті, Әбу Райхон Беруни атындағы Ургенч мемлекеттік университеті, Ургенч, Өзбекстан. Email: aida0330@list.ru; ORCID ID: https://orcid.org/0000-0002-9637-4503*

Нумонов Бахтиёржон Омонжонович — *Техника ғылымдары бойынша философия докторы (PhD), Қоқан мемлекеттік университеті, Химия және экология кафедрасының доценті, Қоқан, Өзбекстан. Email: kimyogar_1985@mail.ru; ORCID ID: https://orcid.org/0009-0004-0110-8002*

Хошимов Ахроржон Ахадович — *Халықаралық азық-түлік технологиялары және инженерия институтының ғылыми істер және инновациялар жөніндегі проректоры, Ферғана, Өзбекстан. Email: axrorhoshimov1989@gmail.com; ORCID ID: https://orcid.org/0009-0003-4276-5538*

Холмуродов Жамшидбек Эркинович	*Техника ғылымдары бойынша философия докторы (PhD), докторант, Наманған мемлекеттік техникалық университеті, Наманған, Өзбекстан. Email: erkinovichjamshid@mail.ru; ORCID ID: https://orcid.org/0009-0004-3413-8144*
Косимов Дилшоджон Мамуржон угли	*Техника ғылымдары бойынша философия докторы (PhD), аға оқытушы, Ферғана мемлекеттік техникалық университеті, Ферғана, Өзбекстан. Email: d.qosimov.m@gmail.com; ORCID ID: https://orcid.org/0009-0000-6698-5293*
Тожимаматова Мукаддам Ёрмахамматовна	*Ферғана политехникалық институтының аға оқытушысы, Ферғана, Өзбекстан. Email: m_tojimamatova@mail.ru; ORCID ID: https://orcid.org/0000-0003-0038-895x*

Физико-химические и товарные свойства микроэлементсодержащего азотного удобрения на основе нитрата аммония и отработанных литий-ионных батарей

[1]Фазилова М.Х., [1]Хасанов Ш.Б., [2]Алимов У.К., [3]Рузметова А.Ш., [4]Нумонов Б.О., [5]Хошимов А.А., [6]Холмуродов Ж.Э., [7]Қосимов Д.М., [7]Тожимаматова М.Ю.

[1] Хорезмская академия Мамуна, Хива, Узбекистан
[2] Институт общей и неорганической химии Академии наук Республики Узбекистан, Ташкент, Узбекистан
[3] Ургенчский государственный университет имени Абу Райхона Беруни, Ургенч, Узбекистан
[4]Кокандский государственный университет, Коканд, Узбекистан
[5]Международный институт пищевых технологий и инженерии, Фергана, Узбекистан
[6]Наманганский государственный технический университет, Наманган, Узбекистан
[7]Ферганский государственный технический университет, Фергана, Узбекистан

Поступила: *26 января 2026*
Рецензирование: *5 февраля 2026*
Принята в печать: *4 августа 2026*

АННОТАЦИЯ

Приведены результаты комплексного исследования физико-химических и товарных свойств (гигроскопическая точка, кинетика сорбции, сорбционная влагоемкость) микроэлементсодержащих азотных удобрений на основе плава нитрата аммония (НА) и катодного порошка от использованных литий-ионовых батарей. Показано использование катодного порошка в качестве полимикроэлементной добавки (ПМД), и они были внесены в плав селитры при различных массовых соотношениях НА: ПМД от 100 (0,5-3,0). Испытаны полученные готовые образцы удобрений с размером гранул 2-3 мм для определения гигроскопической точки, кинетики сорбции и сорбционной влагоемкости при относительных влажностях воздуха 60; 70, 85 и 100%. Изучены исследуемые образцы удобрений при относительной влажности воздуха 60%, и доказано, что при такой относительной влажности образцы не увлажняются, а наоборот подсыхают. Приведены результаты исследования образцов при 4-х часовой выдержки и установлено, что гранулы удобрения имеют низкую гигроскопическую точку от 50 до 60% и высокую скорость поглощения влаги в порядке 1,860; 5,920 и 6,710; 2,052; 6,790 и 9,451, а также 3,481; 6,954 и 9,906 мг/(г мин) при относительной влажности воздуха 70, 85 и 100% соответственно. В связи с тем, что процесс сорбции исследуемых гранул продуктов продолжается до 30 суток (или 720 часов), они имеют гигроскопическую точку от 60 до 70%, относящуюся к гигроскопическим веществам. Сделаны соответствующие выводы, благодаря свойствам исследуемых удобрений они обладают низкой влагоемкостью, а их физические свойства начинают резко ухудшаться только при содержании влаги около 2%. Полученные удобрения по своим характеристикам не уступают известным удобрениям. Приведены рекомендации по упаковке готового продукта в полиэтиленовые мешки для хранения и перевозки на дальние расстояния.

Ключевые слова: нитрат аммония, плав, микроэлемент, гигроскопичность, скорость поглощения, кинетика сорбции, влагоемкость.

Информация об авторах:

Фазилова Мукаддас Халиллаевна	*Базовый докторант, Хорезмская академия Мамуна, Хива, Узбекистан. Email: mukaddasfazilova09@gmail.com; ORCID ID: https://orcid.org/0009-0007-1998-0554*
Хасанов Шодлик Бекпулатович	*Кандидат химических наук, старший научный сотрудник, заместитель председателя по научной работе, Хорезмская академия Мамуна, Хива, Узбекистан. Email: shadlik@mail.ru; ORCID ID: https://orcid.org/0000-0002-0334-6977*
Алимов Умарбек Кадырбергенович	*Старший научный сотрудник, доктор технических наук (DSc), ведущий научный сотрудник лаборатории Фосфорных удобрений Института общей и неорганической химии Академии наук Республики Узбекистан, Ташкент, Узбекистан. Email: umaralihonalimov@mail.ru; ORCID ID: https://orcid.org/0000-0001-5608-5304*
Рузметова Аида Шоназаровна	*Доктор философии по техническим наукам (PhD), доцент кафедры Химические технологии, Ургенчского государственного университета, Ургенч, Узбекистан. Email: aida0330@list.ru; ORCID ID: https://orcid.org/0000-0002-9637-4503*
Нумонов Бахтиёржон Омонжонович	*Доктор философии (PhD) по техническим наукам, доцент кафедры Химия и экология Кокандского государственного университета, Коканд, Узбекистан. Email: kimyogar_1985@mail.ru; ORCID ID: https://orcid.org/0009-0004-0110-8002*

Хошимов Ахроржон Ахадович	*Проректор по научной работе и инновациям Международного института пищевых технологий и инженерии, Фергана, Узбекистан. Email: axrorhoshimov1989@gmail.com; ORCID ID: https://orcid.org/0009-0003-4276-5538*
Холмуродов Жамшидбек Эркинович	*Доктор философии по техническим наукам (PhD), докторант, Наманганский инженерно-технологический институт, Наманган, Узбекистан. Email: erkinovichjamshid@mail.ru; ORCID ID: https://orcid.org/0009-0004-3413-8144*
Косимов Дилшоджон Мамуржон угли	*Доктор философии по техническим наукам (PhD), старший преподаватель, Ферганский государственный технический университет, Фергана, Узбекистан. Email: d.qosimov.m@gmail.com; ORCID ID: https://orcid.org/0009-0000-6698-5293*
Тожимаматову Мукаддам Ёрмахамматовну	*Старший преподаватель, Ферганский государственный технический университет, Фергана, Узбекистан. Email: m_tojimamatova@mail.ru; ORCID ID: https://orcid.org/0000-0003-0038-895x*

References

[1] Yuldasheva A P K, Shamuratov S K U, Kurambayev S R, & Radjabov M F. Mathematical Analysis of CaO Content Variation in Acidic Wastewater and Mineralized Mass Mixture from Central Kyzylkum Phosphorite Based on Exponential Decay Model. Kompleksnoe Ispolzovanie Mineralnogo Syra = Complex Use of Mineral Resources. 2026; 339(4):79–86. https://doi.org/10.31643/2026/6445.42

[2] Daneshgar S, Callegari A, Capodaglio A G, & Vaccari D. The Potential Phosphorus Crisis: Resource Conservation and Possible Escape Technologies: A Review. Resources. 2018; 7(2):37. https://doi.org/10.3390/resources7020037

[3] Latham KG, Ferguson A, & Donne SW. Influence of ammonium salts and temperature on the yield, morphology and chemical structure of hydrothermally carbonized saccharides. SN Appl. Sci. 2019; 1:54. https://doi.org/10.1007/s42452-018-0055-2

[4] U.S. International Trade Commission. Ammonium nitrate from Russia (Investigation No. 731-TA-856. Review, U.S. International Trade Commission. 2006; 3844. https://www.usitc.gov

[5] Gezerman AO, Zorbacıoglu BD. Detonation properties of ammonium nitrate containing calcium carbonate, dolomite, and fly ash. International Journal of Energetic Materials and Chemical Propulsion. 2017; 16:295–302.

[6] Bröckel U, Wahl M, Kirsch R, Feise HJ. Formation and growth of crystal bridges in bulk solids. Chemical Engineering & Technology. 2006; 29(6):691–695.

[7] Komunjer L, Affolter C. Absorption–evaporation kinetics of water vapor on highly hygroscopic powder: the case of ammonium nitrate. Powder Technology. 2005; 157(1):67–71.

[8] Kiiski H. Properties of ammonium nitrate-based fertilizers. PhD Dissertation, University of Helsinki, Helsinki. 2009, 215.

[9] Han Z. Thermal stability of ammonium nitrate. PhD Dissertation, Texas A&M University, USA. 2016, 210.

[10] Gezerman AO, Zorbacıoglu BD. Effects of sodium silicate, calcium carbonate, and silicic acid on ammonium nitrate degradation and analytical investigation of the degradation process on an industrial scale. Chemical Industry & Chemical Engineering Quarterly. 2015; 21:359–368.

[11] Khadzhiev A, Atabaev F. Influence of silica-containing additives on physical and mechanical properties of Portland Cement Co Ltd Karakalpaksement. E3S Web of Conferences. 2023; 401:05051. https://doi.org/10.1051/e3sconf/202340105051

[12] Iskandarova M, Atabaev F, Tursunova G, Tursunov Z, Khadzhiev A. Composite Portland cements: innovations and future directions in cement technology. Innovative Infrastructure Solutions. 2025. https://doi.org/10.1007/s41062-025-02067-x

[13] Khadzhiev A, Abdullaev M, Yakubov Y, Jumaniyozov J. The effect of hybrid mineral additives on the genetic formation and physico-chemical processes of cement composites. E3S Web of Conferences. 2025; 633:08003. https://doi.org/10.1051/e3sconf/202563308003

[14] Samadiy M, Deng T. Lithium recovery from water resources by ion exchange and sorption methods. Journal of the Chemical Society of Pakistan. 2021; 43(4):406–416.

[15] Wu Y, Wu X, Zhang J, Zhou L, & Chen B. Drip Irrigation of Phosphorus Fertilizer Enhances Cotton Yield and Phosphorus Use Efficiency. Agronomy. 2025; 15(6):1328. https://doi.org/10.3390/agronomy15061328

[16] Shamuratov S, Baltaev U, Alimov U, Khoshimov A, Matmuratov A, & Kurambaev S. Formation and agronomic efficiency of phosphorus-based fertilizer produced from cotton soapstock acidic wastewater and high-carbonate phosphorite. Journal of Ecological Engineering. 2026; 27(6):312–325. https://doi.org/10.12911/22998993/217637

[17] Semenova N A, Yakovlev A S, & colleagues. Fertilizers based on nanoparticles as sources of macro- and micronutrients for sustainable agriculture: A review. Agronomy. 2024; 14(8):1646. https://doi.org/10.3390/agronomy14081646

[18] Yadav A K, Gurnule G G, Gour N I, There U, & Choudhary V C. Micronutrients and fertilizers for improving and maintaining crop value: A review. International Journal of Environment, Agriculture and Biotechnology. 2022; 7(1):125–140. https://doi.org/10.22161/ijeab.71.15

[19] Dimkpa C O, & Bindraban P S. Nanofertilizers: New products for the industry? Journal of Agricultural and Food Chemistry. 2018; 66(26):6462–6473. https://doi.org/10.1021/acs.jafc.7b02150

[20] Fazilova M, Hasanov Sh, Alimov U, Rakhmanova M, Sadullaev S. Study of microelement-containing nitrogen fertilizers based on spent lithium-ion batteries. IOP Conference Series: Earth and Environmental Science. 2023; 1142:012047. https://doi.org/10.1088/1755-1315/1142/1/012047

[21] Shevchuk VV, Dikhtievskaya LV, Sokolova TP, Shlomina LF, Poznyak NI. Influence of inorganic salt impurities on the physicochemical and mechanical properties of potassium sulfate. Proceedings of the National Academy of Sciences of Belarus. Chemical Series. 2019; 55(2):223–232.

[22] Turatbekova A, Abdukadirova M, Shamuratov S, Latipov B, Saporboyev M, Shamshiyev J, & Makhmudov Y. Investigation of the effect of fertilizers on the biochemical and physical characteristics of carrots (Daucus carota L.). E3S Web of Conferences. 2024, 563. https://doi.org/10.1051/e3sconf/202456303074

[23] Sotimboev I, Baltaev U, Shamuratov S, Shamsiddin R, Alimov U, & Saporboyev M. Technical and economic efficiency of processing acidic wastewater from the oil and fat industry into necessary agricultural products. E3S Web of Conferences. 2024, 563. https://doi.org/10.1051/e3sconf/202456303072

[24] Baltayev U S, Shamuratov S X, Alimov U K, Madaminov A E, & Jabbarov M E. Extraction of P_2O_5 from the mineralized mass of the Central Kyzylkum using acidic wastewater generated from cotton soapstock processing: scientific analysis based on equilibrium principles. Kompleksnoe Ispolzovanie Mineralnogo Syra = Complex Use of Mineral Resources. 2027; 341(2):83–96. https://doi.org/10.31643/2027/6445.20

2028; 346(3):64-71 ISSN-L 2616-6445, ISSN 2224-5243

Crossref

DOI: 10.31643/2028/6445.29

Mining & Mineral Processing

Functionalized Chitosan-Modified PVDF-co-HFP Polymer Inclusion Membrane for Enhanced Au(III) Extraction

Nor'Azmi N.Z., *Shoparwe N.F.

Universiti Malaysia Kelantan, Malaysia

** Corresponding author email: fazliani.s@umk.edu.my*

Received: *July 19, 2026*
Peer-reviewed: *July 25, 2026*
Accepted: *August 5, 2026*

ABSTRACT

Gold recovery from aqueous solutions requires environmentally sustainable alternatives to conventional cyanide-based extraction processes. This study aimed to develop the polymer inclusion membrane (PIM) by incorporating functionalized chitosan into a poly (vinylidene fluoride-co-hexafluoropropylene) (PVDF-co-HFP) membrane to enhance the transport and extraction efficiency of Au(III). The membrane consisted of PVDF-co-HFP as the base polymer, Aliquat-336 as the carrier, and dioctyl phthalate (DOP) as the plasticizer, while functionalized chitosan was incorporated at concentrations ranging from 0.5 to 2.5 wt.%. The fabricated membranes were prepared using the solvent-casting techniques and characterized using scanning electron microscopy (SEM), Fourier transform infrared spectroscopy (FTIR), thermogravimetric analysis (TGA), contact angle, and ion exchange capacity (IEC). The membrane containing 2.0 wt.% functionalized chitosan (M5) exhibited the highest Au(III) extraction efficiency of 98.19%.The improved extraction performance was attributed to enhanced membrane hydrophilicity, increased ion exchange capacity, and more efficient carrier-mediated transport. These findings demonstrate that the developed PIM system is a promising and sustainable membrane-based technology for high-efficiency gold recovery.

Keywords: extraction, chitosan, membrane, PVDF-co-HFP, Aliquat-336.

Information about authors:

Nor'Azmi N.Z *Master candidate at the Gold, Rare Earth and Materials Technopreneurship (GREAT) Centre, Universiti Malaysia Kelantan, Jeli 17600, Malaysia. Email: norzafirah040200@gmai.com; ORCID ID: https://orcid.org/0009-0006-1794-2450*

Shoparwe N.F *Associate Professor at Gold, Rare Earth and Material Technopreneurship (GREAT) Centre, Universiti Malaysia Kelantan, Jeli 17600, Malaysia. Email: fazliani.s@umk.edu.my; ORCID ID: https://orcid.org/0000-0002-4329-2459*

Introduction

Gold is one of the most valuable metals because of its wide range of applications in the jewellery, electronics, aerospace, medical, and financial industries. The high global demand for gold has increased the need for efficient methods to extract gold from low-grade ores and secondary resources. Cyanide leaching has been the most widely used hydrometallurgical process for gold extraction because of its high recovery efficiency. However, the use of cyanide raises environmental concerns because of its high toxicity and the risk of environmental contamination. These concerns have encouraged researchers to develop more sustainable and environmentally friendly alternatives for gold recovery [1].

Membrane-based separation technologies have emerged as a promising alternative because they offer high selectivity, lower chemical consumption, and reduced secondary generation [2]. Among these technologies, polymer inclusion membranes (PIMs) have gained attention for metal ion separation and recovery. A typical PIM consists of a base polymer, a carrier, and a plasticizer. The carrier selectively binds with the target metal ion and transports it across the membrane, while the polymer provides mechanical support and the plasticizer improves membrane flexibility and transport performance [3].

Compared with conventional solvent extraction, PIMs combine extraction and stripping into a single membrane system. This reduces solvent loss and simplifies the overall separation process. Previous studies have successfully applied PIMs for the recovery of various metal ions, including Pb(II), Cd(II), Zn(II), Cr(VI), As(V), and Au(III). The results showed that PIMs have potential as an environmentally friendly technology for hydrometallurgical applications [2].

The selection of membrane materials is important because it directly affects the membrane

performance during metal ion transport. Poly(vinylidene fluoride-co-hexafluoropropylene) (PVDF-co-HFP) is commonly used as the base polymer due to its good chemical resistance, thermal stability, and mechanical strength. It is also compatible with hydrophobic carriers such as Aliquat-336. Aliquat-336, a quaternary ammonium salt, has been widely used as a carrier for Au(III) extraction because of its strong affinity for anionic metal complexes and good transport performance [4]. Dioctyl phthalate (DOP) is added as a plasticizer to improve membrane flexibility and enhance carrier mobility within the polymer matrix [5].

Chitosan is a natural biopolymer derived from chitin and has been widely studied for membrane application because of its biodegradability, biocompatibility, and the presence of hydroxyl and amino groups. These functional groups provide active sites for metal ion binding and help improve membrane hydrophilicity. However, the use of native chitosan is limited because of its poor stability in acidic media and relatively weak mechanical properties [4]. To overcome these limitations, chitosan can be functionalized to improve its stability and introduce additional active sites. Compared with native chitosan, functionalized chitosan has better compatibility with the polymer matrix and can enhance ion exchange capacity and metal transport. For these reasons, functionalized chitosan has become a promising additive for PIMs used in metal separation.

In this study, functionalized chitosan was incorporated into a PVDF-co-HFP-based membrane that consisted of Aliquat-336 as the carrier and DOP as the plasticizer for Au(III) extraction. The membrane was prepared using the solvent-casting method and characterized using Fourier transform infrared spectroscopy (FTIR), scanning electron microscopy (SEM), thermogravimetric analysis (TGA), contact angle measurement, and ion exchange capacity (IEC). The effects of functionalized chitosan concentration on the PIMs' properties and Au(III) extraction performance were then evaluated.

Experimental part

Materials

Poly(vinylidenefluoride-co-hexafluoropropylene) (PVDF-co-HFP) pellets (Sigma-Aldrich, USA) were used as the base polymer. Aliquat-336 (tricaprylmethylammonium chloride, Sigma-Aldrich, USA) was employed as the ionic carrier. Dioctyl phthalate (DOP, purity > 99.5%, Sigma-Aldrich, USA) served as the plasticizer. Chitosan (Sigma-Aldrich, USA) was used as the membrane additive and was functionalized via the ionic gelation method.

Functionalized Chitosan Preparation

0.3 g chitosan was dissolved in 1 wt.% dilute acetic acid solution under continuous magnetic stirring until a clear and homogeneous solution was obtained. Magnesium sulphate was then added dropwise as an ionic crosslinking agent to induce the functionalization process through ionic gelation. Upon completion of the reaction, the resulting functionalized chitosan was separated by centrifugation (6000 rpm, 50 mins) and repeatedly washed with distilled water to remove residual reactants. The purified product was subsequently dried in a laboratory oven at 50 °C until a constant weight was achieved [6].

Membrane Fabrication

50 wt.% of PVDF-co-HFP was dissolved in THF under continuous magnetic stirring until a clear and homogeneous polymer solution was obtained. Subsequently, the specific amount of DOP and Aliquat-336 was added according to the membrane compositions listed in Table 1 below. Functionalized chitosan was then incorporated into the casting solution at 0.5-2.5 wt.% and stirred continuously to ensure its uniform dispersion throughout the polymer matrix.

The prepared casting solution was uniformly cast onto a clean glass plate using a casting knife with a controlled thickness of 200 µm. Solvent evaporation was carried out at ambient conditions for 24 h, resulting in the formation of self-supporting membranes. The dried membranes were carefully peeled from the casting plate, cut into circular discs, and stored in a desiccator before physicochemical characterization and Au(III) transport experiments [4].

Membrane Characterization

The fabricated PIMs were characterized using various microscopic methods. The surface morphology of the fabricated PIMs was characterized using a JEOL JSM-IT100 scanning electron microscope (SEM, JEOL Ltd., Japan). The fabricated PIMs were cut into 5 x 5 mm sections and sputter-coated with Au-Pt under vacuum conditions. SEM micrographs were obtained at an accelerating voltage of 20.0 kV [7].

Table 1 – Membrane formulation with different functionalized chitosan concentrations

Acronyms	PVDF-co-HFP (wt.%)	Aliquat-336 (wt.%)	DOP (wt.%)	Functionalized Chitosan (wt.%)
M1	50	20	10	0.0
M2	50	20	10	0.5
M3	50	20	10	1.0
M4	50	20	10	1.5
M5	50	20	10	2.0
M6	50	20	10	2.5

The functional groups of the fabricated PIMs were characterized using FTIR-ATR (Thermo Scientific Nicolet iZ10, Thermo Fisher Scientific, USA) over the spectral range of 4000-400 cm^{-1} [8].

The thermal stability was examined using a TGA/DSC 2 HT thermogravimetric analyzer (METTLER TOLEDO, Switzerland). Approximately 5-10 mg of each membrane sample was heated from room temperature to 800 ℃ under a nitrogen atmosphre at a heating rate of 10 ℃ min^{-1} [9].

The membrane hydrophilicity was determined using a DataPhysics OCA15plus contact angle goniometer (DataPhysics Instruments GmbH, Germany). A 5 µL droplet of deionized water was deposited onto the membrane surface, and the contact angle was measured in triplicate [10].

2.5 Rate of Performance

The membrane that showed the best overall properties was selected for Au(III) extraction experiments. A standard Au(III) (Sigma-Aldrich, USA) feed solution was prepared by diluting a 1000 mg/L solution with 0.1 M hydrochloric acid (HCl, Mer, Germany) to obtain the 50 mg L^{-1}. The receiving solution was prepared by dissolving 1 g of thiourea (Thermo Fisher Scientific, USA) in 1% HCl to produce a 1.0 M thiourea solution.

The transport performance of the fabricated PIMs was evaluated using H-cell compartments. The fabricated PIMs were positioned between the feed and receiving compartments, each containing 100 mL of solution. Continuous stirring at 400 rpm was maintained throughout the experiment. Samples were collected at 4 h, 8 h, 12 h, 16 h, 20 h, and 24 h, and the Au(III) concentration was analyzed using inductively coupled plasma optical emission spectrometry (ICP-OES, Agilent Technologies Inc., USA).

Results and Discussion

Figure 1 shows the FTIR spectra of the fabricated PIMs. The spectra confirmed the successful incorporation of functionalized chitosan into the fabricated PIMs. An absorption band at 3200-3500 cm^{-1} was observed. This band corresponds to the stretching vibration of hydroxyl (-OH) and amino (-NH_2) groups [11]. Also, the additional peaks at 1550-1650 cm^{-1} were assigned to the amide and amino groups of chitosan [12]. The increase in intensity at 1100-1130 cm^{-1} were attribute to the asymmetric stretching vibration of sulphate groups, indicating the presence of magnesium sulphate in the membrane [13].

No additional absorption peaks were observed in the functionalized chitosan matrix membrane (M2-M6) compared with the pure PIMs (M1). This indicates that no new chemical bonds were formed during the preparation process [14]. Instead, the small shifts in peak position and changes in intensity. This is due to the membrane interacting mainly through hydrogen bonding [11]. These interactions help improve membrane properties while maintaining the chemical stability of PVDF-co-HFP and Aliquat-336 [15].

Figure 2 shows the SEM images of the fabricated PIMs, illustrating the effect of functionalized chitosan on the membrane surface morphology. M1 has a smooth and compact surface with a dense polymer matrix.

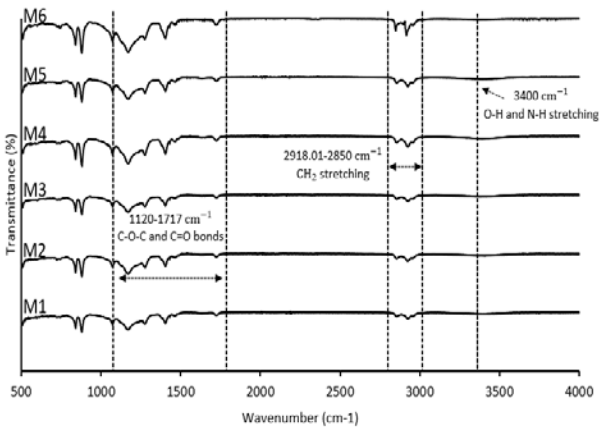

Figure 1 – FTIR spectra of PVDF-co-HFP-based PIMs with different functionalized chitosan (M1-M6)

After the addition of functionalized chitosan, the membrane surface became slightly rougher while maintaining a uniform structure. No obvious cracks, pinholes, or large particle agglomeration were observed, suggesting the functionalized chitosan was well distributed throughout the PVDF-co-HFP matrix. During solvent evaporation, the interaction between PVDF-co-HFP and functionalized chitosan promoted the formation of microstructural irregularities that increased the effective surface area available for ion exchange [16]. A uniform membrane structure was beneficial because it helps reduce transport resistance and provides continuous pathways for ion movement [4].

Among the fabricated membranes, M5 showed the most suitable surface morphology, which could facilitate the carrier-mediated transport of Au(III) [17].

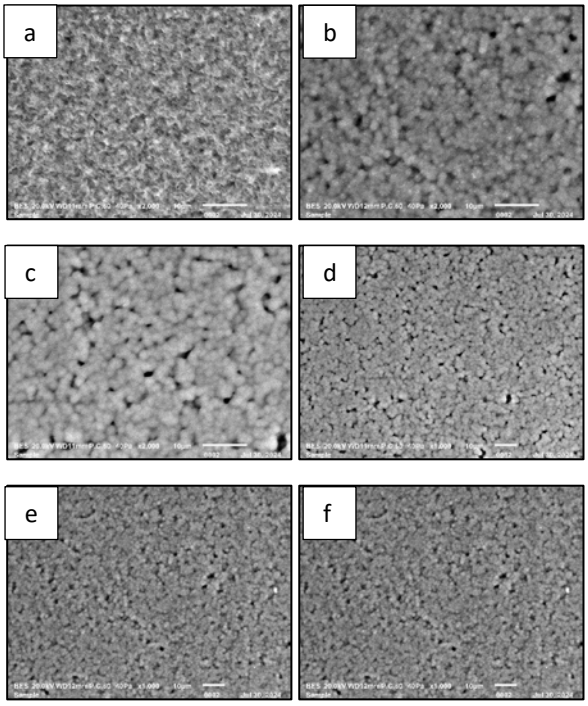

Figure 2 – SEM images of the surface morphology of PVDF-co-HFP-based PIMs with different functionalized chitosan: (a) M1, (b) M2, (c) M3, (d) M4, (e) M5, and (f) M6

Figure 3 shows the TGA curves of the fabricated PIMs. All membranes exhibited a similar thermal degradation pattern. The initial weight loss below approximately 160-200 °C was relatively small and can be attributed to the evaporation of residual moisture and solvent trapped within the membrane during fabrication [13]. This indicates that most of the solvent had been successfully removed during the membrane preparation process.

The second degradation stage was observed at around 250 °C, which is mainly associated with functionalized chitosan and DOP. Membranes with higher functionalized chitosan showed slightly greater weight loss. This is due to the thermal decomposition of the hydroxyl and amino groups [14]. However, all membrane maintained at high degradation temperatures. This means that the functionalized chitosan did not significantly affect the thermal stability of the membrane.

The largest weight loss occurred at approximately 450 °C. This corresponds to the degradation of the PVDF-co-HFP polymer backbone [18]. Similar degradation profiles were observed for all membrane formulations. This is due to the membrane structure remaining stable after the addition of the functionalized chitosan [19].

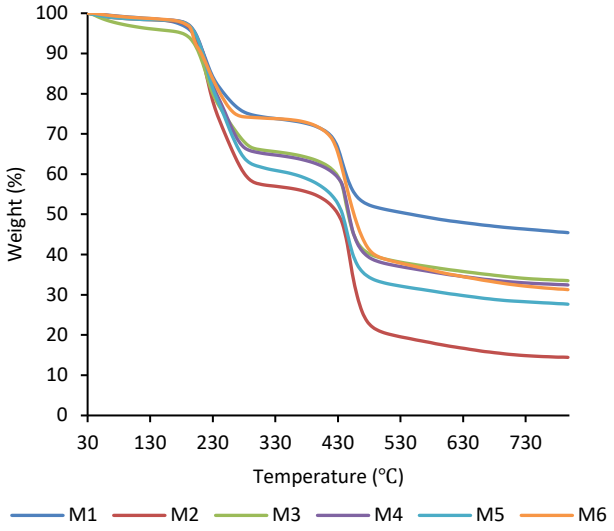

Figure 3 – Thermogravimetric analysis curves of PVDF-co-HFP-based PIMs with different functionalized chitosan (M1-M6), showing the thermal behaviour of the fabricated PIMs

Figure 4 shows the contact angle of fabricated PIMs. M1 exhibited the highest contact angle value of 57.41˚. This behaviour was attributed to the hydrophobicity of the fluorinated polymer backbone, where the presence of C-F bonds in the PVDF-co-HFP-based limits surface interaction with water molecules [4].

The contact angle values decreased with the increasingly functionalized chitosan concentration. This enhancement in the membrane surface hydrophilicity is due to the introduction of the hydroxyl and amino groups. These polar groups promote stronger interaction with water through hydrogen bonding. This can affect the affinity of the membrane surface [4].

The reduction in contact angle confirmed that functionalized chitosan successfully modified the membrane surface by increasing the surface free energy and wettability [20]. Enhanced surface wettability facilitates the adsorption and diffusion of water molecules at the membrane-solution interface. This can contribute to improved hydration of the membrane surface. As a result, the interfacial mass transfer resistance between the feed phase and the interfacial membrane surface was reduced. This can allow a greater accessibility of Au(III) to Aliquat-336. Therefore, the modified PIMs were expected to promote more efficient Au(III) transport during the extraction process.

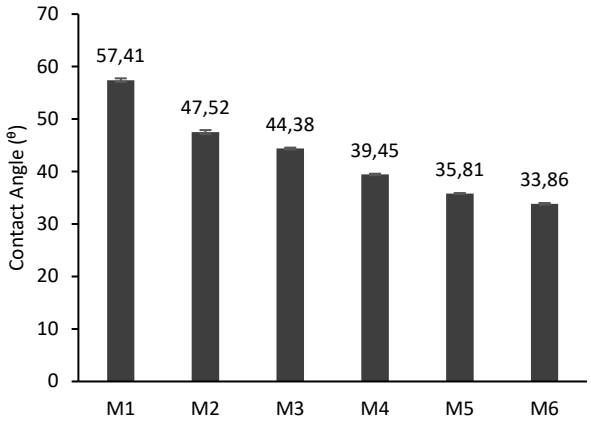

Figure 4 – Contact angle of PVDF-co-HFP-based PIMs with different functionalized chitosan (M1-M6), showing changes in surface hydrophilicity

Figure 5 shows the ion exchange capacity of fabricated PIMs. M1 exhibited the lowest IEC because PVDF-co-HFP is hydrophobic and contains limited availability of ionizable functional groups within the structure.

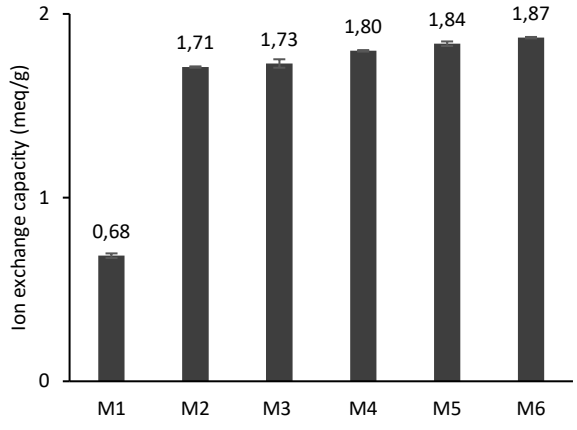

Figure 5 - Ion exchange capacity of PVDF-co-HFP-based PIMs with different functionalized chitosan

Following the addition of functionalized chitosan, the IEC increased because of the amino and hydroxyl groups that provide additional active sites for ion interaction and facilitate ion exchange for Au(III) transport [4]. The increased IEC is due to the higher density of available sites, which can enhance the movement of Au(III) complexes within the membrane [4].

Rate of Performance

Figure 6 shows the Au(III) extraction efficiency of fabricated PIMs with different concentrations of functionalized chitosan. The extraction efficiency increased with the increasing functionalized chitosan up to 2.0 wt.%, achieving a maximum extraction of 98.19%. This is due to the enhanced membrane hydrophilicity and higher ion exchange capacity by the additional hydroxyl and amino groups. This can increase the membrane's affinity and surface wettability, and provide more active sites for ion interaction. Therefore, it can promote the transport of Au(III).

Au(III) diffused toward the membrane surface under the concentration gradient between the feed and receiving phase. As demonstrated by SEM images, the addition of functionalized chitosan produced a more homogeneous membrane with increased surface roughness. It provides a larger effective contact area between the membrane and the solution. At the membrane interface, Au(III) was selectively extracted into the membrane via an ion-exchange reaction with quaternary ammonium groups of Aliquat-336 [21].

Upon reaching the receiving solution interface, Au(III) encounters thiourea in the receiving phase, where Au(III) preferentially forms a stable Au-thiourea complex. The receiving reaction releases Au(III) into the receiving phase while simultaneously regenerating Aliquat-336, allowing the carrier to diffuse back toward the feed phase and participate in transport cycles [22].

However, when the functionalized chitosan concentration was increased to 2.5 wt.%, the extraction decreased slightly. This is because the excessive functionalized chitosan affected the memrbane structure by increasing the density of the polymer matrix and restricting carrier mobility. It may reduce the free volume available for carrier diffusion, increase membrane viscosity during casting, and promote stronger intermolecular interactions that restrict carrier mobility. Consequently, the diffusion of Au(III)-complexes through the membrane becomes slower. Therefore, M5 was selected for subsequent optimization experiments.

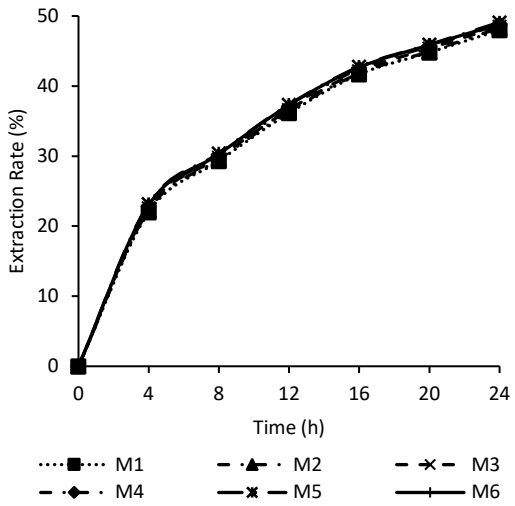

Figure 6 – Receiving phase Au(III) concentration over time of fabricated PIMs

Conclusions

Functionalized chitosan was successfully incorporated into PVDF-co-HFP to enhance Au(III) extraction. Membrane characterization demonstrated that the addition of functionalized chitosan improved membrane morphology, increased surface hydrophilicity, and enhanced ion exchange capacity. These physicochemical improvements facilitated carrier-mediated transport and reduced mass transfer resistance.

Among the fabricated membranes, M5 (2.0 wt.% functionalized chitosan) achieved 98.19% Au(III) extraction. However, further increasing the functionalized chitosan resulted in a decline in extraction percentages. It is indicated that the excessive loading of functionalized chitosan can increase the membrane hydration and diffusion resistance, thereby limiting the Au(III) transport.

Overall, functionalized chitosan is effective for improving the transport and extraction of Au(III) in PVDF-co-HFP. The membrane offers a promising and environmentally friendly alternative that can contribute to the advancement of sustainable separation technologies for metals.

Conflicts of interest. If you agree, you should not delete this statement: On behalf of all authors, the corresponding author states that there is no conflict of interest.

CRediT author statement: **N.Z. Nor'Azmi:** Conceptualization, Methodology, Validation, Formal analysis, Investigation, Writing – original draft, Writing – review & editing, Visualization, Investigation; **N.F. Shoparwe:** Supervision, Writing – Review & Editing.

Acknowledgements. The authors gratefully acknowledge the financial support from the Fundamental Research Grant Scheme (FRGS/1/2023/TK05/UMK/02) under the Ministry of Higher Education (MoHE) and would like to thank the Gold, Rare Earth & Materials Technopreneurship Centre (GREAT), Universiti Malaysia Kelantan (UMK) for providing lab facilities support for this research with sufficient technical support.

Cite this article as: Nor'Azmi NZ, Shoparwe NF. Functionalized Chitosan-Modified PVDF-co-HFP Polymer Inclusion Membrane for Enhanced Au(III) Extraction. Kompleksnoe Ispolzovanie Mineralnogo Syra = Complex Use of Mineral Resources. 2028; 346(3):64-71. https://doi.org/10.31643/2028/6445.29

Функционалдандырылған хитозан-модификацияланған PVDF-co-HFP полимерлі инклюзивті мембрана Au(III) экстракциясын күшейту үшін

Nor'Azmi N.Z., Shoparwe N.F.

Малайзия университеті Келантан, Малайзия

Мақала келді: *19 шілде 2026*
Сараптамадан өтті: *25 шілде 2026*
Қабылданды: *5 тамыз 2026*

ТҮЙІНДЕМЕ

Сулы ерітінділерден алтынды алу дәстүрлі цианид негізіндегі экстракция процестеріне экологиялық тұрғыдан тұрақты баламаларды қажет етеді. Бұл зерттеудің мақсаты Au(III) тасымалдау және экстракция тиімділігін арттыру үшін поли (винилиденфторид пен-гексафторпропилен) (PVDF-пен-HFP) мембранасына функционалданған хитозанды қосу арқылы полимерлік мембрананы (PIM) әзірлеу болды. Мембрана негізгі полимер ретінде PVDF-ко-HFP, тасымалдаушы ретінде Aliquat-336 және пластификатор ретінде диоктилфталат (DOP), сондай-ақ 0,5-тен 2,5 салмақтық % -ға дейінгі концентрацияда функционалдандырылған хитозан қосылды. Дайындалған мембраналар ерітінді құю әдістерін қолдана отырып дайындалды және сканерлеуші электронды микроскопия (SEM), Фурье түрлендіруінің инфрақызыл спектроскопия (FTIR), термогравиметриялық талдау (TGA), жанасу бұрышын өлшеу және ион алмасу сыйымдылығы (IEC) арқылы сипатталды.

	Құрамында 2,0% салмақтық% функционалдандырылған хитозан (M5) бар мембрана Au(III) экстракциясының ең жоғары тиімділігін көрсетті, ол 98,19% құрады. Экстракция өнімділігінің жақсаруы мембрананың гидрофильділігінің жоғарылауына, ион алмасу қабілетінің артуына және тасымалдаушы арқылы тасымалдаудың тиімдірек болуына байланысты болды. Бұл зерттеулер әзірленген PIM жүйесінің жоғары тиімді алтын алу үшін перспективалы және тұрақты мембраналық технология екенін көрсетеді.
	Түйін сөздер: экстракция, хитозан, мембрана, pvdf-co-hfp, aliquat-336.
Nor'Azmi N.Z.	***Авторлар туралы ақпарат:*** *Алтын, сирек жер және материалдар технологиясы (GREAT) орталығында магистр кандидаты, Малайзия университеті Келантан, Джели 17600, Малайзия. Email: norzafirah040200@gmai.com; ORCID ID: https://orcid.org/0009-0006-1794-2450*
Shoparwe N.F.	*Алтын, сирек жер және материалдық технология (GREAT) орталығының доценті, Малайзия университеті Келантан, Джели 17600, Малайзия. Email: fazliani.s@umk.edu.my; ORCID ID: https://orcid.org/0000-0002-4329-2459*

Функционализированная хитозан-модифицированная полимерная мембрана на основе PVDF-co-HFP для повышения эффективности извлечения Au(III)

Nor'Azmi N.Z., Shoparwe N.F.

Университет Малайзии Келантан, Малайзия

Поступила: *19 июля 2026*
Рецензирование: *25 июля 2026*
Принята в печать: *5 августа 2026*

АННОТАЦИЯ

Для извлечения золота из водных растворов необходимы экологически устойчивые альтернативы традиционным процессам экстракции на основе цианида. Целью данного исследования было разработать полимерную мембрану с включениями (PIM) путем включения функционализированного хитозана в мембрану из поли(винилиденфторида-со-гексафторпропилена) (PVDF-co-HFP) для повышения эффективности переноса и экстракции Au(III). Мембрана состояла из PVDF-co-HFP в качестве базового полимера, Aliquat-336 в качестве носителя и диоктилфталата (DOP) в качестве пластификатора, при этом функционализированный хитозан был включен в концентрациях от 0,5 до 2,5 мас.%. Изготовленные мембраны были получены методом литья из раствора и охарактеризованы с помощью сканирующей электронной микроскопии (SEM), инфракрасной спектроскопии с преобразованием Фурье (FTIR), термогравиметрического анализа (TGA), измерения краевого угла смачивания и ионообменной емкости (IEC). Мембрана, содержащая 2,0 мас.% функционализированного хитозана (M5), продемонстрировала наивысшую эффективность извлечения Au(III) — 98,19%. Улучшение эффективности извлечения объясняется повышенной гидрофильностью мембраны, увеличенной ионообменной емкостью и более эффективным транспортом с помощью носителя. Эти результаты показывают, что разработанная система PIM является перспективной и устойчивой мембранной технологией для высокоэффективного извлечения золота.

Ключевые слова: экстракция, хитозан, мембрана, PVDF-CO-HFP, аликвата-336.

Информация об авторах:

Nor'Azmi N.Z.

Магистр Центра технологического предпринимательства в области золота, редких земель и материалов (GREAT), Университет Малайзии Келантан, Джели 17600, Малайзия. Email: norzafirah040200@gmai.com; ORCID ID: https://orcid.org/0009-0006-1794-2450

Shoparwe N.F.

Доцент Центра технологического предпринимательства в области золота, редких земель и материалов (GREAT), Университет Малайзии Келантан, Джели 17600, Малайзия. Email: fazliani.s@umk.edu.my; ORCID ID: https://orcid.org/0000-0002-4329-2459

References

[1] Lee SH. Current status of gold leaching technologies from low grade ores or tailings. Resources Recycling. 2020; 29(2):3-7. https://doi.org/10.7844/kirr.2020.29.2.3

[2] Kaczorowska MA, The use of polymer inclusion membranes for the removal of metal ions from aqueous solutions the latest achievements and potential industrial applications: A review. Membranes. 2022; 12(11):1135. https://doi.org/10.3390/membranes12111135

[3] Wang B, Wang Y, Xu T, Recent advances in the selective transport and recovery of metal ions using polymer inclusion membranes. Advanced Materials Technologies. 2023; 8(22):2300829. https://doi.org/10.1002/admt.202300829

[4] Lim CK, et al. Synergistic role of functionalized chitosan nanoparticles in poly (vinylidene fluoride-co-hexafluoropropylene)(PVDF-HFP) polymer inclusion membranes for high-efficiency gold (III) adsorption. Journal of Polymer Research. 2026; 33(4):148. https://doi.org/10.1007/s10965-026-04841-6

[5] Soo JAL, et al. Characterization and kinetic studies of poly (vinylidene fluoride-co-hexafluoropropylene) polymer inclusion membrane for the malachite green extraction. Membranes. 2021; 11(9):676. https://doi.org/10.3390/membranes11090676

[6] Rastegari A, Mohammadi Z, Faghihi H. Ionotropically cross-linked chitosan-based drug delivery systems, in Ionotropic Cross-Linking of Biopolymers. Elsevier. 2024, 219-244. https://doi.org/10.1016/B978-0-323-96116-5.00013-2

[7] Wu J, et al. Sample preparation matters: Scanning electron microscopic characterization of polymeric membranes. Journal of Membrane Science Letters. 2024; 4(1):100073. https://doi.org/10.1016/j.memlet.2024.100073

[8] Ahmad AL, et al. Graphene oxide-doped polymer inclusion membrane for remediation of pharmaceutical contaminant of emerging concerns: Ibuprofen. Membranes. 2021; 12(1):24. https://doi.org/10.3390/membranes12010024

[9] Husna SM, et al. Effect of graphene oxide on the properties of polymer inclusion membranes for gold extraction from acidic solution. Membranes. 2022; 12(10):996. https://doi.org/10.3390/membranes12100996

[10] Shoparwe NF, et al. Removal of humic acid using 3-methacryloxypropyl trimethoxysilane functionalized MWCNT loaded TiO2/PES hybrid membrane. Membranes. 2021; 11(9):721. https://doi.org/10.3390/membranes11090721

[11] Zhi C, et al. Emerging Gel-Based Organic Electrochemical Transistors: Device Design, Engineering, and Applications. Advanced Functional Materials. 2026; 36(28):e23411. https://doi.org/10.1002/adfm.202523411

[12] Fathanah U, et al. Utilization of chitosan as an additive for enhancing the performance of polyethersulfone membranes for water treatment. in IOP Conference Series: Earth and Environmental Science. IOP Publishing. 2024. https://doi.org/10.1088/1755-1315/1297/1/012094

[13] Elhaes H, et al. Spectroscopic, Hartree–Fock and DFT study of the molecular structure and electronic properties of functionalized chitosan and chitosan-graphene oxide for electronic applications. Optical and Quantum Electronics, 2024; 56(3):458. https://doi.org/10.1007/s11082-023-05978-0

[14] Poovazhagi R, et al. Chitin Derivative from Marine Source Artemia franciscana Cysts Inhibits Colorectal Adenocarcinoma Cells by Regulating Apoptotic Mediators. Pharmacognosy Research. 2025; 17(3).

[15] Edward K, Yuvaraj K, Kapoor A. Chitosan-blended membranes for heavy metal removal from aqueous systems: A review of synthesis, separation mechanism, and performance. International Journal of Biological Macromolecules; 2024; 279:134996.

[16] El-Araby A, et al. Chitosan, chitosan derivatives, and chitosan-based nanocomposites: eco-friendly materials for advanced applications (a review). Frontiers in Chemistry. 2024; 11:1327426. https://doi.org/10.3389/fchem.2023.1327426

[17] Abouricha S, et al. Biopolymers-based proton exchange membranes for fuel cell applications: a comprehensive review. ChemElectroChem. 2024; 11(9):e202300648. https://doi.org/10.1002/celc.202300648

[18] Kazemi D, Yaftian MR. PVDF-HFP-based polymer inclusion membrane functionalized with D2EHPA for the selective extraction of bismuth (III) from sulfate media. Scientific Reports. 2024; 14(1):11622. https://doi.org/10.1038/s41598-024-62401-8

[19] Yu M, et al. Effect of temperature-induced aging on the gas permeation behavior of thin film composite membranes of PIM-1 and carboxylated PIM-1. Industrial & Engineering Chemistry Research. 2024; 63(37):16198-16207. https://doi.org/10.1021/acs.iecr.4c02230

[20] Zareei F, Bandehali S, Hosseini SM. Enhancing the separation and antifouling properties of PES nanofiltration membrane by use of chitosan functionalized magnetic nanoparticles. Korean Journal of Chemical Engineering. 2021; 38(5):1014-1022. https://doi.org/10.1007/s11814-021-0765-9

[21] Alguacil FJ, et al. Transport of Au (III) from HCl Medium across a Liquid Membrane Using R3NH+ Cl−/Toluene Immobilized on a Microporous Hydrophobic Support: Optimization and Modelling. Membranes. 2020; 10(12):432. https://doi.org/10.3390/membranes10120432

[22] Alguacil FJ, Robla JI. Solvent Extraction of Au (III) by 2-ethylhexanol and Kinetic Modelling of the Facilitated Transport Across a Liquid Membrane. 2024. https://doi.org/10.20944/preprints202402.1149.v1

Crossref
DOI: 10.31643/2028/6445.30
Mining & Mineral Processing

Recent Advances in Polymeric Nanocomposite Carriers of Various Active Ingredients for Controlled and Sustained Drug Release: A Review

Moshera Samy

Polymers and Pigments Department, Chemical Industries Research Institute, National Research Centre, Egypt

Email: moshera_samy1984@yahoo.com

Received: *July 8, 2026*
Peer-reviewed: *July 17, 2026*
Accepted: *August 14, 2026*

ABSTRACT

Controlled and sustained drug delivery has emerged as a transformative strategy for overcoming the limitations of conventional pharmaceutical formulations, including poor bioavailability, rapid drug clearance, systemic toxicity, and non-specific distribution. Among the numerous delivery platforms investigated, polymeric nanocomposite carriers have attracted considerable attention because they integrate the excellent biocompatibility, biodegradability, and processability of polymers with the unique physicochemical, mechanical, optical, magnetic, and therapeutic properties of inorganic nanomaterials. This review provides a comprehensive and critical evaluation of recent advances in polymeric nanocomposite-based drug delivery systems, highlighting the synergistic interactions between natural and synthetic polymers and a broad spectrum of nanofillers, including metal and metal oxide nanoparticles, carbon-based nanomaterials, nanoclays, mesoporous materials, and electrospun nanofibers. The influence of nanocomposite composition, fabrication strategies, and physicochemical characteristics on drug loading, encapsulation efficiency, release kinetics, targeting capability, and biological performance is systematically discussed. Furthermore, representative therapeutic applications in cancer therapy, wound healing, antimicrobial treatment, tissue engineering, neurological disorders, and regenerative medicine are critically compared to establish structure–property–performance relationships. This review primarily summarizes individual carrier systems, preparation methods, release mechanisms, and biomedical applications into a unified framework while identifying current limitations related to nanoparticle aggregation, long-term biocompatibility, biodegradation, large-scale manufacturing, regulatory approval, and clinical translation. This review provides valuable insights for researchers working on the rational design of advanced polymeric nanocomposites with enhanced therapeutic efficacy, improved safety, and accelerated clinical applicability.

Keywords: controlled drug delivery, polymeric nanocomposites, precision nanomedicine, smart nanocarriers, stimuli-responsive drug delivery, sustainable nanomanufacturing, therapeutic nanoplatforms.

Moshera Samy

Author information:
PhD, Associate Professor, Polymers and Pigments Department, National Research Centre, 33 El Buhouth St., Dokki, Giza 12622, Egypt. Email: moshera_samy1984@yahoo.com; ORCID ID: https://orcid.org0000-0002-7272-4134

1. Introduction

Over the past years, scientists have become increasingly interested in organic-inorganic composite (OIC) materials, which are composed of two or more different types of components. OIC materials display a wide range of features because they might differ from both organic and inorganic materials in certain ways [1]. Bioactive organic–inorganic composites can be created by combining different organic polymers with inorganic components [2]. As technology advances, active ingredients (drugs) and sustained release remain significant challenges in the field of drug delivery and development. This is because conventional drug therapies have limitations in terms of selectivity, pharmacodynamics, side effects, short lifetime, and limited drug solubility [3]. Novel effective medication delivery techniques are practically crucial for avoiding unnecessary changes to the stability and characteristics of drugs. In this situation, drug delivery is designed to (i) precisely target the desired organ to reduce drug side effects and (ii) control drug release to prevent traditional overdose or underdose. The drug delivery system (DDS) is a combination of a drug and a carrier in which the pharmaceuticals are loaded either chemically or physically onto the carrier's surface

[4]. One of the most promising uses of human health care is DDS, which is a constantly developing area of the medical sciences. The development of organic–inorganic composites as a suitable carrier that is effective for drug delivery to the body with a maximum benefit-to-risk ratio remains a critical problem for scientists despite the rapid advancements in DDS [5]. DDS also enhances the concentration of the medications of interest in the target tissues and shields them from quick removal or degradation [6]. The active pharmaceutical ingredient can be released to produce the desired therapeutic effect thanks to the drug delivery mechanism. Tablets, capsules, syrups, ointments, and other traditional drug delivery methods are unable to offer sustained release due to their low bioavailability and fluctuations in plasma drug levels [7]. Essential benefits of sustained drug delivery are reduced doses, fewer adverse effects, less blood-stream concentration changes, decreased risks of dose-dumping, improved bioavailability, site specificity, and improved drug stability [8]. Many formulations for controlled drug release were created, including tablets, beads, buccal patches, capsules, implants, microparticles, nanoparticles, etc. These drug release systems are frequently made with a variety of ingredients, including inorganic materials (such as metal powders and bioceramics) and natural, synthetic, and semi-synthetic polymers. To maintain the release of certain medicinal compounds for as long as feasible, a range of polymeric nanoparticles and inorganic composites were recently created as fibers or particles at the nano- or micron-scale. Polymeric nanoparticles and inorganic materials combined to generate better loading and encapsulation of several pharmaceutically active substances, more sustainable drug release, and superior mechanical characteristics [9]. Generally speaking, composites are material mixes composed of two or more materials that interact chemically or physically. Each component maintains its unique properties while the other serves as the matrix phase (ceramics, polymers, or metals) and the reinforcing phase (sheets, particles, or fibers). In fact, these materials give the composites additional physico-mechanical characteristics [10]. Composites are classified as either inorganic/inorganic (metal/metal composites, ceramic/ceramic composites, etc.), organic/inorganic (polymer/metal composites, polymer/ceramic composites, etc.), or organic/organic based on the composition of the matrix reinforcement [11]. Numerous composites have recently been created for a range of biomedical applications, including drug delivery, antibacterial agents, cancer treatment, wound dressing, steam cell therapy, and biosensors [12]. A review based on OIC materials for controlled release of active ingredients. A few possibilities for creating organic–inorganic composites for drug delivery are shown in Fig. 1. Composite materials made of organic and inorganic components have long been the subject of intensive research. A review based on OIC materials for controlled release of active ingredients.

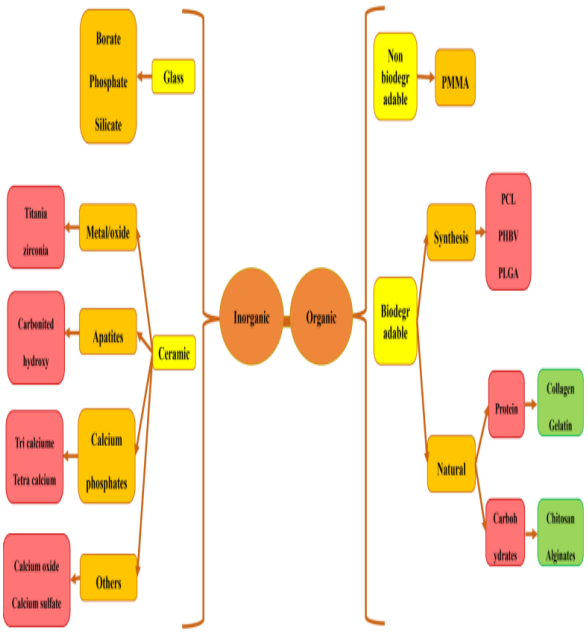

Fig. 1 - Several possibilities for producing organic-inorganic composites for drug delivery [13]

2. Organic–inorganic composite (OIC)

Materials that combine organic and inorganic elements into a single structure are known as organic–inorganic composites. Organic-inorganic composites are referred to as nanocomposites when their inorganic portions reach nanoscale size. Nanotubes, layered silicates (like montmorillonite (MMT) and saponite), metal nanoparticles (like Ag and Au), metal oxides (like TiO_2 and Al_2O_3), semiconductors (like PbS and CdS), and so on are examples of inorganic nanoscale building blocks. Of these, SiO_2 is thought to be particularly significant. As a result, polymer/silica nanocomposites have garnered a lot of attention from both academia and industry. By combining the unique properties of both kinds of materials, these materials aim to create a synergistic set of features. Blending the properties of inorganic and organic components is actually the aim of organic–inorganic composites.

For example, the flexibility and low weight of mechanical strength and thermal stability of inorganic materials. These materials are used in a wide range of OIC applications, such as electronics, sensors, tissue engineering materials, catalysis, and controlled drug release systems [14]. Numerous procedures, such as the sol–gel method [15], solution–processing (SP), soluation casting, electrospinning, chemical vapor deposition (CVD) method [16], in situ polymerization, polyelectrolyte complex (PEC) [17], layer–by–layer (LbL) assembly [18], the Langmuir–Blodgett technique [19], melt processing, atomic layer deposition (ALD) technique [20], and the molecular layer deposition (MLD) techniques that allow for the creation of organic–inorganic networks [21].

2.1. Method of preparation of organic–inorganic composite materials

In order to create several types of OIC materials, including films and fibers, different processing techniques have been used. These composite materials are frequently prepared using important techniques including electrospinning, sol-gel, solution casting, and in situ polymerization.

2.1.1. Sol-gel method (SG)

One way of bottom-up synthesis is the sol-gel procedure. During this process, several irreversible chemical reactions are carried out to create the final compounds. The sol-gel method is one of the essential techniques. The two chemical processes, sol and gel, are referred to as sol-gel. Gel is the interconnected network created between phases, whereas sol is a colloidal suspension of solid particles in a liquid phase [22]. The two primary processes in the sol-gel process are condensation and hydrolysis. Both are sequential processes with multiple steps. Hydrolysis is the cleavage of an organic chain bond to metal followed by a nucleophilic addition that replaces it with -OH groups. The hydrolyzed metal is left as an alcohol (alcoxolation) by the protonated species. The primary reaction parameters include temperature, water, solvent concentrations, metal reactivity, and the employment of complicated agents or catalysts. The compatibility of the sol-gel method with polymers and polymerization processes, which permits the production of nanoparticles in the presence of organic molecules, is one of its most interesting benefits [23]. Fig. 2 shows the sol-gel process technique.

organic polymers can be combined with the

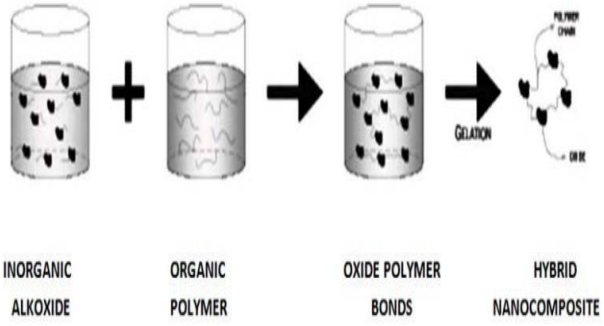

Fig. 2 - Sol-gel polymerization process [24]

2.1.2. Solution casting method

Solution casting is when thick mixtures with polymers, additives, and medicines are dried in a flat layer to create polymer films (Fig. 3). Although this process is simple, it can take a lot of time, and the materials used have a major impact on the final films' stability and qualities [25]. Usually, an organic solvent is used to dissolve or disperse polymers before they are placed onto a supporting surface. A solid layer develops on the substrate when the solvent evaporates during drying. Sometimes the solution contains particles of particular sizes, usually salts. After drying, the mixture is formed into its final shape. To dissolve the particles and leave a porous structure, the composite material can also be immersed in a bath. These solution-cast polymer films are ideal for serving as the base layer in multi-layered compositions because they have improved integrity in structure [26].

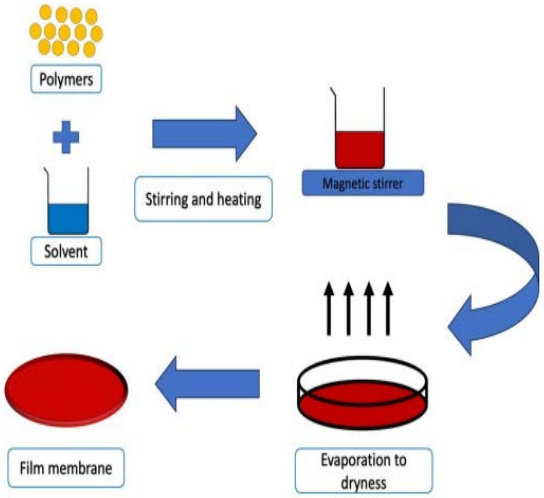

Fig. 3 - Solution casting method [27]

2.1.3. Electrospinning

A flexible technique, electrospinning is used to produce polymeric fibers with a high surface area to volume ratio and superior diffusion characteristics. Because of these qualities, it is useful for wound care applications, helping to reduce bleeding, absorb extra wound fluid, and promote tissue regeneration [28]. Typically, the electrospinning process uses an elevated direct current, or DC, voltage between a few kilovolts (10–20 kV). The application of this voltage creates electrical charges in a stream of polymer solution, which subsequently dries and forms polymer nanofibers. (Fig. 4). The compatibility of the selected polymer or polymers, the solvent or solvents, and any extra additives or active ingredients determines the stability, uniformity, and production efficiency of the electrospinning process. Indeed, in order to produce polymer nanofibers for wound care applications, electrospinning entails a number of crucial steps: Successful electrospinning is largely dependent on the compatibility and characteristics of the solvent and polymer. The syringe tube that is a component of the electrospinning apparatus is then carefully filled with the polymer solution. The solution inside the syringe is subjected to a powerful electric field produced by the electrical voltage differential between the tip of the needle and the collector that holds the solution. At the needle's tip, charges build up on the surface of the polymer solution droplet due to the electric field. The metal collector, which could be a stationary plate or a revolving drum, is where the nanofibers are gathered. On the collector's surface, the fibers create a nonwoven mat. The quality and homogeneity of the nanofibers depend on stable environmental factors, such as temperature and humidity. The ideal fiber qualities are obtained by optimizing variables including chamber temperature, solution vapor pressure, and the distance between the needle and collector. In general, the manufacturing of thin polymer nanofibers with specific qualities for a range of uses, including wound care, is made possible by the intricate yet tightly regulated process of electrospinning. Better absorption, moisture control, and cell contact are just a few of the increased wound healing properties that the resultant nanofibrous mats can offer [29].

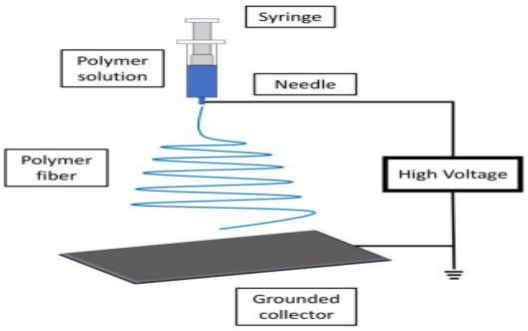

Fig. 4 - System of electrospinning [27]

2.1.4. In situ polymerization

The conducting filler is uniformly dispersed using in situ polymerization, which also preserves the aspect ratio and strengthens the link between the polymer and the filler. It is especially helpful for creating polymers that cannot be made using melt mixing (thermally unstable polymer) and solution (insoluble polymer) procedures. The monomer serves as the starting ingredient in this process. It entails dispersing carbons and polymers in a solvent. This enables the carbons to serve as a template for the growth of the polymer. After that, the mixture is agitated and sonicated to promote growth. Filtration or evaporation to dryness is then used to separate these composite structures from the fluid [30]. Fig. 5 shows a general schematic illustration of the in situ polymerization method. This process creates composite materials that are more conductive. The enhanced interaction between the polymer and the carbons could be the source of this. The product's more advantageous morphology could potentially be the cause.

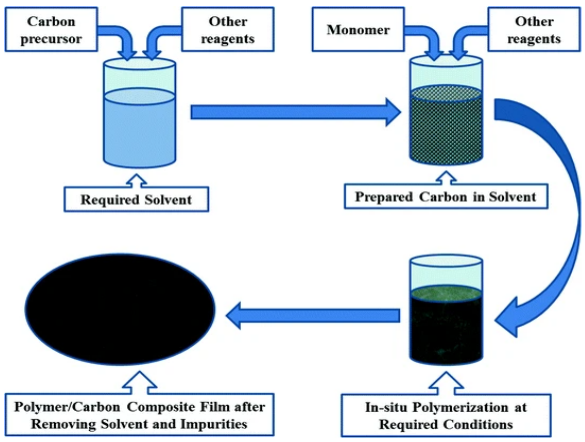

Fig. 5 - Schematic illustration of the in situ polymerization method [27]

3. Drug delivery system (DDS) nanocarriers

The process of delivering drugs to specific body locations and releasing them at the right rate is known as drug delivery. Locally released medications can help reduce the side effects of systemic drugs while maintaining a greater optimal drug concentration. DDS may also increase a drug's bioavailability [31]. Drug carriers, such as hydrogels, implants, films, spheroids, gels, dendrimers, beads, biocomposites, scaffolds, and microparticles, are used in DDS to load and encapsulate medications [32]. Thus, protecting the drug from degradation or destruction and facilitating precise delivery of the drug to the site of action are the main objectives of using polymeric nanoparticle carriers [33]. Drug delivery can therefore be controlled, targeted, or consistent. Common DDS that work with drugs come in bulk, micro, or nanoforms. Drug delivery techniques at the nanoscale offer significant benefits. Richard Feynman, a scientist, is credited with creating the idea of nanotechnology. The use of nanotechnology for medical purposes is known as nanomedicine, and it is a relatively recent scientific discipline. Drug delivery systems such as liposomes, niosomes, micelles, nanospheres, nanocapsules, nanoparticles, microparticles, microspheres, microbubbles, polymeric systems, dendrimers, colloidal gold, gold nanoshells, quantum dots, superparamagnetic particles, carbon nanotubes, cyclodextrins, and sphingosomes are frequently used for the diagnosis and/or treatment of a variety of diseases (Fig. 6 and Table 1) [34].

Table 1 - DDS nanocarriers for the diagnosis or therapy of a variety of diseases

Nanocarriers	Particles Size (nm)	Advantages	Disadvantages
Liposomes, Niosomes, phingosomes	20-3500	May be labeled with various radionuclides. Contrast enhancement for imaging in target and therapy enhancement.	The necessity of a long, time-consuming radiolabeling process and carefull controlling for reproducible efficiency
Micelles	-10 (Very small)	Easily prepared and radiolabeled, and removal by RES decreases depending on hydrophilic polymer shells.	The design of amphiphilic chelators should be given attention.
Nanoparticles, Solid Lipid nanoparticles	10-1000	These systems can be actively or passively targeted to the desired cell or tissue. They can escape from RES uptake. May be labeled with a variety of radionuclides.	Limited control of the size distribution and polydispersity.
Dendrimers	-10 (Very small)	Multivalent conjugation of radionuclides; biodistribution is enhanced depending on low polydispersity and spherical shape.	Toxicity may be formed depending on the positive charge of dendrimers.
Gold Nanoparticles	1-100	They have unique optical properties which are affected by shape and size. They can be used for cancer diagnosis and photothermal therapy.	It is important to discern the toxicity of the nanoparticle core and that of its capping ligands.
Microbubbles	≤10000	Act like red blood cells within the capillaries. Safer than molecular imaging modalities such as radiolabeled imaging.	Have low circulation time due to rapid RES uptake. Heat increase can be formed due to increase in frequency, which should be carefully monitored.
Magnetic Nanoparticles	10-50	They can be functionalized and manipulated with a selective molecule, and magnetic properties can be controlled with a magnetic field produced by an electromagnet or permanent magnet.	Metallic magnetic materials such as iron, cobalt and nickel are toxic and generally susceptible to oxidation. Uncoated magnetic nanoparticles should be chemically stabilized against degradation.
Quantum dots	(Typically <10)	Process long-term, multiplexed, and quantitative imaging and detection. They can be used for ultrasensitive and multicolor imaging of molecular targets.	Their delivery process across cells may be dangerous for the cell and may destroy it. In other cases, a QD may be toxic for cells.

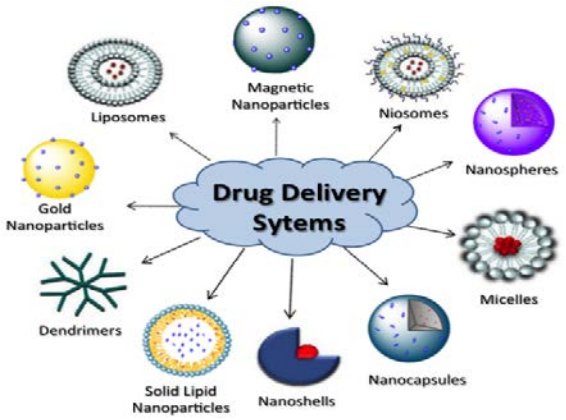

Fig. 6 - DDS nanocarriers for the therapy of various diseases [35]

3.1. Advantages of nanocarriers as delivery systems

Nanotechnology, a multidisciplinary scientific field that is expanding quickly, is the creation of systems and technologies at the molecular level [36]. Nanocarriers can be used to improve the poor solubility, penetration, low bioavailability, poor stability, or uncontrolled release of active substances [37]. As Davies *et al*. [38] reported, the chemical stability, photostability, antioxidant activity, and skin penetration of resveratrol and lipoic acid were all enhanced by their co-nanoencapsulation. Through the lipid-core nanocapsules, the nanoencapsulation also produced a more regulated release [39]. To summarize, the effectiveness of cosmetic goods has been increased through the use of nanocarriers as delivery vehicles **(**Fig. 7).

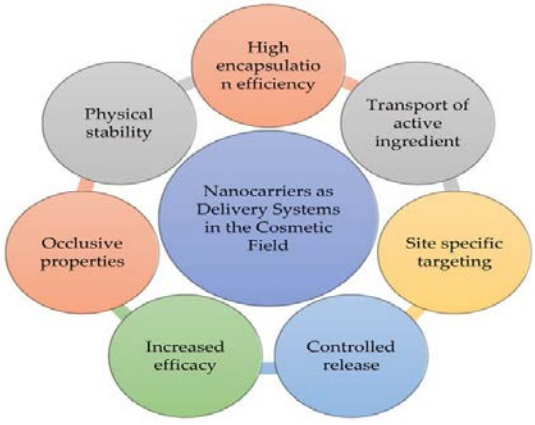

Fig. 7 - Advantages of employing nanocarriers as delivery systems [39]. Copyright 2022. Adapted from MDPI

3.2. Controlled drug delivery systems (CDDS)

Over the past few decades, CDDS have become a very effective technique for addressing issues with traditional dose forms, including frequent dosing, systemic adverse effects, low bioavailability, inefficient drug targeting, and stability, among others [40]. The polymer has become a crucial component of the contemporary pharmaceutical industry to overcome these disadvantages, but there is still a great need for the development of newer polymers that could better control drug release and be used to target bioactives; in other words, they should behave more intelligently [41]. In therapy, the DDS has several benefits (Fig. 8), such as lowering toxicity, raising the drug's therapeutic index, and avoiding frequent, costly, and uncomfortable dosing [5]. There are two ways to accomplish drug loading: integration and impregnation. During preparation, the medication is encapsulated by nanocomposites in the inclusion process. By incubating the nanocomposites in a solution, the impregnation process entraps the medication. Instead of using the impregnation approach, the inclusion method can produce nanocomposites with higher entrapment efficiency [42]. Because active materials may lose their activity during the incorporation process, the impregnation method is marginally better than the incorporation method. It has been suggested that sorption and release kinetic data be examined using a variety of isotherms in order to determine the mechanism of drug binding associated with the impregnation process (such as linear, Freundlich, Langmuir isotherms, and the BET model) [43]. Consequently, the following approaches should be used in drug release investigations depending on the identification of the release mechanism: reverse dialysis sac [42]. Determining the most effective formulations also requires consideration of the drug release from nanobiocomposites and the subsequent biodegradation [44].

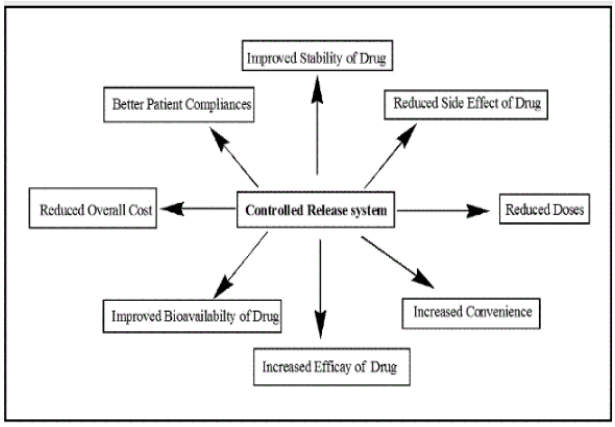

Fig. 8 - Benefits of controlled release of drug delivery system (DDS) [45]

4. Organic polymers as carrier for pharmaceutical applications

Polymers have been used in tissue engineering, DDS, gene therapy, and bioimaging, indicating their interest in pharmaceutical and medical difficulties. In general, polymers can be divided into two categories: synthetic and natural. Before being utilized for controlled drug administration, all natural or synthetic polymers must go through a number of purification, modification, and derivatization steps to guarantee their compatibility and safety for human health [42]. Based on their origin and chemical makeup, Raizada *et al.* [46] have divided commonly used polymers in pharmaceutical applications into six classes. It has been shown that (a) water-soluble artificial polymers, (b) insoluble water polymers that degrade, (c) cellulose-based polymers, (d) starch-based polymers, (e) rubber/plastics-based polymers, and (f) hydrocolloids make excellent scaffold materials for cell culture, especially in bone tissue regeneration strategies [47]. Compared to natural polymers, synthetic polymers that are produced through controlled and reproducible techniques and that are highly pure to prevent harmful effects appear to be more desirable. Among other characteristics, both groups of polymers can be hydrophilic or hydrophobic, hard or soft, thermoplastic or thermosetting, swellable, or degradable. This allows for a wide range of materials to match the anticipated use. Biodegradable polymers are needed for tissue engineering applications [48]. Biodegradable polymers of natural origin, such as polysaccharides (e.g., chitosan (CS), alginate, starch, gelatin, guar gum, carrageenan, albumin, and cellulose), as well as synthetic polymers such as polyorthoesters, polyanhydrides (PA), polyphosphoesters, polyesters (e.g., poly(lactic acid) (PLA) [49], polycaprolactone (PCL) [50], polyethylene glycol (PEG) (Fig. 9) [27], poly(lactic-co-glycoilc acid) (PLGA) [51], polyamides, polyurethane (PU), which are the most commonly used artificial polymers for regulated medication administration [42].

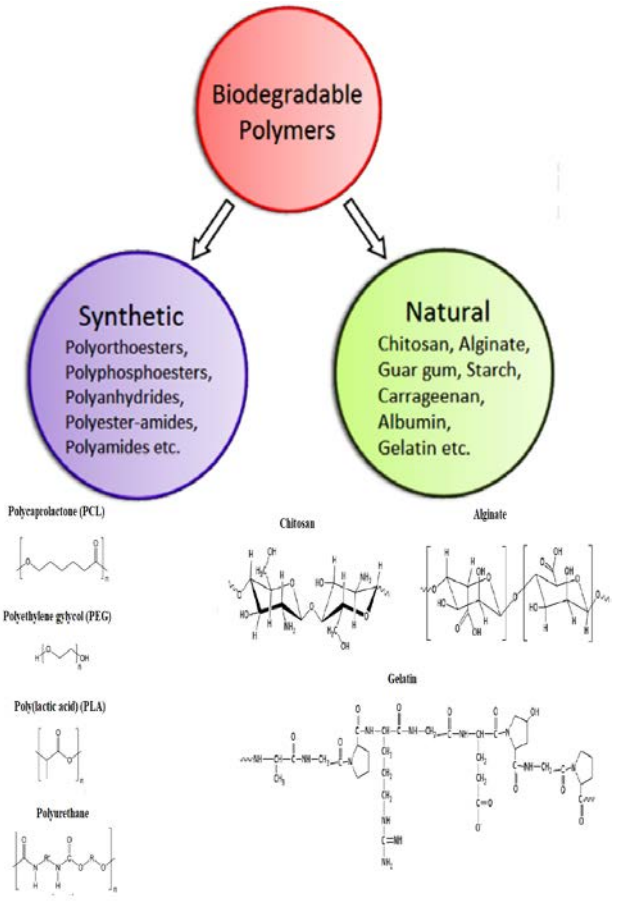

Fig. 9 - Biodegradable polymers classification for pharmaceutical applications [52]. Copyright 2019. Reproduced with permission from Elsevier

5. Inorganic materials in polymer composites

High electrical and thermal conductivity, high antibacterial activity, superior magnetic properties, chemical inertness, ease of surface functionalization, and biocompatibility are just a few of the exceptional qualities of many inorganic materials. Inorganic magnetic nanoparticles give polymeric matrices remarkable characteristics that can be used in a variety of biomedical applications, including medicine administration, therapy, and diagnostics. Numerous inorganic components are used in polymeric nanoparticle composites for drug delivery applications; a few of these are enumerated in the sections that follow (Fig. 10).

Fig. 10 - Inorganic materials that can be mixed with polymers to create organic-inorganic composites that have a lot of potential for use in drug delivery [53]

6. Nanocomposite

"Nanocomposite" is a word used when one of the structural units, in two ways inorganic or organic, falls within a certain size range of 1–100 nm. Generally, inorganic units produced in situ by molecular precursors like sol–gel reactions are referred to as hybrid materials, while separate components of structure in the correct dimension range are known as nanocomposites. Nanoparticles are examples of distinct inorganic units used in nanocomposites, such as nanorods, carbon nanotubes, and galleries of clay minerals [54]. These components are often incorporated into organic polymers to create a nanocomposite.

6.1. Type of nanocomposite

Nanocomposites have been divided into three classes based on the literature: intercalated, flocculated, and exfoliated, as shown in Fig. 11. Intercalated or layered nanocomposites are composites in which the extended polymer is inserted within the host polymers in organized multilayered structures. In flocculated and exfoliated composites, the host polymer may be nanoscale and should be distributed throughout the continuous polymer matrix [42]. The interfacial interactions between extended and host polymers serve as the basis for the classification [55]. We see the following concerning these three groups:

a. Intercalated nanocomposites are composites in which organic components or polymers (referred to as expanded polymers or inorganic materials) are frequently inserted into another polymer (the host polymer), irrespective of the ratio of polymer to inorganic material or polymer to polymer. The composites have characteristics of ceramic materials and are frequently interlayered.

b. Flocculated and intercalated nanocomposites differ only in the way the extended polymer is arranged within the host polymer.

c. Exfoliated nanocomposites: these depend on the loading of the filler to determine the mean space between the extended polymer layer and the continuous polymer matrix. Comparing the various forms of nano-biocomposites, it has been found that the filler amount is generally lower.

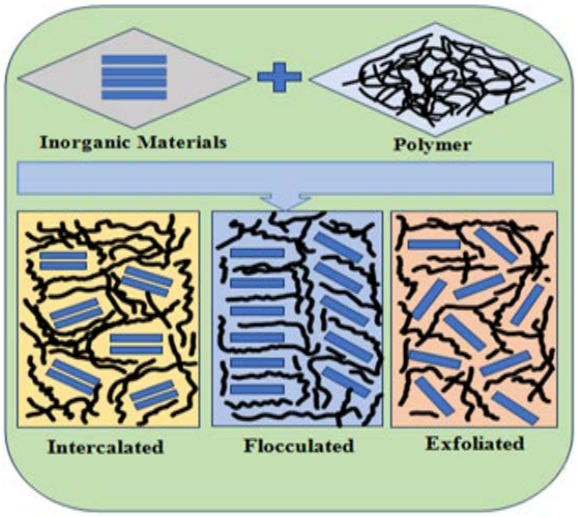

Fig. 11 - Schematic illustration of three main types of nanocomposite [42]

6.2. Properties of polymer nanocomposites

The properties of nanocomposites are influenced by a wide range of factors, such as the method of fabrication, the kinds of filler materials and their orientations, the degree of two-phase mixing, the type of adhesion at the matrix interface, the volume fraction of nanoparticles, the characteristics of the nanoparticles, the type of interphase formed at the matrix interface, the size and shape of the nanofiller materials, and the morphology of the system [56]. The novel family of composite materials known as nanocomposites regularly demonstrates exceptional mechanical, chemical, optical, electrical, and rheological qualities [57]. The nanoparticles must be evenly distributed throughout the matrix material in order to produce improved nanocomposites; if this is not done, the particles will aggregate, and the materials' qualities will decline. Since these aggregates will function as flaws and restrict the nanocomposite's ability to improve its properties, the nanoparticles should be evenly distributed

throughout the matrix to maximize this improvement [58].

6.3. Nanoparticles (NPs)

Materials with at least one dimension smaller than 100 nm are referred to as nanoparticles (NPs) [59].

These materials can have a 0D, 1D, 2D, or 3D overall shape [60]. When researchers found that a substance's size can influence its physicochemical properties, including its optical properties, the importance of these materials became clear. Since NPs are not simple molecules in and of themselves, they are composed of three layers. The surface layer is the first layer and can be functionalized with a variety of metal ions, polymers, surfactants, and small molecules. (b) The shell layer, which is completely chemically distinct from the core, and (c) the core, which is essentially the NPs' center and is usually used to refer to the NPs themselves [61].

6.3.1. Classification of nanoparticles

Nanoparticles can be classified as either inorganic (like metal and metal oxide nanoparticles like iron, zinc oxide, silica, and silver), carbon-based (like fullerenes, graphene, and carbon nanotubes), or organic (like ferritin, denderimers, micelles, liposomes, lipid-based NPs, polymeric nanoparticles, and micelles) [62] (Fig. 12). Because of their nanoscale size and high surface-area-to-volume ratio, nanoparticles can quickly move through the bloodstream and absorb large amounts of medication. Their larger surface area gives them special qualities that improve their mechanical, magnetic, optical, and catalytic properties, which enables a greater variety of medical applications.

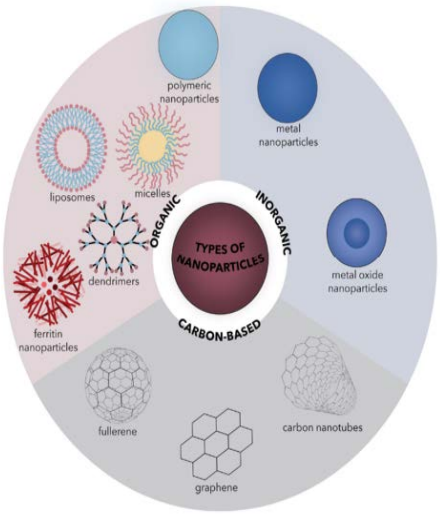

Fig. 12 - Schematic representation of the main classifications of nanoparticles [63]. Copyright 2021. Adapted from MPDI

6.3.1.1. Inorganic metal nanoparticles

In medicinal applications, gold nanoparticles (AuNPs) and silver nanoparticles (AgNPs) have garnered a lot of interest [63], as well as more generally in the development of technology, particularly because of their exceptional optical properties. Interestingly, these NPs exhibit surface plasmon resonance (SPR) behavior, which happens when light stimulates electrons at the material's interface between the conductor and insulator components [64]. These NPs' spectral characteristics are mostly form- and size-dependent; hence, the SPR is likewise influenced by the NPs' size, shape, and composition [65]. Metal nanoparticles' surfaces absorb light, causing electrons to collectively oscillate. This produces local heat that can be used in biomedical applications.

6.3.1.2. Inorganic metal oxide nanoparticles

Researchers are interested in inorganic metal oxide nanoparticles because of their appealing characteristics, which include easy surface functionalization, porosity, high stability, customizable form, and simple manufacturing procedures. Numerous biological applications, including medical imaging, medication transport, gene therapy, treatments linked to hyperthermia, antioxidant treatment, photodynamic therapy, dentistry, and wound healing techniques, have been studied for inorganic metal oxide nanoparticles. Inorganic substances, including gold nanoparticles, ZnO nanoparticles, TiO_2 nanoparticles, and silica-based nanoplatforms. Platforms known as metallic nanocarriers are helpful for the controlled and targeted delivery of macro- and micromolecules in the treatment of disease. These benefits resulted from ligands' variety in dimensions and forms, their high carrier capacity, their ability to form long-lasting interactions [66].

6.3.1.3. Carbon -based materials

Carbon-based nanomaterials include graphene (2D), carbon nanotubes (1D), nanodiamonds (1D), and carbon dots (CDTs) as well as fullerenes (0D), as illustrated in Fig. 13. The incorporation of polymeric nanoparticles into carbon nanomaterials gives them additional desirable characteristics like improved drug encapsulation ability, active functional groups, and superior mechanical stability. Impart qualuities such stability, active fuctional groups, improved drug encapsulation capacity, cellular responsiveness, increased solubility, antibacterial activity, and biocompatibility

that are appropriate for biomedical applications [67].

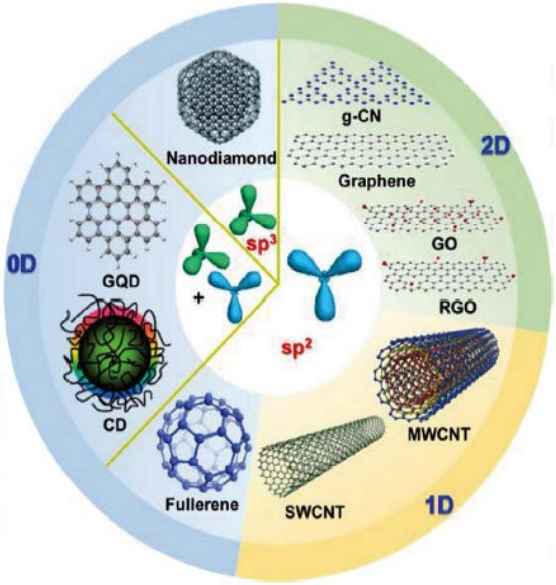

Fig. 13 - Carbon-based nanomaterials are classified according to their dimensionalities and carbon atom orbital hybridization [67].
Copyright 2020. Adapted from Wiley

6.3.2. Polymeric nanoparticles (PNPs)

The majority of PNPs have nanosphere or nanocapsular shapes [68]. The matrix particles have an overall mass that is frequently solid, while the other molecules are adsorbed at the outer edge of the spherical surface. The solid mass in the latter case is completely contained within the particle [69]. We now have access to a large variety of polymers that can be turned into nanoparticulate carriers for different active ingredients thanks to recent developments in nanotechnology. The creation of nanoparticles has already made use of a wide range of natural and synthetic polymeric materials, including biodegradable, biocompatible, and nonbiodegradable compounds. The most prevalent ones are Polycaprolactone (PCL) [70], poly(lactide-co-glycolide) (PLGA), and poly(lactide) (PLA). Polymeric materials with satisfactory biocompatibility include poly(ethylene-co-vinyl acetate) (PEVA) and poly(methylmethacrylate) (PMMA). However, Eudragits® and poly(ethylene glycol) (PEG) are examples of synthetic polymeric materials that are not biodegradable.

6.3.2.1. Classification of polymeric nanoparticles

Polymeric nanoparticles can be classified as either nanospheres or nanocapsules based on their composition [71]. Fig. 14 shows schematic representations of both configurations. Numerous factors, including the drug's physicochemical properties, the medium's pH, the nature of the polymer or NPs' surface characteristics, the quantity of drug added to the formulation, and whether the drug was added before or after the formation of nanostructures [59].

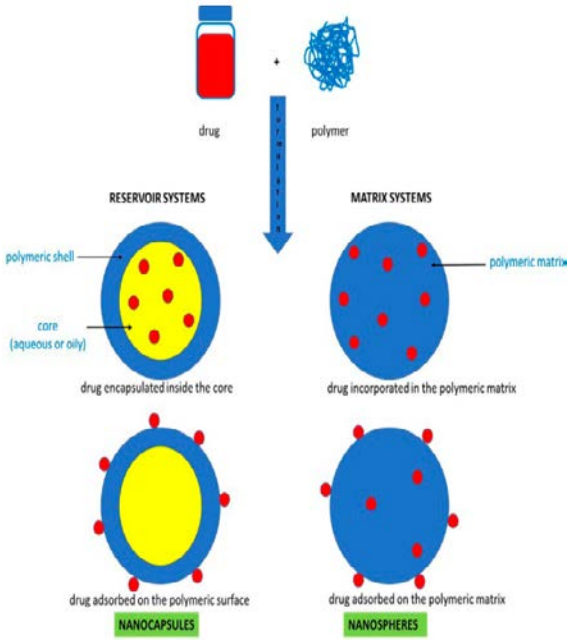

Fig. 14 - Polymeric nanoparticle types based on composition [72]

Drug molecules are adsorbed on a polymeric shell or enclosed in the core of the nanoparticle in nanocapsule systems. The drug is either embedded in the polymeric framework of the nanoparticle or adsorbed on the nanosphere's surface [72]. Both synthetic and natural polymers can serve as the basis for polymer matrices utilized as drug transporters. One can distinguish between natural polymers that come from bacteria, fungi, algae, plants, and animals. Excellent biocompatibility and biodegradability are characteristics shared by all of these matrices. Conversely, polyglycolic acid (PGA), PLA, PLGA [73], PCL [74], and polyvinyl alcohol (PVA) are the most often employed biodegradable synthetic polymers in the creation of nanoparticles.

7. Method of preparation of polymeric nanoparticles (PNPs)

Various techniques have been used to synthesize PNPs, contingent on the physicochemical characteristics of the medication and the application needs. Depending on the specific application, PNPs qualities must be optimized [75]. The kind of polymeric matrix, nanofiller, and desirable qualities for the finished goods are taken into consideration while choosing a process [76].

The process to produce polymeric nanoparticles was illustrated in Fig. 15.

Fig. 15 - Polymeric nanoparticle preparation methods [77]

7.1. Solvent evaporation

Solvent evaporation was the method developed to produce polymeric NPs from a premade polymer [75]. This process first requires the creation of an oil-in-water (O/W) emulsion, which results in the synthesis of nanospheres [78]. The active ingredient (like a medication) is added by dissolution or dispersion after the polymer has been dissolved in a polar organic solvent. Although they were used more often in the past, dichloromethane (DCM) and chloroform ($CHCL_3$) have been used extensively. The entire procedure is depicted in Fig. 16 [79]. Because of their toxicity, ethyl acetate has taken their place. Because of its better toxicological profile, it is more suitable for use in biomedical applications. Additionally, it has long been standard procedure to create an aqueous phase with a surfactant, like polyvinyl acetate (PVA) [80]. Following its emulsification in the aqueous phase with a surfactant, the organic solution is processed using high-speed homogenization or ultrasonication to create a dispersion of nanodroplets [75] To create a suspension of NPs, the polymer solvent diffuses and evaporates throughout the emulsion's continuous phase. After the solvent has evaporated, the solidified nanoparticles can be collected, cleaned by centrifugation, and then freeze-dried for long-term storage. This method enables the production of nanospheres [81].

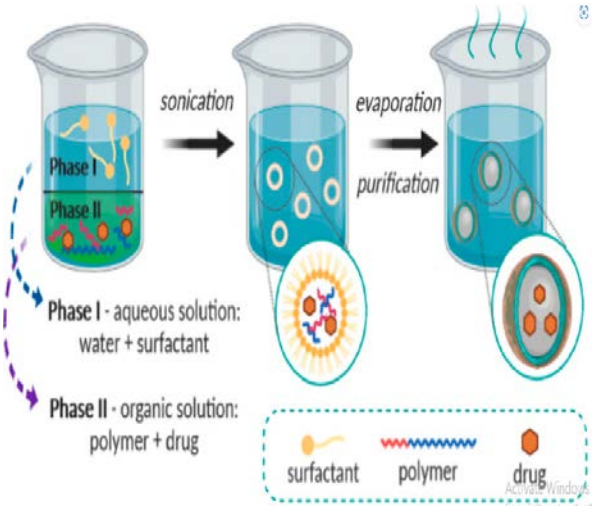

Fig. 16 - Schematic demonstration of the solvent evaporation technique [82].
Copyright 2020. Adapted from MDPI

7.2. Emulsification/solvent diffusion

This procedure creates an O/W emulsion by mixing an aqueous solution with a surfactant and a solvent that is somewhat water-soluble and contains a polymer and medication [83]. This emulsion's internal part is composed of a somewhat hydrophilic organic solvent, such as benzyl alcohol or ethyl acetate, which has been saturated with water beforehand to guarantee that the two phases initially thermodynamically balance at room temperature [84]. When the dispersed droplets are subsequently diluted with a sizable amount of water, the resulting solvent diffuses from the droplets into the outside phase, producing colloidal particles. This process is often used to create nanospheres; however, adding a tiny quantity of oil (such as triglycerides C6, C8, C10, and C12) to the organic phase can also result in nanocapsules. Lastly, this step can be removed by evaporation or filtration, depending on the organic solvent's boiling point [75]. Fig. 17 provides a schematic illustration of this technique. In the end, NPs with sizes ranging from 80 to 900 nm can be produced. This method is frequently used to create PNPs, even though it requires a significant amount of the aqueous phase, which must be extracted from the suspended distribution, and there is a chance that the hydrophilic drug will diffuse into the aqueous phase [85].

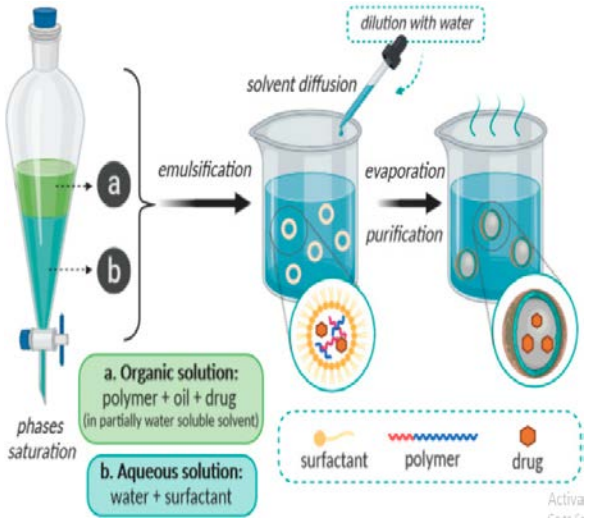

Fig. 17 - Schematic illustration of the emulsification/solvent diffusion technique [82]. Copyright 2020. Adapted from MDPI

7.3. Emulsification/reverse salting-out

This technique can be changed to incorporate the previously described emulsification/solvent diffusion method. The salting-out method, which divides a hydromiscible solvent from an aqueous solution, is based on the salting-out effect, which can result in the formation of nanospheres [86]. The main difference is that the aqueous phase consists of a gel, a colloidal stabilizer, and a salting-out agent, whereas the o/w emulsion is composed of a water-dispersed polymer solvent such as acetone or ethanol [87]. Appropriate salting-out agents include electrolytes such as magnesium chloride ($MgCl_2$), calcium chloride ($CaCl_2$), or magnesium acetate [$Mg(CH_3COO)_2$], as well as non-electrolytes like sucrose. Acetone and water become less miscible when the aqueous phase reaches saturation, enabling the other miscible phases to form an o/w emulsion [75]. The O/W emulsion is created while being vigorously stirred at room temperature. The emulsion is then diluted with an appropriate volume of deionized water or an aqueous solution to aid in the diffusion of the organic solvent to the exterior phase, the precipitation of the polymer, and eventually the formation of nanospheres. The salting-out agent and remaining solvent are eliminated by cross-flow filtering. Complete miscibility between the organic solvent and water facilitates the execution process, though it is not required [[86], [88]]. Fig. 18 shows a schematic representation of this approach. The size of the nanospheres created using this method ranges from 170 to 900 nm. The average size can be adjusted to values between 200 and 500 nm by varying the volume of the external phase and the concentration of polymers in the internal phase [89].

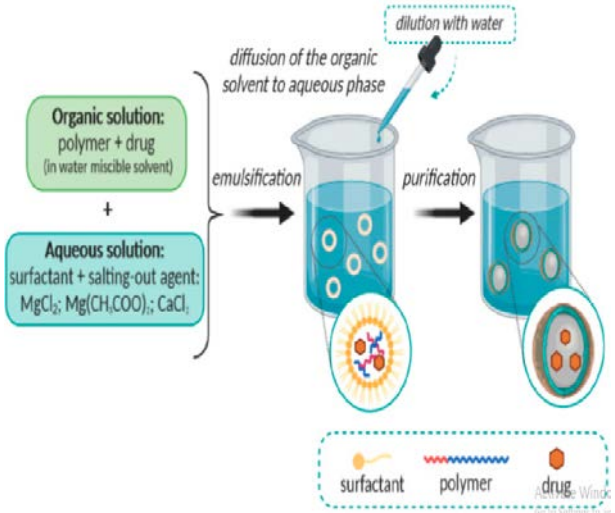

Fig. 18 - Schematic illustration of the emulsification/reverse salting-out technique [82]. Copyright 2020. Adapted from MDPI

7.4. Nanoprecipitation

This method, also called the solvent displacement method, requires two miscible solvents (Fig. 19). The internal phase consists of a polymer dissolved in a miscible organic solvent, such as acetone or acetonitrile [90]. Because they are immiscible in water, they are readily removed by evaporation. Essentially, this process involves the displacement of an organic solvent from a hydrophilic solution to the aqueous phase, followed by the interfacial deposition of a polymer. Following the polymer's dissolution in a water-miscible, intermediately polar solvent, the solution is progressively added to an aqueous solution while being stirred (dropwise) or at a controlled rate. The rapid spontaneous migration of the polymer solution into the aqueous phase causes the nanoparticles to form instantly in an attempt to avoid the water molecules [91]. As the solvent diffuses out of the nanodroplets, the polymer precipitates as nanospheres or nanocapsules. The process can be reversed without influencing the formation of nanoparticles, even though the organic phase is frequently added to the aqueous phase [92]. Surfactants can usually be added to the process to maintain the stability of the colloidal suspension, but their presence is not required to guarantee the formation of nanoparticles. The resultant nanoparticles have a well-defined size and a limited size dispersion, making them frequently superior to those produced by the emulsification

solvent evaporation process. The process of nanoprecipitation is widely employed to create polymeric nanoparticles (PNPs) with a diameter of around 170 nm [93]. However, it also enables the production of nanospheres or nanocapsules [75]. Nanospheres are created when the active ingredient dissolves or spreads throughout the polymeric solution. The drug is first dissolved in an oil and then emulsified in an organic polymeric solution to form nanocapsules, which are then dispersed in the external phase of the emulsion [94].

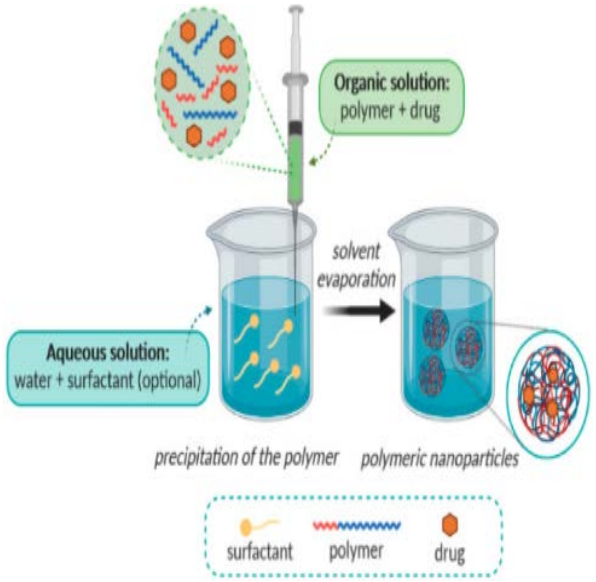

Fig. 19 - Schematic representation of the nanoprecipitation technique [82]. Copyright 2020. Adapted from MDPI

8. Polymer nanocomposite as carriers for active ingredients

The use of polymer-based nanocomposites as drug carriers has been extensively investigated because of their special mechanical and electrical features. Due to their ability to deliver therapeutic agents at the site of action in large and controlled doses, polymer nanocomposites are also being considered as possible drug delivery applicants. There are numerous bioapplications for the polymer-based polymer composites (Fig. 20). These polymer-based nanocomposites are designed with features that create new opportunities for creating advanced biomaterials for a range of biomedical applications, including cancer treatment, wound dressing, drug delivery, and tissue engineering, to meet various functional requirements.

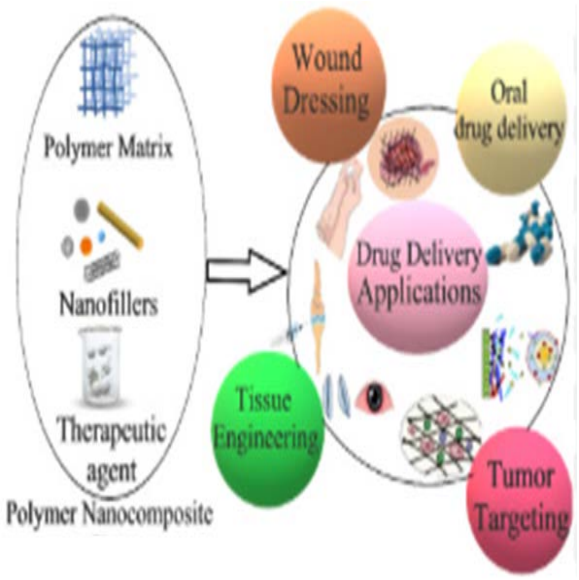

Fig. 20 - Application of polymer nanocomposites as carriers for active ingredients [95]. Copyright 2024. Reproduced with permission from Elsevier

8.1. Polymer nanocomposite-based metal nanoparticles

Pure metal precursors make up metal nanoparticles. Metal nanoparticles (MNPs) are gaining popularity because of their renowned LSPR (localized surface plasmon resonance) properties as well as other intriguing features related to their nanosizes, including optoelectrical, conducting, catalytic, mechanical, sensing, and superparamagnetic properties. Despite these advantageous characteristics, NPs' high toxicity rate, strong reactivity from surface charges, and innate propensity for aggregation are restricting their use in the biomedical industry. In the field of nanomedicine, inorganic nanoparticles such as gold (Au NPs), copper (Cu NPs), silver (Ag NPs), magnetic, silica, and quantum dots are frequently used.

As an antimetabolite, 5-fluorouracil (5-FU, 5-fluoro-2,4-pyrimidinedione) is a pyrimidine A pyrimidine equivalent. When used alone or in combination with other anticancer medications, It has a broad range of effects on solid tumors of the head, neck, brain, breast, ovary, pancreas, and gastrointestinal tract [96]. The main drawbacks of 5-FU use include its extremely low bioavailability, short plasma half-life, and non-specificity, which can result in systemic toxicity. As a result, large dosages are used, which causes adverse effects. Furthermore, the clinical uses of 5-FU have been significantly restricted due to tumor cell resistance development [97]. For instance, silver nanoparticles (AgNPs) are frequently used in biomedical

composites to improve anticancer activity, antibacterial efficacy, and drug encapsulation surface area [98]. N, N, N-trimethyl chitosan chloride (TMC) and carboxymethyl kappa-carrageenan (CMKC)/AgNPs were synthesized for use with different nanocomposites via polyelectrolyte complex PEC, according to Hanna *et al*. [99]. The results indicated that the produced nanocomposite, which was used as a natural carrier for 5-FU anticancer medicines, showed a prolonged and delayed release, hitting 96.3 ± 0.81% for 24 hours at pH 7.4 medium (TMC/CMKC/Ag 3%). The results demonstrated strong antibacterial and biodegradable qualities against several bacterial strains. AgNPs based on green biosynthesis also lessen harmful substances. All things considered, SNC, 3%, can be recommended as a successful solution for both regulated medication administration and antibacterial activity.

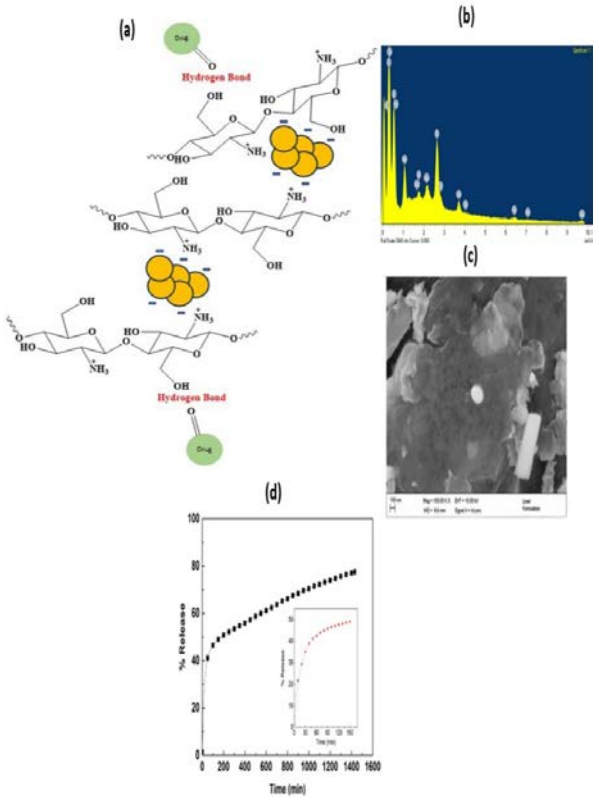

Fig. 21 - (a) Interaction between drug and CS-AuNPs, (b) EDX spectrum of CS-AuNPs nanoparticles, (c) SEM image, and (d) Release profiles of the drug from drug loaded-CS-AuNPs at pH 7.4 [100]. Copyright 2024. Adapted from Materials Research

Since AChE degrades ACh in the nucleus basalis and related regions, donepezil (Donz), a centrally acting, reversible, and noncompetitive acetylcholinesterase (AChE) inhibitor, raises the amount of ACh in the brain and improves cholinergic neurotransmission. Donz is used to treat mild to moderate Alzheimer's disease symptoms in patients [100].

Donz-loaded chitosan/gold nanocomposite (Donz-CS/AuNPs) was made by Saleh Al-Sarayra *et al.* [100] using a co-precipitation method.The produced nanocomposite is used for Alzheimer's disease. Donz and CS/AuNPs' anticipated interaction (Fig. 21a). Strong Au signals (1.5–2, 2–2.5, and 9.5–10 keV) were detected in the EDX data, confirming the particular gold peaks from the Donz-CS/AuNPs that were displayed in Fig. 21b. The AuNPs' spherical forms were visible in the SEM images (Fig. 21c). The results revealed Donz's regulated release profile (Fig. 21d).

8.2. Polymer nanocomposite-based metal oxide

Titanium dioxide (TiO_2) nanoparticles are especially beneficial due to their great chemical stability, low toxicity, high biocompatibility, and anticancer photocatalytic effectiveness [101]. The model drug norfloxacin (NFX) is a member of the fluoroquinolone class of antibiotics. In direct sunshine, it breaks down to produce ethylene and formyl piperazine, and it remains thermally stable up to 200 °C. An NFX overdose can also cause seizures, fever, nausea, breathing difficulties, tendon swelling, etc. [102]. Therefore, to keep the concentration of these medications within the therapeutic window for an extended amount of time, a sustained-release formulation is required. By lowering the frequency of dosages, the sustained-release approach also increases the drug's and the receiver's bioavailability.

For instance, a PLA/TiO_2 (spheres (S), rods (R)) nanocomposite loaded with NFX was made by solution casting and ultrasonication, Salahuddin *et al.* [103]. The produced nanocomposites showed antibacterial and anticancer characteristics. With a modest cellular damage efficiency on regular cell lines, the results validate the formation of the generated nanocomposites, which exhibit the intended antibacterial activity for the treatment of bacterial infections and are a suitable carrier and a good replacement for tumor cell lines. With minor cytotoxicity on normal cell lines, the results validate the production of the nanocomposites, which exhibit the required antibacterial activity for the treatment of bacterial infections and are a suitable carrier and good alternative for tumor cell lines.

8.3. Polymer nanocomposite/carbon-based materials

One famous anticancer drug is gefitinib, which is used to treat non-small cell lung cancer. Its low bioavailability results from its poor solubility in

aqueous solutions with a pH greater than 7. Gefitinib's limited water solubility necessitates a large dose during therapeutic use, which could result in more harmful reactions and side effects [104].

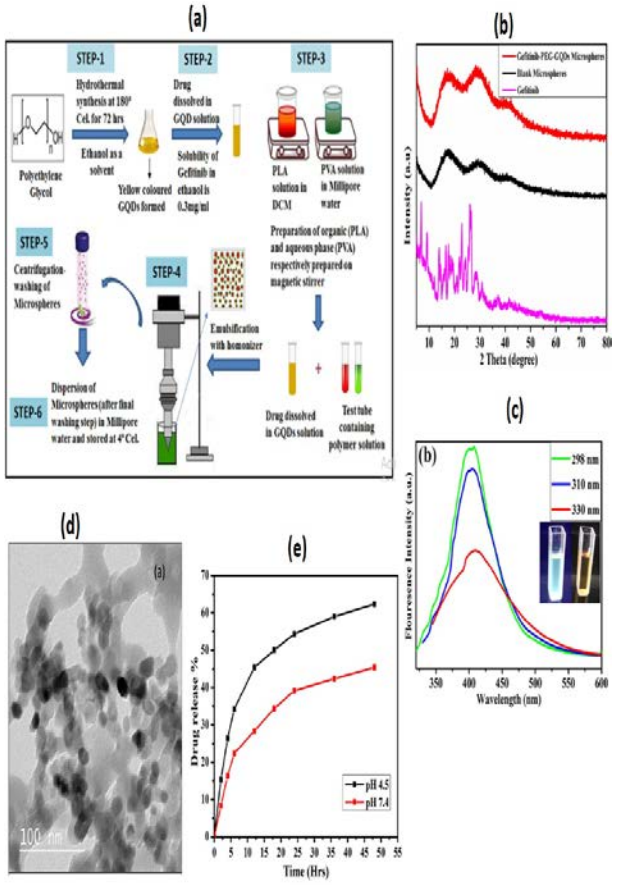

Fig. 22 - (a) Schematic view of the illustration of the creation of anticancer drug-loaded microspheres, (b) spectra of PEG-GQDs at the various excitation wavelengths, (c) X-ray diffraction patterns of drug, PLA/PVA microspheres, and drug-loaded GQD-embedded microspheres, and (d) HRTEM images of GQDs, and (e) Release profile for Gefitinib-loaded microspheres at different pH [105]. Copyright 2022. Adapted from Heliyon

Gautam and Pal [105] mentioned the preparation of gefitinib-loaded PEG-GQDs nanocomposites via the solvent evaporation technique and single emulsification technique using poly(vinyl acetate) (PVA) as a surfactant (Fig. 22a). The prepared nanocomposite was investigated by XRD and FE-FTIR. According to XRD, the obtained nanocomposite does not display any detectable peaks regarding gefitinib (Fig. 22b). The generated nanocomposite exhibits outstanding dispersibility in solvent and fluorescence that falls within the range of blue spectra in the VIBGYOR spectra (Fig. 22c). HRTEM shows that the graphene quantum dots have a constant diameter of 4–26 nm and are nearly evenly distributed. (Fig. 22d). The result showed that controlled release occurred at pH 7.4. (Fig. 22e). Additionally, this drug delivery method can be more effective than oral drug delivery and is appropriate for direct drug delivery to the lung cancer active site.

A nanomaterial made of sp2-bonded carbon atoms arranged in a flat honeycomb structure lattice is called two-dimensional (2D) graphene [106]. Graphene's exceptional biofunctionality and biocompatibility, together with its electrical conductivity, mechanical strength, thermal stability, and structural qualities, have garnered a lot of attention [107]. The most commonly used medication for treating breast cancer is doxorubicin (DOX). It belongs to the anthracycline group of organic compounds. Interaction with the DNA chain and replication inhibition is the foundations of the anti-cancer effect [108]. Ghamkhari *et al.* [109] mentioned the preparation of doxorubicin-loaded graphene oxide/poly(2-hydroxyethylmethacrylate)-g-poly(lacticde)-b-polyethyleneglycol-b-poly(2-hydroxyethyl methacrylate)-g-poly(lactide) nanocomposite was manufactured via reversible addition fragmentation chain (RAFT) and ring open polymerization (ROP). The outcomes demonstrated that the nanocomposite's anticancer medication efficacy was noticeably higher than that of free DOX. This nanoformulation may be studied as a potential delivery system to enable the oral administration of DOX to cancer patients due to its effective solubilization and controlled release properties.

8.4. Polymers nanocomposite-based clay

Clay is a layer of silicates made up of negatively charged silicate layered in layers. Polymer-nanoclay composites exhibit notable enhancements in mechanical and barrier properties when compared to polymers that use silica nanoparticles. Although nanoclay doesn't have antibacterial properties, it can become antimicrobial through chemical modification. Alkylphosphonium ions (Cloisite 30B) have been added to naturally existing montmorillonite clay (Cloisite Na^+) to provide it with antibacterial qualities [67]. The creation of antibacterial materials also makes use of these nanocomposites. Recently, certain morphologies, characteristics, and structures of polymer/clay nanocomposites have drawn attention. The interaction between the polymer and the clay is crucial in regulating mechanical behavior.

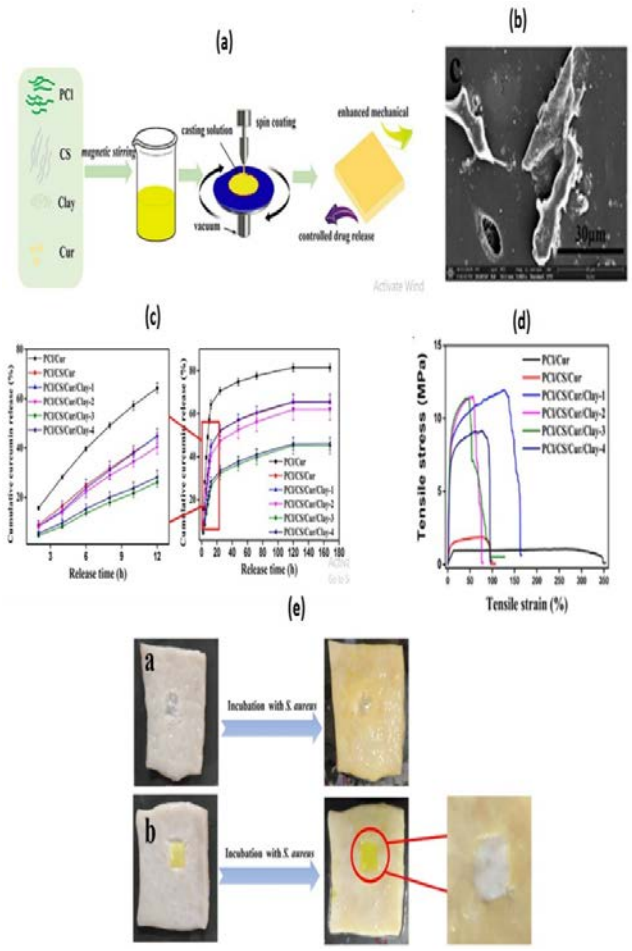

Fig. 23 - (a) Preparation of curloading with/without clay-enhanced flat membrane, (b) SEM image of PCl/CS/Cur/Clay-1, (c) The resulting membranes' in vitro release profiles within 12 and 168 hours of Cur, (d) tensile stress−strain curves of the Cur-loading membranes, and (e) Images of S. aureus infection for pig skin with an open wound and pig skin with a PCl/CS/Clay-3 film covering the wound [111].

Curcumin, often known as Cur, is a polyphenolic active substance obtained from plants that has broad-spectrum antibacterial qualities. It is used for antimicrobial treatment. Its structural characteristics and generation of antioxidant compounds prevent bacteria from growing. By means of the bacterial quorum regulator, it inhibits the adherence of bacteria to host receptors. When exposed to blue light, curcumin functions as a light sensitizer, causing phototoxicity and preventing bacterial growth [110]. For example, Huang *et al.* [111] mentioned the preparation of clay-reinforced polycaprolactone/chitosan/Cur (PCl/CS/Clay/Cur) nanocomposite film via the method of spin coating as shown in Fig. 23a. According to the SEM image (Fig. 23b), porous sponge-like morphology with disconnected structures was obtained. Good clay dispersion in the composite films was demonstrated by the physical and chemical characteristics. Compared to membranes without clay, the resulting nanocomposite film showed superior controlled-release profiles of Cur (Fig. 23c). It was discovered that adding nanoclay greatly increased the tensile strength (Fig. 23d). Additionally, the obtained film effectively prevented bacterial infection of the wound (Fig. 23e). The composite films' good biocompatibility was validated by cytotoxicity analysis. The obtained nanocomposite film would be promising candidates for wound dressing.

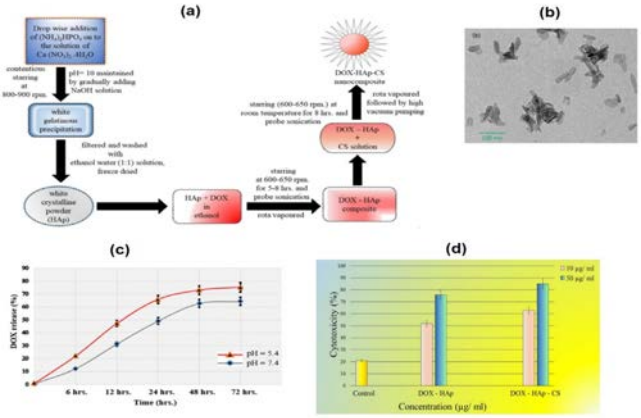

Fig. 24 - (a) Preparation of HAp and DOX-HAp-CS nanocomposite, (b) TEM images of DOX-HAp-CS nanocomposite, (c) In vitro DOX release patterns from the obtained nanocomposite under different pH, and (d) Cytotoxicity activity of drug loaded-HAp and drug loaded-HAp-CS [113]. Copyright 2019. Reproduced with permission from Springer.

Bone is a hard, mineralized tissue made up of strong, intricate hierarchical structures. The inorganic mineral nanohydroxyapatite (HAp) crystals, which are occasionally found in the osteoid matrix, make up human bone tissue. The hardness and stiffness of bone tissue are attributed to HAp. The calcium and phosphate combination HAp [$Ca_{10}(PO_4)_6(OH)_2$] has a molar ratio of Ca/P of approximately 1.67 [112]. According to Ghosh *et al.* [113], the preparation of DOX-loaded hydroxyapatite (HAp)-chitosan (CS) nanocomposite via the in situ precipitation method (Fig. 24a) was mentioned. It is used as an anticancer agent for osteosarcoma inhibition. Reducing the outermost energy of HAp particles and then regulating their size resulted in less agglomeration between the particles in the resulting nanocomposite, according TEM (Fig. 24b). The resultant nanocomposite offers outstanding mechanical properties with controlled drug release (Fig. 24c). The produced nanocomposite produces no significant cytotoxicity

towards cultured osteosarcoma cells (Fig. 24d). The obtained nanocomposite could be a promising drug carrier for cancer therapy.

8.5. Polymer nanocomposite-based nanofibers

For a variety of wound healing applications, tetracycline hydrochloride (TCH), a hydrophilic antibiotic, is used to prevent and treat bacterial infections that occur in burns, cuts, and surgeries [114].

For intense drug release, tetracycline hydrochloride (TC)-loaded polycaprolactone (PCL) nanofibers were prepared by electrospinning for regulated drug administration, according to Karuppuswamy *et al.* [115]. According to the observed results, TC loading for the controlled release caused the PCL to gradually change from a hydrophobic to a hydrophilic condition (TC, 5%). Drug-loaded membranes demonstrated the maximum tensile strength (3.9 MPa) at 2% drug membrane and the highest resistance to deformation. As the drug concentration rose, so did the fibrous scaffolds' porosity. According to in vitro release trials, the drug's burst release occurred within the first hour at the lowest and was followed by 8-day continuous controlled release. The resulting nanofibers may hold promise for use in biomedicine and healthcare applications, including medication delivery.

In another study, the creation of DOX-loaded PLGA/Atapulgite (ATT) nanocomposite using electrospinning was described by Wang *et al.* [116]. The obtained nanocomposite nanofibers exhibit better mechanical durability and a homogeneous, smooth morphology. The payload was continuously released from the generated nanofibers under both neutral and acidic pH settings. Furthermore, the released DOX from the nanofibers may considerably slow the proliferation of malignant cells. Because ATT/DOX-doped PLGA nanofibers can greatly enhance the mechanical properties of electrospun PLGA nanofibers and have a much lower burst release profile, they may be employed as a functional material for tissue engineering scaffolds for more effective local tumor treatment applications. To demonstrate the anticancer efficacy of these composite nanofibers, more in vivo studies had to be conducted.

PCL/gelatin nanofibers embedded with Dox-loaded mesoporous silica nanoparticles/silver nanoparticles were prepared by blow spinning, according to Tavira *et al.* [117]. The obtained nanocomposite exhibited a slow-release profile of AgNPs and DOX together with high encapsulation effectiveness. Furthermore, in addition

n to blocking AgNP infection, the obtained nanocomposite has the potential to efficiently eliminate melanoma cancer cells. The ability of normal cells to adhere to the scaffold made of fibrous mats loaded with nanoparticles demonstrated the potential for repairing melanoma cancer wounds.

For instance, TCH-loaded PLA/polyvinylpyrrolidone (PVP)/TCH-MWCNTs composite fibrous mats were prepared by electrospinning (Fig. 25a) according to Emre Bulbul *et al.* [118] SEM shows a smooth morphology free of bead defects (Fig. 25b). AFM reported that the surfaces of all the electrospun fibrous mats were smooth (Fig. 25c). Additionally, MWCNT-loaded electrospun mats showed a much more controlled drug release manner, reduced the burst release of TCH, and significantly increased the drug encapsulation efficiency (EE%) (Fig. 25d). According to in vitro cytotoxicity tests, the generated nanocomposite mats did not cause any harm to human umbilical vein endothelial cells (HUVECs). The resulting composite nanofiber mats may find use in biomedical applications as therapeutic materials or drug delivery systems.

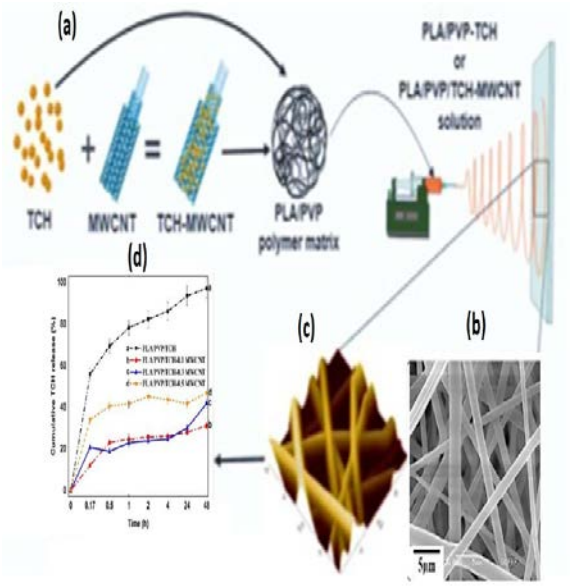

Fig. 25 - (a) Electrospinning method, (b) SEM image of the prepared nanofiber at 0.3 MWCNT, (C) 3D AFM images of the electrospun nanofiber at 0.3 MWCNT, and (d) Cumulative release profile of Drug the electrospun fibrous mats PLA/PVP/TCH, PLA/PVP/TCH-MWCNT at different concentration of MWCNT [118]. Copyright 2019. Reproduced with permission from Elsevier.

Table 2 - Method of preparation of various polymeric nanocomposites as carrier of various active ingredients for controlled drug release

Polymeric nanocomposite	Active ingredients	Method of preparation	Resultes	References
TMC/carboxymethyl kappa-carrageenan (CMKC)/ AgNPs nanocomposite	5-Flourouracil (5-FU)	Polyelectrolyte complex (PEC)	- Controlled drug delivery. - Exhibited good biodegradability and antimicrobial properties against different bacterial strains. -Acts as an effective carrier for anticancer drug at 3% Ag.	[99]
Chitosan/gold (CS/AuNPs) nanocomposite	Donepezil (Donz)	Co-precipitation technique	- Exhibited controlled release profile of Donz. -The produced nanocomposite was used for Alzheimer's Disease Therapy.	[100]
PLA/ Titanium dioxide nanocomposite	Norfloxacin (NFX)	Ultrasonic/ solution casting method	- Exhibited antibacterial and antitumor Activities. - Showed moderate cytotoxicity efficacy on normal cell lines and the formulation, making it a good substitute and appropriate carrier for tumor cell lines.	[103]
PEG-GQDs nanocomposite	Gefitinib	Solvent evaporation /single emulsification method	- Act as an effective carrier for anticancer drug. - Exhibited controlled release at PH 7.4. – Exhibited a suitable approach for direct drug delivery to the lung cancer's active site, which may be more effective than oral drug delivery.	[105]
GO/poly(2-hydroxyethyl methacrylate)-g-poly(lacticde)-b-polyethyleneglycol-b-poly(2-hydroxyethyl methacrylate)-g-poly(lactide)	Doxorubicin (DOX)	Reversible addition fragmentation chain (RAFT)/ ring-opening polymerization (ROP)	-Exhibited superior anticancer efficacy when compared to free DOX. - Demonstrated the capacity to effectively solubilize DOX and offer controlled release. -Serves as a potential delivery vehicle so that DOX can be given orally to cancer patients.	[109]
Clay-reinforced polycaprolactone/chitosan (PCl/CS/Clay) nanocomposite film	Curcumin (Cur)	Spin coating method	- Showed porous sponge-like morphology. - Demonstrated superior Cur controlled-release profiles compared to membranes devoid of clay - Protected the wound from bacterial infection. -The tensile strength was found to be considerably increased by the addition of nanoclay. - Proved good biocompatibility. -It would be promising candidate films might be promising candidate for wound dressing.	[110]

Hydroxyapatite (HAp)-chitosan (CS) nanocomposite	Doxorubicin (DOX)	In situ precipitation method	-It is used as an anticancer agent for osteosarcoma inhibition. - Provides outstanding mechanical properties with controlled drug release. -The produced nanocomposite produces no significant cytotoxicity towards cultured osteosarcoma cells. -The obtained nanocomposite could be a promising drug carrier for cancer therapy.	[112]
Polycaprolactone (PCL) nanofibers	Tetracycline hydrochloride (TC)	Electrospinning	- Sustained controlled release of TC. - Exhibited the highest tensile strength of 3.9 MPa at 2% drug membrane. - The obtained nanofibers could be promising for drug delivery applications in biomedicine and healthcare.	[115]
Poly(lactic-co-glycolic acid)/ Attapulgite (ATT) nanocomposite nanofibers	Doxorubicin (DOX)	Electrospinning	-Exhibited a smooth and uniform morphology. -Exhibited sustained controlled release of ATT/DOX-doped PLGA nanofibers. - The released DOX from the nanofibers may considerably slow the growth of tumor cells. -Reduced burst release profile of ATT/DOX-doped PLGA nanofibers. -Improved the mechanical properties. - It serves as a useful component for tissue engineering scaffolds, which improves the application of local tumor therapy. -Exhibited antitumor efficacy of produced nanofibers.	[116]
PCL/gelatin nanofibers embedded	Doxorubicin (DOX)	Blow spinning	-Exhibited good encapsulation efficiency with a slow-release profile of DOX and AgNPs. -Preventing infection by AgNPs. -The obtained nanocomposite could effectively destroy melanoma cancer cells. - It is used to heal wounds caused by melanoma cancer.	[117]
Poly (lactic acid) (PLA) /polyvinylpyrrolidone (PVP)/ MWCNTs composite fibrous mats	Hydrochloride (TCH*)*	Electrospinning	-Smooth morphology and smooth surfaces. -Displayed a significantly more regulated drug release mechanism. -Demonstrated a significant improvement in drug encapsulation efficiency. Decreased TCH burst release. -Showed no harmful effects on the endothelial cells of the human umbilical vein (HUVECs). -It serves as a therapeutic material for drug delivery systems in biomedical applications.	[118]

According to Mosallanezhad *et al.* [119], PCL/chitosan-loaded zinc oxide nanoparticles and curcumin (Cur) were prepared by electrospinning. SEM examination revealed bead-free, silky nanofibers. The elemental analysis also demonstrated that ZnO was distributed well among the scaffolds. The addition of ZnO greatly enhanced the mechanical properties, and the sample with 3 weight percent Cur had the maximum water uptake value. After a quick release, the Cur medication stabilized in around twenty-four hours. When applied to experimental data, the Peppas model yielded the best results. Effective inhibition of bacterial growth was demonstrated by the resulting nanocomposite. Additionally, research conducted in vitro showed that a high Cur content reduces cell attachment and survival. Table 2 provides an overview of the many alterations that can be used to challenge the characteristics of various drug-loaded polymeric nanocomposites as carriers for controlled drug release.

9. Conclusion

Polymeric nanocomposites have emerged as a transformative class of multifunctional drug delivery platforms by integrating the favorable biocompatibility, biodegradability, and structural versatility of polymeric matrices with the unique physicochemical properties of nanoscale fillers. Recent advances in nanomaterial engineering, surface functionalization, and fabrication technologies have enabled the development of carriers with enhanced drug-loading capacity, programmable release kinetics, improved targeting efficiency, and superior therapeutic performance. The convergence of natural and synthetic polymers with metallic nanoparticles, metal oxides, carbon-based nanomaterials, nanoclays, mesoporous nanostructures, and electrospun nanofibers has expanded the scope of applications in cancer therapy, antimicrobial treatment, wound healing, regenerative medicine, neurological disorders, and other precision therapeutic strategies. Collectively, these developments demonstrate the significant potential of polymeric nanocomposites to overcome many limitations associated with conventional drug delivery systems.

Despite these remarkable advances, several scientific and translational challenges continue to hinder widespread clinical implementation. Achieving reproducible large-scale manufacturing while maintaining consistent nanoparticle dispersion, structural homogeneity, and batch-to-batch reproducibility remains a major obstacle. Long-term biosafety, biodegradation behavior, immunogenicity, nanoparticle accumulation, and chronic toxicity require comprehensive in vivo evaluation using standardized experimental protocols. In addition, the complexity of nano–bio interactions, limited understanding of pharmacokinetic and pharmacodynamic behavior, insufficient long-term clinical evidence, and the absence of internationally harmonized regulatory guidelines continue to delay regulatory approval and commercialization. Economic considerations, manufacturing costs, process scalability, sterilization compatibility, storage stability, and quality assurance further complicate industrial translation. Addressing these multidisciplinary challenges will require close collaboration among materials scientists, pharmaceutical researchers, biomedical engineers, clinicians, toxicologists, regulatory agencies, and industrial partners.

Future research should focus on the rational design of intelligent, multifunctional polymeric nanocomposites capable of simultaneously integrating targeted delivery, controlled drug release, real-time therapeutic monitoring, and diagnostic imaging within a single platform. Greater emphasis should be placed on stimuli-responsive systems that respond to physiological and pathological triggers, including pH, temperature, enzymatic activity, redox potential, magnetic fields, ultrasound, and light, thereby enabling highly localized and personalized therapy. Furthermore, environmentally sustainable manufacturing based on green chemistry principles, renewable biopolymers, solvent-free processing, and energy-efficient production should become a central objective for future research to minimize environmental impact while improving industrial feasibility.

Looking ahead, the convergence of advanced polymer science, nanotechnology, computational intelligence, additive manufacturing, and precision medicine is expected to redefine the next generation of drug delivery systems. Continued interdisciplinary innovation, combined with rigorous biological validation, standardized characterization methods, and well-designed clinical studies, will be essential for translating laboratory-scale discoveries into clinically approved therapeutic products. Ultimately, polymeric nanocomposites are poised to play a pivotal role in the development of safer, smarter, and more effective therapeutic platforms that support personalized healthcare and improve patient outcomes across a broad spectrum of diseases.

Cite this article as: Moshera Samy. Recent Advances in Polymeric Nanocomposite Carriers of Various Active Ingredients for Controlled and Sustained Drug Release: A Review. Kompleksnoe Ispolzovanie Mineralnogo Syra = Complex Use of Mineral Resources. 2028; 346(3):72-98. https://doi.org/10.31643/2028/6445.30

Бақыланатын және ұзақ мерзімді дәрілік заттардың шығарылуына арналған әртүрлі белсенді ингредиенттердің полимерлі нанокомпозиттік тасымалдаушыларындағы соңғы жетістіктер: шолу

Moshera Samy

Химиялық өнеркәсіптерді зерттеу институты, Ұлттық зерттеу орталығы, Египет

Мақала келді: *8 шілде 2026*
Сараптамадан өтті: *17 шілде 2026*
Қабылданды: *14 тамыз 2026*

ТҮЙІНДЕМЕ

Дәрі-дәрмектерді бақылаумен және ұзақ уақыт бойы жеткізу дәстүрлі фармацевтикалық препараттардың шектеулерін, соның ішінде биожетімділігінің төмендігі, дәрі-дәрмектерді тез жою, жүйелік уыттылық және спецификалық емес таралуды жеңудің трансформациялық стратегиясына айналды. Зерттелген көптеген жеткізу платформаларының ішінде полимер нанокомпозиттік тасымалдаушылар айтарлықтай назар аударды, себебі олар полимерлердің тамаша биоүйлесімділігін, биоыдырағыштығын және өңдеуге қабілеттілігін бейорганикалық наноматериалдардың бірегей физика-химиялық, механикалық, оптикалық, магниттік және терапиялық қасиеттерімен біріктіреді. Бұл шолу полимер нанокомпозиттеріне негізделген дәрілік заттарды жеткізу жүйелеріндегі соңғы жетістіктерді кешенді және сыни бағалауды ұсынады, табиғи және синтетикалық полимерлер мен металл және металл оксиді нанобөлшектері, көміртегі бар наноматериалдар, наноклейлер, мезокеуекті материалдар және электроспинделген нанобөлшектер сияқты кең ауқымды нанобөлшектер арасындағы синергетикалық өзара әрекеттесуге баса назар аударады. Нанокомпозиттік құрамның, өндіріс стратегияларының және физика-химиялық сипаттамаларының дәрілік заттардың жүктелуіне, капсулалау тиімділігіне, босату кинетикасына, нысанаға алу мүмкіндігіне және биологиялық өнімділікке әсері жүйелі түрде талқыланады. Сонымен қатар, қатерлі ісік терапиясындағы, жараларды емдеудегі, микробқа қарсы емдеудегі, ұлпалық инженериясындағы, неврологиялық бұзылуларда және регенеративті медицинадағы типтік терапиялық қолданыстар құрылым, қасиеттер мен сипаттамалар арасындағы байланысты анықтау үшін сындарлы түрде салыстырылады. Бұл шолу негізінен жеке тасымалдаушы жүйелерді, дайындау әдістерін, босату механизмдерін және биомедициналық қолданыстарды бір жүйеде қорытындылайды, сонымен қатар нанобөлшектердің агрегациясына, ұзақ мерзімді биоүйлесімділікке, биоыдырауға, ірі көлемді өндіріске, , реттеуші органдардың бекітуіне және клиникалық енгізуге қатысты қолданыстағы шектеулерді анықтайды. Бұл шолу терапиялық тиімділігі, қауіпсіздігі және жеделдетілген клиникалық қолданылуы бар озық полимерлі нанокомпозиттерді рационалды жобалаумен айналысатын зерттеушілер үшін құнды ақпарат береді.

Түйін сөздер: бақыланатын дәрілік заттарды жеткізу, полимерлі нанокомпозиттер, полимер нанокомпозиттері, дәлме-дәл наномедицина, ақылды нанотасымалдаушылар, тітіркендіргіштерге жауап беретін дәрілік заттарды жеткізу, тұрақты наноөндіріс, терапиялық наноплатформалар.

Moshera Samy

Автор туралы ақпарат:
PhD, доцент, Полимерлер және пигменттер кафедрасы, Ұлттық зерттеу орталығы, 33 Эль Бухут көшесі, Докки, Гиза 12622, Египет. Email: moshera_samy1984@yahoo.com; ORCID ID: https://orcid.org0000-0002-7272-4134

Последние достижения в области полимерных нанокомпозитных носителей различных активных ингредиентов для контролируемого и пролонгированного высвобождения лекарственных средств: обзор

Moshera Samy

Научно-исследовательский институт химической промышленности, Национальный исследовательский центр, Египет

Поступила: *8 июля 2026*
Рецензирование: *17 июля 2026*
Принята в печать: *14 августа 2026*

АННОТАЦИЯ

Контролируемая и пролонгированная доставка лекарственных средств стала преобразующей стратегией для преодоления ограничений традиционных фармацевтических препаратов, включая низкую биодоступность, быстрое выведение лекарственных средств, системную токсичность и неспецифическое распределение. Среди многочисленных исследованных платформ доставки полимерные нанокомпозитные носители привлекли значительное внимание, поскольку они сочетают в себе превосходную биосовместимость, биоразлагаемость и технологичность полимеров с уникальными физико-химическими, механическими, оптическими, магнитными и терапевтическими свойствами неорганических наноматериалов. В данном обзоре представлена всесторонняя и критическая оценка последних достижений в области систем доставки лекарственных средств на основе полимерных нанокомпозитов, с акцентом на синергетическое взаимодействие между природными и синтетическими полимерами и широким спектром нанонаполнителей, включая наночастицы металлов и оксидов металлов, углеродсодержащие наноматериалы, наноглины, мезопористые материалы и электроформованные нановолокна. Систематически обсуждается влияние состава нанокомпозита, стратегий изготовления и физико-химических характеристик на загрузку лекарственного средства, эффективность инкапсуляции, кинетику высвобождения, способность к таргетной доставке и биологические характеристики. Кроме того, критически сравниваются типичные терапевтические применения в лечении рака, заживлении ран, антимикробной терапии, тканевой инженерии, неврологических расстройствах и регенеративной медицине для установления взаимосвязи между структурой, свойствами и характеристиками. Этот обзор в основном обобщает отдельные системы-носители, методы получения, механизмы высвобождения и биомедицинские применения в единой системе, выявляя при этом существующие ограничения, связанные с агрегацией наночастиц, долгосрочной биосовместимостью, биоразложением, крупномасштабным производством, получением разрешений регулирующих органов и клиническим внедрением. Данный обзор предоставляет ценную информацию для исследователей, работающих над рациональным проектированием передовых полимерных нанокомпозитов с повышенной терапевтической эффективностью, улучшенной безопасностью и ускоренным клиническим применением.

Ключевые слова: контролируемая доставка лекарств, полимерные нанокомпозиты, прецизионная наномедицина, интеллектуальные наноносители, доставка лекарств в ответ на внешние воздействия, устойчивое нанопроизводство, терапевтические наноплатформы

Moshera Samy

Информация об авторе:
Доктор философии, доцент, кафедра полимеров и пигментов, Национальный исследовательский центр, ул. Эль-Бухут, 33, Докки, Гиза 12622, Египет. Email: moshera_samy1984@yahoo.com; ORCID ID: https://orcid.org0000-0002-7272-4134

References

[1] Kukhta AV. Organic-inorganic nanocomposites and their applications, Book Organic-inorganic nanocomposites and their applications, Information and Energy Security, Springer. 2015, 207-225. https://doi.org/10.1007/978-94-017-9697-2_22

[2] Wang X, Chang J, and Wu C. Bioactive inorganic/organic nanocomposites for wound healing, Applied Materials Today. 2018; 11:308-319. https://doi.org/10.1016/j.apmt.2018.03.001

[3] Pal D, and Nayak AK. Alginates, blends and microspheres: controlled drug delivery, Encyclopedia of Biomedical Polymers and Polymeric Biomaterials, 11 , CRC Press. 2015,182-192. https://doi.org/10.1081/E-EBPP-120049967

[4] Mallakpour S, and Javadpour M. Sonochemical assisted synthesis and characterization of magnetic PET/Fe3O4, CA, AS nanocomposites: Morphology and physiochemical properties, Ultrasonics sonochemistry. 2018; 40:611-618. http://dx.doi.org/10.1016/j.ultsonch.2017.08.006

[5] Chandrakala V, Aruna V, and Angajala G. Review on metal nanoparticles as nanocarriers: Current challenges and perspectives in drug delivery systems, Emergent Materials. 2022; 5(6):1593-1615. https://doi.org/10.1007/s42247-021-00335-x

[6] Jeon S, Subbiah R, Bonaedy T, Van S, Park K and Yun K. Surface functionalized magnetic nanoparticles shift cell behavior with on/off magnetic fields'. Journal of Cellular Physiology. 2018; 233(2):1168-1178. https://doi.org/10.1002/jcp.25980

[7] Adepu S, and Ramakrishna S. Controlled drug delivery systems: current status and future directions, Molecules. 2021; 26(19):5905. https://doi.org/10.3390/molecules26195905

[8] Nayak AK, and Pal D. Natural starches-blended ionotropically gelled microparticles/beads for sustained drug release, Handbook of composites from renewable materials. 2017, 527-559. https://doi.org/10.1002/9781119441632.ch167

[9] Hasnain MS, Nayak AK, Singh M, Tabish M, Ansari MT, and Ara TJ. Alginate-based bipolymeric-nanobioceramic composite matrices for sustained drug release, International journal of biological macromolecules. 2016; 83:71-77. http://dx.doi.org/10.1016/j.ijbiomac.2015.11.044

[10] Saxena M, Pappu A, Sharma A, Haque R, and Wankhede S. Composite materials from natural resources: recent trends and future potentials: IntechOpen. 2011. http://dx.doi.org/10.5772/18264

[11] Angadi SC, Manjeshwar LS, and Aminabhavi TM, Novel composite blend microbeads of sodium alginate coated with chitosan for controlled release of amoxicillin, International journal of biological macromolecules. 2012; 51(1-2):45-55. http://dx.doi.org/10.1016/j.ijbiomac.2012.04.018

[12] Ullah H, Wahid F, Santos HA, and Khan T. Advances in biomedical and pharmaceutical applications of functional bacterial cellulose-based nanocomposites, Carbohydrate polymers. 2016; 150:330-352. https://doi.org/10.1016/j.carbpol.2016.05.029

[13] Azadani RN, Sabbagh M, Salehi H, Cheshmi A, Raza A, Kumari B, and Erabi G. Sol-gel: Uncomplicated, routine and affordable synthesis procedure for utilization of composites in drug delivery. Journal of Composites and Compounds. 2021; 3(6):57-70. https://doi.org/10.52547/jcc.3.1.6

[14] Di Martino A, Guselnikova OA, Trusova ME, Postnikov PS, and Sedlarik V. Organic-inorganic hybrid nanoparticles controlled delivery system for anticancer drugs. International journal of pharmaceutics. 2017; 526(1-2):380-390. http://dx.doi.org/10.1016/j.ijpharm.2017.04.061

[15] Rane AV, Kanny K, Abitha V, and Thomas S. Methods for synthesis of nanoparticles and fabrication of nanocomposites, Synthesis of inorganic nanomaterials. Elsevier. 2018, 121-139. https://doi.org/10.1016/B978-0-08-101975-7.00005-1

[16] Hoyos-Palacio LM, Castro DPC, Ortiz-Trujillo, IC, Palacio, LEB, Upegui BJG, Mora NJE. Compounds of carbon nanotubes decorated with silver nanoparticles via in-situ by chemical vapor deposition (CVD), Journal of materials research and technology. 2019; 8(6):5893-5898. https://doi.org/10.1016/j.jmrt.2019.09.062

[17] Al Zoubi W, and Ko YG. Self-assembly of hierarchical N-heterocycles-inorganic materials into three-dimensional structure for superior corrosion protection. Chemical Engineering Journal. 2019; 356:850-856. https://doi.org/10.1016/j.cej.2018.09.089

[18] Wang C, Park MJ, Yu H, Matsuyama H, Drioli E, and Shon HK. Recent advances of nanocomposite membranes using layer-by-layer assembly. Journal of Membrane Science. 2022; 661:120926. https://doi.org/10.1016/j.memsci.2022.120926

[19] Yu C, Wang J, Yan J , Xia J, and Zhang X. Langmuir–Blodgett assisted alignment of 2D nanosheets in polymer nanocomposites for high-temperature dielectric energy storage applications. Journal of Materials Chemistry C. 2024; 12(13):4728-4736. https://doi.org/10.1039/d4tc00024b

[20] Vempati S, Ranjith KS, Topuz F, Biyikli N, and Uyar T. Electrospinning combined with atomic layer deposition to generate applied nanomaterials: a review. ACS Applied Nano Materials. 2020; 3(7):6186-6209. https://doi.org/10.1021/acsanm.0c01120

[21] Al Zoubi W, Kamil MP, Fatimah S, Nashrah N, and Ko YG. Recent advances in hybrid organic-inorganic materials with spatial architecture for state-of-the-art applications. Progress in Materials Science. 2020; 112:100663. https://doi.org/10.1016/j.pmatsci.2020.100663

[22] Singh I, and Birajdar B. Synthesis, characterization and photocatalytic activity of mesoporous Na-doped TiO2 nano-powder prepared via a solvent-controlled non-aqueous sol–gel route, RSC advances. 2017; 7(85):54053-54062. https://doi.org/10.1039/c7ra10108b

[23] Pandey PP. Preparation and characterization of polymer nanocomposites, Soft Nanoscience Letters. 2020; 10(01):1-15. https://doi.org/10.4236/snl.2020.101001

[24] Oliveira M, and Machado A. Preparation of polymer-based nanocomposites by different routes', Nanocomposites: synthesis, characterization and applications. 2013, 1-22. https://repositorium.sdum.uminho.pt/bitstream/1822/26120/1/Chapter.pdf

[25] Prete S, Dattilo M, Patitucci F, Pezzi G, Parisi OI, and Puoci F. Natural and synthetic polymeric biomaterials for application in wound management, Journal of Functional Biomaterials. 2023; 14(9):455. https://doi.org/10.3390/jfb14090455

[26] Palo M, Rönkönharju S, Tiirik K, Viidik L, Sandler N, and Kogermann K. Bi-layered polymer carriers with surface modification by electrospinning for potential wound care applications, Pharmaceutics. 2019; 11(12):678. https://doi.org/10.3390/pharmaceutics11120678

[27] Prete S, Dattilo M, Patitucci F, Pezzi G, Parisi OI, and Puoci F. Natural and synthetic polymeric biomaterials for application in wound management. Journal of Functional Biomaterials. 2023; 14(9):455. https://doi.org/10.3390/jfb14090455

[28] Rodríguez-Tobías H, Morales G, and Grande D. Comprehensive review on electrospinning techniques as versatile approaches toward antimicrobial biopolymeric composite fibers. Materials Science and Engineering. 2019; 101:306-322. https://doi.org/10.1016/j.msec.2019.03.099

[29] Ghosal K, Chandra A, Roy S, Agatemor C, Thomas S, and Provaznik I. Electrospinning over solvent casting: tuning of mechanical properties of membranes. Scientific reports. 2018; 8(1):5058. https://doi.org/10.1038/s41598-018-23378-3

[30] Rahaman M, Aldalbahi A, and Bhagabati P. Preparation/processing of polymer–carbon composites by different techniques, Carbon-Containing Polymer Composites. Springer. 2018, 99-124. https://doi.org/10.1007/978-981-13-2688-2_3

[31] Maher S, Mazinani A, Barati MR, and Losic D. Engineered titanium implants for localized drug delivery: recent advances and perspectives of Titania nanotubes arrays, Expert opinion on drug delivery. 2018; 15(10):1021-1037. https://doi.org/10.1080/17425247.2018.1517743

[32] Bedoya DA, Figueroa FN, Macchione MA, and Strumia MC. Stimuli-responsive polymeric systems for smart drug delivery, Advanced Biopolymeric Systems for Drug Delivery. Springer. 2020, 115-134. https://doi.org/10.1007/978-3-030-46923-8_5

[33] Hoogenboom R. Temperature-responsive polymers: properties, synthesis, and applications, Smart polymers and their applications, Elsevier, 2019, 13-44. https://doi.org/10.1016/B978-0-08-102416-4.00002-8

[34] Shah A, Aftab S, Nisar J, Ashiq MN, and Iftikhar FJ. Nanocarriers for targeted drug delivery. Journal of Drug Delivery Science and Technology. 2021; 62:102426. https://doi.org/10.1016/j.jddst.2021.102426

[35] Silindir Gunay M, Yekta Ozer A, and Chalon S. Drug delivery systems for imaging and therapy of Parkinson's disease, Current neuropharmacology. 2016; 14(4):376-391. https://doi.org/10.2174/1570159x14666151230124904

[36] Nikolova M, Slavchov R, and Nikolova G. Nanotechnology in medicine, Drug discovery and evaluation: methods in clinical pharmacology. 2020, 533-546. https://doi.org/10.1007/978-3-319-68864-0_45

[37] Esfanjani AF, Assadpour E, and Jafari SM. Improving the bioavailability of phenolic compounds by loading them within lipid-based nanocarriers, Trends in Food Science & Technology. 2018; 76:56-66. https://doi.org/10.1016/j.tifs.2018.04.002

[38] Davies S, Contri RV, Guterres SS, and Pohlmann AR, Guerreiro ICK. Simultaneous nanoencapsulation of lipoic acid and resveratrol with improved antioxidant properties for the skin, Colloids and Surfaces B: Biointerfaces. 2020; 192:111023. https://doi.org/10.1016/j.colsurfb.2020.111023

[39] Oliveira C, Coelho C, Teixeira JA, Ferreira-Santos P,and Botelho CM. Nanocarriers as active ingredients enhancers in the cosmetic industry—The European and North America regulation challenges. Molecules. 2022; 27(5):1669. https://doi.org/10.3390/molecules27051669

[40] Cojocaru E, Petriș OR, and Cojocaru C. Nanoparticle-Based Drug Delivery Systems in Inhaled Therapy: Improving Respiratory Medicine, Pharmaceuticals. 2024; 17(8):1059. https://doi.org/10.3390/ph17081059

[41] Pandey SP, Shukla T, Dhote VK, Mishra DK, and Maheshwari R, Tekade RK. Use of polymers in controlled release of active agents. Basic fundamentals of drug delivery, Elsevier. 2019, 113-172. https://doi.org/10.1016/B978-0-12-817909-3.00004-2

[42] Rahim M, Mas Haris MRH,and Saqib NU. An overview of polymeric nano-biocomposites as targeted and controlled-release devices, Biophysical reviews. 2020; 12(5):1223-1231. https://doi.org/10.1007/s12551-020-00750-0

[43] Chung H-K, Kim W-H, Park J, Cho J, Jeong T-Y, and Park P-K. Application of Langmuir and Freundlich isotherms to predict adsorbate removal efficiency or required amount of adsorbent. Journal of Industrial and Engineering Chemistry. 2015; 28:241-246. https://doi.org/10.1016/j.jiec.2015.02.021

[44] Kaczmarek B,and Sionkowska A. Drug release from porous matrixes based on natural polymers, Current Pharmaceutical Biotechnology. 2017; 18(9):721-729. https://doi.org/10.2174/1389201018666171103141347

[45] Saikia C, Gogoi P, and Maji T. Chitosan: A promising biopolymer in drug delivery applications. J Mol Genet Med S. 2015; 4(006):899-910. https://doi.org/10.4172/1747-0862.S4-006

[46] Raizada A, Bandari A, and Kumar B. Polymers in drug delivery: a review, Int J Pharm Res Dev. 2010; 2(8):9-20.

[47] Sharma K, Porat Ze,and Gedanken A. Designing natural polymer-based capsules and spheres for biomedical applications—a review. Polymers. 2021; 13(24):4307. https://doi.org/10.3390/polym13244307

[48] Mukherjee C, Varghese D, Krishna J, Boominathan T, Rakeshkumar R, Dineshkumar S, et al. Recent advances in biodegradable polymers–properties, applications and future prospects. European Polymer Journal. 2023; 192:112068. https://doi.org/10.1016/j.eurpolymj.2023.112068

[49] Purnama P, Saldi ZS, and Samsuri M. The Development of Polylactide Nanocomposites: A Review. Journal of Composites Science. 2024; 8(8):317. https://doi.org/10.3390/jcs8080317

[50] Samy M, Ekram B, Abd El-Hady BM, and Ayoub MM. In vitro release study of electrospun poly (ε-caprolactone)/gelatin nanofiber mats loaded with 5-fluorouracil. Polymer Bulletin. 2020; 63(1):255-267. https://doi.org/10.1007/s00289-023-04930-2

[51] Idumah CI. Emerging trends in poly (lactic-co-glycolic) acid bionanoarchitectures and applications. Cleaner Materials. 2022; 5:100102. https://doi.org/10.1016/j.clema.2022.100102

[52] George A, Shah PA, and Shrivastav PS. Natural biodegradable polymers based nano-formulations for drug delivery: A review. International journal of pharmaceutics. 2019; 561:244-264. https://doi.org/10.1016/j.ijpharm.2019.03.011

[53] Khalid SA, Abo Dena AS, and El-Sherbiny IM. Biopolymeric-inorganic composites for drug delivery applications. Polymeric and Natural Composites: Materials, Manufacturing and Biomedical Applications. 2022, 271-298. https://doi.org/10.1007/978-3-030-70266-3_9

[54] Zhang S, Pelligra CI, Feng X, and Osuji CO. Directed assembly of hybrid nanomaterials and nanocomposites. Advanced Materials. 2018; 30(18):1705794. https://doi.org/10.1002/adma.201705794

[55] Valapa RB, Loganathan S, Pugazhenthi G, Thomas S, and Varghese T. An overview of polymer–clay nanocomposites, Clay-Polymer Nanocomposites. 2017, 29-81. https://doi.org/10.1016/B978-0-323-46153-5.00002-1

[56] Khan WS, Hamadneh NN, and Khan WA. Polymer nanocomposites–synthesis techniques, classification and properties, Science and applications of Tailored Nanostructures. 2016; 50.

[57] Hill LJ, and Pyun J. Colloidal polymers via dipolar assembly of magnetic nanoparticle monomers. ACS applied materials & interfaces. 2014; 6(9):6022-6032. https://doi.org/10.1021/am405786u

[58] Alsayed AF, and Aqeel Ashraf M. Synthesis of polymer nanocomposite films, Handbook of polymer and ceramic nanotechnology. Springer. 2021, 157-176. https://doi.org/10.1007/978-3-030-40513-7_9

[59] Khan I, Saeed K, and Khan I. Nanoparticles: Properties, applications and toxicities, Arabian journal of chemistry. 2019; 12(7):908-931. https://doi.org/10.1016/j.arabjc.2017.05.011

[60] Tiwari JN, Tiwari RN, and Kim KS, Zero-dimensional, one-dimensional, two-dimensional and three-dimensional nanostructured materials for advanced electrochemical energy devices. Progress in Materials Science. 2012; 57(4):724-803. https://doi.org/10.1016/j.pmatsci.2011.08.003

[61] Shin W-K, Cho J, Kannan AG, Lee Y-S, and Kim D-W. Cross-linked composite gel polymer electrolyte using mesoporous methacrylate-functionalized SiO2 nanoparticles for lithium-ion polymer batteries. Scientific reports. 2016; 6(1):26332. https://doi.org/10.1038/srep26332

[62] Haleem A, Javaid M, Singh RP, Rab S, and Suman R. Applications of nanotechnology in medical field: a brief review. Global Health Journal. 2023; 7(2):70-77. https://doi.org/10.1016/j.glohj.2023.02.008

[63] Spirescu VA, Chircov C, Grumezescu AM, Vasile BȘ, and Andronescu E. Inorganic nanoparticles and composite films for antimicrobial therapies. International journal of molecular sciences. 2021; 22(9):4595. https://doi.org/10.3390/ijms22094595

[64] Philip A, and Kumar AR. The performance enhancement of surface plasmon resonance optical sensors using nanomaterials: A review. Coordination Chemistry Reviews. 2022; 458:214424. https://doi.org/10.1016/j.ccr.2022.214424

[65] Amendola V, Pilot R, Frasconi M, Maragò OM,and Iatì MA. Surface plasmon resonance in gold nanoparticles: a review. Journal of physics: Condensed matter. 2017; 29(20):203002. https://doi.org/10.1088/1361-648X/aa60f3

[66] Saha S, Ali M, Khaleque M, Bacchu M, Aly MAS, and Khan M. Metal oxide nanocarrier for targeted drug delivery towards the treatment of global infectious diseases: A review. Journal of Drug Delivery Science and Technology. 2023, 104728. https://doi.org/110.1016/j.jddst.2023.104728

[67] Wang Cy, Makvandi P, Zare EN, Tay FR, and Niu Ln. Advances in antimicrobial organic and inorganic nanocompounds in biomedicine. Advanced Therapeutics. 2020; 3(8):2000024. https://doi.org/10.1002/adtp.202000024

[68] Mansha M, Khan I, Ullah N, and Qurashi A. Synthesis, characterization and visible-light-driven photoelectrochemical hydrogen evolution reaction of carbazole-containing conjugated polymers. International Journal of Hydrogen Energy. 2017; 42(16):10952-10961. https://doi.org/10.1016/j.ijhydene.2017.02.053

[69] Rao JP, and Geckeler KE. Polymer nanoparticles: Preparation techniques and size-control parameters, Progress in polymer science. 2011; 36(7):887-913. https://doi.org/10.1016/j.progpolymsci.2011.01.001

[70] Sukhanova TyEe, Vylegzhanina M, Volkov AY, Gasilova, ER, Kutin AA, Samy M, Abdallah HM, and Ayoub M. Comparative Study of Polymer Nanoparticles on the Basis of Caprolactone–Polyvinyl Alcohol Mixtures with an Encapsulated Antitumor Preparation by Atomic Force Microscopy, X-Ray Diffraction, and Dynamic Light Scattering. Technical Physics. 2019; 64(12):1729-1737. https://doi.org/10.1134/S1063784219120235

[71] Lima AL, Gratieri T, Cunha-Filho M, Gelfuso GM, Polymeric nanocapsules: A review on design and production methods for pharmaceutical purpose. Methods. 2022; 199:54-66. https://doi.org/10.1016/j.ymeth.2021.07.009

[72] Geszke-Moritz M, and Moritz M. Biodegradable polymeric nanoparticle-based drug delivery systems: comprehensive overview, perspectives and challenges. Polymers. 2024; 16(17):2536. https://doi.org/10.3390/polym16172536

[73] Samy M, Abdallah HM, Awad HM, and Ayoub MM. Preparation, Characterization and In vitro Biological activity of 5-Fluorouracil Loaded onto poly (D, L-lactic-co-glycolic acid) Nanoparticles. Polymer Bulletin. 2023; 80(6):6197-6219. https://doi.org/10.1007/s00289-022-04308-w

[74] Samy M, Abdallah HM, Awad HM, and Ayoub MM. In vitro release and cytotoxicity activity of 5-fluorouracil entrapped polycaprolactone nanoparticles. Polymer Bulletin. 2022, 1-27.

[75] Zielińska A, Carreiró F, Oliveira AM, Neves A, Pires B, Venkatesh DN, et al. Polymeric nanoparticles: production, characterization, toxicology and ecotoxicology. Molecules. 2020; 25(16):3731. https://doi.org/10.3390/molecules25163731

[76] Prajapati SK, Jain A, Jain A, and Jain S. Biodegradable polymers and constructs: A novel approach in drug delivery. European polymer journal. 2019; 120:109191. https://doi.org/10.1016/j.eurpolymj.2019.08.018

[77] Maqbool I, and Noreen S. A review of novel techniques for nanoparticles preparation. GDDDR. 2019; 4(1):41-50. http://dx.doi.org/10.31703/gdddr.2019(IV-I).05

[78] Vieira R, Souto SB, Sánchez-López E, López Machado A, Severino P, Jose S, et al. Sugar-lowering drugs for type 2 diabetes mellitus and metabolic syndrome—Review of classical and new compounds: Part-I. Pharmaceuticals. 2019; 12(4):152. https://doi.org/10.3390/ph12040152

[79] Grumezescu AM. Design and development of new nanocarriers, William Andrew, 017

[80] Bohrey S, Chourasiya V, and Pandey A. Polymeric nanoparticles containing diazepam: preparation, optimization, characterization, in-vitro drug release and release kinetic study. Nano Convergence. 2016; 3(1):3. https://doi.org/10.1186/s40580-016-0061-2

[81] Szczęch M, and Szczepanowicz K. Polymeric core-shell nanoparticles prepared by spontaneous emulsification solvent evaporation and functionalized by the layer-by-layer method. Nanomaterials. 2020; 10(3):496. https://doi.org/10.3390/nano10030496

[82] Carreiró F, Oliveira AM, Neves A, Pires B, Nagasamy Venkatesh D, Durazzo A, Lucarini M, Eder P, Silva AM, and Santini A. Polymeric nanoparticles: Production, characterization, toxicology and ecotoxicology. Molecules. 2020; 25:3731. https://hdl.handle.net/11588/939198

[83] Souto EB, Souto SB, Campos JR, Severino P, Pashirova TN, Zakharova LY, Silva AM, Durazzo A, Lucarini M, and Izzo AAJM. Nanoparticle delivery systems in the treatment of diabetes complications. 2019; 24(23):4209.

[84] Souto EB, Severino P, Santana MHA. Preparation of polymeric nanoparticles by polymerization of monomers: part I. Polímeros. 2012; 22:96-100. https://doi.org/10.1590/S0104-14282012005000006

[85] Vasile C. Polymeric nanomaterials in nanotherapeutics, lsevier. 2018. https://doi.org/10.3390/polym11091452

[86] Wang Y, Li P, Truong-Dinh Tran T, Zhang J, and Kong L. Manufacturing techniques and surface engineering of polymer based nanoparticles for targeted drug delivery to cancer. Nanomaterials. 2016; 6(2):26. https://doi.org/10.3390/nano6020026

[87] Lim K, and Hamid ZA. Polymer nanoparticle carriers in drug delivery systems: Research trend. Applications of nanocomposite materials in drug delivery. Elsevier. 2018, 217-237. https://doi.org/10.1016/B978-0-12-813741-3.00010-8

[88] Krishnamoorthy K, and Mahalingam M. Selection of a suitable method for the preparation of polymeric nanoparticles: multi-criteria decision making approach. Advanced pharmaceutical bulletin. 2015; 5(1):57. https://doi.org/10.5681/apb.2015.008

[89] Crucho CI, and Barros MT. Polymeric nanoparticles: A study on the preparation variables and characterization methods, Materials Science and Engineering: C. 2017; 80:771-784. https://doi.org/10.1016/j.msec.2017.06.004

[90] Sánchez-López E, Ettcheto M, Egea MA, Espina M, Cano A, Calpena AC, et al. Memantine loaded PLGA PEGylated nanoparticles for Alzheimer's disease: In vitro and in vivo characterization. Journal of nanobiotechnology. 2018; 16(1):32. https://doi.org/10.1186/s12951-018-0356-z

[91] Salatin S, Barar J, Barzegar-Jalali M, Adibkia K, Kiafar F, and Jelvehgari M. Development of a nanoprecipitation method for the entrapment of a very water soluble drug into Eudragit RL nanoparticles, Research in pharmaceutical sciences. 2017; 12(1):1-14. https://doi.org/10.4103/1735-5362.199041

[92] Rivas CJM, Tarhini M, Badri W, Miladi K, Greige-Gerges H, Nazari QA, Rodríguez SAG, Román RÁ, Fessi H, and Elaissari A. Nanoprecipitation process: From encapsulation to drug delivery. International journal of pharmaceutics. 2017; 532(1):66-81. https://doi.org/10.1016/j.ijpharm.2017.08.064

[93] Chidambaram M, and Krishnasamy K. Modifications to the conventional nanoprecipitation technique: an approach to fabricate narrow sized polymeric nanoparticles. Advanced Pharmaceutical Bulletin. 2014; 4(2):205. https://doi.org/10.5681/apb.2014.030

[94] Salatin S, Barar J, Barzegar-Jalali M, Adibkia K, Kiafar F, and Jelvehgari M. Development of a nanoprecipitation method for the entrapment of a very water soluble drug into Eudragit RL nanoparticles, Research in pharmaceutical sciences. 2017; 12(1):1. https://doi.org/10.4103/1735-5362.199041

[95] Romina HMTShirazi, Toraj Mohammadi, Maryam Ahmadzadeh Tofighy. 22-Polymer nanocomposite films and coating for drug delivery application. Polymer Nanocomposite Films and Coatings. Elsevier. 2024, 759-783. https://doi.org/10.1016/B978-0-443-19139-8.00019-X

[96] Srinivasan Ayyanaar, R Bhaskar, Selvaraj Esthar, Manokaran Vadivel, Jegathalaprathaban Rajesh, Gurusamy Rajagopal. Design and development of 5-fluorouracil loaded biodegradable magnetic microspheres as site-specific drug delivery vehicle for cancer therapy. Journal of Magnetism and Magnetic Materials. 2022; 546:168853. https://doi.org/10.1016/j.jmmm.2021.168853

[97] Martins VFS. Benefits and drawbacks for the clinical use of 5-fluorouracil. 2023. http://hdl.handle.net/10451/64085

[98] Prabhu S, and Poulose EK. Silver nanoparticles: mechanism of antimicrobial action, synthesis, medical applications, and toxicity effects, International nano letters. 2012; 2:1-10. https://doi.org/ 10.1186/2228-5326-2-32

[99] Hanna DH, El-Mazaly MH, Mohamed RR. Synthesis of biodegradable antimicrobial pH-sensitive silver nanocomposites reliant on chitosan and carrageenan derivatives for 5-fluorouracil drug delivery toward HCT116 cancer cells, International Journal of Biological Macromolecules. 2023; 231:123364. https://doi.org/10.1016/j.ijbiomac.2023.123364

[100] Al-Sarayra LMS, Hussein-Al-Ali SH, Haddad MK, and Qader AA. Gold Nanoparticles Loaded with Chitosan Encapsulate Donepezil as a Novel Nanocomposite for Alzheimer's Disease Therapy. Materials Research. 2024; 27: e20230365. https://doi.org/10.1590/1980-5373-MR-2023-0365

[101] Du Y, Ren W, Li Y, Zhang Q, Zeng L, Chi C, et al. The enhanced chemotherapeutic effects of doxorubicin loaded PEG coated TiO 2 nanocarriers in an orthotopic breast tumor bearing mouse model, Journal of Materials Chemistry B. 2015; 3(8):1518-1528. https://doi.org/10.1039/c4tb01781a

[102] Kumari SVG, Manikandan NA, Pakshirajan K, and Pugazhenthi G. Sustained drug release and bactericidal activity of a novel, highly biocompatible and biodegradable polymer nanocomposite loaded with norfloxacin for potential use in antibacterial therapy. Journal of Drug Delivery Science and Technology. 2020; 59:101900. https://doi.org/10.1016/j.jddst.2020.101900

[103] Salahuddin N, Abdelwahab M, Gaber M, and Elneanaey S. Synthesis and Design of Norfloxacin drug delivery system based on PLA/TiO2 nanocomposites: Antibacterial and antitumor activities. Materials Science and Engineering: C. 2020; 108:110337. https://doi.org/10.1016/j.msec.2019.110337

[104] Lin Q, Liu G, Zhao Z, Wei D, Pang J, and Jiang Y. Design of gefitinib-loaded poly (l-lactic acid) microspheres via a supercritical anti-solvent process for dry powder inhalation. International journal of pharmaceutics. 2017; 532(1):573-580. https://doi.org/10.1016/j.ijpharm.2017.09.051

[105] Gautam A, and Pal K. Gefitinib conjugated PEG passivated graphene quantum dots incorporated PLA microspheres for targeted anticancer drug delivery. Heliyon. 2022; 8(12). https://doi.org/10.1016/j.heliyon.2022.e12512

[106] Papageorgiou DG, Kinloch IA, and Young RJ. Mechanical properties of graphene and graphene-based nanocomposites. Progress in materials science. 2017; 90:75-127. https://doi.org/10.1016/j.pmatsci.2017.07.004

[107] Yu X, Cheng H, Zhang M, Zhao Y, Qu L, andShi G. Graphene-based smart materials. Nature Reviews Materials. 2017; 2(9):1-13. https://doi.org/10.1038/natrevmats.2017.46

[108] Misiak P, Niemirowicz-Laskowska K, Markiewicz KH, Wielgat P, Kurowska I, Czarnomysy R, et al. Doxorubicin-loaded polymeric nanoparticles containing ketoester-based block and cholesterol moiety as specific vehicles to fight estrogen-dependent breast cancer. Cancer Nanotechnology. 2023; 14(1):23. https://doi.org/10.1186/s12645-023-00176-9.

[109] Ghamkhari A, Abbaspour-Ravasjani S, Talebi M, Hamishehkar H, and Hamblin MR. Development of a graphene oxide-poly lactide nanocomposite as a Smart Drug Delivery System. International Journal of Biological Macromolecules. 2021; 169:521-531. https://doi.org/0.1016/j.ijbiomac.2020.12.084

[110] Sadeghi-Ghadi Z, Behjou N, Ebrahimnejad P, Mahkam M, Goli HR, Lam M, et al. Improving antibacterial efficiency of curcumin in magnetic polymeric nanocomposites. Journal of Pharmaceutical Innovation. 2023; 18(1):13-28.

[111] Huang Y, Dan N, Dan W, and Zhao W. Reinforcement of polycaprolactone/chitosan with nanoclay and controlled release of curcumin for wound dressing, ACS omega. 2019; 4(27):22292-22301. https://doi.org/10.1021/acsomega.9b02217

[112] Ghosh S, Raju RSK, Ghosh N, Chaudhury K, Ghosh S, Banerjee I, et al. Development and physicochemical characterization of doxorubicin-encapsulated hydroxyapatite–polyvinyl alcohol nanocomposite for repair of osteosarcoma-affected bone tissues. Comptes Rendus Chimie. 2019; 22(1):46-57. https://doi.org/10.1016/j.crci.2018.10.005

[113] Ghosh S, Ghosh S, and Pramanik N, Bio-evaluation of doxorubicin (DOX)-incorporated hydroxyapatite (HAp)-chitosan (CS) nanocomposite triggered on osteosarcoma cells. Advanced Composites and Hybrid Materials, 2020, 3, pp. 303-314 https://doi.org/10.1007/s42114-020-00154-4

[114] Yu H-Y, Wang C, and Abdalkarim SYH. Cellulose nanocrystals/polyethylene glycol as bifunctional reinforcing/compatibilizing agents in poly (lactic acid) nanofibers for controlling long-term in vitro drug release. Cellulose. 2017; 24(10):4461-4477. https://doi.org/10.1007/s10570-017-1431-6

[115] Karuppuswamy P, Venugopal JR, Navaneethan B, Laiva AL, and Ramakrishna S. Polycaprolactone nanofibers for the controlled release of tetracycline hydrochloride. Materials Letters. 2015; 141:180-186. https://doi.org/10.1016/j.matlet.2014.11.044

[116] Wang Z, Zhao Y, Shen M, Tomás H, Zhou B, and Shi X. Antitumor Efficacy of Doxorubicin-Loaded Electrospun Attapulgite–Poly (lactic-co-glycolic acid) Composite Nanofibers. Journal of Functional Biomaterials. 2022; 13(2):55. https://doi.org/10.3390/jfb13020055

[117] Tavira M, Mousavi-Khattat M, Shakeran Z, and Zarrabi A. PCL/gelatin nanofibers embedded with doxorubicin-loaded mesoporous silica nanoparticles/silver nanoparticles as an antibacterial and anti-melanoma cancer. International Journal of Pharmaceutics. 2023; 642:123162. https://doi.org/10.1016/j.ijpharm.2023.123162

[118] Bulbul YE, Eskitoros-Togay ŞM, Demirtas-Korkmaz F, and Dilsiz N. Multi-walled carbon nanotube-incorporating electrospun composite fibrous mats for controlled drug release profile. International Journal of Pharmaceutics. 2019; 568:118513. https://doi.org/10.1016/j.ijpharm.2019.118513

[119] Mosallanezhad P, Nazockdast H, Ahmadi Z, and Rostami A. Fabrication and characterization of polycaprolactone/chitosan nanofibers containing antibacterial agents of curcumin and ZnO nanoparticles for use as wound dressing. Frontiers in bioengineering and biotechnology. 2022; 10:1027351. https://doi.org/10.3389/fbioe.2022.1027351

Crossref
DOI: 10.31643/2028/6445.31
Mining and Mineral Processing

Synthesis Process of Silica–Activated Carbon Composite Ceramic Membranes for Integrated Filtration and Adsorption in Acid Mine Drainage

[1*] Primandari S.R.P., [2]Aprianti T., [3]Sugiarto Y., [1]Mulianti, [4]Elshaarani T.

[1] Department of Mechanical Engineering, Faculty of Engineering, Universitas Negeri Padang, Indonesia
[2] Department of Chemical Engineering, Faculty of Engineering, Universitas Sriwijaya, Palembang, Indonesia
[3] Department of Biosystems Engineering, Faculty of Agricultural Technology, Universitas Brawijaya, Malang, Indonesia
[4] Sharjah Marine Science Research Center, Faculty of Marine Sciences and Aquatic Biology, University of Khorfakkan, Sharjah, United Arab Emirates; Institute of Chemistry and Nuclear Physics, Sudan Atomic Energy Commission, Khartoum, Sudan

** Corresponding author email: sri.primandari@ft.unp.ac.id*

Received: *July 12, 2026*
Peer-reviewed: *August 10, 2026*
Accepted: *August 19, 2026*

ABSTRACT
Acid Mine Drainage (AMD) is a liquid waste from coal mining by-products. AMD is a highly corrosive liquid (pH 1.5 – 4.0) and contains heavy metals, which is one of the problems in coal mining. Filtration technology using ceramic membranes can offer greater corrosion resistance than other membranes. Therefore, the study aims to fabricate and characterize composite ceramic membranes made from silica extracted from rice husk ash (RHA) and modified with high-performance activated carbon (Maxsorb III) to boost heavy metal adsorption capacity. The membranes are produced through extrusion molding and stepwise sintering processes. The results were analyzed using SEM-EDS, XRF, XRD, and BET. XRF analysis showed that the silica purity increased from 88.42 to 98.62 wt%, while XRD confirmed a predominantly amorphous structure with a broad peak centered at approximately 22° (2θ). SEM-EDS revealed the formation and distribution of pores, with Si, O, and C as the main elements. Increasing the activated carbon content from 10 to 20 wt% increased the BET specific surface area from 238 to 412 m^2/g and the average pore diameter from 16 to 25 nm, indicating increased pore development and surface area. These results indicate that activated carbon effectively modifies the porous structure and textural properties of the ceramic membrane.

Keywords: filtration, ceramic membrane, wastewater, heavy metal adsorption.

Information about authors:

Primandari Sri Rizki Putri — *Assistant Professor of Mechanical Engineering, Faculty of Engineering, Universitas Negeri Padang, Indonesia. Email: sri.primandari@ft.unp.ac.id; ORCID ID: https://orcid.org/0000-0002-1279-7331*

Aprianti Tine — *Dr., Chemical Engineering, Faculty of Engineering, Universitas Sriwijaya, Palembang, Indonesia. Email: tineaprianti@unsri.ac.id; ORCID ID: https://orcid.org/0000-0003-0183-2557*

Sugiarto Yusron — *Dr., Department of Biosystems Engineering, Faculty of Agricultural Technology, Universitas Brawijaya, Malang, Indonesia. Email: yusronsugiarto@ub.ac.id; ORCID ID: https://orcid.org/0000-0001-5736-1972*

Mulianti — *Dr., Department of Mechanical Engineering, Faculty of Engineering, Universitas Negeri Padang, Indonesia. Email: mulianti@ft.unp.ac.id; ORCID ID: https://orcid.org/0009-0006-0149-7364*

Elshaarani Tarig — *Dr., Sharjah Marine Science Research Center, Faculty of Marine Sciences and Aquatic Biology, University of Khorfakkan, Sharjah, United Arab Emirates, and Institute of Chemistry and Nuclear Physics, Sudan Atomic Energy Commission, Khartoum, Sudan. Email: Tarig.Ali@ukf.ac.ae; ORCID ID: https://orcid.org/0000-0002-5769-4758*

Introduction

Globally, the coal mining industry continues to play a crucial role in meeting energy needs, particularly in countries that rely on coal as a primary source of electricity generation and industrial energy. In this global context, Indonesia is a significant case in point due to its extensive coal mining activities and significant contribution to its energy sector and economy. The growth of the coal mining industry in Indonesia has supported the national energy supply, industrial development, employment, and export revenues. However, this activity also produces liquid waste in the form of Acid Mine Drainage (AMD), which remains a problem in mining environmental management [1]. AMD is formed due to the oxidation of sulfide minerals, especially pyrite (FeS_2), when in contact with water and oxygen, resulting in water with a very low pH (1.5–4.0). AMD also contains dissolved heavy metals such as Fe, Mn, Cu, Zn, Al, and sulfate in high concentrations. If not adequately treated, AMD can cause water pollution, soil degradation, damage to aquatic ecosystems, and increased health risks for

communities around mining areas [2]. Therefore, the development of effective, economical, and sustainable AMD processing technology is a priority in environmental engineering and mining technology.

The Indonesian government, through the Decree of the Minister of Environment Number 113 of 2003, has established wastewater quality standards for coal mining activities that must be met before the wastewater is discharged into the environment. However, the characteristics of highly acidic AMD and containing heavy metals in high concentrations make the treatment process complex [3]. Conventional technologies such as neutralization using lime, chemical precipitation, coagulation-flocculation, bioremediation, and adsorption have been widely applied on an industrial scale. However, these methods still face various limitations, including high chemical consumption, the formation of large amounts of secondary sludge, the need for relatively long processing times, and high operating and maintenance costs [4]. These conditions indicate that alternative technologies are still needed that have high efficiency and are able to reduce the environmental impact of the waste processing process itself.

In recent years, membrane technology has emerged as a promising separation method due to its ability to produce high-quality effluent, small land footprint, and easy integration with other treatment processes. However.

However, most membranes used in wastewater treatment are still polymer-based and lack chemical and thermal stability. Their performance and structural stability can be negatively affected by extreme pH and high-temperature conditions, making them susceptible to degradation, fouling, permeability changes, and reduced service life when applied to acid mine wastewater (AMD) treatment [5].

As an alternative, ceramic membranes offer significantly better mechanical, thermal, and chemical stability, enabling them to operate in highly corrosive environments. In addition to their longer lifespan, ceramic membranes can also be regenerated through chemical or thermal cleaning processes without significant structural damage [6]. Therefore, the development of ceramic membranes based on local materials is an important research direction in producing more efficient and sustainable AMD processing technology.

In line with the increasing attention to the concept of circular economy and waste valorization, the utilization of agricultural waste as raw material for advanced materials has become a rapidly growing research topic. Indonesia is one of the largest rice producers in the world, producing millions of tons of rice husks annually. Burning rice husks produces rice husk ash (RHA), which contains around 80–95% amorphous silica, depending on the combustion conditions and extraction process [7]. To date, most of the rice husk ash is still used as backfill or even disposed of as solid waste, thus not providing optimal added value. In fact, the high silica content makes RHA a potential source of raw materials for the synthesis of ceramic materials, adsorbents, catalysts, and membranes. The utilization of silica from rice husk ash not only reduces agricultural waste but also supports the development of environmentally friendly materials based on renewable resources.

Silica extracted from rice husk ash has high chemical stability in acidic environments, purity that can be improved through a purification process, and an amorphous structure that supports the formation of ceramic membranes. However, silica has a relatively limited specific surface area, so the number of active sites for heavy metal adsorption is still not optimal [8]. One approach to improving these characteristics is to combine silica with highly porous activated carbon. Maxsorb III is a commercial activated carbon with a specific surface area of approximately 3,000 m^2/g, thus potentially increasing the membrane's adsorption capacity for heavy metal ions. In addition to functioning as an adsorbent, activated carbon can also act as a pore-forming agent during the sintering process. During the combustion process, activated carbon will decompose and leave micropore cavities, thereby increasing the porosity, effective surface area, and permeability of the membrane [[9], [10]]. Controlling the pore structure is one of the main factors that determine the performance of ceramic membranes in the filtration process. In this study, Maxsorb III was selected because of its highly porous structure and exceptionally high specific surface area, which can provide additional active sites for adsorption and facilitate the development of membrane porosity. However, the low bulk density and relatively low thermal conductivity of Maxsorb III should also be considered in the design of the composite membrane. The low density may affect particle packing and interparticle contact within the silica matrix, while the low thermal conductivity can influence heat transfer during thermal treatment. Excessive incorporation of activated carbon may therefore result in increased porosity at the expense

of structural integrity and mechanical strength if the pore-forming phase is not adequately controlled. Consequently, optimizing the activated carbon content is essential to achieve a balance between porosity, permeability, adsorption capacity, and mechanical stability. Controlling the pore structure is therefore one of the key factors determining the filtration performance and durability of ceramic membranes.

Although research on the utilization of rice husk ash as a source of silica and the development of ceramic membranes has been widely reported, most of the research is still focused on its application as an adsorbent, geopolymer, catalyst, or membrane for domestic water treatment and general industrial wastewater. Research that integrates silica extracted from rice husk ash with Maxsorb III activated carbon as a ceramic membrane component for Acid Mine Drainage treatment applications is still very limited [11]. In addition, the effect of variations in activated carbon content on the development of pore structure, specific surface area, and morphology of RHA silica-based membranes has not been studied systematically. This research gap indicates the need for the development of new membrane materials that not only have high resistance to acidic environments, but are also able to utilize biomass waste as a source of value-added raw materials.

Based on the description, the novelty of this research lies in the development of a silica-based composite ceramic membrane extracted from rice husk ash with the addition of Maxsorb III activated carbon, which functions as an adsorbent and pore-forming agent. This approach integrates the concept of biomass waste utilization (waste-to-value) with ceramic membrane technology to produce a material that has higher porosity, larger specific surface area, and good chemical resistance to acidic environments. Thus, this research not only offers a solution to the problem of Acid Mine Drainage treatment, but also contributes to the development of sustainable material technology that supports a circular economy and the achievement of the Sustainable Development Goals (SDGs), especially SDG 6 (Clean Water and Sanitation), SDG 9 (Industry, Innovation and Infrastructure), and SDG 12 (Responsible Consumption and Production).

This article aims to fabricate and charatarization of new type of membrane for integrated filtration and adsorption in acid mine drainage. It also aims to characterize the morphology, porosity, and specific surface area of the resulting membranes, and analyze the effect of the addition of activated carbon on the physical characteristics of the membrane as a basis for evaluating its potential for Acid Mine Drainage treatment applications.

Experimental part

Materials and tools

The main raw material used in this study was rice husk obtained from a local rice mill in Padang City, Indonesia. It was rice husk freshly collected in April, 2026. The rice husk was collected immediately after the rice milling process and was used as the starting material for subsequent washing, drying, and preparation.

The chemicals used included a 10% hydrochloric acid (HCl) solution as an acid leaching agent, Maxsorb III activated carbon as a pore-forming agent, polyvinyl alcohol (PVA) as a binder, sodium hydroxide (NaOH) for the silica extraction process, and deionized water as a solvent and washing medium.

The main equipment used includes an electric furnace for calcination and sintering processes, a ball mill for powder refinement, a 200-mesh sieve, a hydraulic extruder for tubular membrane molding, a drying oven, and an analytical balance. The characterizations were conducted using X-Ray Fluorescence (XRF) to determine chemical composition, X-Ray Diffraction (XRD) to identify crystal phases, Scanning Electron Microscopy (SEM) to observe surface morphology, and a Brunauer–Emmett–Teller (BET) Surface Area Analyzer to determine specific surface area and pore characteristics.

Silica Extraction from Rice Husk Ash

Silica is extracted from rice husk ash using a combination of acid dissolution and calcination. The extraction process includes preparing the rice husk, dissolving it with acid, calcination, and extracting the silica.

Rice Husk Preparation

The rice husks were gently rinsed with running water to remove surface dirt. The husks were then dried in an oven at 105°C for 24 hours until a constant weight was achieved. The rice husks are gently rinsed with running water to remove surface dirt and other adhering impurities. The washed husks are then dried in an oven at 105°C for 24 hours, or until a constant weight is reached. The drying temperature of 105°C was chosen to effectively remove free and physically bound moisture from the rice husks while minimizing thermal changes or decomposition of their organic

constituents. Achieving a constant weight ensures that the moisture content is sufficiently stable before further processing. After drying, the samples were weighed as a reference for the next extraction process [12].

Acid Leaching

Dry rice husks were soaked in a 10% HCl solution for 24 hours at room temperature to remove metal oxides and mineral impurities. Then, they were washed with deionized water until a neutral pH was reached. Once the filtrate reached neutral pH, the solution was dried for 24 hours at 105°C.

Calcination

Rice husk ash (RHA) is obtained by calcining rice husks from an acid leaching process for 4 hours at 650°C with a heating rate of 5°C per minute. This is done to keep the silica in an amorphous phase, making it suitable as a raw material for ceramic membranes. After naturally cooling in the furnace, the rice husk ash is ground using a ball mill and then sieved through a 200-mesh screen to ensure uniform size [7].

Silica Extraction

Silica is extracted from rice husk ash using the alkali–sol–gel method [[13], [14]]. 50 g of rice husk ash is heated in a 1 M NaOH solution at 100°C for 1 hour. The solution is filtered to separate the solid residue. The filtered solution is then titrated with 1 M HCl until reaching pH 7 to form a silica gel precipitate and aged overnight. Next, it is rinsed with deionized water until free of chloride ions. The resulting silica gel is dried at 105°C for 24 hours and then calcined again for 2 hours at 600°C. This is done to obtain amorphous silica powder. The resulting amorphous silica powder is analyzed for its composition using X-Ray Fluorescence (XRF) to determine the SiO_2 content, oxide impurities, and the effectiveness of the purification process. The crystal structure was characterized using XRD, while the specific surface area and pore distribution were analyzed using a BET Surface Area Analyzer.

Composite Ceramic Membrane Fabrication

Composite ceramic membranes were fabricated using an extrusion method followed by drying and sintering [[13], [15]]. The extracted silica was mixed with Maxsorb III activated carbon at varying compositions of 10% (membrane i) and 20 wt% (membrane ii) by weight of silica. Before mixing, the activated carbon was dried at 100°C for 12 hours to remove moisture that could affect the homogeneity of the mixture.

A mixture of silica and activated carbon was added with a 5 wt% PVA solution as a binder, then mixed with deionized water to obtain a plastic mixture with a water content of around 20–25 wt%. The mixture was homogenized using a mechanical mixer at 300 rpm for 30 min to ensure uniform dispersion of the silica, activated carbon, PVA binder, and water throughout the mixture. The mixing speed and duration were kept constant for all samples to maintain consistent processing conditions and minimize variations in the homogeneity and subsequent structural properties of the ceramic membrane.

The plastic mixture was molded into a tubular membrane using a hydraulic extruder. The ceramic membrane in this study is 3 cm long with an inner diameter of 0.6 cm and an outer diameter of 0.8 cm [16]. To get a uniform membrane thickness and diameter, the pressure was kept constant during the extrusion process. The process continued with slow drying. The dry membrane then underwent sintering with a heating rate up to 1000°C at a rate of 3°C/min. The heating was held for 2 hours before allowing it to cool naturally in the furnace. This process decomposes the PVA and burns the activated carbon, creating pores in the silica matrix and acting as a pore-forming agent [[17], [18]].

Membrane Characterization

After the sintering process, the resulting membrane is characterized, including its morphological structure and elemental composition, crystal structure, surface area, and porosity.

Morphological Characterization and Elemental Composition (SEM)

The surface morphology of the membrane was analyzed using a Scanning Electron Microscope (SEM) at magnifications of 750x and 2000x with an accelerating voltage of 5–15 kV. This analysis was done to determine the membrane's microstructure in terms of shape and pore distribution of the ceramic membrane made from rice husk ash silica and activated carbon.

Crystal Structure Characterization (XRD)

The crystal structure was analyzed using X-Ray Diffraction (XRD). The wavelength of Cu-Kα radiation is 1.5406 Å with a scan speed of 2°/minute in a diffraction angle range of 2θ = 10–80°. The presence of amorphous silica was identified by the appearance of a broad halo at an angle of around 2θ = 22°, while the formation of crystalline silica, such as quartz or cristobalite, was indicated by the appearance of sharp diffraction peaks at their characteristic positions. Phase identification was carried out by matching the diffraction pattern to

the International Centre for Diffraction Data (ICDD PDF-4) database [19].

Surface Area and Porosity (BET) Characterization

The membrane texture characteristics were analyzed using a Brunauer–Emmett–Teller (BET) Surface Area Analyzer through the nitrogen adsorption–desorption method at a temperature of -196°C (77 K). Before testing, the samples were degassed at 180°C for 4 hours under vacuum conditions to remove water and gas molecules adsorbed on the surface.

The specific surface area was calculated using the BET equation, while the pore size distribution and pore volume were analyzed using the Barrett–Joyner–Halenda (BJH) method. The parameters obtained included the specific surface area (m^2/g), total pore volume (cm^3/g), and average pore diameter (nm). These parameters were used to evaluate the effect of variations in activated carbon content on the development of the membrane pore structure.

Chemical Composition Characterization (XRF)

The chemical composition of rice husk ash, extracted silica, and composite ceramic membranes was analyzed using X-Ray Fluorescence (XRF) with the Fundamental Parameters (FP) method. Prior to testing, the samples were dried to constant weight, ground until homogeneous, and then pressed into pellets according to the instrument's standard preparation procedure.

XRF analysis was conducted to determine the content of major oxides and impurities, so that the effectiveness of the silica purification process could be evaluated quantitatively. The parameters analyzed included the content of SiO_2, Al_2O_3, Fe_2O_3, CaO, MgO, K_2O, Na_2O, TiO_2, P_2O_5, and other minor oxides expressed in weight percent (wt%). The analysis results were used to ensure that the rice husk extraction process did indeed contain silica.

Results and Discussions

Characteristics of Silica Raw Materials

XRF results show that quartz sand contains 97.3% SiO_2, with major impurities Al_2O_3 (1.4%) and Fe_2O_3 (0.5%).

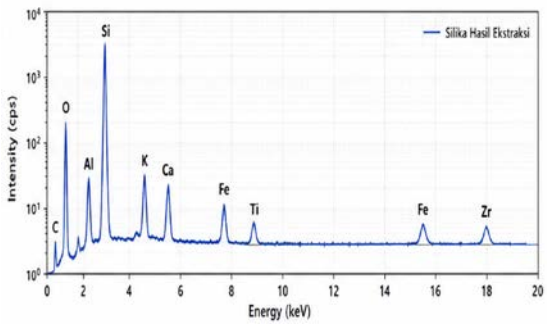

Figure 1 - XRF Spectrum of Silica Extracted from Rice Husk

The overall XRF results can be seen in Table 1.

Table 1 - Rice husk components and extraction results

Parameter	Component	
	RHA (wt%)	***Silica from extraction***
SiO_2	88.42	98.62
Al_2O_3	1.86	0.18
Fe_2O_3	0.92	0.07
CaO	1.48	0.05
MgO	0.71	0.04
K_2O	2.73	0.12
Na_2O	0.32	0.03

The XRF analysis results showed that the extraction process successfully increased the purity of silica from 88.42 wt% to 98.62 wt% (10.20 wt%). The content of the main impurities (Al_2O_3, Fe_2O_3, CaO, MgO, K_2O, Na_2O) decreased significantly (>90%). The LOI value also decreased from 3% to 0.84%, indicating a reduction in organic/volatile compounds after purification. Silica produced from rice husks is generally amorphous (not crystalline), which is very good for adsorption and membrane applications because it has high surface reactivity [[3], [20]].

Characteristics of Silica Crystal Structure from RHA Extraction

XRD results show that silica from rice husk has an amorphous structure, which is characterized by a broad diffraction peak at an angle of 2θ of around 20–30° (the main peak is around 22°) and no sharp peaks indicating a crystalline structure (such as quartz). Pretreatment with acid (HCl) can maintain the amorphous structure of silica up to a firing temperature of 750°C-800°C [21].

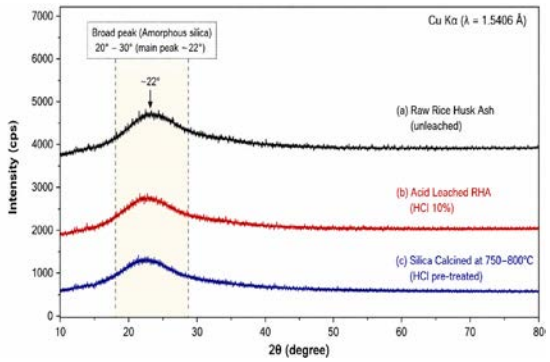

Figure 2 - XRD result of Silica from Rice Husk Ash

Characteristics of Ceramic Membranes from Rice Husk Silica

The morphology of ceramic membranes with a composition of 10% activated carbon (membrane i) and a composition of 20% (membrane ii) at various magnifications can be seen in Figure 3.

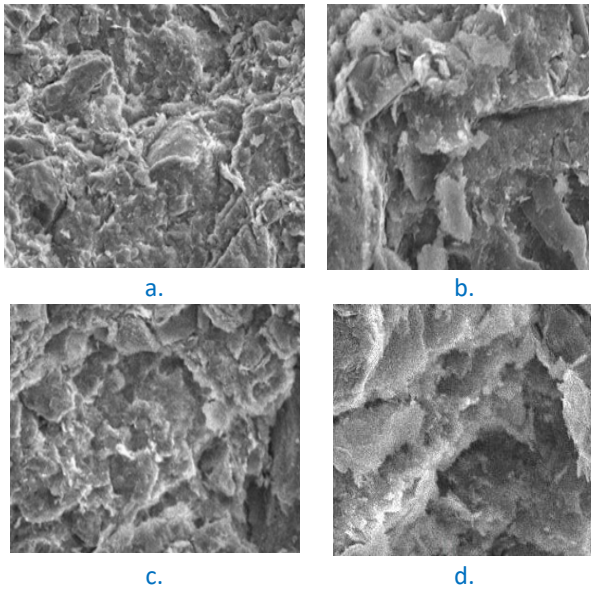

Figure 3 - Morphology of membrane i at zoom a. 750x; b. 2000x; and Morphology of membrane ii at zoom c. 750x; d. 2000x

Activated carbon clumps form interparticle bonds that overlap, leading to a visible reduction in pore size from the surface to the interior. This indicates the formation of a microporous membrane. Activated carbon forms interparticle bonds that overlap, leading to a visible reduction in pore size from the surface to the interior. The morphology of extracted silica particles is generally irregular with a porous structure [21].

SEM morphological structures of each membrane at various magnifications show that the membrane pore structure is random. From the SEM observations, the pores and uneven membrane surface texture are visible due to the influence of temperature. The pores in the membrane with the addition of activated carbon. The more activated carbon added, the more pores formed and still appear less uniform (asymmetric). It can be seen that the pores formed are already small enough to be used in the ultrafiltration process with a pore size of 0.001 – 0.1 µm. The pore surface appears to be evenly distributed on each membrane. For membranes with different concentrations, it can be seen that the pores become denser with increasing amounts of activated carbon additives, and the pores are evenly distributed on the membrane surface due to the addition of these additives [13]. This behavior can be attributed to the porous nature of activated carbon and its role as a pore-forming agent; a higher amount of activated carbon provides more sites for void formation within the silica matrix during subsequent thermal treatment, thereby resulting in a denser pore structure.

Surface Area Characterization (BET)

Analysis using N_2 physisorption at -196 °C (77 K) showed very significant differences in textural characteristics.

Table 2 - Membrane Surface Area Characteristics

Parameter	Membrane I (10%)	Membrane II (20%)
Surface area (m^2/g)	23 8 ± 12	412 ± 18
Total pore volume (cm^3/g)	0.38 ± 0.02	0.72 ± 0.04
Average pore diameter (nm)	16.20	24.80

Increasing the activated carbon content from 10% to 20% resulted in a nearly twofold increase in surface area (from 238 to 412 m^2/g). This was due not only to the remaining unburned carbon, but primarily to the micro-etching of the silica surface by the CO_2 gas released during combustion [22].

The shift in pore diameter from 16 nm to 25 nm indicates that in M-II, the pore structure shifts from mesopore dominance towards macropores, which is very beneficial for increasing permeability, but slightly reduces the adsorption capacity per unit volume [23].

Conclusion

This study has developed a potential ceramic membrane based on agricultural waste and carbon activation. The utilization of rice husk as an agricultural waste contributes significant impact on solid waste solutions and increases the added value of rice husk. Furthermore, the manufacturing process is relatively simple, using extrusion and sintering techniques, which makes this technology adoptable for small- and medium-scale industries.

The recommended further research includes: (1) modifying membranes with metal oxides like ZnO and TiO2, to be able to improve the simultaneous adsorption capacity of heavy metals and sulfate; (2) evaluating the technical and economic feasibility in pilot plant testing.

Conflicts of interest. On behalf of all authors, the corresponding author states that there is no conflict of interest.

CRediT author statement: **S.R.P.Primandari:** Conceptualization, Methodology, Investigation; **Mulianti**: Data curation, Writing draft preparation; **T. Aprianti**: Supervision, Validation; **Y. Sugiarto**: Reviewing and Editing; **T. Elshaarani:** Data analysis and validation.

Acknowledgements. This research is funded by the Indonesian Endowment Fund for Education (LPDP) on behalf of the Indonesian Ministry of Higher Education, Science and Technology and managed under the EQUITY Program (Contract No. 4310/B3/DT.03.08/2025 and 2692/UN35/KS/2025).

Cite this article as: Primandari SRP, Aprianti T, Sugiarto Y, Mulianti, Elshaarani T. Synthesis Process of Silica–Activated Carbon Composite Ceramic Membranes for Integrated Filtration and Adsorption in Acid Mine Drainage. Kompleksnoe Ispolzovanie Mineralnogo Syra = Complex Use of Mineral Resources. 2028; 346(3):99-107. https://doi.org/10.31643/2028/6445.31

Қышқыл шахта ағындыларын кешенді сүзу және адсорбциялау үшін кремний диоксиді мен белсендірілген көмірден композиттік керамикалық мембраналарды синтездеу процесі

[1]Primandari S.R.P., [2]Aprianti T., [3]Sugiarto Y., [1]Mulianti, [4]Elshaarani T.

[1]Машина жасау бөлімі, Инженерлік факультет, Негери Паданг университеті, Индонезия
[2]Химиялық инженерия кафедрасы, Инженерлік факультеті, Университас Сривиджая, Палембанг, Индонезия
[3]Биожүйелік инженерия кафедрасы, агротехнологиялар факультеті, Бравиджая университеті, Маланг, Индонезия
[4]Шарджа теңіз ғылымын зерттеу орталығы, теңіз ғылымдары және су биологиясы факультеті, Хорфаккан университеті, Шарджа, Біріккен Араб Әмірліктері; Химия және ядролық физика институты, Суданның Атом энергиясы жөніндегі комиссиясы, Хартум, Судан

Мақала келді: *12 шілде 2026*
Сараптамадан өтті: *10 тамыз 2026*
Қабылданды: *19 тамыз 2026*

ТҮЙІНДЕМЕ

Қышқылды шахта ағындылары (ҚША) – бұл көмірді өңдеу нәтижесінде пайда болған сұйық қалдықтар. ҚША – жоғары коррозиялық сұйықтық (pH 1,5 – 4,0) және құрамында ауыр металдар бар, бұл көмір өнеркәсібінің мәселелерінің бірі болып табылады. Керамикалық мембраналарды пайдаланатын сүзу технологиясы басқа мембраналарға қарағанда коррозияға төзімділікті арттыра алады. Бұл зерттеудің мақсаты- күріш қабығының күлінен (RHA) алынған және ауыр металдардың адсорбциялық қабілетін арттыру үшін жоғары өнімді белсендірілген көмірмен (Maxsorb III) модификацияланған кремний диоксидінен жасалған композиттік керамикалық мембраналарды жасау және сипаттау. Мембраналар экструзиялық қалыптау және сатылы күйдіру процестері арқылы өндіріледі. Нәтижелер SEM-EDS, XRF, XRD және BET көмегімен талданды. XRF талдауы кремний диоксидінің тазалығы 88,42-ден 98,62 салмақтық%-ға дейін өскенін, ал XRD шамамен 22° (2θ) орталығында орналасқан кең шыңы бар негізінен аморфты құрылымды растағанын көрсетті. SEM-EDS әдісі негізгі элементтер ретінде Si, O және C бар кеуектердің пайда болуы мен таралуын анықтады. Белсендірілген көміртегі мөлшерін 10-нан 20 салмақтық пайызға дейін арттыру BET меншікті бетінің ауданын 238-ден 412 м²/г-ға дейін және орташа кеуек диаметрін 16-дан 25 нм-ге дейін арттырды, бұл кеуектердің өсуі мен бетік ауданының артқанын көрсетеді. Бұл нәтижелер белсендірілген көмірдің керамикалық мембрананың кеуекті құрылымы мен текстуралық қасиеттерін тиімді түрде өзгертетінін көрсетеді.

Түйін сөздер: сүзу, керамикалық мембрана, ағынды сулар, ауыр металдардың адсорбциясы.

Primandari Sri Rizki Putri	***Авторлар туралы ақпарат:*** *Инженерлік факультеттің машина жасау кафедрасының ассистенті, Негери Паданг университеті, Индонезия. Email: sri.primandari@ft.unp.ac.id; ORCID ID: https://orcid.org/0000-0002-1279-7331*
Aprianti Tine	*Доктор, Химиялық инженерия, Инженерлік факультеті, Сривиджая университеті, Палембанг, Индонезия. Email: tineaprianti@unsri.ac.id; ORCID ID: https://orcid.org/0000-0003-0183-2557*
Sugiarto Yusron	*Доктор, Биожүйелік инженерия кафедрасы, агротехнология факультеті, Бравиджая университеті, Маланг, Индонезия. Email: yusronsugiarto@ub.ac.id; ORCID ID: https://orcid.org/0000-0001-5736-1972*
Mulianti	*Доктор, Машина жасау бөлімі, Инженерлік факультет, Негери Паданг университеті, Индонезия. Email: mulianti@ft.unp.ac.id; ORCID ID: https://orcid.org/0009-0006-0149-7364*
Elshaarani Tarig	*Шарджа теңіз ғылымдарын зерттеу орталығының докторы, Хорфаккан университетінің теңіз ғылымдары және су биологиясы факультеті, Шарджа, Біріккен Араб Әмірліктері және Судан атом энергиясы комиссиясының химия және ядролық физика институты, Хартум, Судан.Email: Tarig.Ali@ukf.ac.ae; ORCID ID: https://orcid.org/0000-0002-5769-4758*

Процесс синтеза композитных керамических мембран из диоксида кремния и активированного угля для комплексной фильтрации и адсорбции кислых шахтных стоков

[1]Primandari S.R.P., [2]Aprianti T., [3]Sugiarto Y., [1]Mulianti, [4]Elshaarani T.

[1] Кафедра машиностроения, инженерный факультет, Университет Негери Паданг, Индонезия
[2] Кафедра химической инженерии, инженерный факультет, Университет Шривиджая, Палембанг, Индонезия
[3] Кафедра биосистемной инженерии, факультет сельскохозяйственных технологий, Университет Бравиджая, Маланг, Индонезия
[4]Исследовательский центр морских наук Шарджи, факультет морских наук и водной биологии, Университет Хорфаккана, Шарджа, Объединенные Арабские Эмираты; Институт химии и ядерной физики Суданской комиссии по атомной энергии, Хартум, Судан

Поступила: *12 июля 2026*
Рецензирование: *10 августа 2026*
Принята в печать: *19 августа 2026*

АННОТАЦИЯ

Кислотные шахтные стоки (КШС) — это жидкие отходы, образующиеся в результате переработки угля. КШС представляют собой высококоррозионную жидкость (pH 1,5–4,0) и содержат тяжелые металлы, что является одной из проблем угольной промышленности. Технология фильтрации с использованием керамических мембран может обеспечить более высокую коррозионную стойкость, чем другие мембраны. Поэтому целью данного исследования является изготовление и характеристика композитных керамических мембран из диоксида кремния, извлеченного из золы рисовой шелухи (ЗРШ), и модифицированных высокоэффективным активированным углем (Maxsorb III) для повышения адсорбционной способности по отношению к тяжелым металлам. Мембраны изготавливаются методом экструзионного формования и ступенчатого спекания. Результаты анализировались с помощью SEM-EDS, XRF, XRD и BET. Анализ XRF показал, что чистота диоксида кремния увеличилась с 88,42 до 98,62 мас.%, в то время как XRD подтвердил преимущественно аморфную структуру с широким пиком, центрированным примерно на 22° (2θ). Метод SEM-EDS выявил образование и распределение пор с основными элементами Si, O и C. Увеличение содержания активированного угля с 10 до 20 мас.% привело к увеличению удельной поверхности по методу BET с 238 до 412 м²/г и среднего диаметра пор с 16 до 25 нм, что указывает на увеличение развития пор и площади поверхности. Эти результаты показывают, что активированный уголь эффективно модифицирует пористую структуру и текстурные свойства керамической мембраны.

Ключевые слова: фильтрация, керамическая мембрана, сточные воды, адсорбция тяжелых металлов.

Primandari Sri Rizki Putri	***Информация об авторах:*** *Доцент кафедры машиностроения инженерного факультета Университета Негери Паданг, Индонезия. Email: sri.primandari@ft.unp.ac.id; ORCID ID: https://orcid.org/0000-0002-1279-7331*
Aprianti Tine	*Доктор, Химические науки, инженерный факультет, Университет Шривиджая, Палембанг, Индонезия. Email: tineaprianti@unsri.ac.id; ORCID ID: https://orcid.org/0000-0003-0183-2557*
Sugiarto Yusron	*Доктор, кафедра биосистемной инженерии, факультет сельскохозяйственных технологий, Университет Бравиджая, Маланг, Индонезия. Email: yusronsugiarto@ub.ac.id; ORCID ID: https://orcid.org/0000-0001-5736-1972*
Mulianti	*Доктор кафедры машиностроения, инженерный факультет, Университет Негери Паданг, Индонезия. Email: mulianti@ft.unp.ac.id; ORCID ID: https://orcid.org/0009-0006-0149-7364*

Elshaarani Tarig	*Доктор наук, Научно-исследовательский центр морских наук Шарджи, Факультет морских наук и водной биологии, Университет Хорфаккана, Шарджа, Объединенные Арабские Эмираты; Институт химии и ядерной физики, Суданская комиссия по атомной энергии, Хартум, Судан. Email: Tarig.Ali@ukf.ac.ae; ORCID ID: https://orcid.org/0000-0002-5769-4758*

References

[1] Kiswanto K and Wintah W. Processing Coal Mine Acidic Water Using Nanofiltration Membrane in West Aceh. Ecological Engineering & Environmental Technology. 2024; 25(7):34–45. https://doi.org/10.12912/27197050/187923

[2] Ighalo J O, et al. A review of treatment technologies for the mitigation of the toxic environmental effects of acid mine drainage (AMD). Process Safety and Environmental Protection. 2022; 157:37–58. https://doi.org/10.1016/j.psep.2021.11.008

[3] Zaki D E Z, et al. Sustainable Acid Mine Drainage Water Reclamation Using Silica-pectin Multichannel Tubular Membrane: A Comparison of Ultrafiltration Vs Pervaporation. Leuser Journal of Environmental Studies. 2024; 2(2):86–94. https://doi.org/10.60084/ljes.v2i2.215

[4] Du G, Ho H-J, and Iizuka A. A critical review of current treatment methods of acid mine drainage with an assessment of associated CO2 emissions toward carbon neutrality. Journal of Water Process Engineering. 2025; 77:108347. https://doi.org/10.1016/j.jwpe.2025.108347

[5] Lagdali S, et al. Low-cost ceramic membranes: Manufacturing methods, cost analysis and application in water and wastewater treatment: A review. ChemPhysMater. 2026; 5(1):22–49. https://doi.org/10.1016/j.chphma.2025.08.002

[6] Lee M, Wu Z, and Li K. Advances in ceramic membranes for water treatment. in Advances in Membrane Technologies for Water Treatment, Elsevier. 2015, 43–82. https://doi.org/10.1016/B978-1-78242-121-4.00002-2

[7] Suhot M A, Hassan M Z, Aziz S A, and Md Daud M Y. Recent progress of rice husk reinforced polymer composites: A review. Polymers (Basel). 2021; 13(15):2391. https://doi.org/10.3390/polym13152391

[8] Fernandes I J, Moraes C A M, Egea J R J, and Sousa V C. Production and characterization of silica materials from rice husk ash by different combustion processes. Powder Technol. 2024; 436:119473. https://doi.org/10.1016/j.powtec.2024.119473

[9] Banurea I R, Setyawan N, Yuliani S, Herawati H, and Hoerudin. Utilization of rice husk silica as solid catalyst in the transesterification process for biodiesel production. IOP Conf. Ser. Earth Environ. Sci. 2021; 739(1):012083. https://doi.org/10.1088/1755-1315/739/1/012083

[10] Dorairaj D, and Govender N T. Rice and paddy industry in Malaysia: governance and policies, research trends, technology adoption and resilience. Front. Sustain. Food Syst. 2023; 7. https://doi.org/10.3389/fsufs.2023.1093605

[11] Kusdarini E, Onofrisan S M, Cahyono Y D G, and Budianto A. Innovative coconut frond-derived activated carbon for treating acid mine drainage. Journal of Ecological Engineering. 2026; 27(7):109–124. https://doi.org/10.12911/22998993/218292

[12] Ratnawulan, Rahmadhani D, Zulkifli, Yuliani K D, Frida E, and Taufiq A. Hydrophobic and antibacterial properties of textiles using nanocomposite chitosan and SiO2 from rice husk ash as-coating. S. Afr. J. Chem. Eng. 2024; 48:366–374. https://doi.org/10.1016/j.sajce.2024.03.010

[13] Alsubei M D, Reid B, Aljlil S A, Coppens M-O, and Campos L C. Fabrication and characterization of coated ceramic membranes from natural sources for water treatment applications. J. Memb. Sci. 2024; 690:122226. https://doi.org/10.1016/j.memsci.2023.122226

[14] Surya I, Sembiring AM, Nasution K S, and Hayeemasae N. The porosity and morphology properties of ceramic membrane. J. Phys. Conf. Ser. 2024; 2733(1):012014. https://doi.org/10.1088/1742-6596/2733/1/012014

[15] Dashtban Kenari SL, Mortazavi S, Mosadeghsedghi S, Atallah C, and Volchek K. Advancing Ceramic Membrane Technology for Sustainable Treatment of Mining Discharge: Challenges and Future Directions. Membranes (Basel). 2025; 15(4):112. https://doi.org/10.3390/membranes15040112

[16] Hamad K H, Abdallah H, Aly S T, Abobeah R, and Amin Sh K. Fabrication and assessment of performance of clay based ceramic membranes impregnated with CNTs in dye removal. Sci. Rep. 2024; 14(1):26728. https://doi.org/10.1038/s41598-024-77015-3

[17] Chakraborty S, Uppaluri R, and Das C. Effect of pore former (saw dust) characteristics on the properties of sub-micron range low-cost ceramic membranes. International Journal of Ceramic Engineering & Science. 2020; 2(5):243–253. https://doi.org/10.1002/ces2.10061

[18] Vicente R, Cesca K, da Silva A F V, de Oliveira D, de Andrade C J, and Ambrosi A. Hierarchical membrane by centrifugal casting and effects of incorporating activated carbon as pore-former. J. Eur. Ceram. Soc. 2023; 43(8):3447–3453. https://doi.org/10.1016/j.jeurceramsoc.2023.02.040

[19] International Centre for Diffraction Data, PDF-4+ 2024: Powder diffraction file [Database]. International Centre for Diffraction Data. 2024.

[20] Gashawtena E, Kidane A, and Sirahbizu B. The effect of nanocellulose and silica filler on the mechanical properties of natural fiber polymer matrix composites. Results in Engineering. 2024; 24:102898. https://doi.org/10.1016/j.rineng.2024.102898

[21] Xu M, Wang J, and Wu J. Recent advances of silicate materials for wastewater treatment: a review. Mater. Res. Express. 2024; 11(3):032001. https://doi.org/10.1088/2053-1591/ad2c63

[22] Taha Y R, et al. Optimum content of incorporated nanomaterials: Characterizations and performance of mixed matrix membranes a review. Desalination Water Treat. 2024; 317:100088. https://doi.org/10.1016/j.dwt.2024.100088

[23] Mohamed F, et al. Activated carbon derived from sugarcane and modified with natural zeolite for efficient adsorption of methylene blue dye: experimentally and theoretically approaches. Sci. Rep. 2022; 12(1):18031. https://doi.org/10.1038/s41598-022-22421-8

Crossref
DOI: 10.31643/2028/6445.32
Mining & Mineral Processing

Blast Furnace Slag as an Alternative to Natural Mineral Materials in Pavement Engineering: A Review

[1]Kunaev V.A., [1]Akhmetova G.E., [1*]Ospanova A.Z., [1]Kenzhaliyev O.B., [1]Tavshanov I.S., [2]Fathi M.S., [1]Ulyeva G.A., [1]Batyrbek A.E., [1]Charnyi D.Yu.

[1] Karaganda Industrial University, Karaganda region, Temirtau, Kazakhstan
[2]Universiti Teknologi Malaysia, Kuala Lumpur, Malaysia

** Corresponding author email: a.ospanova@tttu.edu.kz*

Received: *July 30, 2026*
Peer-reviewed: *August 28, 2026*
Accepted: *September 8, 2026*

ABSTRACT
The presented literature review contains the results of the analysis of scientific articles for 2000-2026 years, considering the use of blast furnace slag in various areas of road construction. It has been established that there are clear differences between the application options for different types of blast furnace slag. Air-cooled blast furnace slag (ACBFS) is more often used as a coarse or fine aggregate for cement concrete and asphalt concrete, and ground granulated blast furnace slag (GGBFS) is used as an additional binder or as a mineral/reactive filler. When using blast furnace slag in the production of concrete, the highest results in a number of studies were achieved when replacing 20-40% of the aggregate with slag, although this indicator was not a universal optimal value. In some articles, it was pointed out that the use of blast furnace slag as part of the base of a highway or for soil stabilization was associated with an increase in CBR. Some authors point to a reduction in the consumption of Portland cement when using complex binders containing granular blast furnace slag. Data on the improvement of water resistance, fatigue resistance, Marshall stability, and rutting resistance of asphalt concrete with the introduction of ACBFS and GGBFS in various proportions are also presented. Pretreatment of porous ACBFS was also important: selective crushing and related separation methods reduced water absorption, crushing value, and the proportion of weak porous particles. The main practical conclusion is that BFS should not be treated as a single interchangeable material. Its use should be selected according to slag type, particle quality, the component being replaced, and the required pavement property. Further studies should examine whether improvements achieved by slag pretreatment at the aggregate level are retained in concrete, asphalt mixtures, and pavement-base materials under long-term service conditions.

Keywords: air-cooled blast furnace slag, ground granulated blast furnace slag, natural mineral resource substitution, aggregate enrichment, cement concrete, asphalt concrete, pavement base materials.

Information about authors:

Kunaev Vyacheslav Alexandrovich — *PhD, Associate Professor, Director of the Department of Science and Innovations, Karaganda Industrial University JSC, Republic Ave., 30, 101400, Temirtau, Karaganda region, Kazakhstan. E-mail: v.kunayev@tttu.edu.kz; ORCID ID: https://orcid.org/0000-0001-8283-7186*

Akhmetova Gulzhainat Esenzholovna — *PhD, Associate Professor, Karaganda Industrial University JSC, Republic Ave., 30, 101400, Temirtau, Karaganda region, Kazakhstan. E-mail: agulzhajnat@bk.ru; ORCID ID: https://orcid.org/0000-0001-8244-5027*

Ospanova Ayaulym Zaynullaevna — *PhD student, Karaganda Industrial University JSC, Republic Ave., 30, 101400, Temirtau, Karaganda region, Kazakhstan. E-mail: a.ospanova@tttu.edu.kz; ORCID ID: https://orcid.org/0009-0002-0597-1220*

Kenzhaliyev Olzhas Bagdauletovich — *PhD, docent, Karaganda Industrial University JSC, Republic Ave., 30, 101400, Temirtau, Karaganda region, Kazakhstan. E-mail: o.kenzhaliyev@tttu.edu.kz; ORCID ID: https://orcid.org/0000-0002-3776-9724*

Tavshanov Ilgar Suleimanovich — *Researcher, Karaganda Industrial University JSC, Republic Ave., 30, 101400, Temirtau, Karaganda region, Kazakhstan. E-mail: i.tavshanov@tttu.edu.kz; ORCID ID: https://orcid.org/0000-0002-9427-9748*

Fathi Mohamad Syazli — *PhD, Associate Professor, Universiti Teknologi Malaysia, Jalan Sultan Yahya Petra, 54100, Kuala Lumpur, Malaysia. E-mail: syazli@utm.my; ORCID ID: https://orcid.org/0000-0002-0474-6278*

Ulyeva Gulnara Anatolyevna — *PhD, Professor, Karaganda Industrial University JSC, Republic Ave., 30, 101400, Temirtau, Karaganda region, Kazakhstan. E-mail: g.ulyeva@tttu.edu.kz; ORCID ID: https://orcid.org/0009-0002-7300-1277*

Batyrbek Alibek Yesimbekuly — *PhD student, Karaganda Industrial University JSC, Republic Ave., 30, 101400, Temirtau, Karaganda region, Kazakhstan. E-mail: a.batyrbek@tttu.edu.kz; ORCID ID: https://orcid.org/0000-0002-3369-6804*

Charnyi Dmitryi Yurievich — *Junior Researcher, Karaganda Industrial University JSC, Republic Ave., 30, 101400, Temirtau, Karaganda region, Kazakhstan. E-mail: dmitryi.charnyy@gmail.com; ORCID ID: https://orcid.org/0009-0005-9438-2330*

Introduction

Road construction requires large volumes of natural aggregates and cementitious materials. At the same time, metallurgical production generates mineral by-products that can partly replace these conventional resources. Blast furnace slag (BFS) is one of the most widely studied materials of this type and is used in concrete, pavement layers, soil stabilization, and asphalt mixtures [[1], [2], [3], [4], [5], [6]].

The physical and mechanical properties of blast furnace slag largely depend on the cooling method. Slow air cooling produces air-cooled blast furnace slag (ACBFS), which is mostly crystalline, angular, and often porous and is used primarily as a coarse or fine aggregate. During rapid cooling, granulated blast furnace slag (GBFS) is formed, which has a higher content of the glassy phase. After grinding, GBFS is converted into ground granulated blast furnace slag (GGBFS), which exhibits latent hydraulic activity and is used mainly as a supplementary cementitious material or as a mineral or reactive filler [[7], [8], [9], [10], [11]]. The differences in the appearance and microstructure of ACBFS and GBFS are shown in Figure 1. The porous structure of some ACBFS fractions may increase water absorption and reduce resistance to cyclic environmental effects, whereas denser or processed slag fractions can show substantially better engineering properties [[6],[12], [13], [14], [15]].

Published studies address several distinct applications of BFS, including aggregate replacement in cement concrete, partial replacement of cement by GGBFS, use in pavement bases and subbases, soil stabilization, and incorporation into asphalt mixtures. Direct comparison of these studies is difficult because the term “BFS replacement” may refer to replacement of coarse aggregate, fine aggregate, cement, total binder, or mineral filler. In addition, the studies differ in slag type, dosage basis, treatment method, mixture composition, curing conditions, and performance criteria. As a result, replacement percentages reported in different studies cannot be interpreted independently of the function of the slag in the material.

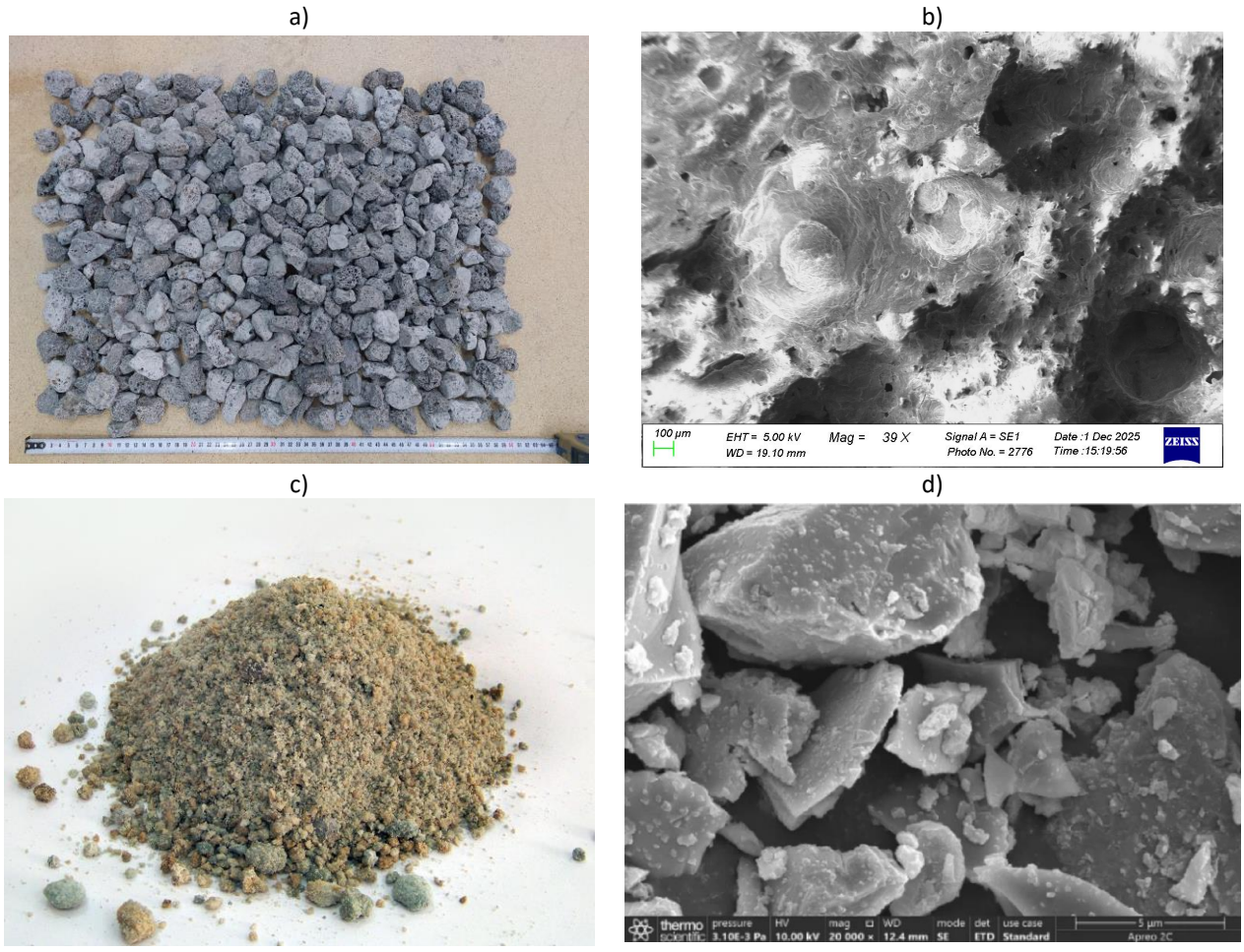

Figure 1 – General view and SEM images of blast-furnace slag: a) air-cooled blast-furnace slag (ACBFS); (b) SEM micrograph of ACBFS; (c) granulated blast-furnace slag (GBFS); and (d) SEM micrograph of GBFS

The aim of this review is to compare the reported use of ACBFS, GBFS, and GGBFS in road construction materials and to identify the main relationships between slag type, processing method, replacement level, and engineering performance. Particular attention is given to cement concrete, cementitious systems, pavement bases and subbases, soil stabilization, and asphalt mixtures. The review also examines the limitations associated with untreated slag and the effect of processing and modification on its potential use in pavement materials

Materials and methods

The literature search covered publications issued between 2000 and 2026 and was completed on 25 July 2026. The main search was conducted in Scopus, Web of Science, ScienceDirect, and eLIBRARY.RU. ResearchGate and Academia.edu were used as additional sources for locating full-text publications. The search was based on a combination of terms describing blast furnace slag and its application in road and construction materials. The following search expression was used: (“blast furnace slag” OR “GGBFS” OR “ACBFS”) AND (“pavement” OR “asphalt concrete” OR “road construction” OR “cementitious composites”).

The search expression was adapted to the syntax of the individual databases while retaining the same set of keywords and the same publication period. The reference lists of relevant publications were also examined to identify additional studies that could be useful for the analysis.

The database search identified a total of 1120 records published between 2000 and 2026. At the title and abstract screening stage, 370 records were excluded because their subject matter was outside the scope of the review. Of the remaining 750 records, full-text versions were available for 342 publications. The full texts were subsequently assessed with regard to the subject of the study, the type of slag investigated, the presence of an experimental component, and the availability of quantitative results suitable for comparative analysis.

After the full texts were checked, 262 publications were removed from the final sample. The main reasons were the absence of experimental work, the lack of separately reported data for blast furnace slag, insufficient experimental detail, or a topic outside the scope of this review. Publications that could not be obtained in full text were not included in the detailed assessment.

The final set included 80 publications: 77 primary research papers and three review articles. The quantitative comparisons in this review are based mainly on the primary studies. The three review papers were used only for background information, terminology, general research trends, and for identifying additional primary studies from their reference lists.

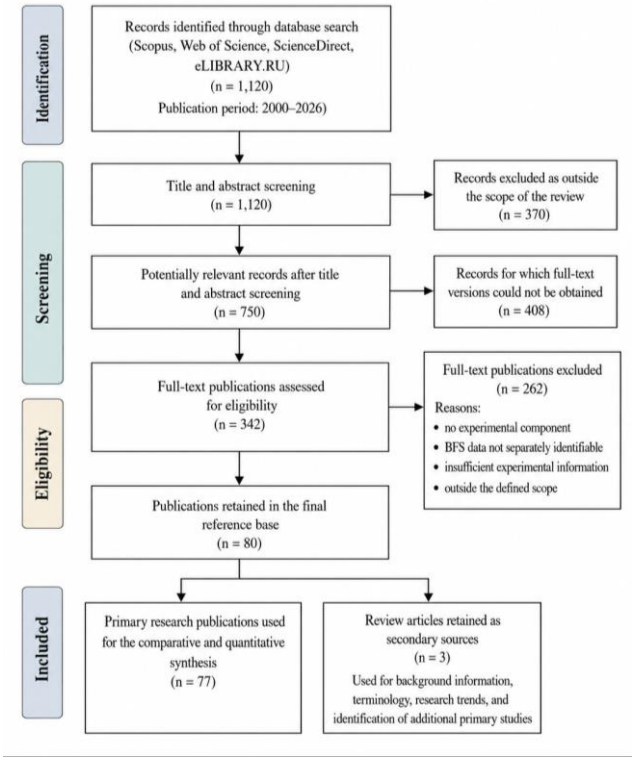

Figure 2 – Flow diagram of the literature search and selection procedure

Primary studies were considered suitable for comparative analysis when they met the following conditions:

- they investigated blast furnace slag or one of its principal forms;

- contained an experimental component;

- examined its use as an aggregate, cementitious component, mineral or reactive filler, pavement-base or subbase material, or soil-stabilization component;

- reported quantitative results allowing the influence of slag incorporation or treatment to be evaluated;

- provided sufficient information on the experimental conditions and composition of the investigated material.

Studies were excluded from comparative analysis when they dealt exclusively with metallurgical slags other than blast furnace slag, did not report the BFS-related results separately, did not contain original experimental data, lacked sufficient information for interpretation of the experimental results, or addressed applications outside the scope of road construction and related construction materials. Duplicate records and repeated publications reporting the same experimental dataset were considered only once.

The methodological suitability of the primary studies was assessed during full-text analysis. Particular attention was given to clear identification of the blast furnace slag type, description of the investigated materials and mixture composition, specification of the slag content or replacement level, description of the experimental procedure, and availability of quantitative performance data. Studies for which these parameters could not be established with sufficient confidence were not used for quantitative comparison.

To ensure a uniform interpretation of the studies reviewed, the following terms and definitions were used. Blast furnace slag (BFS) was used as a general term encompassing various forms of blast furnace slag. Air-cooled blast furnace slag (ACBFS) was defined as a slowly cooled, predominantly crystalline slag mainly used as coarse or fine aggregate. Granulated blast furnace slag (GBFS) was defined as a rapidly cooled, unground slag used as a granular material or fine aggregate. Ground granulated blast furnace slag (GGBFS) was defined as ground GBFS, primarily used as a supplementary cementitious material or as a mineral or reactive filler. The abbreviation GGBFS is used consistently throughout the main text, tables, and figures, whereas the alternative abbreviation GGBS is retained only when reproducing the terminology of the source, including article titles and the corresponding entries in the comparative tables.

Coarse aggregate refers to the larger particle-size fraction, whereas fine aggregate refers to the smaller particle-size fraction. The nominal boundary between these fractions varies among standards; a value of 4 mm is commonly used in European practice, while other national systems use different limits.

The primary studies were compared by slag type, application, mixture composition, replacement approach, test conditions, and reported performance. They were grouped into four application areas:

1) BFS as aggregate in cement concrete;

2) BFS as a supplementary cementitious component;

3) BFS in pavement bases, subbases, and soil stabilization;

4) BFS in asphalt mixtures.

The main experimental conditions and quantitative results for each group were compiled in tables 2-5. Particular attention was given to the slag type, the component being replaced, the replacement or dosage level, the modification or activation method, and the resulting changes in mechanical properties, durability, and other performance characteristics.

Direct comparison of replacement percentages reported in different studies was carried out with caution because the same numerical value may refer to different material functions. ACBFS is generally used as a replacement for natural coarse or fine aggregate, whereas GBFS and GGBFS may be used as granular material, supplementary cementitious components, or mineral and reactive fillers. Accordingly, the interpretation of the reported replacement levels was based on the type of slag, the component being replaced, and the basis on which the dosage was calculated.

Results and Discussion

Table 1 shows the chemical compositions of blast furnace slag given in various scientific studies. As can be seen from Table 1, the chemical composition differs significantly depending on the source of the slag. Nevertheless, CaO, SiO_2, Al_2O_3, and MgO are the principal oxide components in most of the investigated slags. The reported contents are approximately 29–50% CaO, 27–42% SiO_2, 5–22% Al_2O_3, and up to 21% MgO. Together, these oxides generally account for more than 90% of the slag composition [[12], [13], [16], [17], [18], [19], [20], [21], [22], [23], [24], [25], [26], [27], [28], [29], [30], [31], [32], [33], [34], [35], [36], [37], [38], [39], [40], [41], [42], [43]].

Table 1 - Chemical composition of blast furnace slags reported in the reviewed studies, wt.%

Slag	CaO	SiO_2	Al_2O_3	Fe_2O_3	MgO	MnO	S	SO_3	Na_2O	K_2O	Source
WBFS	32.54	32.53	12.14	1.59	17.60	1.03	1.05		0.12	0.60	Kambole C, et al. [12]
FBFS	35.09	35.51	13.72	1.75	9.16	1.37	0.59		0.30	1.26	
BFS	34-43	27-38	7-12		7-15	0.15-0.76	1.0-1.9				Ren Q, et al. [13]
GGBFS	44.9	35.4	13.0	0.47	5.01			1.31		0.37	Lee G, et al. [16]
GBFS	39.1	35.1	12.8	0.7	10.1			-			Bonavetti VL, et al. [17]
BFS	42.69	40	7.35	2.28	5.19			1.24		0.74	Deboucha W, et al. [18]
ACBFS	30-40	28-42	5-22	0.3-1.7	5-15	0.2-1	1-2				Kanniyappa N, et al. [19]
GBFS	35.7	36.9	9.41	2.28	9.03		1.6	0.06	1.1	1.2	Fuentes-Romero M, et al. [20]
GBFS	37.8	35.11	17.54	-	5.54			0.7	0.38	0.98	Özkan O. [21]
BFS	38.96	35.5	12.52	0.54	9.88			0.54	0.07	0.43	Carrasco MF, et al. [22]
GBFS	38.05	34.87	14.38	0.89	8.03			1.96	<0.01	0.72	Kovtun M, et al. [23]
BFS	40.8	35.4	13	0.5	8.0			0.1	0.2	0.5	Zhou J, et al. [24]
GBFS	37.8	33.4	11.3	0.5	8.9	0.5		3.4	0.5	0.9	Burciaga-Díaz O, et al. [25]
ACBFS	41.37	39.01	9.14		7.57	0.51			0.01	0.64	Nicula LM, et al. [26]
GGBFS	40.80	38.10	9.50	0.56	8.10	0.23			0.30	0.68	
BFS	40.47	35.28	9.71	0.56	8.76			3.79	0.41	0.45	Bleszynski R, et al. [27]
BFS	21.98	33.69	8.69	23.73	0.88	2.47		0.949		0.89	Vadhera K, et al. [28]
GGBFS	32.61	36.70	14.21	0.98	10.12			0.99	0.42	0.76	Yahyaee T, Elize HS [29]
ACBFS	31.1	31.3	11.9	1.67	13.7	0.291			0.515	0.639	Tole I, et al. [30]
GGBFS	30.3	34	11.6	0.291	12.1	0.516			0.531	0.811	
BFS	39.63	38.3	8.81	0.98	5.54			1.35	0.13	0.59	Benmammar M, et al. [31]
GBFS	37.79	35.09	17.54		5.50	0.83	0.66		0.30		Yuksel I, et al. [32]
BFS	32.45	32.47	9.94	1.25	9.31	3.51	0.33	0.82	0.31	0.85	Geçkil T, et al. [33]
BFS	44.50	33.84	10.35	0.67	7.99			-	0.20	0.40	Lübeck A, et al. [34]
GGBFS	41.81	36.44	11.60	0.78	5.8	0.55			0.345	0.428	Nicula L. M, et al. [35]
BFS	30.4	35	14.3	0.3	16.1	0.5		0.7	0.6	0.7	Humad AM, et al. [36]
GBFS	37.09	35.91	12.56	0.34	11.23			1.19	0.25	0.49	Tan K, et al. [37]
ACBFS	44.3	40.7	8.0		5.2	0.2	0.65				Kunaev V, et al. [38]
GBFS	33.9-40.9	34.3-42.0	9.0-12.9	0.00-1.74	8.7-14.0	0.10-1.11			0.19-0.72	0.19-1.52	Adigamov RR, et al. [39]
GGBFS	37.34	37.73	14.42	1.11	8.71	0.02	0.39				Karikatti V, et al. [40]
GBFS	34.4	42.0	12.2	1	6.8	1.1	0.6			0.9	Soğanci AS, et al. [41]
GGBS	32.61	36.7	14.21	0.98	10.12			0.99	0.42	0.76	Yahyaee T, et al. [42]
BFS	38.10	36.00	13.00	0.60	6.60			0.60	0.50	1.10	Bagheri AR, et al. [43]

The differences between individual samples are most noticeable for MgO and Al_2O_3. CaO and SiO_2 contents are comparatively less variable, although their ratio also changes between slag sources. These variations reflect differences in raw materials, blast-furnace operation, cooling conditions, and subsequent processing. Therefore, slags classified under the same general term may differ substantially in mineral structure and engineering behaviour.

The cooling method is particularly important when the slag is considered for construction applications. Slowly cooled ACBFS is mainly crystalline and commonly has a rough and porous particle surface. These characteristics are relevant when the material is used as aggregate because they affect water absorption, particle strength, compaction, and the quality of the aggregate–paste or aggregate–bitumen interface. Rapidly cooled GBFS contains a larger glassy fraction, while grinding increases its specific surface and produces GGBFS suitable for use as a cementitious component.

The $CaO–SiO_2–Al_2O_3–MgO$ composition of GBFS and GGBFS provides the chemical basis for their latent hydraulic behaviour. During hydration or activation, these materials can contribute to the formation of calcium silicate hydrate and calcium aluminosilicate hydrate phases. However, chemical composition alone is insufficient to predict performance. Fineness, glass content, activation conditions, replacement level, and the composition of the surrounding binder also influence the resulting properties.

Blast furnace slag as aggregate in cement concrete.

Blast furnace slag is used as both coarse and fine aggregate in cement concrete. The studies summarized in Table 2 show that the resulting properties depend not only on the replacement level but also on slag type, particle porosity, grading, mixture composition, and compaction conditions.

Several studies reported favourable results at moderate replacement levels. About 30% ACBFS replacement of natural coarse aggregate gave the best overall result in M25 concrete [19]. For unground GBFS used as fine aggregate, favourable results were reported at about 20–30% replacement [[32], [44]], while 30% replacement of natural river sand with GBFS produced the highest compressive, splitting tensile, and flexural strengths in [45]. In road concrete containing a constant GGBFS dosage and 20–60% ACBFS sand, the mixture with 20% ACBFS showed the lowest pore density after 300 freeze–thaw cycles [35], the highest wear resistance among the slag mixtures [46], and lower shrinkage [47]. These results explain why replacement levels of approximately 20–40% occur repeatedly in the reviewed studies. This range, however, should be regarded only as a recurring tendency and not as a universal optimum.

Table 2 – Blast furnace slag as coarse or fine aggregate in cement concrete for road and civil construction

Authors	Year	Substitution approach	Key quantitative results
Kanniyappan SP, et al. [19]	2018	Replacement of natural coarse aggregate with ACBFS at 0%, 10%, 20%, 30%, 40%, and 50% in M25 concrete.	At 28 days, compressive strength peaked at 35.64 MPa with 30% ACBFS, 19.4% above the control (29.86 MPa). Split tensile strength reached a maximum of 4.99 MPa at 40% ACBFS, 28.6% above the control (3.88 MPa). The authors recommended ACBFS contents up to 30% for overall use.
Özkan Ö [21]	2007	Fly ash replaced part of the cement, while unground CBA and GBFS replaced fine aggregate (FA). Two series were studied: M1 with CBA+GBFS and M2 with FA+CBA+GBFS; properties were measured at 7, 28 and 90 days.	Compressive strength, bulk density and water absorption all decreased as the combined waste content increased. The authors considered the modest strength reduction acceptable only for low-strength concrete when CBA and GBFS contents were kept within reasonable limits.
Nicula LM, et al. [26]	2023	Road-concrete mixes contained 15% GGBS replacing cement and either 25% or 50% ACBFS replacing natural sand; reference mix contained conventional cement and natural aggregate. Mortars with 50% GGBS were also studied for HAI.	Flexural strength increased from 28 to 90 days by 20.72% and 20.26% for the two slag concretes, versus 18.58% for the reference. The 15% GGBS + 25% ACBFS concrete reached performance similar to the control at 90 days. GGBS was strength class 80 at 28 days and class 100 at 90 days by HAI.
Vadhera K, et al. [28]	2017	BFS incorporated into rigid-pavement concrete replacing stone coarse aggregate (0%, 20%, 40%, 60% and 100%)	Concrete with 100% slag aggregate showed 10% higher compressive strength than conventional. Split tensile strength dropped 48% at 40% slag but rose ~10% at higher replacements.
Yahyaee T, et al. [29]	2024	GGBFS replaced 30%, 40%, and 50% of Portland cement by mass; steel or carbon fibers were added at 0.5%, 1.0%, and 1.5% by concrete volume; w/c = 0.40.	At 28 days, G50S1.5 reached 30.1 MPa, only 5.5% below the control. At 90 days, G50S1.5 showed >38% higher compressive strength than the control. G30S1.5 increased flexural strength by 33.3% at 28 days and 32.22% at 90 days. G50S1.5 improved abrasion resistance by 25%, while G50S0.5 reduced CO_2 emissions by 40.34%.
Yuksel I, et al. [32]	2007	Non-ground GBFS, bottom ash (BA), or an equal GBFS+BA blend replaced 10%, 20%, 30%, 40%, and 50% of the natural 0–3 mm fine aggregate. Durability was assessed by high-temperature, freeze–thaw, drying–wetting, capillarity, and abrasion tests.	Freeze–thaw resistance improved at low-to-moderate replacement levels, with the best performance around 20% and an acceptable range of 20–30%. The 10% replacement level gave the lowest capillarity, while all mixtures remained within abrasion limits. Overall, the authors identified 20% fine-aggregate replacement as the optimum level for normal concrete.

Nicula LM, et al. [35]	2021	Three slag road-concrete mixes used a constant 54 kg/m³ GGBS and 20%, 40% or 60% crushed ACBFS aggregate; two conventional concretes used 360 and 414 kg/m³ Portland cement. Samples were subjected to 300 freeze–thaw cycles.	After 300 freeze–thaw cycles, S54/20 (containing 360 kg/m^3 (cement) + 54 kg/m^3 (GGBS) and 20% (ACBFS)_0/4 mm + 80% (natural sand)_0/4); showed the lowest pore density and the highest compressive strength. Mixtures with 40–60% ACBFS exhibited increased gel and capillary pore sizes.
Adigamov RR, et al. [39]	2020	Milled granulated BFS replaced 40% of Portland cement in road-pavement concrete.	40% GGBFS replacement yielded 6.80 MPa flexural and 53.5 MPa compressive strength, reduced water absorption by 45% (to 2.6%), doubled frost resistance, and improved abrasion resistance by 40%.
Nicula LM, et al. [48]	2020	Three road-concrete mixtures contained a constant 54 kg/m³ GGBFS (13% cement replacement relative to the 414 kg/m³ cement control) and 20%, 40% or 60% crushed ungranulated blast-furnace slag (0/4 mm) replacing natural sand.	After 300 freeze–thaw cycles, S54/20 showed no measurable reduction in freeze–thaw resistance (UPV = 4.642 km/s; dynamic modulus = 41.26 GPa), while the reduction was only 0.12% for S54/40 and 2.74% for S54/60. Water penetration remained below 8 mm for S54/20 and S54/40 but increased to 16 mm for S54/60.
Cao Q, et al. [49]	2022	ACBFS coarse aggregate replaced limestone coarse aggregate by volume at 30%, 50% and 100%; both straight and hooked steel fibres were incorporated in ultra-high-performance fiber-reinforced concrete (UHPFRC) mixtures.	A 30% ACBFS replacement produced mechanical properties close to, and in some cases slightly higher than, those of natural-aggregate UHPFRC. At 100% replacement, compressive strength decreased by about 4.5% in UR100 and 14.4% in UB100; elastic modulus decreased by about 2%, while flexural strength decreased by 9.44% and 30.25%, respectively. Workability and density decreased as ACBFS content increased.
Nicula LM, et al. [47]	2023	Five road-concrete mixtures: controls S360 and S414; slag mixtures contained 360 kg/m³ cement + 54 kg/m³ GGBS and replaced natural 0/4 mm sand with ACBFS at 20%, 40% and 60%.	At 150 days, flexural tensile strength reached 6.57 MPa for S54/20 (mix with 20 % BFS) and 6.31 MPa for S54/60. Shrinkage versus S414 decreased by 32.02% for S54/20 and 27.53% for S54/60 (mix with 60 % BFS). At 480 days, all slag concretes exceeded controls in compressive strength; S54/60 was highest. S54/20 showed the lowest portlandite content and Ca/Si = 1.96.
Verian KP, et al. [50]	2015	Natural dolomite coarse aggregate was replaced with ACBFS. Four pavement concretes were studied: ACBFS - and dolomite-based mixtures with either 100 % ordinary Portland cement (OPC) or 20% Class C fly ash replacing OPC by mass; w/cm = 0.42.	ACBFS concrete developed up to ~6% higher compressive strength but up to ~15% lower flexural strength than dolomite concrete. Under $CaCl_2$ freeze–thaw exposure, plain ACBFS concrete failed after 111 cycles versus 151 cycles for plain dolomite concrete, whereas the corresponding fly-ash concretes remained intact after 321 and 350 cycles, respectively.
Sawant AB, et al. [51]	2019	Natural coarse aggregate was replaced by BFS at 50%, 75% and 100%. Two M40 concrete mixtures with w/c = 0.50 (Mix A) and 0.45 (Mix B) were investigated.	Among the BFS mixtures, 50% coarse-aggregate replacement gave the highest compressive strength. At 28 days, 50% BFS reached 48.15 MPa versus 48.74 MPa for the Mix A control and 48.74 MPa versus 50.52 MPa for the Mix B control. At 56 days, the corresponding BFS concretes exceeded the controls, reaching 50.07 vs. 49.04 MPa and 55.70 vs. 53.93 MPa, respectively.
Ta Y, et al. [52]	2023	Granulated blast-furnace slag fine aggregate replaced silica sand at 25%, 50%, 75% and 100% by volume. Freeze–thaw resistance under 3% NaCl exposure, electrical resistivity, chloride-ion diffusion, and ITZ microstructure were evaluated.	Freeze–thaw resistance improved as the BFS fine-aggregate fraction increased. At w/c = 40%, mortar with BFS-H retained >80% of its mass after 28 cycles, whereas the crushed-sand mortar was nearly destroyed by 24 cycles. Mixtures containing ≥75% BFS-I retained >90% of their mass after 10 cycles, while the silica-sand reference was almost completely deteriorated. BFS also increased electrical resistivity and reduced chloride-ion diffusion. A 0.45–1.4 μm reaction layer containing hydrotalcite-like phases was identified at the BFS–cement-paste ITZ.

Dhanasri K, et al. [53]	2013	Natural coarse aggregate was replaced with BFS and natural fine aggregate with crusher dust simultaneously at 0–100% in 10% increments; concrete proportion 1:1.86:3.77, w/c = 0.45.	At 30% replacement, 28-day compressive strength remained approximately equal to the control, while splitting tensile and flexural strength showed only a marginal increase. Above 30%, the mechanical properties declined.
Ríos JD, et al. [54]	2019	ACBFS used as industrial-waste aggregate in self-compacting concrete; the study compares concrete containing slag aggregate with conventional SCC.	50% ACBFS in self-compacting concrete lowered density (3-5%) and strength (23.7-26.5 MPa vs. 41.2 MPa), but vibrated mixes reached 56.7 MPa - 37% higher than reference overcoming porosity via compaction. Fracture energy rose 10.5-30% (51.3-60.6 N/m), with minor tensile loss. Leaching confirmed ACBFS as inert (EU 2003/33/EC).
Vamsi Mohan U, et al. [44]	2017	Natural fine aggregate and sand were replaced with 10%, 20%, and 30% GBFS.	Concrete with 20% GBFS reached 48.04 MPa at 28 days (w/c=0.3), 14% higher than the reference (42.14 MPa); at 30%, strength fell to 27.81 MPa (34% lower), indicating ~20% as optimal. Gains were strongest at low w/c (0.3-0.4), where GBFS densified the microstructure and enhanced long-term strength.
Džananović A, et al. [55]	2018	The authors used BFS (fraction 0/4mm, 4/8mm, 8/16mm, 16/31,5mm, 8- 11,2 mm, 11,2- 16 mm, 16-22,4mm) in concrete.	100% BFS aggregate concrete reached 39.5 MPa at 28 days, 32% above the C25/30 benchmark.
Nicula LM, et al. [46]	2020	Three slag concretes contained 54 kg/m³ GGBS and replaced natural 0/4 mm sand with ACBFS at 20%, 40% and 60%; compared with conventional S360 and S414 mixtures. Abrasion was tested at 100 and 150 days by the Böhme method.	Wear resistance was highest for the mix with 20 % BFS and lowest for the mix with 60 % BFS. Abrasion resistance followed compressive strength inversely through volume loss: stronger mixtures had lower abrasion loss. 20 % BFS and 40 % BFS exceeded S414, but slag mixtures were below the richer S360 control.
Sawant AB, et al. [56]	2019	Natural coarse aggregate was replaced by BFS at 50%, 75% and 100%. Two M40 concrete mixtures with w/c = 0.50 (Mix A) and 0.45 (Mix B) were investigated.	Among the BFS mixtures, 50% coarse-aggregate replacement gave the highest compressive strength. At 28 days, 50% BFS reached 48.15 MPa versus 48.74 MPa for the Mix A control and 48.74 MPa versus 50.52 MPa for the Mix B control. At 56 days, the corresponding values were 50.07 vs. 49.04 MPa and 55.70 vs. 53.93 MPa, respectively.
Singh G, et al. [57]	2015	GBFS used as replacement for natural sand in concrete; several contents were investigated together with compressive-strength and cost analysis.	Under normal curing, maximum compressive strength occurred at 50% GBFS (35.62 MPa at 28 d and 40.63 MPa at 90 d), compared with 20.79 and 22.56 MPa for the control. Under artificial marine conditions, maximum strength occurred at 60% GBFS (32.63 and 36.58 MPa at 28 and 90 d). Considering both strength and economy, the authors identified 40–50% GBFS as optimum under normal conditions and 50–60% under marine conditions.
Mujedu KA, et al. [58]	2018	100% replacement of crushed granite coarse aggregate by BFS in two nominal mixes, 1:1.5:3 and 1:2:4, both with w/c = 0.55.	Slump decreased from 47–48 to 41–43 mm for the 1:1.5:3 mix and from 45–46 to 39–40 mm for the 1:2:4 mix. At 28 days, compressive strength decreased from 20.00 to 18.96 MPa and from 17.93 to 17.33 MPa, respectively. BFS concrete also had lower density, although all measured densities remained within the normal-concrete range (2200–2550 kg/m³).
Pawar VS, et al. [45]	2022	Natural river sand was replaced with GBFS. Compressive strength was evaluated at replacement levels of 25%, 30%, 35%, 40%, and 50%, while splitting tensile and flexural strengths were evaluated at 25%, 30%, and 35%.	The best overall mechanical performance was reported at 30% replacement. Relative to the control concrete, compressive strength increased by 11.80%, splitting tensile strength by 22.64%, and flexural strength by 12.53%. Strength generally decreased when the GBFS content exceeded 30%.

The effect of slag aggregate also differs between individual performance indicators. In [32], the lowest capillarity was obtained at 10% GBFS, whereas the best freeze–thaw performance occurred at about 20%, with 20–30% considered an acceptable range. All mixtures tested in that study remained within the abrasion limits. In UHPFRC, 30% ACBFS produced mechanical properties close to those of the natural-aggregate reference, while further replacement reduced workability, flexural strength, fracture toughness, and fracture energy [49]. In pavement concrete, ACBFS increased compressive strength by approximately 6% compared with dolomite aggregate, but flexural strength was about 15% lower [50]. These results show that the replacement level associated with the highest compressive strength may not provide the best response for other properties relevant to pavement performance.

Higher replacement levels can nevertheless be effective in some mixtures. Complete replacement of natural aggregate with BFS gave higher compressive strength than conventional concrete in [28] and [55]. In contrast, self-compacting concrete containing ACBFS aggregate showed compressive strengths of 23.7–26.5 MPa compared with 41.2 MPa for the reference mixture, while vibration increased the strength to 56.7 MPa [54]. This difference indicates that the performance of high slag contents is strongly affected by particle quality and the degree of compaction.

Figure 3 summarizes the BFS replacement levels for which favourable values of selected performance indicators were reported. The ranges represent the span between the lowest and highest reported contents associated with favourable results and should not be interpreted as continuous optimum intervals. Intermediate contents were not necessarily tested in all studies and did not necessarily produce the same level of performance. Isolated favourable values outside the main ranges are shown separately.

Pretreatment can substantially improve the properties of ACBFS aggregate. Density-based separation reduced water absorption from approximately 4.9–6.8% to 2.19–3.13%, decreased the crushing value from 30–31% to 20–21%, and increased frost resistance from about 150 to 300–400 cycles [6]. Selective crushing followed by hydrophobization reduced water absorption to 1.08% and the mass loss after 15 sodium-sulfate cycles to 1.87% [38]. These results indicate that the replacement level should be considered together with the physical quality of the slag fraction. Removal of weak and highly porous particles can reduce variability and allow higher slag contents to be used without the same loss of aggregate quality.

GGBFS as a supplementary cementitious material.

In addition to its aggregate function, blast furnace slag is frequently used as a supplementary cementitious material in various composites (Table 3). In [18], replacement levels up to 30% provided equal or higher medium- and later-age strength, whereas 40% GGBFS reduced capillary absorption by approximately 40%. In [31], contents above 40% produced a marked increase in 28-day porosity. Conversely, long-term testing of pavement concrete showed that slag mixtures could exceed control strength at 480 days [47]. Assessment at only 7 or 28 days therefore systematically underestimates the later-age contribution of GGBFS.

The replacement levels associated with the highest strength and the best durability performance did not necessarily coincide in the studies summarized in Table 3. Several studies reported favourable combinations of early strength, workability, and later-age performance at GGBFS contents within approximately 20–40% of the cementitious component [[18], [31], [39], [59], [60]]. This interval should be regarded as a recurring tendency in the reviewed evidence rather than as a generally applicable optimum. Higher contents of 50–70% may be justified when electrical resistivity, chloride resistance, clinker reduction or specialized performance is prioritized. For example, 50% GGBFS in white cement produced approximately 35–60 MPa compressive strength, about five times the electrical resistivity and 14.6% lower cost, whereas further slag addition increased resistivity but reduced strength [34]. Increasing the GGBFS content from 10% to 50% resulted in a denser pore structure. At 50% replacement, the average pore diameter decreased by 47% at 28 days. The same mixtures also showed lower chloride permeability and higher electrical resistivity in long-term tests, although carbonation became more pronounced at higher GGBFS contents [42].

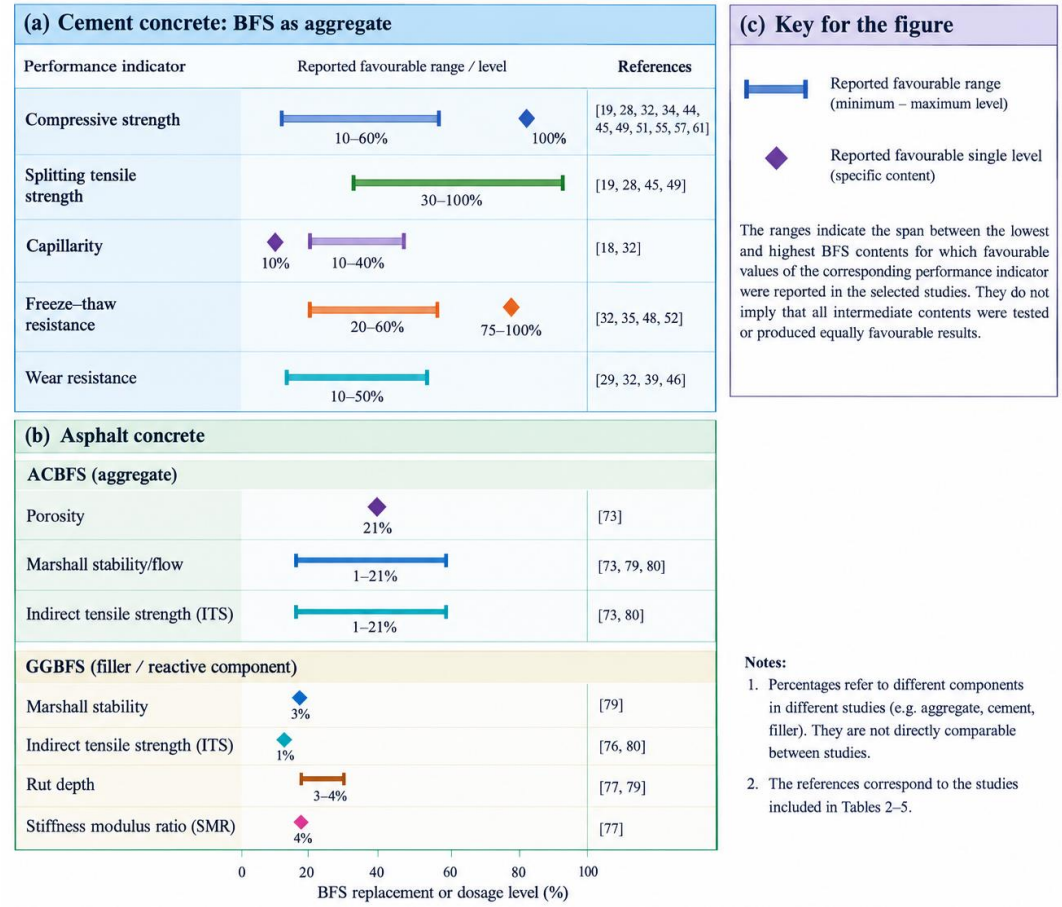

Figure 3 – Reported BFS replacement levels associated with favourable values of selected performance indicators

Table 3 – BFS as a supplementary cementitious material in cement-based composites

Authors	Year	Substitution approach	Key quantitative results
Bonavetti VL [17]	2014	Portland cement was replaced by silica fume up to 10% and/or GBFS up to 70%; binary and ternary binders were studied under sealed curing.	Silica fume provides early-age acceleration, while GBFS contributes to later-age strength; their synergy enables high clinker replacement without proportionate strength loss.
Deboucha W, et al. [18]	2015	Cement replaced separately with BFS or natural pozzolana at 10%, 20%, 30% and 40%.	BFS replacement up to 30% produced equal or better medium- and long-term strength than the control. At 40% BFS, capillary water absorption decreased by approximately 40% relative to the control; the control absorption was about 3.32 kg/m².
Fuentes-Romero M, et al. [20]	2011	100% H-class cement; 100% GBFS activated with 2% or 5% NaOH; and H-class cement/GBFS blends containing 20%, 40%, 60% and 80% GBFS. Sulfate resistance and alkali-aggregate reactivity were evaluated.	Pure H-class cement exceeded 20 MPa by 7 days; the 20% GBFS blend exceeded 20 MPa by 14 days. Increasing NaOH from 2% to 5% increased activated-slag strength. However, slag addition reduced early strength and the authors concluded that overall durability was limited for the tested composites.
Carrasco MF, et al. [22]	2005	Portland cement was replaced by combined limestone filler and BFS, with the experimental domain including up to 22% limestone filler and varying BFS content; strengths were measured at 2, 7, 14, 28, 90 and 360 days.	The ternary LF–BFS–PC blend outperformed the individual binary systems because limestone filler improved early strength and BFS improved later strength. Quadratic strength models had R^2 values of at least 0.80.

Zhou J, et al. [24]	2009	ECC matrices contained Portland cement, limestone powder and BFS; BFS replacement of cement increased from 50% to 70%. A simplified mixture used CEM III/B slag cement and limestone powder. PVA fibre content was 2% by volume.	At 28 days, the optimized mixture achieved 3.3% tensile strain capacity, 57 µm crack width and 38 MPa compressive strength. The simplified CEM III/B mixture achieved 3.1%, 76 µm and 40 MPa, respectively. All mixtures had average crack widths below 100 µm.
Bleszynski R, et al. [27]	2002	Seven field and laboratory concretes, including three ternary Portland cement–silica fume–blast-furnace slag mixtures.	After approximately 2 years of outdoor exposure, significant alkali–silica expansion occurred in the high-alkali control, whereas it was not observed in the ternary mixtures. Ternary systems also showed improved resistance to chloride ingress and deicer-salt deterioration.
Benmammar M, et al. [31]	2019	Reference concrete plus silica-fume concretes at 5%, 10% and 15% cement replacement and BFS concretes at 20%, 40% and 60%; binder = 350 kg/m³ and w/p = 0.50.	At 28 days, ultrasonic pulse velocity of all mixtures was approximately 3.96–4.36 km/s. Silica-fume concretes had higher dynamic modulus, UPV and compressive strength than the control. BFS slowed early hydration; porosity increased markedly above 40% replacement.
Lübeck A, et al. [34]	2012	White Portland cement replaced with 50% or 70% GGBFS; corresponding grey-cement mixtures and 100% white/grey cement controls were tested at several w/b ratios. Some mixtures used Na2SO4 activation.	The 50% GGBFS + 50% white-cement concrete delivered approximately 35–60 MPa compressive strength, about five times the electrical resistivity of the reference, 14.6% lower cost per m³, and nearly unchanged whiteness. Higher slag contents increased resistivity but reduced strength.
Divsholi BS, et al. [42]	2024	Portland cement replaced with 10, 30 and 50% GGBFS; w/cm = 0.4, 0.5 and 0.6	Increasing GGBFS content refined the pore structure; at 50% replacement the average pore diameter decreased by 47% at 28 d. At 4 years, chloride permeability remained very low (~400–800 C, depending on w/cm), while electrical resistivity reached 33–72 kΩ·cm. Compressive strength was maintained or slightly increased, although carbonation increased at 30–50% replacement.
Bagheri AR, et al. [43]	2012	Binary slag concretes contained 15%, 30% and 50% low-reactivity Grade 80 slag; binary silica-fume concretes contained 2.5%, 5%, 7.5% and 10% SF; ternary combinations were also tested. Total binder = 420 kg/m³ and w/b = 0.38.	Silica fume only moderately accelerated strength development of low-reactivity slag concrete but substantially improved electrical resistance, RCPT and chloride-migration performance up to 180 days. Ternary blends also required less superplasticizer than silica-fume-only mixes.
Familusi AO, et al. [59]	2017	A partial replacement of cement in concrete with 0%, 5%, 10%, 15%, and 20% BFS.	20% BFS replacement gave peak 28-day strength (20.87 N/mm²), 67% above control (12.50 N/mm²; F=5.873, p<0.01), despite lower workability at w/c=0.5.
Verma N, et al. [61]	2016	Replacement of fine and coarse aggregate of cement with 10%, 20%, 30% BFS and sand with Cast Iron Chips	Replacing cement with 10-20% BFS (with 30% cast iron chips) slightly increased compressive strength, but at 30% BFS + 30% chips, strength dropped by 6.12% (7 days) and 1.4% (28 days).
Okba SH, et al. [62]	2006	Addition of 0%, 17,5%, 23,3%, 25%, 35%, 75% BFS into concrete (instead of cement)	Higher slag replacement reduced 28-day strength but increased it significantly by 360 days. Slag mixes showed markedly improved corrosion and sulfate resistance at late ages, with resistance rising as slag content increased. Strength loss was greater in 5% MgSO4 than 2% MgSO4 solutions.
Iravani A, et al. [63]	2022	The study evaluated the effect of ground granulated blast furnace slag on the thermal performance of concrete under repeated heating–cooling cycles.	BFS cement (CEMIII/A) can significantly improve the residual compressive and flexural strengths, particularly after exposure to 20 thermal cycles and in combination with thermally stable aggregates such as basalt.

Babu KG, et al. [60]	2000	Addition of GGBS in concrete at the replacement levels: 0%, 10%, 30%, 50%, 60%, 65%, 70%, 80%	GGBS concrete strength depends on replacement level and age: 10-30% replacement yields 28-day strength comparable to or exceeding control, while 50-80% causes significant reduction. To match conventional concrete strength at 50% and 65% GGBS replacement, binder content must increase by 8.5% and 19.5%, respectively.
Huang H, et al. [64]	2014	BFS in cement paste containing 66% of slag and saturated Ca (OH)2 solution as an activator	66% BFS cement paste achieved ~60% filling of 10 μm cracks after 240 h self-healing in Ca(OH)2 solution. Crack ettringite (9.5 wt.%) doubled bulk content (5 wt.%); carbonation initially raised filling to 56% but declined to 47% upon completion.
De Matos PR, et al. [65]	2020	Pastes and self-compacting concrete (SCC) with GBFS, ACS and LF	ACS as SCM raised paste yield stress by 44-88% and viscosity vs. limestone, needing 0.95-1.36 kg/m³ superplasticizer for target flow. Despite no pozzolanic activity up to 91 days, ACS matched limestone in strength (~50 MPa) and hydration heat (~440 J/g), especially in 50/50 blends.

The efficiency of high replacement levels increases in multicomponent systems. Silica fume accelerates early hydration and compensates for the delayed strength development of GGBFS, while slag provides later-age strength and structural densification [17]. Limestone filler has a similar kinetic role: it improves early strength, whereas GGBFS improves later strength, allowing ternary systems to outperform corresponding binary mixtures [22]. Field exposure of Portland cement–slag–silica fume concretes showed no significant alkali–silica expansion and improved resistance to chloride ingress and deicer salts relative to the high-alkali control [27]. The optimum slag content should therefore not be selected in isolation; it depends on slag reactivity, fineness, activating components, and the target age.

Specialized composites permit even higher GGBFS contents. Engineered cementitious composites containing 50–70% slag replacement achieved 3.3% tensile strain capacity, a mean crack width of 57 μm, and 38 MPa compressive strength [24]. In alkali-activated systems, 100% GGBFS with 5% Na_2O reached up to 120 MPa [25], while chemical acceleration of carbonate-activated slag yielded up to 15 MPa after 24 h, compared with about 2.5 MPa after 48 h without an accelerator [23]. These values cannot be transferred directly to conventional Portland-cement concrete because high alkali concentrations, shrinkage, carbonation, efflorescence, activator safety, and the environmental burden of sodium silicate require separate assessment.

Thus, maximizing the benefits of GGBFS requires an integrated optimization of replacement level, binder composition, and intended service performance rather than pursuing compressive strength alone.

Road bases, subbases and soil stabilization.

In pavement base and subbase layers, the performance of ACBFS is determined mainly by its bearing capacity, resistance to crushing and abrasion, volumetric stability, and behaviour in the presence of water. The studies summarized in Table 4 show that blast furnace slag can provide high bearing capacity, although this result alone is insufficient for assessing its suitability for road-base applications. Fresh and weathered BFS in [12] showed CBR values of 128% and 153%, respectively, with long-term expansion of 0.39% and 0.32%. In [66], CBR values of 95.3%, 88.7%, and 76.1% were obtained for base, subbase, and subgrade conditions, respectively, while the Los Angeles loss reached 49.2%, exceeding the specified 35% limit. These results show that high CBR values may coexist with insufficient resistance to aggregate degradation.

The physical quality of the slag aggregate is therefore an important factor in base and subbase applications. In [6] and [38], selective crushing, density or friction separation, and hydrophobization reduced water absorption, crushing value, and cyclic mass loss. Such treatment can remove weak and highly porous particles and improve the uniformity of the resulting aggregate. For practical use, the assessment of ACBFS should therefore include not only volumetric stability and chemical safety, but also particle density, open porosity, crushing resistance, abrasion resistance, and consistency between batches.

A different relationship applies to bound soil and base stabilization. Adding 20% BFS to clay increased CBR from 25.6% to 222.9%, reduced calculated pavement thickness from 66 to 51 cm, and lowered estimated cost by 5.65% [33]. In a slag–gypsum–reclaimed-asphalt cement-free binder, mixtures with 47.5% GGBFS achieved about 27–29 MPa at 28 days, while 60% GGBFS reached approximately 41

MPa at 90 days [67]. A ternary binder containing 50% GGBFS, 30% electrolytic manganese residue, and 20% cement, used at 5% of dry sediment mass, exceeded 6 and 8 MPa at 7 and 28 days; relative to 8% cement, cement use fell by 87.5%, CO_2 emissions by 84.5%, and cost by 67% [68]. Road bases are therefore among the most promising applications for deep decarbonization because the required strength can be achieved with substantially less clinker than in structural concrete.

Nevertheless, most studies in Table 4 are based on laboratory CBR, UCS, or individual material properties. Reliable service-life prediction requires repeated-load testing, resilient modulus and permanent-deformation measurements, saturation, freeze–thaw cycles, seasonal moisture variation, and long-term leaching. Chemically bound stabilization using GGBFS must also be distinguished from the mechanical action of ACBFS, since identical CBR values may be associated with different failure mechanisms and moisture sensitivities.

BFS in asphalt concrete mixtures.

In recent years, the use of blast furnace slag in asphalt mixtures has attracted increasing attention as a promising approach to improving pavement performance while reducing the consumption of natural aggregates.

Table 5 and Figure 3 confirm the applicability of both ACBFS and GGBFS in asphalt, although the evidence base is smaller than for cementitious composites.

Table 4 – Blast furnace slag for road bases, subbases and soil stabilization

Authors	Year	Substitution approach	Key quantitative results
Kunaev V, et al. [6]	2023	ACBFS aggregate, fraction 20–40 mm; enrichment by grain density. The study compares progressively denser/less porous grain groups.	Water absorption decreased from 4.9–6.8% to 2.19–3.13%; resistance without significant destruction increased from about 150 to 300–400 freeze–thaw cycles; crushing value decreased from 30–31% to 20–21%.
Kambole C, et al. [12]	2019	Weathered blast-furnace slag (WBFS) and freshly produced blast-furnace slag (FBFS) used directly as granular road-base/subbase aggregates.	Soaked CBR: 153% for WBFS and 128% for FBFS. Long-term expansion: 0.32% and 0.39%, respectively. Aggregate crushing, 10% fines, flakiness, plasticity, and compaction complied with South African base/subbase specifications.
Geçkil T, et al. [33]	2020	Clay soil was stabilized with 5%, 10%, 15% and 20% BFS by dry mass of soil; NaOH solution was used to promote the pozzolanic reaction.	At 20% BFS, CBR increased from 25.6% to 222.9% (about 8.71 times). Calculated pavement thickness decreased from 66 to 51 cm (−22.7%; the paper/table reports approximately 29.4% reduction depending on calculation basis), and estimated cost decreased by 5.65%.
Kunaev V, et al. [38]	2024	Selection of the strongest 75% of ACBFS grains by friction enrichment or selective crushing, followed by hydrophobization.	Friction enrichment: water absorption 4.45→3.64%, freeze–thaw mass loss 5.05→2.82%, ACV 30.71→23.80%. Selective crushing: water absorption 4.45→3.15%. Subsequent hydrophobization reduced absorption to 1.34% after friction enrichment and 1.08% after selective crushing. Selective crushing + hydrophobization reduced mass loss after 15 sodium-sulfate cycles to 1.87%.
Soğanci AS, et al. [41]	2023	Low- (CL) and high-plasticity (CH) clay soils were stabilized separately with 5%, 10%, 15% and 20% GBFS by dry mass of soil.	The optimum GBFS content was 10% for CL soil and 15% for CH soil. At 28 days, the unconfined compressive strength increased by 73% (255→442 kPa) for CL soil and by 127% (227.4→508 kPa) for CH soil. At 20% GBFS, the maximum dry density increased by 5.4% for CL and 13.1% for CH soil, while the optimum moisture content decreased by 6.5% and 18.1%, respectively.
Kamara KB, et al. [67]	2021	Portland cement was fully replaced by ternary binders containing GGBS, reclaimed asphalt filler (RAF), and either plasterboard waste gypsum (PWG) or vitamin B5 gypsum (V-B5G). Selected mixtures contained 47.5% or 60% GGBS.	At 28 days, mixtures containing 47.5% GGBS reached 27.02 MPa with PWG and 29.45 MPa with V-B5G. At 90 days, mixtures containing 60% GGBS reached 41 MPa and 40 MPa, respectively.

Hsiung BCB, et al. [69]	2025	ACBFS was used directly as a 30-cm subgrade layer beneath embedded tram track slabs. Its performance was compared with two alternative ground-improvement systems: QS1 + QS2 and QS2 + cement–soil mixture (CSM).	An elastic modulus of 400 MPa was adopted for ACBFS, and a 30-cm layer was selected for the tramway model. The calculated maximum settlement was 3.7 mm with ACBFS, compared with 4.0 mm for QS1 + QS2 and 3.4 mm for QS2 + CSM. For a 6 × 100 m area, the ACBFS layer required 180 m³ of material, whereas the QS2 + CSM alternative required 300 m³ of QS2 and 1,800 m³ of CSM.
Rondón H, et al. [66]	2018	ACBFS was characterized as coarse aggregate for base, subbase, and subgrade applications.	CBR values were reported as 95.3% for base conditions, 88.7% for subbase, and 76.1% for subgrade. Micro-Deval loss: 29.2%; 10% fines value: 123 kN; Los Angeles abrasion/degradation: 49.2%, exceeding a 35% limit. Mineralogy included about 58.9% quartz and 18.1% cristobalite.
Bulko R, et al. [70]	2023	BFS from the Kremnica region tested as a geotechnical bulk material; multiple particle-size fractions and states were characterized.	BFS exhibited CBR values of 31.8–42.8%, an internal friction angle of 38.9–43.0°, and an oedometer modulus of 13.8–24.8 MPa, demonstrating its suitability as a substitute for conventional aggregates in road and earthwork construction.
Kadyrov A, et al. [71]	2019	The study developed a hydrophobized blast furnace slag aggregate for pavement subbase layers, replacing conventional natural crushed stone. The optimized composition consisted of 89.6 wt.% blast furnace slag, 3.7 wt.% microsilica, 6.3 wt.% cement, and 0.4 wt.% used engine oil as a hydrophobic modifier	Compared with untreated slag aggregate, the modified material showed a reduction in water absorption (5.22% to 1,29%), a decrease in ACV (30.23 % to 25.02 %), and a 2.1-fold increase in frost resistance, demonstrating its suitability for road pavement subbase applications
Lang L, et al. [68]	2025	Ternary GEC binder: 50% GGBFS, 30% electrolytic manganese residue, and 20% cement. The optimized binder was used at 5% dry sediment waste and compared with 8% cement.	Reported 7- and 28-day unconfined compressive strengths exceeded 6 MPa and 8 MPa, respectively. Using 5% GEC instead of 8% cement reduced total binder dosage by 37.5%, cement use by 87.5%, CO_2 emissions by 84.5%, and cost by 67%, while improving water and sulfate resistance.
Al-Chaar G, et al. [72]	2019	The study evaluated the use of ground granulated blast furnace slag (GGBFS) as a 30–50 wt.% replacement for Portland cement in concrete intended for rigid pavement and structural applications, comparing its performance with conventional Portland cement concrete.	Concrete containing 30–50 wt.% GGBFS achieved compressive and flexural strengths comparable to or higher than those of the control mix while maintaining satisfactory density and porosity, confirming its suitability for rigid pavement concrete.

Table 5 – Applications of blast furnace slag in asphalt mixtures

Authors	Year	Substitution approach	Key quantitative results
Rondón-Quintana HA, et al. [73]	2019	Replacement of the coarse natural limestone aggregate with treated blast furnace slag (BFS); mixtures incorporating BFS pre-coated with Portland cement paste (BFS-C) were investigated.	PC-treated BFS (BFS-C) at 21% replacement reduced porosity, increased stability/flow by 35%, ITS (dry/wet) by 26.5%/34.4%, and TSR to 90.7%. It showed 6-72% higher resilient modulus and better abrasion resistance, overcoming slag's porosity limitations.
Rondón HA, et al. [74]	2018	21% replacement of the coarse natural aggregate (in WMA) with blast furnace slag (BFS).	At 21% BFS replacement, a significant increase in stiffness and moisture damage resistance was achieved, while the abrasion resistance remained comparable to the control mixture.
Kunaev V, et al. [75]	2025	Selective crushing of air-cooled blast furnace slag (ACBFS) in a ball mill for 30–40 min using a grinding media composition of 50% steel balls and 50% cylpebs.	Bulk density: 1169 → 1396 kg/m³ (+19.4%); water absorption: 4.96 → 2.38% (−52.0%); aggregate crushing value (ACV): 30.98 → 18.40% (−40.6%); sulfate soundness loss: 5.48 → 1.23% (−77.6%); surface pore content: 45.06 → 15.68% (−65.2%).

Al-Hdabi A, et al. [76]	2019	The study investigated ground granulated blast furnace slag (GGBFS) as a complete replacement for ordinary Portland cement (OPC) mineral filler in hot mix asphalt (HMA). Asphalt mixtures containing GGBFS filler (GGBFSAC) were compared with conventional mixtures containing OPC filler (OPCAC) using Marshall stability, indirect tensile strength, moisture susceptibility, and long-term aging tests.	Marshall stability was 12.09 kN for the GGBFS-filled mixture and 8.62 kN for the OPC-filled control. ITS increased from 1153.93 to 1286.35 kPa, while the index of retained strength increased from 73.5% to 88.5%. Marshall stiffness was 3.11 kN/mm with GGBFS compared with 2.28 kN/mm for the control.
Dulaimi A, et al. [77]	2023	Cold asphalt emulsion mixture containing 4% GGBFS and 2% calcium carbide residue (CCR); 3% pre-wetting water was replaced with waste alkaline $Ca(OH)_2$ solution to produce geopolymer-based cold asphalt emulsion mixture (GCAE).	GCAE: ITSM = 2465 MPa after 3 days; rut depth = 1.7 mm after 10,000 cycles; fracture toughness = 7985 $N/mm^{2/3}$; SMR = 103%. Corresponding traditional limestone filler values were 188 MPa, about 9 mm, 7325 $N/mm^{2/3}$, and 75%.
Del-Valle-Corte J, et al. [78]	2024	The study evaluated ground granulated blast furnace slag (GGBFS) as a partial replacement for virgin mineral filler in warm mix asphalt. Replacement levels of 75% and 100% were investigated, and the optimum mixture containing 75% GGBFS was selected for further mechanical evaluation.	GGBFS-2 mix (75 % GGBFS) exhibited the best fatigue performance but the highest axial deformation and rut depth.
Chegenizadeh A, et al. [79]	2022	Ground-granulated blast-furnace slag (GGBFS) was investigated as a replacement for the conventional 1.5% hydrated lime (HL) filler in dense-graded hot mix asphalt. Four mixtures were evaluated: a control mixture containing 1.5% HL and three mixtures containing 1.5%, 3%, and 5% GGBFS as the sole filler.	The mixture containing 3% GGBFS demonstrated the best overall performance, with Marshall stability of 19.16 kN (an 18.56% increase over the control), fatigue life of 92,524 cycles (a 26% increase), and rut depth of 2.70 mm, representing a 27% reduction compared with the control mixture (3.73 mm). Increasing the GGBFS content to 5% reduced performance, with fatigue life decreasing by 14.68% and rut depth increasing by 16% compared with the 3% GGBFS mixture.
Lu D, et al. [80]	2021	This study developed a cold mix asphalt (CMA) incorporating ground-granulated blast furnace slag (GGBS) as part of a ternary blended cementitious filler replacing conventional limestone filler. The optimum mixture (CMA-B) contained 2% ordinary Portland cement (OPC), 1% fly ash (FA), 1% GGBS, and 2% limestone filler, while the total filler content remained 6% by weight of aggregate.	The optimum mixture containing 2% OPC + 1% FA + 1% GGBS exhibited approximately 20% higher indirect tensile strength, 55% lower raveling loss, residual Marshall stability of about 95%, and dynamic stability approximately 10 times higher than the mixture containing 2% OPC only. T

ACBFS mainly replaces coarse mineral aggregate, whereas GGBFS acts as a mineral or reactive filler. Replacement percentages from different studies must therefore not be compared directly. A 21% BFS content in the coarse fraction of warm-mix asphalt increased stiffness and moisture resistance while maintaining abrasion resistance at the control level [74]. Coating porous BFS with cement paste mitigated water-absorption effects: BFS-C increased the stability/flow ratio by 35%, dry and wet ITS by 26.5% and 34.4%, TSR to 90.7%, and resilient modulus by 6–72% [73]. Surface condition, rather than slag content alone, is therefore a decisive parameter.

Results for GGBFS filler also indicate a distinct optimum. When 1.5% hydrated lime was replaced with 1.5%, 3%, and 5% GGBFS, the best performance occurred at 3%: Marshall stability reached 19.16 kN (+18.56%), fatigue life 92,524 cycles (+26%), and rut depth decreased from 3.73 to 2.70 mm (−27%) [79]. Increasing GGBFS to 5% reduced fatigue and rutting performance relative to the 3% mixture, probably because of excess fines and a changed bitumen–filler volumetric ratio. Conversely, complete replacement of Portland-cement filler with GGBFS increased Marshall stability from 8.62 to 12.09 kN, ITS from 1153.93 to 1286.35 kPa, and retained strength from 73.5% to 88.5% [76]. “100% filler

replacement" is not equivalent to "5% of aggregate mass"; the absolute fine content and its role in the mixture are different.

The strongest effects were obtained in cold mixtures, where GGBFS contributes to an inorganic binder rather than acting solely as an inert powder. A mixture containing 4% GGBFS, 2% calcium carbide residue and alkaline $Ca(OH)_2$ solution reached an ITSM of 2465 MPa after three days, approximately 13 times the control; rut depth after 10,000 cycles decreased from about 9.0 to 1.7 mm, and the stiffness modulus ratio increased from 75% to 103% [77]. In another cold mixture, 2% Portland cement, 1% fly ash and 1% GGBFS produced about 20% higher ITS, 55% lower raveling loss and nearly ten times higher dynamic stability than the mixture with 2% cement alone [80]. Weak-alkali activation of GGBFS within asphalt is therefore promising, but long-term ageing, low-temperature cracking, and compatibility with different emulsions and binders must be verified.

Open porosity remains the principal limitation of ACBFS in asphalt. Selective crushing for 30–40 min increased bulk density from 1169 to 1396 kg/m³, reduced water absorption from 4.96% to 2.38%, crushing value from 30.98% to 18.40%, sulfate soundness loss from 5.48% to 1.23%, and surface pore content from 45.06% to 15.68% [75]. These values refer to the aggregate rather than the finished mixture. The next step is to determine whether improved grain quality produces proportional gains in TSR, fatigue life, rutting resistance, and ageing performance.

Future Research Perspectives.

This review presents the results reported in 80 selected scientific articles focusing on the use of blast furnace slag as a binding component and as an aggregate of various size fractions in cement concrete, road bases, soil stabilization, and road asphalt concrete. It has been established that blast furnace slag cannot be considered a uniform and interchangeable secondary raw material. The function performed by blast furnace slag as part of cement concrete, asphalt concrete, or road base depends on its cooling method, phase composition, particle-size fraction, water absorption, aggregate crushing value, bulk density, other physical and mechanical characteristics, as well as pre-treatment. ACBFS, GBFS, and GGBFS perform completely different functions when used in construction. ACBFS is primarily used as coarse or fine aggregate, GBFS as a granular material or fine aggregate, and GGBFS as a supplementary cementitious component or as a mineral and reactive filler.

Differences in the method of cooling and solidification of liquid blast furnace slag, its phase composition, bulk density and particle density, porosity, water absorption, and surface condition make it difficult to compare the results obtained by different researchers and, at the same time, to some extent explain their significant differences. Based on this, the authors of this review consider it necessary, in future studies, to go beyond optimizing the proportion of blast furnace slag in cement concrete or asphalt concrete and to pay more attention to the quality, chemical composition, and variability of the physical and mechanical characteristics of the blast furnace slag itself.

Possible ways to improve the physical and mechanical properties of ACBFS may include hydrophobization (to reduce its water absorption and improve frost resistance) and selective crushing, which makes it possible to remove weak, high-porosity grains while preserving the integrity of stronger grains (to potentially increase the strength of the final product). Studies in these areas are included in this literature review. However, the effects of hydrophobization and selective crushing have been evaluated exclusively at the aggregate level. Future studies should answer the question of whether these additional treatment methods provide a consistent improvement in the physical and mechanical properties and durability of cement concrete, asphalt concrete, and road base materials made using ACBFS of various origins (from different metallurgical enterprises).

Another gap in research identified based on the analysis of the literature is related to the interaction of untreated or pre-treated ACBFS with various binders, including cementitious and bituminous binders. The available data indicate that the surface characteristics of slag can affect interfacial adhesion, moisture resistance, and the performance characteristics of the mixture. Thus, the combined use of ACBFS that has undergone preliminary selective crushing and modified binders, including, for example, bituminous binder containing microsilica or other industrial by-products, may affect the performance characteristics of the finished product (asphalt concrete or cement concrete). Nevertheless, the reviewed literature does not contain sufficient evidence to establish a general synergistic effect, and this concept should be considered a hypothesis requiring experimental verification rather than an established conclusion.

Conclusion

The cooling method largely determines how blast furnace slag is used. Air-cooled slag is mainly crystalline and often has a rough, porous surface, so it is used primarily as aggregate in concrete, asphalt mixtures, and unbound pavement layers. Rapidly quenched slag contains a larger glassy fraction; after grinding, it becomes GGBFS and can be used as a partial Portland cement replacement, a cementitious component in stabilized bases, or a mineral or reactive filler in asphalt.

In cement concrete, many studies reported good results (increased compressive strength and other properties) at ACBFS replacement levels of about 20–40%. This range is not a universal optimum. The outcome changed with slag origin, particle porosity and density, concrete composition, compaction, curing, and the property being measured.

For pavement bases and soil stabilization, BFS often gave high CBR values. Fresh and weathered slag reached 128% and 153%, and adding 20% BFS to clay increased CBR from 25.6% to 222.9%. GGBFS-containing binders also reduced cement use, CO_2 emissions, and cost. At the same time, CBR alone is not enough to judge long-term suitability; abrasion, deformation, moisture, freeze–thaw action, and leaching also matter. Both ACBFS and GGBFS can improve asphalt performance, but through different mechanisms. Treated BFS aggregate at 21% increased the stability/flow ratio by 35%, dry and wet ITS by 26.5% and 34.4%, raised TSR to 90.7%, and increased resilient modulus by 6–72%. For GGBFS used as filler, 3% provided the best overall balance in one study, increasing Marshall stability by 18.56% and fatigue life by 26% while reducing rut depth by 27%. In activated cold mixtures, 4% GGBFS contributed to an approximately 13-fold increase in early ITSM and a reduction in rut depth from about 9.0 to 1.7 mm.

No universal optimum BFS content can be established. Reported dosages refer variously to cement mass, total binder, coarse or fine aggregate, mineral filler, or total aggregate. The optimum consequently depends on slag form, particle quality, processing method, replaced component, mixture technology, curing or ageing conditions, and targeted performance.

The most effective development pathway is an integrated one in which the quality and surface properties of the slag aggregate are engineered together with the cementitious or bituminous binder. The integrated valorization of metallurgical slag and silica-rich industrial by-products can provide a scientifically grounded route to durable pavement materials while reducing both the disposal of industrial residues and the consumption of virgin mineral resources.

Conflicts of interest. The authors declare that they have no known competing financial interests or personal relationships that could have appeared to influence the work reported in this paper.

CRediT author statement: **V.Kunaev:** Conceptualization, Supervision, Methodology, Validation, Writing - Original Draft; **G.Akhmetova:** Methodology, Formal analysis, Investigation; **A.Ospanova**: Investigation, Software, Visualization; **O.Kenzhaliyev**: Conceptualization. **I. Tavshanov:** Formal analysis, Investigation; **M.S.Fathi:** Writing – Review & Editing; **G.Ulyeva:** Investigation, Resources; **A.Batyrbek:** Resources; **D.Charnyi:** Visualization, Writing – Review & Editing.

Funding statement. This research has been funded by the Science Committee of the Ministry of Science and Higher Education of the Republic of Kazakhstan (Grant No. AP22786668).

Cite this article as: Kunaev VA, Akhmetova GE, Ospanova AZ, Kenzhaliyev OB, Tavshanov IS, Fathi MS, Ulyeva GA, Batyrbek AE, Charnyi DYu. Blast Furnace Slag as an Alternative to Natural Mineral Materials in Pavement Engineering: A Review. Kompleksnoe Ispolzovanie Mineralnogo Syra = Complex Use of Mineral Resources. 2028; 346(3):108-130. https://doi.org/10.31643/2028/6445.32

Жол құрылысында табиғи минералдық материалдарға балама ретіндегі домна қожы: шолу

[1]Кунаев В.А., [1]Ахметова Г.Е., [1]Оспанова А.З., [1]Кенжалиев О.Б., [1]Тавшанов И.С., [2]Fathi M.S., [1]Ульева Г.А., [1]Батырбек Ә.Е., [1]Чарный Д.Ю.

[1]Қарағанды индустриялық университеті КЕАҚ, Теміртау, Қазақстан
[2]Малайзия технологиялық университеті, Куала-Лумпур, Малайзия

Мақала келді: *30 шілде 2026*
Сараптамадан өтті: *28 тамыз 2026*
Қабылданды: *8 қыркүйек 2026*

ТҮЙІНДЕМЕ

Ұсынылған әдеби шолу 2000–2026 жылдар аралығындағы ғылыми мақалалардың талдау нәтижелерін қамтиды, онда домендік қожды жол құрылысының әртүрлі бағыттарында қолдану қарастырылады. Домна қожының әртүрлі түрлерін қолдану нұсқалары арасында айқын айырмашылықтардың бар екені анықталды. Үйінді домна қожы көбінесе цементбетон мен асфальтбетон үшін ірі немесе ұсақ толтырғыш ретінде қолданылады, ал ұнтақталған түйіршіктелген домна қожы қосымша байланыстырушы компонент ретінде немесе минералдық/реакциялық белсенді толтырғыш ретінде қолданылады. Домна қожын бетон өндірісінде қолданған кезде бірқатар зерттеулерде ең жоғары нәтижелер толтырғыштың 20-40%- аралығында қожбен алмастыру кезінде алынған, дегенмен бұл көрсеткіш әмбебап оңтайлы мән болып табылмаған. Кейбір мақалаларда домна қожын автомобиль жолының негізі құрамында пайдалану немесе топырақты тұрақтандыру CBR-дің артуымен байланыстырылғаны көрсетілген. Кейбір авторлар құрамында түйіршіктелген домна қожы бар кешенді байланыстырушы материалдарды қолдану кезінде портландцемент шығынының төмендейтінін атап көрсетеді. Сондай-ақ үйінді және түйіршіктелген домна қожын әртүрлі пропорцияларда енгізу кезінде асфальтбетонның суға төзімділігі, шаршауға төзімділігі, Маршалл бойынша ығысуға тұрақтылығы және із түсуге төзімділігінің жақсаруы туралы деректер келтірілген. Кеуектілігі әртүрлі үйінді домна қожын алдын ала өңдеудің де маңызы зор болды: селективті ұсату және кейінгі бөлшектерді бөлу су сіңіруін, ұсақталу көрсеткішін және әлсіз кеуекті түйірлердің үлесін төмендетті. Негізгі практикалық қорытынды домна қожын біртекті және өзара алмастырылатын материал ретінде қарастыруға болмайтынын көрсетеді. Оны қолдану тәсілі қож түрін, түйірлердің сапасын, алмастырылатын компонентті және жол-құрылыс материалының талап етілетін пайдалану қасиеттерін ескере отырып таңдалуы тиіс. Алдағы зерттеулерде қож толтырғышын алдын ала өңдеу нәтижесінде алынған қасиеттердің жақсаруы цементбетонда, асфальтбетон қоспаларында және жол жамылғысы негіздерінің материалдарында ұзақ мерзімді пайдалану кезінде сақтала ма, соны анықтау қажет.

Түйін сөздер: үйінді домна қожы, ұнтақталған түйіршіктелген домна қожы, табиғи минералдық шикізатты алмастыру, толтырғышты байыту, цементбетон, асфальтбетон, жол төсемі негіздерінің материалдары.

Авторлар туралы ақпарат:

Кунаев Вячеслав Александрович — *PhD, доцент, Ғылым және инновациялар департаментінің директоры, Қарағанды индустриялық университеті КеАҚ, 101400, Республика даңғылы, 30, Теміртау, Қазақстан. E-mail: v.kunayev@tttu.edu.kz; ORCID ID: https://orcid.org/0000-0001-8283-7186*

Ахметова Гульжайнат Есенжоловна — *PhD, доцент, Қарағанды индустриялық университеті КеАҚ, 101400, Республика даңғылы, 30, Теміртау, Қазақстан. E-mail: agulzhajnat@bk.ru; ORCID ID: https://orcid.org/0000-0001-8244-5027*

Оспанова Аяулым Зайнуллаевна — *Докторант, Қарағанды индустриялық университеті КеАҚ, 101400, Республика даңғылы, 30, Теміртау, Қазақстан. E-mail: a.ospanova@tttu.edu.kz; ORCID ID: https://orcid.org/0009-0002-0597-1220*

Кенжалиев Олжас Багдаулетович — *PhD, доцент, Қарағанды индустриялық университеті КеАҚ, 101400, Республика даңғылы, 30, Теміртау, Қазақстан. E-mail: o.kenzhaliyev@tttu.edu.kz; ORCID ID: https://orcid.org/0000-0002-3776-9724*

Тавшанов Ильгар Сулейманович — *Ғылыми қызметкер, Қарағанды индустриялық университеті КеАҚ, 101400, Республика даңғылы, 30, Теміртау, Қазақстан. E-mail: i.tavshanov@tttu.edu.kz; ORCID ID: https://orcid.org/0000-0002-9427-9748*

Fathi Mohamad Syazli — *PhD, қауымдастырылған профессор, Малайзия технологиялық университеті, Сұлтан Яхья Петра көшесі, 54100, Куала-Лумпур, Малайзия. E-mail: syazli@utm.my; ORCID ID: https://orcid.org/0000-0002-0474-6278*

Ульева Гульнара Анатольевна — *PhD, профессор, Қарағанды индустриялық университеті КеАҚ, 101400, Республика даңғылы, 30, Теміртау, Қазақстан. E-mail: g.ulyeva@tttu.edu.kz; ORCID ID: https://orcid.org/0009-0002-7300-1277*

Батырбек Әлібек Есімбекұлы — *Докторант, Қарағанды индустриялық университеті КеАҚ, Республика даңғылы, 30, Теміртау, Қарағанды облысы, Қазақстан. E-mail: a.batyrbek@tttu.edu.kz; ORCID ID: https://orcid.org/0000-0002-3369-6804*

Чарный Дмитрий Юрьевич — *Кіші ғылыми қызметкер, Қарағанды индустриялық университеті КеАҚ, 101400, Республика даңғылы, 30, Теміртау, Қазақстан. E-mail: dmitryi.charnyy@gmail.com; ORCID ID: https://orcid.org/0009-0005-9438-2330*

Доменный шлак как альтернатива природным минеральным материалам в дорожном строительстве: обзор

[1]Кунаев В.А., [1]Ахметова Г.Е., [1]Оспанова А.З., [1]Кенжалиев О.Б., [1]Тавшанов И.С., [2]Fathi M.S., [1]Ульева Г.А., [1]Батырбек Ә.Е., [1]Чарный Д.Ю.

[1]НАО «Карагандинский индустриальный университет», Темиртау, Карагандинская область, Казахстан
[2]Технологический университет Малайзии, Куала-Лумпур, Малайзия

Поступила: *30 июля 2026*
Рецензирование: *28 августа 2026*
Принята в печать: *8 сентября 2026*

АННОТАЦИЯ

Представленный литературный обзор содержит результаты анализа научных статей за 2000-2026 годы, рассматриваемых применение доменного шлака в разных направлениях дорожного строительства. Установлено наличие четких различий между вариантами применения разных типов доменного шлака. Отвальный доменный шлак чаще все применяется в качестве крупного или мелкого заполнителя для цементобетона и асфальтобетона, а измельченный гранулированный доменный шлак – в роли дополнительного вяжущего компонента либо как минеральный/реактивный наполнитель. При использовании доменного шлака при производстве бетона наиболее высокие результаты в ряде исследований достигались при замене шлаком в пределах 20-40 % заполнителя, хотя данный показатель и не был универсальным оптимальным значением. В отдельных статьях указывалось на связь использования доменного шлака в составе основания автомобильной дороги либо для стабилизации грунта с повышением CBR. Некоторые авторы указывают на снижение расхода портландцемента при применении комплексных вяжущих, содержащих гранулированный доменный шлак. Также приведены данные об улучшении водостойкости, усталостной стойкости, сдвигоустойчивости по Маршаллу, колейности асфальтобетона при введении отвального и гранулированного доменного шлака в различных пропорциях. Важное значение имела и предварительная обработка разнопористого отвального доменного шлака: избирательное дробление и последующее разделение частиц снижали водопоглощение, показатель дробимости и долю слабых пористых зерен. Основной практический вывод состоит в том, что доменный нельзя рассматривать как однородный взаимозаменяемый материал. Способ его применения должен выбираться с учетом типа шлака, качества зерен, заменяемого компонента и требуемых эксплуатационных свойств дорожно-строительного материала. В дальнейших исследованиях необходимо установить, сохраняются ли улучшения свойств, полученные после предварительной обработки шлакового заполнителя, в цементобетоне, асфальтобетонных смесях и материалах оснований дорожных одежд при длительной эксплуатации.

Ключевые слова: отвальный доменный шлак, молотый гранулированный доменный шлак, замещение природного минерального сырья, обогащение заполнителя, цементобетон, асфальтобетон, материалы оснований дорожных одежд.

Информация об авторах:

Кунаев Вячеслав Александрович *PhD, доцент, директор департамента науки и инноваций, НАО Карагандинский индустриальный университет, 101400, пр. Республики, 30, Темиртау, Казахстан. E-mail: v.kunayev@tttu.edu.kz; ORCID ID: https://orcid.org/0000-0001-8283-7186*

Ахметова Гульжайнат Есенжоловна *PhD, доцент, НАО Карагандинский индустриальный университет, 101400, пр. Республики, 30, Темиртау, Казахстан. E-mail: agulzhajnat@bk.ru; ORCID ID: https://orcid.org/0000-0001-8244-5027*

Оспанова Аяулым Зайнуллаевна *Докторант, НАО Карагандинский индустриальный университет, 101400, пр. Республики, 30, Темиртау, Казахстан. E-mail: a.ospanova@tttu.edu.kz; ORCID ID: https://orcid.org/0009-0002-0597-1220*

Кенжалиев Олжас Багдаулетович *PhD, доцент, НАО Карагандинский индустриальный университет, 101400, пр. Республики, 30, Темиртау, Казахстан. E-mail: o.kenzhaliyev@tttu.edu.kz; ORCID ID: https://orcid.org/0000-0002-3776-9724*

Тавшанов Ильгар Сулейманович *Научный сотрудник, НАО Карагандинский индустриальный университет, 101400, пр. Республики, 30, Темиртау, Казахстан. E-mail: i.tavshanov@tttu.edu.kz; ORCID ID: https://orcid.org/0000-0002-9427-9748*

Fathi Mohamad Syazli *PhD, ассоциированный профессор, Технологический университет Малайзии, ул. Султан Яхья Петра, 54100, Куала-Лумпур, Малайзия. E-mail: syazli@utm.my; ORCID ID: https://orcid.org/0000-0002-0474-6278*

Ульева Гульнара Анатольевна *PhD, профессор, НАО Карагандинский индустриальный университет, 101400, пр. Республики, 30, Темиртау, Казахстан. E-mail: g.ulyeva@tttu.edu.kz; ORCID ID: https://orcid.org/0009-0002-7300-1277*

Батырбек Әлібек Есімбекұлы *Докторант, НАО Карагандинский индустриальный университет, 101400, пр. Республики, 30, Темиртау, Казахстан. E-mail: a.batyrbek@tttu.edu.kz; ORCID ID: https://orcid.org/0000-0002-3369-6804*

Чарный Дмитрий Юрьевич *Младший научный сотрудник, НАО Карагандинский индустриальный университет, 101400, пр. Республики, 30, Темиртау, Казахстан. E-mail: dmitryi.charnyy@gmail.com; ORCID ID: https://orcid.org/0009-0005-9438-2330*

References

[1] Liu Z, Feng T, Zhu X, Gao J, Hu K, Guo M, Gu F, Li F. Bird's-eye view of recycled solid wastes in road engineering. Journal of Road Engineering. 2024; 4(2):93-150. https://doi.org/10.1016/j.jreng.2024.05.002

[2] Kunaev V, Tavshanov I, Asanov R. Laboratory evaluation of a complex treatment technology for reducing water absorption of the pavement subbase aggregate from the blast-furnace slag. Engineering Research Express. 2023; 6:015048. https://doi.org/10.1088/2631-8695/ad1e16

[3] Ulyeva GA, Tuyskhan K, Matsugina EM, Volokitina IE, Akhmetova GE. Actual progress of production waste disposal problems. Izvestiya Ferrous Metallurgy. 2025; 68(2):131-138. https://doi.org/10.17073/0368-0797-2025-2-131-138

[4] Georgiadi I, Kadyrov A, Kunaev V. Development of the universal working equipment of the excavator for preparation of materials based on waste during the road building. Communications - Scientific Letters of the University of Žilina. 2023; 25(2):B62-B76. https://doi.org/10.26552/COM.C.2023.022

[5] Zhang Y, Tang Z, Zhou X. Effect of alkali activator and granulated blast furnace slag on the properties of lithium slag-based high-strength lightweight aggregates. Scientific Reports. 2025; 15:30115. https://doi.org/10.1038/s41598-025-16048-8

[6] Kunaev V, Bazarov B, Tavshanov I, Kadyrov A, Abdugaliyeva G, Kydyrbaeva S. Evaluation of the effect of enrichment of slag aggregate for pavement subbase by grains density on its physical and mechanical characteristics. Results in Engineering. 2023; 18:101181. https://doi.org/10.1016/j.rineng.2023.101181

[7] Yasipourtehrani S, Strezov V, Bliznyukov S, Evans T. Investigation of thermal properties of blast furnace slag to improve process energy efficiency. Journal of Cleaner Production. 2017; 149:137-145. https://doi.org/10.1016/j.jclepro.2017.02.052

[8] Silva LHP, Nehring V, Paiva FFG, Tamashiro JR, Galvín AP, López-Uceda A, Kinoshita A. Use of blast furnace slag in cementitious materials for pavements - Systematic literature review and eco-efficiency. Sustainable Chemistry and Pharmacy. 2023; 33:101030. https://doi.org/10.1016/j.scp.2023.101030

[9] Zhuang S, Zhang L, Cao J, Luo Y, Zeng X, Xin F, Zhao Z, Zhou Z. Synergistic utilization of high-volume magnesium slag and blast furnace slag in sustainable ternary binders: From macro-performance to environmental benefits. Construction and Building Materials. 2026; 539;147469. https://doi.org/10.1016/j.conbuildmat.2026.147469

[10] Kudryashov YuP, Semenov GI, Nesterova ER, Odnorob OS. Perspektiva ispol'zovaniya otval'nykh shlakov Novolipetskogo metallurgicheskogo kombinata pri ustroistve osnovanii dorozhnykh odezhd [Prospect of using dump slags of the Novolipetsk Metallurgical Plant in the device of road pavements bases]. In: Innovatsionnye materialy i tekhnologii v transportnom stroitel'stve i dorozhnom khozyaistve: sbornik nauchnykh trudov bakalavrov i magistrov kafedry Dorozhno-stroitel'nye materialy MADI [Innovative materials and technologies in transport construction and road management: proceedings of bachelors and masters of the Department Road construction materials MADI]. Moscow: Tekhpolygrafcenter. 2022; 6:91-94. (in Russ.).

[11] Chien HT, Chang JR, Hsu HM. Determining the content of steel furnace slag in asphalt concrete. Case Studies in Construction Materials. 2023; 19:e02399. https://doi.org/10.1016/j.cscm.2023.e02399

[12] Kambole C, Paige-Green P, Kupolati WK, Ndambuki JM, Adeboje A. Comparison of technical and short-term environmental characteristics of weathered and fresh blast furnace slag aggregates for road base applications in South Africa. Case Studies in Construction Materials. 2019; 11:e00239. https://doi.org/10.1016/j.cscm.2019.e00239

[13] Ren Q, Qi W, Zhao Q, Jia Y, Feng Y, Han Y. Preparation and characterization of low-carbon cementitious materials based on soda-residue-activated ground granulated blast-furnace slag: a case study on cemented paste backfills. Metals. 2023; 13(4):694. https://doi.org/10.3390/met13040694

[14] Akkurt I. A test of radiation absorption characteristics of blast-furnace slag concrete. NWSA Engineering Sciences. 2011; 6(4). https://doi.org/10.12739/NWSAES.V6I4.5000066929.G5000062296

[15] Dong QG, Li J, Kang ZQ, Imran Anwar M, Asad M, Miao B, Wang S, Younas A. Unlocking the potential: A comprehensive review on blast furnace slag and silica analog adsorbents for sustainable industrial and pharmaceutical pollution control and resource utilization. Emerging Contaminants. 2024; 10(4):100387. https://doi.org/10.1016/j.emcon.2024.100387

[16] Lee J, Lee T. Durability and engineering performance evaluation of CaO content and ratio of binary blended concrete containing ground granulated blast-furnace slag. Applied Sciences. 2020; 10(7):2504. https://doi.org/10.3390/app10072504

[17] Bonavetti VL, Castellano C, Donza H, Rahhal VF, Irassar EF. Cement with silica fume and granulated blast-furnace slag: strength behavior and hydration. Materiales De Construcción. 2014: 64(315)e025. https://doi.org/10.3989/mc.2014.04813

[18] Deboucha W, Benchaa M, Mouli M, Khadraoui A. Effect of incorporating blast furnace slag and natural pozzolana on compressive strength and capillary water absorption of concrete. Procedia Engineering. 2015; 108:254-261. https://doi.org/10.1016/j.proeng.2015.06.033

[19] Kanniyappan SP, Saravanakumar S. Use of air cooled blast furnace slag as a sustainable material in cement concrete. International Journal of Innovative Research & Studies. 2018; 8:545-558.

[20] Fuentes-Romero M, Rocha-Rangel E, Díaz S, Cruz M. Durability of H-class cement and blast furnace slag-based cementitious composites. Epitoanyag - Journal of Silicate Based and Composite Materials. 2011; 63:18-22. https://doi.org/10.14382/epitoanyag-jsbcm.2011.4

[21] Özkan Ö, Yüksel I, Muratoğlu Ö. Strength properties of concrete incorporating coal bottom ash and granulated blast furnace slag. Waste Management. 2007; 27(2):161-167. https://doi.org/10.1016/j.wasman.2006.01.006

[22] Carrasco MF, Menéndez G, Bonavetti V, Irassar EF. Strength optimization of 'tailor-made cement' with limestone filler and blast furnace slag. Cement and Concrete Research. 2005; 35(7):1324-1331. https://doi.org/10.1016/j.cemconres.2004.09.023

[23] Kovtun M, Kearsley EP, Shekhovtsova J. Chemical acceleration of a neutral granulated blast-furnace slag activated by sodium carbonate. Cement and Concrete Research. 2015; 72:1-9. https://doi.org/10.1016/j.cemconres.2015.02.014

[24] Zhou J, Qian S, Sierra Beltran MG. Development of engineered cementitious composites with limestone powder and blast furnace slag. Materials and Structures. 2010; 43:803–814. https://doi.org/10.1617/s11527-009-9549-0

[25] Burciaga-Díaz O, Magallanes-Rivera RX, Escalante-García JI. Alkali-activated slag-metakaolin pastes: strength, structural, and microstructural characterization. Journal of Sustainable Cement-Based Materials. 2013; 2(2):111-127. https://doi.org/10.1080/21650373.2013.801799

[26] Nicula LM, Manea DL, Simedru D, Cadar O, Dragomir ML, Ardelean I, Corbu O. Potential role of GGBS and ACBFS blast furnace slag at 90 days for application in rigid concrete pavements. Materials. 2023; 16(17):5902. https://doi.org/10.3390/ma16175902

[27] Bleszynski R, Matthews JD, Hooton RD, Thomas MDA. Durability of ternary blend concrete with silica fume and blast-furnace slag: laboratory and outdoor exposure site studies. ACI Materials Journal. 2002; 99(5):499-508. https://doi.org/10.14359/12329

[28] Vadhera K, Berwal P. Behavior of blast furnace slag in rigid pavement (compressive and splitting tensile strength). International Journal of Current Engineering and Technology. 2017; 7(4):1490-1495. https://ijcet.evegenis.org/index.php/ijcet/article/view/2416

[29] Yahyaee T, Elize HS. A comprehensive study on mechanical properties, durability, and environmental impact of fiber-reinforced concrete incorporating ground granulated blast furnace slag. Case Studies in Construction Materials 2024; 20:e03190. https://doi.org/10.1016/j.cscm.2024.e03190

[30] Tole I, Rajczakowska M, Humad A, Kothari A, Cwirzen A. Geopolymer based on mechanically activated air-cooled blast furnace slag. Materials. 2020; 13(5):1134. https://doi.org/10.3390/ma13051134

[31] Benmammar M, Boukli Hacene SME, Taleb O. Influence of silica fume and blast furnace slag on the dynamic and mechanical properties of concrete. Asian Journal of Civil Engineering. 2019: 20: 581–589. https://doi.org/10.1007/s42107-019-00126-0

[32] Yüksel I, Bilir T. Özkan Ö. Durability of concrete incorporating non-ground blast furnace slag and bottom ash as fine aggregate. Building and Environment. 2007; 42(7):2651-2659. https://doi.org/10.1016/j.buildenv.2006.07.003

[33] Geçkil T, Tanyildizi MM, İnce CB, Yildiran ES. Influence of a clay subgrade stabilized with blast furnace slag on flexible road pavement thickness and cost. NATURENGS, MTU Journal of Engineering and Natural Sciences. 2020; 1(2):17-31. https://doi.org/10.46572/nat.2020.13

[34] Lübeck A, Gastaldini ALG, Barin DS, Siqueira HC. Compressive strength and electrical properties of concrete with white Portland cement and blast-furnace slag. Cement & Concrete Composites. 2012; 34(3):392-399. https://doi.org/10.1016/j.cemconcomp.2011.11.017

[35] Nicula LM, Corbu O, Ardelean I, Sandu AV, Iliescu M, Simedru D. Freeze–thaw effect on road concrete containing blast furnace slag: NMR relaxometry investigations. Materials. 2021; 14(12):3288. https://doi.org/10.3390/ma14123288

[36] Humad AM, Kothari A, Provis JL, Cwirzen A. The effect of blast furnace slag/fly ash ratio on setting, strength, and shrinkage of alkali-activated pastes and concretes. Frontiers in Materials. 2019; 6:9. https://doi.org/10.3389/fmats.2019.00009

[37] Tan K, Zhang T, Zhu W, Yang D, Lin D, Wang H, Wei J, Yu Q. Innovative high-strength, high-permeability concrete for large-scale applications in permeable subgrade of highway tunnel. Case Studies in Construction Materials. 2024; 20:e02977. https://doi.org/10.1016/j.cscm.2024.e02977

[38] Kunaev V, Bazarov B, Kadyrov A, Konakbaeva A. Selective crushing, enrichment by friction properties and hydrophobization for obtaining the sustainable blast furnace slag aggregate for road subbase. Ain Shams Engineering Journal. 2024; 15(9):art. 102928. https://doi.org/10.1016/j.asej.2024.102928

[39] Adigamov RR, Mityukova EV, Solovyeva VYa, Gunin SO. Beton dlya dorozhnykh pokrytiy, soderzhashchiy molotyy granulirovannyy domennyy shlak [Concrete for road pavements containing ground granulated blast furnace slag]. Tsement i ego primenenie = Cement and its application. 2020; 2:71-73. (in Russ.). https://jcement.ru/magazine/vypusk-2-2020/beton-dlya-dorozhnykh-pokrytiy-soderzhashchiy-molotyy-granulirovannyy-domennyy-shlak/

[40] Karikatti V, Chitawadagi MV, Devarangadi M, Sanjith J, Reddy NG. Influence of bagasse ash powder and marble powder on strength and microstructure characteristics of alkali activated slag concrete cured at room temperature for rigid pavement application. Cleaner Materials. 2023; 9:100200. https://doi.org/10.1016/j.clema.2023.100200

[41] Soğanci AS, Yenginar Y, Orman A. Geotechnical properties of clayey soils stabilized with marble dust and granulated blast furnace slag. KSCE Journal of Civil Engineering. 2023; 27(11):4622-4634. https://doi.org/10.1007/s12205-023-0384-6

[42] Divsholi BS, Lim TYD, Teng S. Durability Properties and Microstructure of Ground Granulated Blast Furnace Slag Cement Concrete. International Journal of Concrete Structures and Materials. 2014; 8:157–164. https://doi.org/10.1007/s40069-013-0063-y

[43] Bagheri AR, Zanganeh H, Moalemi MM. Mechanical and durability properties of ternary concretes containing silica fume and low reactivity blast furnace slag. Cement & Concrete Composites. 2012; 34:663-670. https://doi.org/10.1016/j.cemconcomp.2012.01.007

[44] Vamsi Mohan U, Nagendra Prasad K, Vijaya Bhaskar S. Analysis and assessment of strength development in concrete cubes using granulated blast furnace slag as marginal material. International Journal of Earth Sciences and Engineering. 2017; 10(2):326-333.

[45] Pawar VS, Kundlik A, Fatkal G, Kori S. Experimental investigation of granulated blast furnace slag as fine aggregate in concrete. International Research Journal of Engineering and Technology (IRJET). 2022;.9(5):302-305. https://www.irjet.net/archives/V9/i5/IRJET-V9I564.pdf

[46] Nicula LM, Corbu O, Iliescu M. The influence of blast furnace slag on abrasion resistance for road concretes. In: IOP Conference Series: Materials Science and Engineering. Bristol, UK: IOP Publishing. 2020. https://doi.org/10.1088/1757-899X/877/1/012040

[47] Nicula LM, Manea DL, Simedru D, et al. The influence of blast furnace slag on cement concrete road by microstructure characterization and assessment of physical-mechanical resistances at 150/480 days. Materials. 2023; 16(9):3332. https://doi.org/10.3390/ma16093332

[48] Nicula LM, Corbu O, Iliescu M. Influence of blast furnace slag on the durability characteristic of road concrete such as freeze-thaw resistance. Procedia Manufacturing. 2020; 46:194-201. https://doi.org/10.1016/j.promfg.2020.03.029

[49] Cao Q, Nawaz U, Jiang X, Zhang L, Ansari WS. Effect of air-cooled blast furnace slag aggregate on mechanical properties of ultra-high-performance concrete. Case Studies in Construction Materials. 2022; 16:e01027. https://doi.org/10.1016/j.cscm.2022.e01027

[50] Verian KP, Panchmatia P, Olek J, Nantung T. Pavement concrete with air-cooled blast furnace slag and dolomite as coarse aggregates: Effects of deicers and freeze-thaw cycles. Transportation Research Record: Journal of the Transportation Research Board. 2015; 2508:55-64. https://doi.org/10.3141/2508-07

[51] Sawant AB, Lavangare VH, Kolekar SM, Sawant AA. Suitability of blast furnace slag in concrete. International Research Journal of Engineering and Technology (IRJET). 2019; 6(3):2927-2933. https://www.irjet.net/archives/V6/i3/IRJET-V6I3566.pdf

[52] Ta Y, Minagawa H, Takahashi H, Takahashi K, Miyamoto S, Hisada M. Durability enhancement mechanism of mortar using blast furnace slag fine aggregate against combined deterioration of frost and salt damage. Construction and Building Materials. 2023; 367:130237. https://doi.org/10.1016/j.conbuildmat.2022.130237

[53] Dhanasri K, Kishore Kumar M. Performance of concrete by replacing coarse aggregate and fine aggregate with blast furnace slag and crusher dust. International Journal of Innovative Research in Science, Engineering and Technology. 2013; 2(12):7608-7612. https://ijirset.com/upload/2013/december/67_-Performance.pdf

[54] Ríos JD, Vahí A, Leiva C, Martínez-De La Concha A, Cifuentes H. Analysis of the utilization of air-cooled blast furnace slag as industrial waste aggregates in self-compacting concrete. Sustainability. 2019; 11(6):1702. https://doi.org/10.3390/su11061702

[55] Džananović A, Manić N. The possibility of using blast furnace slag as concrete aggregate. Građevinski Materijali i Konstrukcije. 2018; 61(3):67-78. https://doi.org/10.5937/GRMK1803067D

[56] Sawant AB, Kolekar SM, Sawant AA. Utilization of blast furnace slag in concrete. IRE Journals. 2019; 2(9):86-93. https://www.academia.edu/90419069/Utilization_Of_Blast_Furnace_Slag_In_Concrete_IRE_Journals

[57] Singh G, Das S, Ahmed AA, Saha S, Karmakar S. Study of granulated blast furnace slag as fine aggregates in concrete for sustainable infrastructure. Procedia - Social and Behavioral Sciences. 2015; 195:2272-2279. https://doi.org/10.1016/j.sbspro.2015.06.316

[58] Mujedu KA, Lamidi IO, Familusi AO, Olatunji AA. Utilization of blast furnace slag as coarse aggregate in concrete production. The International Journal of Engineering and Science (IJES). 2018; 7(11):50-57. https://doi.org/10.9790/1813-0711025057

[59] Familusi AO, Adewumi BE, Oladipo FI, Ogundare DA, Olusami JO. Effects of blast furnace slag as a partial replacement for cement in concrete. In: 9th International Conference on Sciences, Engineering and Environmental Technology. Federal Polytechnic Ede, Osun State, Nigeria. 2017.

[60] Babu KG, Kumar VSR. Efficiency of GGBS in concrete. Cement and Concrete Research. 2000; 30(7):1031-1036. https://doi.org/10.1016/S0008-8846(00)00271-4

[61] Verma N, Verma A, Bansal RS, Quadir M. Effect of partial replacement of cement with blast furnace slag and sand with cast iron chips on the strength of concrete. International Journal of Engineering Research & Technology (IJERT). 2016; 5(10):174-178. http://dx.doi.org/10.17577/IJERTV5IS100178

[62] Okba SH, Nasr EA, El-Dieb AS, Abd el-Megeed MR. Effect of blast-furnace slag replacement level on concrete durability. In: 6th International Conference on Civil and Architecture Engineering (ICCAE). Cairo, Egypt. 2006 Military Technical College, Kobry Elkobbah. 2006, 234-247. https://doi.org/10.21608/iccae.2006.45730

[63] Iravani A, Feldrappe V, Ehrenberg A, Anders S. Stability of concrete containing blast-furnace slag following exposure to cyclic elevated temperature. Acta Polytechnica CTU Proceedings. 2022; 33:238-244. https://doi.org/10.14311/APP.2022.33.0238

[64] Huang H, Ye G, Damidot D. Effect of blast furnace slag on self-healing of microcracks in cementitious materials. Cement and Concrete Research. 2014; 60:68-82. https://doi.org/10.1016/j.cemconres.2014.03.010

[65] De Matos PR, Oliveira JCP, Medina TM, Magalhães DC, Gleize PJP, Schankoski RA, Pilar R. Use of air-cooled blast furnace slag as supplementary cementitious material for self-compacting concrete production. Construction and Building Materials. 2020; 262:120102. https://doi.org/10.1016/j.conbuildmat.2020.120102

[66] Rondón H, Fernández W, Patiño D, Ruge J, Vacca H, Reyes F. Characterization of blast furnace slag for road projects. Revista Ingeniería de Construcción. 2018; 33(1):83-92. https://doi.org/10.4067/S0718-50732018000100083

[67] Kamara KB, Ganjian E, Khorami M. Use of waste gypsum, reclaimed asphalt filler, and GGBS as a full replacement of cement in road base. Journal of Materials in Civil Engineering. 2021; 33(6):04021109. https://doi.org/10.1061/(ASCE)MT.1943-5533.0003744

[68] Lang L, Zhu M, Pu S. Recycling engineering sediment waste as sustainable subgrade material using ground granulated blast-furnace slag, electrolytic manganese residue and cement. Environmental Technology & Innovation. 2025; 37:103969. https://doi.org/10.1016/j.eti.2024.103969

[69] Hsiung BCB, Prakasa MDA. Innovative use of air-cooled blast furnace slag as a subgrade material for embedded track slabs: In situ and laboratory tests and simulations. Results in Engineering. 2025; 25:103899. https://doi.org/10.1016/j.rineng.2024.103899

[70] Bulko R, Masarovičová S, Gago F. Determination of the basic geotechnical parameters of blast-furnace slag from the Kremica region. Materials. 2023; 16(17):5966. https://doi.org/10.3390/ma16175966

[71] Kadyrov A, Kunaev V, Georgiadi I, Khaibullin R. Advanced methods for solving the problems of road construction in central kazakhstan. Tehnicki Vjesnik. 2019; 26(4):1159–1163. https://doi.org/10.17559/TV-20170225144013

[72] Al-Chaar G, Landi M. Flow test for ground granulated blast furnace slag-fly ash inorganic polymer mix designed for pre-placed gravel pavement. The Open Construction and Building Technology Journal. 2019; 13(2):27-35. https://doi.org/10.2174/1874836801913010027

[73] Rondón-Quintana HA, Ruge-Cárdenas JC, Bastidas-Martínez JG. Evaluation of hot-mix asphalt containing Portland cement treated blast furnace slag. Archives of Civil Engineering. 2019; 65(2):193-207. https://doi.org/10.2478/ace-2019-0028

[74] Rondón HA, Chaves S, Escobar D. Evaluation of a warm mix asphalt manufactured with blast furnace slag. Modern Applied Science. 2018; 12(12):28-40. https://doi.org/10.5539/mas.v12n12p28

[75] Kunaev V, Akhmetova G, Zhautikov B, Batyrbek A, Tavshanov I, Charnyi D, Kydyrbaeva S, Kamarova S, Fathi MS, Suleyev B. Enhancing physical-mechanical properties of coarse slag aggregate via selective crushing for asphalt concrete. Results in Engineering. 2025; 26:105368. https://doi.org/10.1016/j.rineng.2025.105368

[76] Al-Hdabi A, Al-Sahaf NA, Mahdi LA, Yesar Z, Moeid H, Hassan M. Laboratory investigation on the properties of asphalt concrete mixture with GGBFS as filler. IOP Conference Series: Materials Science and Engineering. 2019; 557(1):012063. https://doi.org/10.1088/1757-899X/557/1/012063

[77] Dulaimi A, Al Busaltan S, Mydin MAO. Lu D, Özkılıç YO, Jaya RP, Ameen A. Innovative geopolymer-based cold asphalt emulsion mixture as eco-friendly material. Scientific Reports. 2023; 13:17380. https://doi.org/10.1038/s41598-023-44630-5

[78] Del-Valle-Corte J, Orosa P, Pasandín AR, Pérez I. Assessing the impact of various industrial wastes on the volumetric and mechanical properties of warm mix asphalt (WMA). Case Studies in Construction Materials. 2024; 21:e04073. https://doi.org/10.1016/j.cscm.2024.e04073

[79] Chegenizadeh A, Hanson SW, Nikraz H, Scott Kress C. Effects of Ground-Granulated Blast-Furnace Slag Used as Filler in Dense Graded Asphalt. Applied Sciences. 2022; 12(6):2769. https://doi.org/10.3390/app12062769

[80] Lu D, Wang Y, Leng Z, Zhong J. Influence of ternary blended cementitious fillers in a cold mix asphalt mixture. Journal of Cleaner Production 2021; 318: 128421. https://doi.org/10.1016/j.jclepro.2021.128421

Crossref
DOI: 10.31643/2028/6445.33
Metallurgy and Metallurgical Engineering

Image-Based FEM Modeling of the Stress State in Hypereutectic High-Chromium Cast Irons

[1]Perezhogin V.Yu., [1]Panichkin A.V., [2]Małgorzata R.G., [1*]Abyl S.S.

[1] Institute of Metallurgy and Ore Beneficiation JSC, Satbayev University, Almaty, Kazakhstan
[2]Wroclaw University of Science and Technology, Wroclaw, Poland

** Corresponding author email: Abyl.S@stud.satbayev.university*

Received: *June 17, 2026*
Peer-reviewed: *July 26, 2026*
Accepted: *September 8, 2026*

ABSTRACT

We developed an approach to analyze local thermal stresses in hypereutectic high-chromium cast irons using image-based finite element modeling (FEM) based on real metallographic images. Model preparation included Otsu thresholding of the microstructure, filtering noise objects, and directly assigning the spatial phase distribution from the binarized image without intermediate geometry construction in computer-aided design (CAD) systems. To verify the proposed approach, Drawing Exchange Format (DXF)-based and image-based FEM models constructed from the same microstructural data were compared, and the influence of finite element size on the calculated stress state was investigated. The results showed that, with a progressive reduction in finite element size, the image-based simulation results approached those obtained using the DXF-based models despite the discrete pixel-based representation of the phase boundaries. The image-based approach reproduces the main features of the local stress distributions obtained using the DXF-based models while eliminating the need for image vectorization and intermediate CAD/DXF geometry construction, thereby substantially simplifying the preparation of computational models of real microstructures. The obtained results confirm the applicability of image-based FEM for comparative analysis of local thermal stress distributions in complex multiphase microstructures of high-chromium cast irons.

Keywords: hypereutectic high-chromium cast iron, image-based FEM, thermal stresses, M_7C_3 carbides, microstructure analysis, finite element modeling.

Information about authors:

Perezhogin Vitaliy Yurievich — *PhD, Researcher, Materials Science Laboratory, Institute of Metallurgy and Ore Beneficiation JSC, Satbayev University, 050010, Shevchenko str., 29/133, Almaty, Kazakhstan. E-mail: v.perezhogin@satbayev.university; ORCID ID: https://orcid.org/0009-0006-7881-4786*

Panichkin Alexander Vladimirovich — *Candidate of Technical Sciences, Leading Researcher at the Materials Science Laboratory, Institute of Metallurgy and Ore Beneficiation JSC, Satbayev University, 050010, Shevchenko str., 29/133, Almaty, Kazakhstan. Email: a.panichkin@satbayev.university; ORCID ID: https://orcid.org/0000-0002-2403-8949*

Małgorzata Rutkowska-Gorczyca — *PhD, Habilitated Doctor of Engineering, Department of Mechanics, Wroclaw University of Science and Technology, 50-370 Wroclaw, Poland. E-mail: Malgorzata.Rutkowska-Gorczyca@pwr.wroc.pl; ORCID ID: https://orcid.org/0000-0003-2712-5914*

Abyl Salima Serikkyzy — *Doctoral student, Junior Researcher, Materials Science Laboratory, Institute of Metallurgy and Ore Beneficiation JSC, Satbayev University, 050010, Shevchenko str., 29/133, Almaty, Kazakhstan. E-mail: Abyl.S@stud.satbayev.university; ORCID ID: https://orcid.org/0009-0006-1904-3483*

Introduction

Hypereutectic high-chromium cast irons are widely used under severe abrasive wear conditions due to their high hardness and significant content of the M_7C_3 ($(Fe, Cr)_7 C_3$) carbide phase [[1], [2], [3], [4], [5], [6]]. The performance of these materials is largely determined by the size and volume fraction of primary and eutectic carbides, their morphology, distribution within the austenitic matrix, and the characteristics of the phase boundaries [[7], [8], [9], [10]].

The presence of extended and branched carbide structures can lead to local stress concentrations and significantly affect crack initiation and fracture processes [[2], [11], [12]]. The local stress state in the carbide-matrix system has a significant influence on fracture resistance, wear resistance, and the likelihood of carbide-phase fracture during the service of high-chromium cast irons under thermal cycling and mechanical loading conditions.

Finite element modeling (FEM) methods are widely used to analyze local stress states in

multiphase materials. One of the traditional approaches to constructing computational models of real microstructures involves vectorization of metallographic images followed by the generation of CAD/DXF geometry [[13], [14]]. However, when applied to complex real microstructures, this approach is characterized by labor-intensive model preparation, difficulties in finite element mesh generation, and the need for additional geometry processing. Furthermore, geometry simplification may result in the loss of specific features of the actual phase morphology.

An alternative approach is image-based FEM, which is based on the direct use of binarized metallographic images for constructing computational models [[13], [14], [15]]. This approach enables the actual geometry and spatial distribution of phases to be represented without intermediate CAD/DXF geometry construction, thereby substantially simplifying the preparation of finite element models of complex microstructures.

FEM methods are widely applied to the analysis of residual stresses in additive manufacturing and heterogeneous materials [[16], [17]]; however, their application to the microstructure-based analysis of multiphase alloys remains comparatively limited. Therefore, it is of interest to assess the feasibility of directly using binarized metallographic images for finite element modeling of such structures and to compare the resulting predictions with those obtained using the traditional DXF-based approach.

The aim of this study was to develop and verify an image-based FEM approach for analyzing the local distribution of thermal stresses in real microstructures of hypereutectic high-chromium cast irons by comparison with DXF-based modeling and by evaluating the influence of finite element discretization on the simulation results.

Materials and Methods

A hypereutectic high-chromium cast iron containing the M_7C_3 carbide phase was used as the material investigated in this study. The specimen used for the development of the methodology was melted in a UIFV-0.005 vacuum induction melting furnace. The charge consisted of a Ø50 mm bar of 50Kh steel in accordance with GOST 4543-2016 and high-carbon ferrochromium FeCr60C90Si2 in accordance with GOST 4757-91. The required carbon content was achieved by adding graphite powder with a particle size of 0.5-1 mm to the charge. Melting was carried out at a residual pressure of 50-70 Pa. The melt temperature was monitored using a stationary spectral-ratio infrared pyrometer, Termoskop-800-2S-VT1. After the melt surface reached a temperature of 1500 °C, the inductor current was reduced to prevent further overheating, and the melt was held for 20 min. Air was then admitted into the furnace, the vacuum chamber lid was moved aside, and the melt was poured into a mold (Figure 1) made of PKhKTs-20-grade periclase-chromite bricks.

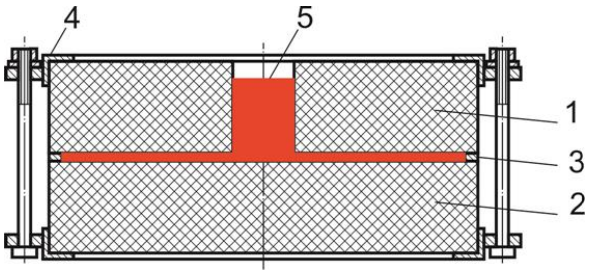

Figure 1 – Casting mold (1 – upper plate, 2 – lower plate, 3 – steel frame, 4 – mold clamping fixture, 5 – casting)

The resulting casting was a plate with a thickness of 6 ± 0.5 mm and dimensions of 100×350 mm, with a sprue located at its center. A 100×29 mm plate was cut from the resulting casting by wire electrical discharge machining using a DK7720 machine. The specimen was not subjected to any heat treatment. One surface of the plate was then leveled by electrical discharge machining by removing a thin layer up to 0.7 mm thick. The actual alloy composition was determined by semiquantitative X-ray fluorescence analysis and quantitative carbon analysis (Table 1).

Table 1 - Actual chemical composition of the alloy

Element	Fe	Cr	C	Mn	Ni	Mo
wt.%	70.17	24.3	4.48	0.72	0.17	0.16

Table 2 - Fraction and dimensional characteristics of the carbide phase in the investigated alloy

Structure parameter	Measurement result
Carbide fraction, %	25.6
Primary carbide fraction, %	16.5
Average length of primary carbides in the cross-sectional plane, μm	32.9
Average thickness of primary carbides in the cross-sectional plane, μm	15.8
Average area of primary carbides, μm^2	312

The prepared surface was ground using SiC abrasive paper and polished using diamond pastes. The microstructure was revealed by rubbing the polished surface with a cotton swab soaked in an etchant containing 100 mL HCl, 7 mL H_2SO_4, and 30 g $CuSO_4$. Metallographic images were acquired using a Leica DM IRM metallographic workstation. Microstructural analysis was performed using images obtained by optical microscopy. Image processing was carried out using ImageJ/Fiji software [18]. The total carbide fraction, primary carbide fraction, and dimensional characteristics of the primary carbides are presented in Table 2.

Image preparation included conversion of the metallographic images to 8-bit grayscale, Otsu thresholding [19], and subsequent filtering of the binarized images to identify the carbide phase [20]. A distinction should be made between the preliminary removal of noise objects with an area of less than 4 px^2, which was performed for all images, and the subsequent structural filtering of carbide objects by area, which was used to generate one of the investigated microstructural variants. Filtering was performed using the standard Analyze Particles tools available in ImageJ/Fiji. The threshold value of 4 px^2 corresponded to a minimum object size of 2×2 pixels. Objects with smaller areas were regarded as binarization noise artifacts because their dimensions were substantially smaller than the characteristic dimensions of the carbide inclusions. For the DXF-based models, objects intersecting the image boundaries were additionally removed because they resulted in open contours during CAD geometry construction. This step was not required for image-based FEM because the phase distribution was assigned directly from the binarized image.

According to thermodynamic calculations for the Fe-Cr-C system [[21], [22]] and experimental studies [[3], [9], [23]], the predominant carbide phase in hypereutectic high-chromium cast irons within the investigated composition range is M_7C_3, with Cr and Fe being the predominant elements in its metallic sublattice. Accordingly, the finite element model of the microstructure was considered as a two-phase system consisting of an austenitic matrix and an M_7C_3 carbide phase. This representation is a modeling approximation because the composition of M_7C_3 carbides in real high-chromium cast irons may vary due to differences in the Fe-to-Cr ratio in the metallic sublattice; consequently, their thermophysical and mechanical properties may also differ from those of pure Cr_7C_3. In the present study, the properties of Cr_7C_3 were therefore used as effective parameters for the M_7C_3 carbide phase. Accordingly, the calculated stress values should primarily be interpreted comparatively, for analyzing the characteristics of stress distribution and localization within the real microstructure, rather than as exact absolute stress values for a specific alloy.

Constant thermophysical and mechanical properties of the austenitic matrix and the M_7C_3 carbide phase were used for finite element modeling. Austenitic stainless steel 316L (1.4435, X2CrNiMo18-12) was selected as the model material for the austenitic matrix and was used as an effective approximation of the properties of the austenitic metallic matrix of high-chromium cast iron rather than as its exact chemical analogue. The matrix properties were selected taking into account published data for 316L steel [24]. The properties of the Cr_7C_3 carbide phase were selected based on published experimental and computational data for carbides of this type [[25], [26]]. The thermophysical and mechanical properties used in the calculations are presented in Table 3.

Table 3 - Thermophysical and mechanical properties of the carbide phase and austenitic matrix

Property	Value		Unit
	Austenite	***Cr_7C_3 carbide***	***Unit***
Coefficient of thermal expansion	1.7e-5	1e-5	1/K
Thermal conductivity	20	16	W/(m·K)
Density	8e3	7e3	kg/m³
Young's modulus	200e9	310e9	Pa
Poisson's ratio	0.30	0.23	-

Finite element modeling was performed in COMSOL Multiphysics using a two-dimensional steady-state thermomechanical formulation. The plane strain approximation was adopted for the mechanical problem. The thermal problem was defined using the Heat Transfer in Solids interface, while the stress-strain state was modeled using the Solid Mechanics interface. The thermal and mechanical problems were coupled through the Thermal Expansion multiphysics interface. The calculations were performed using a thermal strain reference temperature of T_{ref} = 1420.15 K and a final temperature of T = 293.15 K, corresponding to a temperature decrease of 1127 K. In this

formulation, the kinetics of the cooling process and the spatial and temporal evolution of the temperature field were not modeled. To prevent rigid-body motion of the computational domain, kinematic constraints were applied at two lower corner points of the square computational domain. At the lower-left corner, displacements were constrained in both directions (u_x=0, u_y=0), whereas at the lower-right corner, only the vertical displacement was constrained (u_y=0), leaving the horizontal displacement free. This constraint scheme eliminated translational and rotational rigid-body motion of the computational domain without rigidly fixing its external boundaries.

To evaluate the influence of spatial discretization, calculations were performed using different levels of finite element mesh refinement. At the initial stage, the standard COMSOL Multiphysics mesh refinement levels were used, after which the element size was specified using user-defined mesh parameters. The maximum finite element size was progressively reduced to evaluate the sensitivity of the calculated stress state to spatial discretization and to select rational mesh parameters.

The calculations were performed using a stationary solver in a Fully Coupled formulation. A Direct solver was used to solve the linear system of equations, while the nonlinear iterations were performed using Newton's method with automatic parameter selection.

The DXF-based FEM models were generated by vectorizing the preprocessed binarized images in Inkscape using the standard tracing parameters. The resulting vector contours were saved in DXF format and imported into COMSOL Multiphysics [27] to construct the geometry of the computational domain and subsequently generate the finite element mesh. Thus, the DXF-based approach included an intermediate step in which the raster image was converted into vector geometry. This approach provided explicit phase boundaries and enabled the construction of topologically consistent FEM models based on the real microstructure.

The image-based FEM models were constructed directly from the preprocessed binarized images without intermediate vectorization or CAD/DXF geometry construction [[13], [14], [15]]. The binarized image was imported directly into COMSOL Multiphysics [27] using the built-in Image function. Pixel values were used to define the spatial distribution of the properties of the matrix and M_7C_3 carbide phase within a single two-dimensional computational domain. The finite element mesh was generated directly over the computational domain. The image-based FEM approach was implemented entirely using the built-in capabilities of COMSOL Multiphysics and did not require additional programming scripts or external automation tools.

The stress state was analyzed using the distributions of the first and second principal stresses, SP1 and SP2. SP2 maps were used to visualize the localization of compressive stresses in the model and real microstructures, whereas quantitative comparison between the DXF-based and image-based models was performed using SP1 as a measure of local tensile stresses, which are of primary interest with respect to potential microcrack initiation. For quantitative comparison, the mean SP1 value and the 95th percentile (P95) of SP1 were determined. The use of P95 reduced the influence of isolated local extrema associated with the geometry of the phase boundaries and finite element mesh discretization.

The developed model was primarily intended for comparative analysis of the effects of the microstructure representation method, finite element discretization parameters, and carbide-phase morphology on the distribution of local thermal stresses. Because constant phase properties and a stationary formulation were used, the calculated stress values were not interpreted as exact absolute values of residual stresses in the real material.

Results and Discussion

For a preliminary assessment of the influence of carbide-phase morphology and for the development of the FEM approach, model carbide structures of different shapes were used (Figure 2). These models were used to analyze the local distribution of thermal stresses and to evaluate the influence of carbide-phase geometry on the formation of stress concentrations [[2], [11]].

The obtained results showed the formation of localized regions of elevated stress near sharp-angled regions of the carbide phase and in areas with complex phase-boundary geometry [28]. This confirms the significant influence of carbide morphology on the local stress state and supports the need to analyze real microstructures without additional geometric idealization.

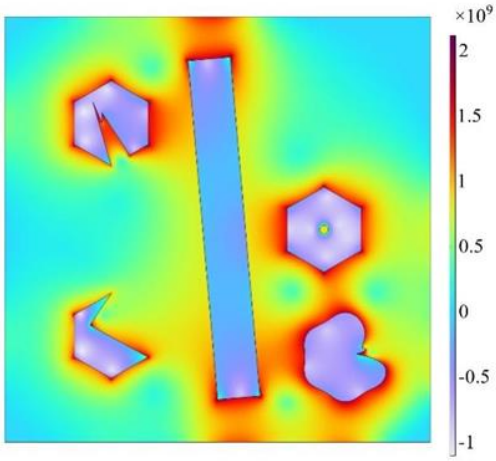

Figure 2 – Distribution of the second principal stress SP2 (Pa) for model carbide structures with complex geometries

The formation of local stress concentrations is associated with differences in the thermophysical and mechanical properties of the M_7C_3 carbide phase and the austenitic matrix, primarily their coefficients of thermal expansion and elastic properties [[3], [11], [12]]. The difference in the coefficients of thermal expansion results in different thermal strains of the phases under the imposed temperature change and, due to strain compatibility at the phase boundary, leads to the formation of local stress concentrations. The most pronounced stress localization occurs near sharp-angled, elongated, and geometrically complex regions of the carbide phase [[2], [11]].

Local tensile stresses in the carbide phase may contribute to microcrack initiation and subsequent carbide fracture during both the production and service of high-chromium cast iron components. Therefore, analysis of the stress distribution in the carbide - matrix system is of practical interest for assessing the potential fracture resistance and performance of this class of materials.

Following the analysis of the model structures, the developed approach was applied to real metallographic images of hypereutectic high-chromium cast irons (Figure 3).

To evaluate the influence of preliminary microstructural image processing on the FEM simulation results, different representations of the carbide structure were considered. At the first stage, objects were filtered by area. At an image scale of 50 μm = 839 px, the threshold area of 7701 px^2 corresponded to approximately 27.35 μm^2; objects with smaller areas were removed from the binarized image. The threshold value was selected based on a characteristic change in the object area distribution that separated numerous small microstructural constituents from a group of larger carbide objects (Figure 4a).

In addition, morphological filtering of the remaining objects was performed using the parameter P^2/S, where P is the object perimeter, and S is its area. This dimensionless parameter was used to quantitatively characterize contour complexity and branching. A threshold value of 207.05 was adopted; objects with higher parameter values, characterized by more complex and branched morphologies, were removed, whereas more compact objects were retained (Figure 4b).

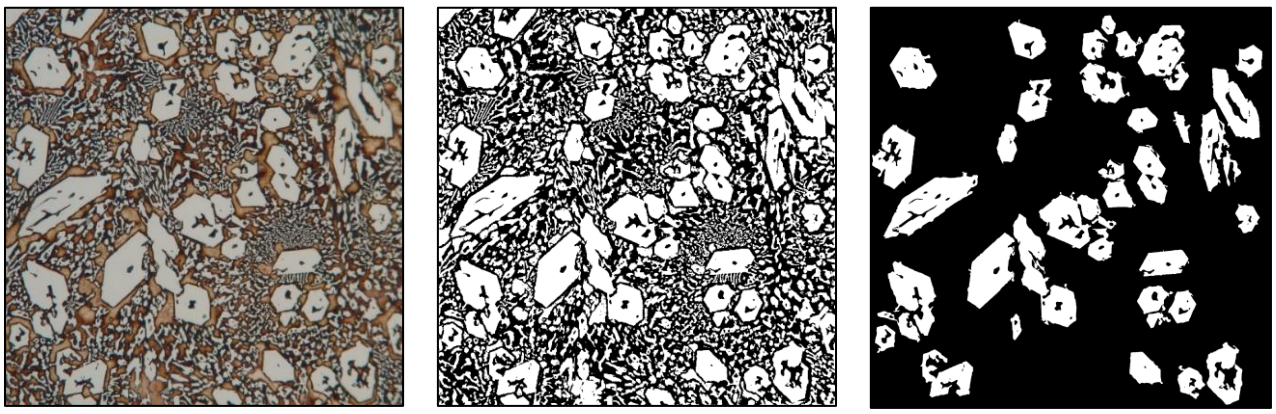

a b c

Figure 3 – Image processing stages (×750) a – original image; b – Otsu thresholding; c – idealized representation of primary carbide morphology

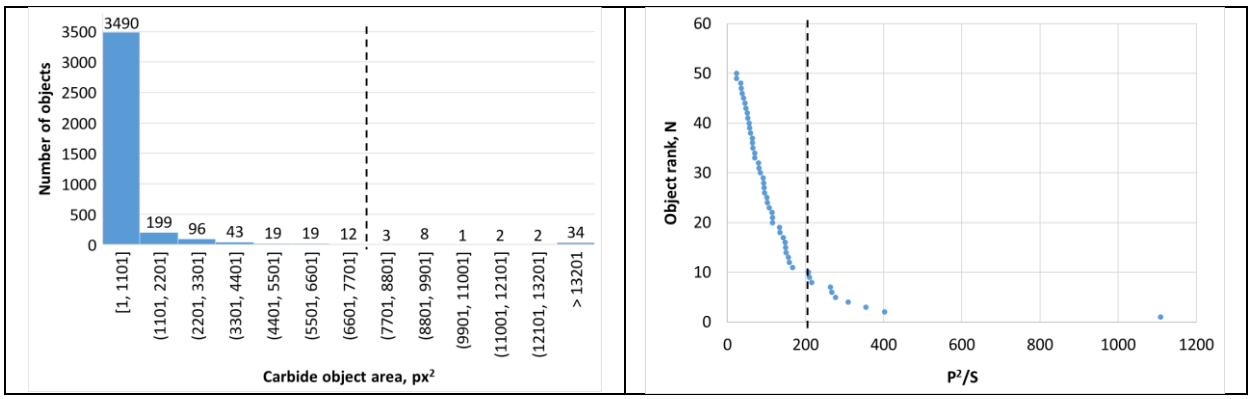

Figure 4 – Criteria for filtering carbide objects during preprocessing of the binarized image
a – distribution of carbide objects by area; b – morphological parameter P^2/S as a function of object number

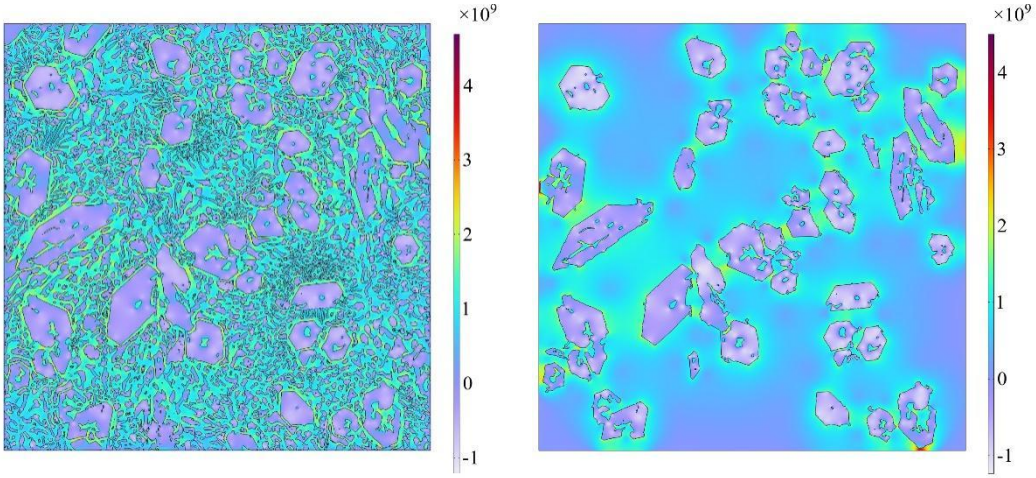

a b

Figure 5 – Distribution of the second principal stress SP2 (Pa) in DXF-based FEM models of the real microstructure: a – model based on the complete binarized image;
b – model based on the idealized representation of primary carbides

For quantitative comparison of the DXF-based and image-based FEM models, five microstructure representations were used: 1 – idealized representation of primary carbide morphology; 2 – image after morphological filtering using the P^2/S parameter; 3 – image after filtering carbide objects by area; 4 – image after removing objects intersecting the boundaries of the analyzed region; and 5 – complete binarized image after removal of only small noise objects with areas below 4 px^2. The same image variants were used to construct both the DXF-based and image-based FEM models, enabling direct comparison of the two approaches using identical representations of the initial microstructure.

The DXF-based FEM simulation of the real microstructure showed that the maximum stresses were localized predominantly near the phase boundaries, particularly near sharp-angled regions of the carbide phase (Figure 5). The obtained results confirmed the significant influence of carbide morphology on the distribution of local stresses. This stress distribution pattern is consistent with the established understanding of strain localization in systems containing rigid carbide inclusions [[2], [11], [12]].

Comparison of the complete binarized microstructure with its idealized representation showed that the removal of part of the carbide network changes the local stress distribution pattern. This indicates the importance of preserving the actual morphology of both primary and eutectic carbides when analyzing the local stress state.

Despite its ability to explicitly represent phase boundaries, the DXF-based approach was characterized by labor-intensive model preparation. Vectorization of binarized images, generation of CAD/DXF geometry, and subsequent finite element mesh generation became increasingly difficult as the geometric complexity of the carbide network increased. Therefore, further work focused on the development of an image-

based FEM approach that enables calculations to be performed directly from binarized microstructural images without intermediate CAD geometry construction.

In the image-based FEM models, the phase distribution was defined directly from the binary image map. Unlike the DXF-based approach, this method did not require vectorization of phase boundaries or the construction of separate geometric domains for the carbide phase and the matrix. However, the discrete pixel-based representation of the phase boundaries necessitates an assessment of the influence of finite element size on the representation of the local stress state.

To evaluate the influence of finite element discretization, calculations were performed with a progressive reduction in the maximum finite element size. Reducing the maximum finite element size resulted in a more detailed representation of the phase-boundary geometry and local stress distribution and led to a gradual convergence of the image-based model results toward those obtained using the DXF-based representation (Figure 6). As part of the mesh sensitivity analysis, the maximum element size was progressively reduced to 0.2 µm; representative stages of this refinement are shown in the figure. Further mesh refinement, however, was accompanied by a substantial increase in computational cost.

Based on the results of the mesh sensitivity analysis, a maximum finite element size of 0.5 µm was selected for subsequent calculations, providing a reasonable balance between the level of detail in the calculated stress state and computational cost.

When larger mesh sizes were used, local stress maxima were smoothed due to insufficient representation of the complex phase-boundary geometry. Reducing the maximum finite element size enabled a more accurate representation of the local features of the stress distribution near the carbide phase and provided better agreement with the DXF-based modeling results [[13], [14], [15]].

For quantitative verification of the image-based FEM approach, the results of DXF-based and image-based simulations were compared for the five investigated microstructure representations (1-5), corresponding to different preprocessing variants. Maximum finite element sizes of 0.2 and 0.5 µm were used for the image-based models. For quantitative comparison, the mean SP1 value and the 95th percentile (P95) of SP1 in the M_7C_3 carbide phase were determined (Figure 7).

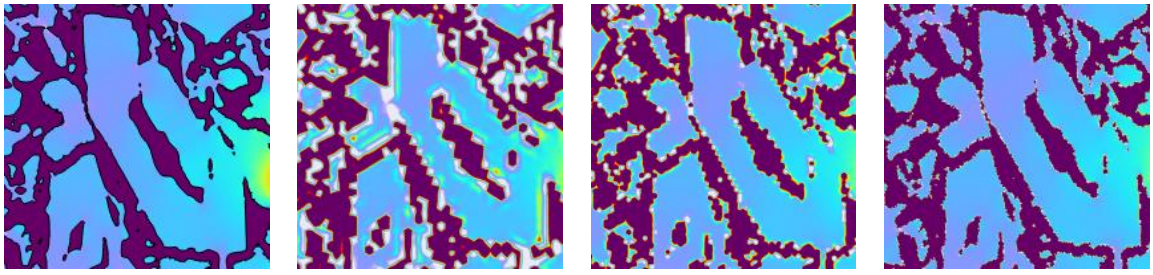

Figure 6 – Comparison of SP1 stress fields for different models: a – DXF-based model; b – image-based model, mesh size 1.65 µm; c – image-based model, mesh size 0.5 µm; d – image-based model, mesh size 0.2 µm

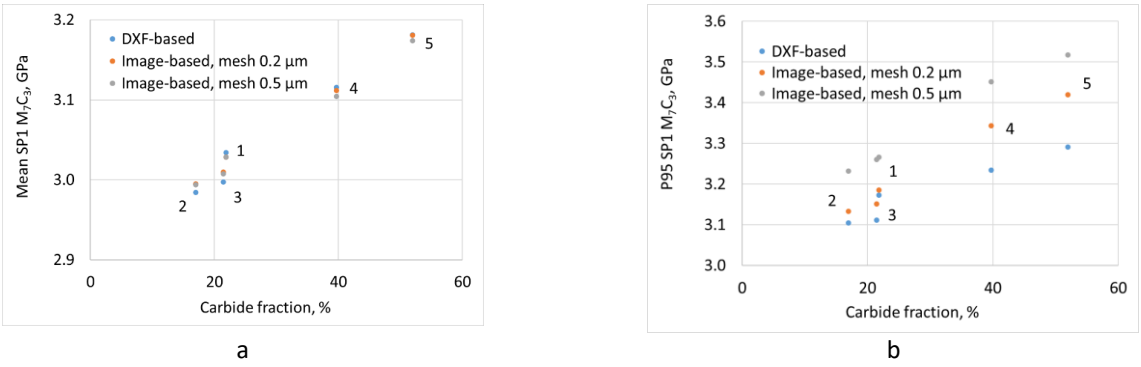

Figure 7 – Comparison of stress-state characteristics in M_7C_3 carbides for the DXF-based and image-based FEM models a – mean SP1; b – P95 SP1

The obtained results show that the mean SP1 values in the M_7C_3 carbide phase calculated using the DXF-based and image-based FEM models are in good agreement for all investigated microstructure representations (Figure 7a). Reducing the maximum finite element size in the image-based model from 0.5 to 0.2 µm has only a minor effect on the mean SP1 values, indicating their relatively low sensitivity to further finite element mesh refinement.

More pronounced differences are observed for the P95 SP1 values (Figure 7b). Overall, at a maximum finite element size of 0.5 µm, the P95 values show greater deviations from the corresponding values obtained using the DXF-based model, particularly for the variants with a higher carbide-phase fraction. Reducing the maximum element size to 0.2 µm results in closer agreement in most of the investigated variants. This indicates a higher sensitivity of the upper part of the local stress distribution to spatial discretization and to the accuracy with which the complex phase-boundary geometry is represented.

Thus, the finite element size has a substantially smaller influence on the integral characteristics of the stress state represented by the mean SP1 values than on the characteristics of the upper part of the stress distribution. A mesh with a maximum element size of 0.5 µm provides stable representation of the mean stress characteristics at substantially lower computational cost, whereas further mesh refinement to 0.2 µm improves the representation of high local stress values.

Some differences between the models are associated with the different representations of the phase boundaries. The DXF-based model uses smoothed vector contours, whereas in image-based FEM the phase boundaries are represented by the discrete pixel structure of the image.

Despite the differences in phase-boundary representation, the image-based FEM approach provides results comparable to those obtained using DXF-based modeling and enables calculations to be performed directly from binarized microstructural images without intermediate CAD geometry construction. The obtained results confirm the applicability of image-based FEM for comparative analysis of the stress state in high-chromium cast irons with different representations and morphologies of the carbide phase.

It should be noted that constant thermophysical and mechanical properties of the phases were used in the present study, without accounting for their temperature dependence, plastic deformation, or possible phase transformations in the matrix. In addition, microcrack formation and fracture of the carbide phase, which may lead to relaxation of local stresses in the real material, were not considered. Therefore, the calculated stress values should be regarded as model characteristics of the stress state, and the obtained results should primarily be considered as a basis for comparative analysis of the DXF-based and image-based FEM approaches, the influence of spatial discretization, and the representation of the carbide phase.

The developed approach can be used for further investigation of the effects of carbide-phase morphology, its volume fraction, and the structural state of the matrix on the local stress state of high-chromium cast irons. The ability to directly use binarized metallographic images provides a basis for comparative analysis of a large number of real microstructures without labor-intensive intermediate CAD geometry construction. Experimental verification of the absolute residual stress values using independent experimental methods, together with further improvement of the FEM model to account for internal stress relaxation associated with local plastic deformation, represents an important direction for further development of the proposed approach.

Conclusions

An image-based FEM approach was developed for the analysis of local thermal stresses in hypereutectic high-chromium cast irons directly from binarized metallographic images without intermediate CAD geometry construction.

It was demonstrated that image-based FEM models reproduce the main features of the stress distributions obtained using DXF-based models while substantially reducing the effort required for computational model preparation.

It was established that the influence of finite element size depends on the stress-state characteristic considered. The mean SP1 values change only slightly when the maximum element size of the image-based model is reduced from 0.5 to 0.2 µm, whereas P95 SP1 is more sensitive to spatial discretization and approaches the results of DXF-based modeling with mesh refinement.

It was shown that the representation and morphology of the carbide phase have a significant influence on stress localization in the carbide-matrix system, while the highest local stress values are sensitive to the method used to represent the phase boundaries.

Conflicts of interest. On behalf of all authors, the corresponding author states that there is no conflict of interest.

CRediT author statement: **V. Perezhogin**: Methodology, Calculations, Results summary, Article preparation; **A. Panichkin**: Article concept, Results discussion, Article editing; **G. Małgorzata**: Discussion and interpretation of scientific results, Provision of scientific and methodological recommendations for the manuscript; **S. Abyl**: literature review, Article design, Reviewing and Editing.

Acknowledgements. This research is funded by the Science Committee of the Ministry of Science and Higher Education of the Republic of Kazakhstan (Grant No. AP26102933).

Cite this article as: Perezhogin VYu, Panichkin AV, Małgorzata RG, Abyl SS. Image-Based FEM Modeling of the Stress State in Hypereutectic High-Chromium Cast Irons. Kompleksnoe Ispolzovanie Mineralnogo Syra = Complex Use of Mineral Resources. 2028; 346(3):131-141. https://doi.org/10.31643/2028/6445.33

Жоғары хромды гиперэвтектикалық шойындардағы кернеу күйін Image-based FEM-модельдеуі

[1] Пережогин В.Ю., [1]Паничкин А.В., [2]Małgorzata R.G., [1]Абыл С.С.

[1] Металлургия және кен байыту институты АҚ, Сәтбаев университеті, Алматы, Қазақстан
[2]Вроцлав ғылым және технология университеті, Вроцлав, Польша

Мақала келді: *17 маусым 2026*
Сараптамадан өтті: *26 шілде 2026*
Қабылданды: *8 қыркүйек 2026*

ТҮЙІНДЕМЕ

Нақты металлографиялық кескіндерге негізделген image-based шекті элементтік модельдеуді қолдана отырып, жоғары хромды гиперэвтектикалық шойындардағы жергілікті термиялық кернеулерді талдауға арналған тәсіл әзірленді. Есептік модельдерді дайындау Оцу әдісін қолдана отырып микроқұрылымды бинаризациялауды, шулы әсері бар объектілерді сүзгіден өткізуді және CAD автоматтандырылған жобалау жүйелерінде аралық геометрия құрусыз бинарланған кескін бойынша фазалардың кеңістіктік таралуын тікелей беруді қамтыды. Ұсынылған тәсілді верификациялау үшін Drawing Exchange Format (DXF) және бірдей микроструктуралық деректер негізінде құрылған image-based FEM-модельдер салыстырылды, сондай-ақ ақырғы элементтің өлшемінің есептелген кернеулік күйге әсері зерттелді. Көрсетілгендей, соңғы элемент тердің өлшемін біртіндеп азайтқан кезде image-based модельдеу нәтижелері, фазааралық шекаралардың дискретті пиксельдік бейнеленуіне қарамастан, DXF-based модельдердің нәтижелеріне сәйкес келетіні көрсетілді. Image-based тәсіл DXF-based модельдерді пайдалану арқылы алынған жергілікті кернеулердің таралуының негізгі заңдылықтарын қайталайды және бұл ретте кескінді векторизациялауды және аралық CAD/DXF-геометриясын құруды талап етпейді, бұл нақты микроқұрылымдардың есептеу модельдерін дайындауды айтарлықтай жеңілдетеді. Алынған нәтижелер жоғары хромды шойындардың күрделі көпфазалы микроқұрылымдарында термиялық кернеулердің локальды таралуын салыстырмалы талдау үшін image-based FEM модельдеуді қолдану мүмкіндігін растайды.

Түйін сөздер: жоғары хромды гиперэвтектикалық шойын, Image-based FEM, термиялық кернеулер, M_7C_3 карбидтері, микроқұрылымды талдау, ақырлы элементтерді модельдеу.

Авторлар туралы ақпарат:

Пережогин Виталий Юрьевич
PhD, Материалтану зертханасының ғылыми қызметкері, Металлургия және кен байыту институты АҚ, Сәтбаев университеті, 050010, Шевченко көш., 29/133, Алматы, Қазақстан. E-mail: v.perezhogin@satbayev.university; ORCID ID: https://orcid.org/0009-0006-7881-4786

Паничкин Александр Владимирович
Техника ғылымдарының кандидаты, Материалтану зертханасының жетекші ғылыми қызметкері, Металлургия және кен байыту институты АҚ, Сәтбаев университеті, 050010, Шевченко көш., 29/133, Алматы, Қазақстан. Email: a.panichkin@satbayev.university; ORCID ID: https://orcid.org/0000-0002-2403-8949

Małgorzata Rutkowska-Gorczyca
PhD, Инженерия ғылымдарының докторы, Механика кафедрасы, Вроцлав ғылым және технология университеті, Вроцлав, 50-370, Польша. E-mail: Malgorzata.Rutkowska-Gorczyca@pwr.wroc.pl; ORCID ID: https://orcid.org/0000-0003-2712-5914

Абыл Салима Серикқызы
Докторант, Материалтану зертханасының ғылыми қызметкері, Металлургия және кен байыту институты АҚ, Сәтбаев университеті, 050010, Шевченко көш., 29/133, Алматы, Қазақстан. E-mail: Abyl.S@stud.satbayev.university; ORCID ID: https://orcid.org/0009-0006-1904-3483

Image-based FEM-моделирование напряжённого состояния в высокохромистых заэвтектических чугунах

[1]Пережогин В.Ю., [1]Паничкин А.В., [2]Małgorzata R.G., [1]Абыл С.С.

[1] АО Институт металлургии и обогащения, Satbayev University, Алматы, Казахстан
[2] Вроцлавский университет науки и техники, Вроцлав, Польша

Поступила: *17 июня 2026*
Рецензирование: *26 июля 2026*
Принята в печать: *8 сентября 2026*

АННОТАЦИЯ

Разработан подход к анализу локальных термических напряжений в высокохромистых заэвтектических чугунах с использованием image-based конечно-элементного моделирования на основе реальных металлографических изображений. Подготовка расчётных моделей включала бинаризацию микроструктуры методом Оцу, фильтрацию шумовых объектов и непосредственное задание пространственного распределения фаз по бинаризованному изображению без промежуточного построения геометрии в системах автоматизированного проектирования (CAD). Для верификации предложенного подхода выполнено сопоставление Drawing Exchange Format (DXF) и image-based FEM-моделей, построенных на основе одинаковых микроструктурных данных, а также исследовано влияние размера конечного элемента на рассчитанное напряжённое состояние. Показано, что при последовательном уменьшении размера конечных элементов результаты image-based моделирования приближаются к результатам DXF-based моделей, несмотря на дискретное пиксельное представление межфазных границ. Image-based подход воспроизводит основные закономерности локального распределения напряжений, полученные с использованием DXF-based моделей, и при этом не требует векторизации изображения и построения промежуточной CAD/DXF-геометрии, что существенно упрощает подготовку расчётных моделей реальных микроструктур. Полученные результаты подтверждают возможность применения image-based FEM-моделирования для сравнительного анализа локального распределения термических напряжений в сложных многофазных микроструктурах высокохромистых чугунов.

Ключевые слова: высокохромистый заэвтектический чугун, image-based FEM, термические напряжения, карбиды M_7C_3, анализ микроструктуры, конечно-элементное моделирование.

Информация об авторах:

Пережогин Виталий Юрьевич — *PhD, научный сотрудник, Лаборатория металловедения, АО Институт металлургии и обогащения, Satbayev University, 050010, ул. Шевченко, 29/133, Алматы, Казахстан. E-mail: v.perezhogin@satbayev.university; ORCID ID: https://orcid.org/0009-0006-7881-4786*

Паничкин Александр Владимирович — *Кандидат технических наук, старший научный сотрудник, Лаборатория металловедения, АО Институт металлургии и обогащения, Satbayev University, 050010, ул. Шевченко, 29/133, Алматы, Казахстан. Email: a.panichkin@satbayev.university; ORCID ID: https://orcid.org/0000-0002-2403-8949*

Małgorzata Rutkowska-Gorczyca — *Кандидат наук, Доктор технических наук, Кафедра механики, Вроцлавский университет науки и техники, 50-370 Вроцлав, Польша. E-mail: Malgorzata.Rutkowska-Gorczyca@pwr.wroc.pl; ORCID ID: https://orcid.org/0000-0003-2712-5914*

Абыл Салима Серикқызы — *Докторант, младший научный сотрудник, Лаборатория металловедения, АО Институт металлургии и обогащения, Satbayev University, 050010, ул. Шевченко, 29/133, Алматы, Казахстан. E-mail: Abyl.S@stud.satbayev.university; ORCID ID: https://orcid.org/0009-0006-1904-3483*

References

[1] Karantzalis E, Lekatou A, Mavros H. Microstructure and properties of high chromium cast irons: effect of heat treatments and alloying additions. International Journal of Cast Metals Research. 2009; 22(6):448-456. https://doi.org/10.1179/174313309X436637

[2] Coronado J.J. Effect of $(Fe,Cr)_7C_3$ carbide orientation on abrasion wear resistance and fracture toughness. Wear. 2011; 270(3-4):287-293. https://doi.org/10.1016/j.wear.2010.10.070

[3] Jokari-Sheshdeh M, Ali Y, Gallo SC, Lin W, Gates JD. Effect of Cr: Fe ratio on the mechanical properties of $(Cr, Fe)_7C_3$ ternary carbides in abrasion-resistant white cast irons. Journal of Materials Science. 2023; 58:7504-7521. https://doi.org/10.1007/s10853-023-08461-z

[4] Wiengmoon A. Carbides in high chromium cast irons. Naresuan University Engineering Journal. 2011; 6(1):64-71. https://doi.org/10.14456/nuej.2011.6

[5] Li Y, Gu L, Du M, et al. Microstructure and properties of hypereutectic high chromium cast iron containing nitrogen. Materials Science and Technology. 2024; 40(1):26-41. https://doi.org/10.1177/02670836231212611

[6] Panichkin AV, Korotenko RY, Kenzhegulov AK, et al. Porosity and non-metallic inclusions in cast iron produced with a high proportion of scrap. Kompleksnoe Ispolzovanie Mineralnogo Syra = Complex Use of Mineral Resources. 2022; 323(4):68–76. https://doi.org/10.31643/2022/6445.42

[7] Panichkin A, Uskenbayeva A, Kenzhegulov A, Mamaeva A, Imbarova A, Kshibekova B, Alibekov Zh, Nurhadiyanto D, Yunita I. Assessment of the effect of small additions of some rare earth elements on the structure and mechanical properties of castings from hypereutectic chromium white irons. AIMS Materials Science. 2023; 10(3):517–540. https://doi.org/10.3934/matersci.2023029

[8] Panichkin AV, Wieleba WK, Uskenbayeva AM, Kenzhegulov AK, Mamayeva AA, Kvyatkovskii SA, Kasenova BA, Imbarova AT. Effect of thermal treatment of chromium iron melts on the structure and properties of castings. Materials Research Express. 2023; 10:086502. https://doi.org/10.1088/2053-1591/acead7

[9] Panichkin AV, Mamaeva AA, Kenzhegulov AK, Kshibekova BB, Uskenbaeva AM, Imbarova AT. The influence of cooling rate on the structure and properties of castings of hypereutectic high-chromium cast iron when they are modified with B, Bi, Sb, Sn, Ca. AIMS Materials Science. 2024; 11(1):58–80. https://doi.org/10.3934/matersci.2024003

[10] Panichkin AV, Mamaeva AA, Kenzhegulov AK, Kshibekova BB, Uskenbaeva AM, Imbarova AT, Alibekov Zh. Effect of carbon and cooling rate on the structure of hypereutectic high chromium cast iron in the cast state and after heat treatment. Journal of Composites Science. 2023; 7(12):483. https://doi.org/10.3390/jcs7120483

[11] Albertin E, Sinatora A. Effect of carbide fraction and matrix microstructure on the wear of cast iron balls tested in a laboratory ball mill. Wear. 2001; 250:492-501. https://doi.org/10.1016/S0043-1648(01)00664-0

[12] Wang J, Liu T, Xing X, Li J, Qi X, Yang Q. Study of the wear resistance of hypereutectic Fe-Cr-C hardfacing alloy reinforced with carbide particles. Materials Research Express. 2022; 9:106507. https://doi.org/10.1088/2053-1591/ac94b6

[13] Evans LM, Sözümert E, Keenan BE, et al. A Review of Image-Based Simulation Applications in High-Value Manufacturing. Archives of Computational Methods in Engineering. 2023; 30:1495-1552. https://doi.org/10.1007/s11831-022-09836-2

[14] Reid A, Langer S, Lua RC, et al. Image-based finite element mesh construction for material microstructures. Computational Materials Science. 2008; 43(4):989-999. https://doi.org/10.1016/j.commatsci.2008.02.016

[15] Golt MC, Hernández-Rivera E. An Automated Workflow for Meshing Evolving Microstructures from High-Throughput Grain Growth Simulations. Proceedings of the COMSOL Conference, Boston, USA. 2018.

[16] Gu D, He B. Finite Element Simulation and Experimental Investigation of Residual Stresses in Selective Laser Melted Ti-Ni Shape Memory Alloy. Computational Materials Science. 2016; 117:221-232. https://doi.org/10.1016/j.commatsci.2016.01.044

[17] Li Y, Zhou K, Tan P, Tor SB, Chua CK, Leong KF. Modelling temperature and residual stress fields in selective laser melting. International Journal of Mechanical Sciences. 2018; 136:24-35. https://doi.org/10.1016/j.ijmecsci.2017.12.001

[18] Schneider CA, Rasband WS, Eliceiri KW. NIH Image to ImageJ: 25 Years of Image Analysis. Nature Methods. 2012; 9:671-675. https://doi.org/10.1038/nmeth.2089

[19] Otsu N. A Threshold Selection Method from Gray-Level Histograms. IEEE Transactions on Systems, Man, and Cybernetics. 1979; 9:62-66. https://doi.org/10.1109/TSMC.1979.4310076

[20] Gonzalez RC, Woods RE. Digital Image Processing. 4th ed. Pearson Education. 2018, 1022.

[21] Raghavan V. C-Cr-Fe (Carbon-Chromium-Iron). Journal of Phase Equilibria. 2002; 23:513–514. https://doi.org/10.1361/105497102770331226

[22] Khvan AV, Hallstedt B, Broeckmann C. A thermodynamic evaluation of the Fe–Cr–C system. CALPHAD: Computer Coupling of Phase Diagrams and Thermochemistry. 2014; 46:24-33. https://doi.org/10.1016/j.calphad.2014.01.002

[23] Maldonado-Ruiz SI, et al. Effect of V-Ti on the Microstructure and Abrasive Wear Behavior of 6CrC Cast Steel Mill Balls. Journal of Minerals and Materials Characterization and Engineering. 2014; 2:383-391. http://dx.doi.org/10.4236/jmmce.2014.25043

[24] Richter F. The Physical Properties of Steels: The 100 Steels Programme. Part I: Tables and Figures. Mülheim an der Ruhr, Germany. https://www.tugraz.at/fileadmin/user_upload/Institute/IEP/Thermophysics_Group/Files/Staehle-Richter.pdf

[25] Xiao B, Xing JD, Feng J, Li YF, Zhou CT, Su W, Xie XJ, Chen YH. Theoretical study on the stability and mechanical property of Cr_7C_3. Physica B. 2008; 403(13-16):2273–2281. https://doi.org/10.1016/j.physb.2007.12.012

[26] Sun L, Ji X, Zhao L, Zhai W, Xu L, Dong H, Liu Y, Peng J. First Principles Investigation of Binary Chromium Carbides Cr_7C_3, Cr_3C_2 and $Cr_{23}C_6$: Electronic Structures, Mechanical Properties and Thermodynamic Properties under Pressure. Materials. 2022; 15(2):558. https://doi.org/10.3390/ma15020558

[27] COMSOL Multiphysics® v. 6.1. Reference Manual. COMSOL AB, Stockholm, Sweden. 2022.

[28] Wang J, Xing X, Zhou Y, et al. Formation mechanism of ultrafine M_7C_3 carbide in a hypereutectic Fe-25Cr-4C-0.5Ti-0.5Nb-0.2N-2LaAlO3 hardfacing alloy layer. Journal of Materials Research and Technology. 2020; 9(4):7711-7720. https://doi.org/10.1016/j.jmrt.2020.05.039

2028; 346(3):142-152 ISSN-L 2616-6445, ISSN 2224-5243

Crossref

DOI: 10.31643/2028/6445.34

Metallurgy and Metallurgical Engineering

Integrity-Constrained Laboratory Screening of EOR Methods for Heavy-Oil Carbonate Reservoirs

[1*]Niyazbayeva A.B., [2]Ismail M. Saaid

[1] Atyrau University of Oil and Gas, Atyrau, Kazakhstan
[2]Universiti Teknologi PETRONAS, Seri Iskandar, Malaysia

** Corresponding author email: n.aynur22@aogu.edu.kz*

Received: *June 29, 2026*
Peer-reviewed: *July 29, 2026*
Accepted: *September 8, 2026*

ABSTRACT

Enhanced oil recovery (EOR) screening is commonly initiated from reservoir and fluid properties, displacement mechanisms, and expected recovery potential. In technically complex offshore systems, however, a candidate method may be unsuitable for further development if the associated fluids and operating conditions intensify corrosion, inorganic scaling, organic deposition, emulsion persistence, phase instability, or near-wellbore damage. This study develops an integrity-constrained pre-pilot laboratory screening workflow for the integrated Field X-Field Y system. The workflow integrates brine chemistry and water-compatibility calculations, corrosion and inhibitor tests, wax-appearance-temperature (WAT) and viscosity data, emulsion stability, PVT recombination, and filtration compatibility. Untreated corrosion rates reached 11.586 mm/year at the electrical submersible pump outlet and 2.942 mm/year at the wellhead. Field X-Field Y formation-water mixing was compatible at 60 °C, whereas cooling to 30–50 °C increased predicted BaSO4-dominated precipitation, with 18.849 mg/L at 30 °C for the 75/25 mixture; the broader marine-water case reached 58.79 mg/L under the evaluated low-temperature/low-pressure condition. Field Y DST-1 was the most restrictive oil in the organic-deposition screen, with 10.6 wt.% paraffin and WAT evidence spanning 17.4–22.4 °C. Artificial emulsions retained up to 70% water for Field X DST-3 and 80% for Field Y DST-1. For the selected associated-gas analogue, a gas-oil ratio not above 90 m^3/t at 18 MPa and 60.5 °C was used as the single-phase recombination boundary. The six-domain matrix was reformulated as an equal-weight ordinal qualification-burden index rather than a recovery-ranking tool; WAG had the highest burden (S=15; R=2.50), and this position remained unchanged under ±25% one-at-a-time criterion-weight perturbations. The framework therefore identifies operational-integrity constraints and the laboratory qualification required before direct displacement corefloods, compositional simulation, and pilot validation; it does not quantify incremental oil recovery.

Keywords: enhanced oil recovery, EOR screening, operational integrity, corrosion, barium sulfate scale, wax appearance temperature, PVT stability.

Information about authors:

Niyazbayeva Ainur Bauyrzhankyzy — *PhD student, Oil and Gas Faculty, Atyrau University of Oil and Gas, Atyrau 060000, Kazakhstan. Email: n.aynur22@aogu.edu.kz; ORCID ID: https://orcid.org/0009-0001-4586-7578*

Ismail Mohd Saaid — *Associate Professor, Universiti Teknologi PETRONAS, Seri Iskandar, Malaysia. Email: ismailsaaid@utp.edu.my; ORCID ID: https://orcid.org/0000-0003-0747-2724*

Introduction

Mature and technically complex oil fields require recovery strategies that extend productive life and strengthen technical justification before pilot-scale implementation. Traditional EOR screening relies on reservoir temperature, oil viscosity, permeability, depth, pressure, oil composition, and displacement mechanisms [[1], [2], [3], [4], [5], [6], [7], [8]]. These criteria remain necessary, while field-development concepts involving multiple reservoirs, commingled production, alternative injection waters, offshore surface facilities, and high-salinity produced fluids require a broader integrity-based qualification. In such systems, the selected EOR method must be compatible not only with the reservoir rock and oil, but also with produced-water treatment, metallurgy, flow assurance and chemical protection requirements.

The Field X-Field Y system represents a case in which preliminary EOR selection requires a separate operational-integrity gate in addition to conventional reservoir-displacement screening. Water-based methods are affected by sulfate-barium compatibility and corrosion; gas-based methods require phase stability and PVT qualification; chemical methods are constrained by salinity, hardness, emulsification, and reagent

compatibility; and WAG couples the aqueous- and gas-phase constraints. Accordingly, the objective of this paper is to construct a pre-pilot laboratory screening workflow that translates the available Field X-Field Y compatibility and flow-assurance evidence into explicit qualification requirements for EOR method groups. The workflow is intended to identify what must be controlled or tested before displacement-efficiency evaluation, not to predict recovery factors or incremental oil production.

The scientific novelty lies in the decision layer applied between conventional EOR screening and method-specific displacement testing. Classical screening, multi-criteria decision-making, and recent data-driven approaches primarily rank EOR alternatives using reservoir/fluid suitability, expert-weighted criteria, sustainability indicators, or analog project databases. The present framework asks a different question: which operational-integrity constraints are directly coupled to each candidate method, and how much laboratory qualification is required before that method advances to coreflood, simulation, or pilot stages? Six independently generated evidence domains corrosion, inorganic scaling, organic deposition, emulsion behavior, PVT/phase stability, and filtration compatibility – are converted into a traceable ordinal coupling matrix. The matrix is deliberately separated from expected recovery, economics, and field-performance prediction, thereby avoiding the interpretation of laboratory compatibility data as a displacement-efficiency result.

Literature review

EOR screening has historically been structured around reservoir and oil-property thresholds. The classical screening approach separates thermal, gas, chemical, and microbial methods using parameters such as oil gravity, viscosity, reservoir temperature, permeability, and remaining oil saturation [[1], [2]]. Broader EOR reviews emphasize that method selection must be updated as field maturity, economics, and technology readiness change [[3], [4], [5]]. Textbook frameworks further show that displacement mechanisms alone do not guarantee field applicability because injectivity, mobility ratio, phase behavior, chemical loss, and facility constraints may dominate practical performance [[6], [7], [8]]. Water-based and chemical EOR methods are particularly sensitive to brine composition. High salinity and hardness can reduce polymer performance, destabilize surfactant systems, and increase the risk of inorganic scale. For low-salinity or engineered-water flooding, the target is not only salinity reduction but also controlled ion composition, clay response, and surface chemistry [[6], [7]]. In carbonate and high-salinity systems, sulfate and barium/strontium interactions become important because injected or mixed waters may cross the saturation threshold for sulfate scales. Oilfield scale literature identifies $BaSO_4$ as one of the most persistent and difficult scales to remove, and its formation is commonly associated with mixing of sulfate-bearing and barium-rich brines under changing temperature and pressure [[9], [10]].

Recent EOR-screening research has expanded beyond fixed property windows. Multi-criteria approaches have used fuzzy AHP/FTOPSIS or hybrid FAHP-goal-programming formulations to combine technical, environmental, economic, and social criteria [[11], [12]]. Statistical and machine-learning frameworks have also ranked EOR classes from global project databases [[13], [14]], while VIKOR coupled with Monte-Carlo analysis has been used to quantify ranking robustness under changing criterion weights [15]. These developments improve method prioritization, but their principal inputs remain reservoir/fluid descriptors, expert preferences, sustainability criteria, or analog-project outcomes. In contrast, the present study uses field-specific laboratory compatibility and flow-assurance evidence as a pre-pilot integrity gate and explicitly does not infer displacement efficiency from that evidence.

Corrosion is another screening barrier. Internal corrosion in oilfield systems is controlled by water chemistry, CO_2/H_2S, oxygen contamination, flow regime, temperature, solids, microbiology, and inhibitor performance [[16], [17], [18], [19]]. An EOR method that increases water circulation, gas-water contact, or sulfate-reducing bacterial activity may change the corrosion regime even if it improves sweep. Therefore, corrosion must be evaluated as part of the EOR decision rather than only as a production-chemistry issue.

Organic deposition and emulsion behavior influence both subsurface and surface performance. Wax and asphaltene deposition are controlled by oil composition, temperature history, pressure depletion, gas liberation, and mixing. The wax appearance temperature (WAT) and viscosity-temperature response are therefore essential for gas injection, cold-water injection, thermal methods, and offshore transport [[20], [21]]. Emulsion stability affects separation, chemical flooding, WAG, and any method that increases water cut or changes interfacial conditions. Stable

emulsions increase the load on surface processing, can trap water and solids, and may demand additional demulsification capacity [[22], [23]].

PVT behavior is the bridge between fluid displacement and laboratory representativeness. Gas injection, miscible or near-miscible processes, and coreflood studies require recombined fluids to remain single-phase under test conditions. Single-phase stability preserves the representativeness of measured recovery and pressure response during filtration experiments [[24], [25]]. For this reason, PVT constraints are treated here as an integral screening criterion for gas-based and hybrid EOR methods.

Experimental part

The study integrates an existing laboratory and engineering dataset for the anonymized Field X-Field Y fluid system. The evidence base comprises: (i) formation-water chemistry and water-mixing precipitation calculations; (ii) steel-coupon corrosion measurements for production and wellbore conditions; (iii) corrosion-inhibitor screening; (iv) scale-control screening records; (v) viscosity-temperature and WAT measurements; (vi) recombination of degassed oil with associated-gas analogues; (vii) artificial-emulsion stability and optical-microscopy observations; and (viii) filtration compatibility of a potential injection water with Field X brine and rock. For traceability, study outputs were classified as directly measured, calculated/predicted, or derived screening quantities. Corrosion rate, inhibitor response, viscosity/WAT, emulsion behavior, PVT recombination response, and filtration permeability change are treated as laboratory observations; scale precipitation is explicitly reported as calculated/predicted; and the EOR matrix and weight-sensitivity results are derived screening quantities. This classification prevents calculated scale values and derived scores from being presented as direct experimental measurements. The overall laboratory screening workflow and the equipment configuration are shown in Figures 1 and 2, respectively.

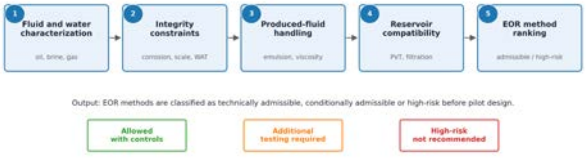

Figure 1 - Laboratory workflow for integrity-constrained EOR screening

Figure 2 - Laboratory equipment schematic used for integrity-constrained EOR screening

Water compatibility was evaluated from ionic composition, total dissolved solids, and calculated precipitation for Field X/Field Y formation-water mixtures at 30, 40, 50, and 60 °C; additional alternative-injection-water and marine-water cases were used to examine sensitivity to sulfate input and lower-temperature/lower-pressure conditions. Corrosion screening used steel coupons and reported corrosion rate in mm/year. Inhibitor protective effect was calculated as IE = (CRblank − CRtreated)/CRblank × 100%, where CR is the corrosion rate. Organic-deposition screening used the available kinematic/dynamic viscosity and WAT evidence, including rheological and acoustic-resonance records. Artificial emulsions were prepared at varying water contents and assessed by retained-water behavior, aggregative stability, and optical microscopy of globule size. PVT recombination was used to identify gas-oil ratios that maintained a homogeneous single-phase fluid at 18 MPa and 60.5 °C; for the selected analogue, the screening boundary was ≤90 m^3/t. Filtration compatibility was expressed as permeability decline after contact between the alternative injection water, Field X brine, and rock, with the supplied archive reporting a maximum decline of 7%. These tests provide compatibility and integrity information; they are not direct EOR displacement experiments.

Methodological traceability and uncertainty

The supplied archive does not contain complete instrument manufacturer/model information, specimen dimensions and preparation records, exposure duration, replicate-level raw observations, calibration certificates or traceable standard identifiers for every legacy laboratory domain. These values were therefore not reconstructed or estimated. Where replicate-level observations are unavailable, Figures 3–9 report the supplied endpoint values without fabricated standard-deviation or confidence-interval error bars. The vertical range shown for WAT in Figure 8 represents the span of method-specific WAT evidence, not

statistical uncertainty. Full reproducibility of the legacy tests requires the additional metadata listed in the revision supporting file; the present manuscript reports all methodological conditions that are directly supported by the supplied study archive. The laboratory screening domains, primary indicators, and their roles in EOR decision-making are summarized in Table 1.

Table 1 - Laboratory screening domains and EOR selection role

Domain	Primary indicator	EOR decision role/data type
Corrosion	Corrosion rate, mm/year; inhibitor performance	Infrastructure compatibility and chemical-protection requirement. Directly measured/calculated inhibitor efficiency.
Inorganic scaling	$BaSO_4$/total precipitate, mg/L; water chemistry	Aqueous-phase compatibility and sulfate-control requirement. Water chemistry measured; precipitation calculated/predicted.
Organic deposition	Paraffin content; WAT; viscosity-temperature response	Low-temperature flow-assurance qualification. Laboratory-observed properties.
Emulsion behavior	Maximum retained water; aggregative stability; globule size	Produced-fluid handling and separation qualifications. Laboratory-observed.
PVT stability	Gas-oil ratio; viscosity; single-phase recombination condition	Gas/hybrid fluid preparation and phase-stability qualification. Laboratory-observed.
Filtration compatibility	Permeability decline after fluid-rock interaction	Injectivity / near-wellbore damage qualification. Laboratory-observed endpoint response.

Results and Discussion

Corrosion as an infrastructure-screening barrier

The strongest constraint identified in the screening dataset is corrosion. Untreated rates are strongly aggressive in all tested operating points, with the most severe values at the ESP outlet and wellhead. These rates exceed the range that can be considered acceptable for long-term EOR operation without chemical protection. For EOR selection, this means that methods increasing water circulation, gas-water interaction, or oxygen/SRB exposure should be qualified using both reservoir displacement performance and operational-integrity criteria. The untreated corrosion rates are summarized in Table 2 and illustrated in Figure 3.

Table 2 - Untreated corrosion rates used as EOR screening constraints

Operating point	Corrosion rate, mm/year
General multiphase stream from wells	0.91
General multiphase stream after primary treatment	0.575
Crude oil before separator after hot-oil treatment	1.095
ESP outlet	11.586
Wellhead	2.942

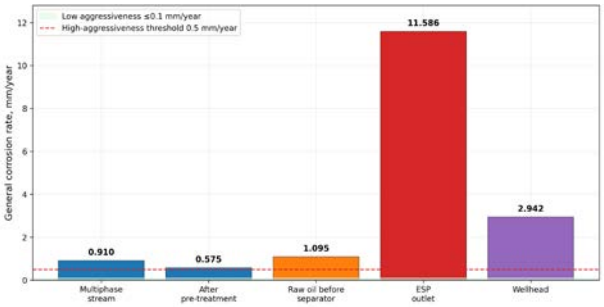

Figure 3 - Untreated corrosion rates in production and wellbore conditions

Inhibitor screening substantially reduced corrosion rates. The best tested treatments reached 0.107-0.112 mm/year under the specified laboratory conditions. This shifts corrosion from a blocking factor into a manageable design constraint if inhibitor selection, dosage optimization, and field validation are incorporated into the EOR design. The corrosion-inhibitor screening results are reported in Table 3 and illustrated in Figure 4.

Table 3 - Corrosion-inhibitor response under Field X conditions

Treatment	Dose, g/t	Corrosion rate, mm/year	Protective effect, %
Blank sample	0	0.575	0
CI-1	50	0.132	77.1
CI-1	70	0.118	79.6
CI-2	50	0.125	78.38
CI-2	70	0.107	81.4
CI-3	50	0.122	78.7
CI-3	70	0.112	80.5
Complex CI-4	90	0.109	81.1

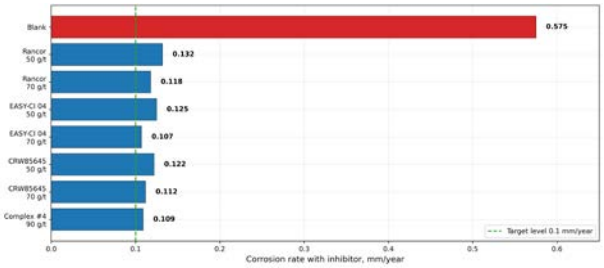

Figure 4 - Corrosion-inhibitor screening response

Water chemistry and sulfate-barium scale risk

The two formation waters differ in total salinity and sulfate-barium balance. Field X water is more saline and barium-rich, whereas Field Y water contains sulfate. This contrast creates a clear scale mechanism: mixing can introduce sulfate into a barium-containing system and cause $BaSO_4$ precipitation. The predicted precipitation depends strongly on temperature. At 60 °C, the waters are compatible in all ratios, but decreasing the temperature to 50, 40, and 30 °C produces a $BaSO_4$-dominated precipitate. The maximum predicted

precipitate for Field X-Field Y formation-water mixing is 18.849 mg/L at 30 °C for the 75/25 Field X/Field Y mixture. The formation-water chemistry is presented in Table 4, while the temperature-dependent precipitation results are summarized in Table 5 and Figure 5.

Table 4 - Formation-water chemistry used in the screening calculation

Water type	pH	Density, g/cm³	TDS, g/L	SO_4, mg/L	Cl, mg/L	Ca, mg/L	Mg, mg/L	Ba, mg/L
Field X formation water	5.9	1.154	225.9	0.0	138069.2	6727.4	1718.9	46.5
Field Y formation water	6.8	1.122	185.1	118.6	113404.2	6800.2	1867.7	17.0

Table 5 - Predicted precipitate during Field X-Field Y formation-water mixing, mg/L

Field X/Field Y ratio, %	30 °C	40 °C	50 °C	60 °C
100/0	16.499	12.022	6.22	0.0
75/25	18.849	13.293	6.7	0.0
50/50	13.639	8.543	2.53	0.0
25/75	3.829	0.072	0.0	0.0
0/100	0.009	0.003	0.0	0.0

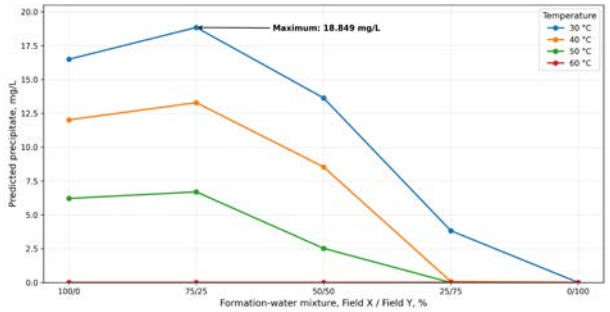

Figure 5 - Temperature-dependent scale potential during Field X-Field Y water mixing

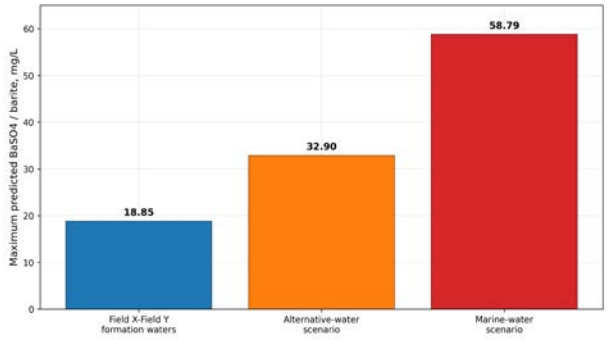

Figure 6 - Maximum predicted barite risk across water-mixing scenarios

The wider screening dataset shows that alternative and marine-water options can introduce a higher scale burden than formation-water mixing alone. Marine-water mixing is the most restrictive case, with a maximum predicted barite concentration of 58.79 mg/L under low-temperature and low-pressure conditions. This result directly affects waterflooding, engineered-water flooding, chemical flooding, and WAG selection because each of these methods requires an aqueous phase to be injected, recycled, or produced. The maximum predicted barite risk across the evaluated water-mixing scenarios is compared in Figure 6.

Organic deposition and low-temperature flow assurance

Organic-deposition screening separates Field X and Field Y oils into different risk groups. Field X DST-3 has moderate paraffin content and a WAT of approximately 9-10 °C, while Field Y DST-1 is the limiting oil with 10.6 wt.% paraffin and a WAT range of 17.4-22.4 °C depending on the method. Field Y DST-2 is less restrictive than DST-1 but still requires consideration during commingled production. For EOR selection, this means that injection methods causing temperature decrease, pressure depletion, gas liberation, or fluid mixing must be evaluated against wax/asphaltene deposition risk. The key organic-deposition indicators are summarized in Table 6; the Field X DST-3 viscosity-temperature relationship and the comparison across the tested oils are shown in Figures 7 and 8, respectively.

Table 6 - Organic-deposition screening indicators

Oil sample	Paraffin, wt.%	Pour point, °C	WAT by rheometer, °C	Additional WAT evidence
Field X DST-3	3.0	-15	9.0	below 10 by viscosity curve
Field Y DST-1	10.6	10.0	17.4	22 by ARS; 22.4 by viscosity curve
Field Y DST-2	7.3	-3.0	5.8	12.7 by viscosity curve

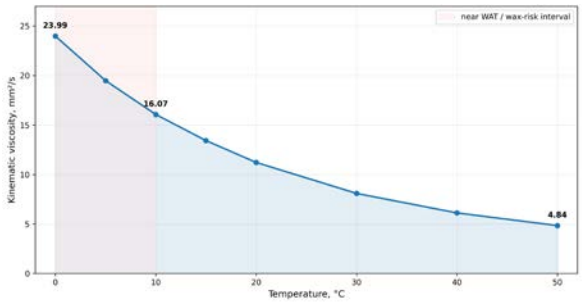

Figure 7 - Field X DST-3 viscosity-temperature relationship

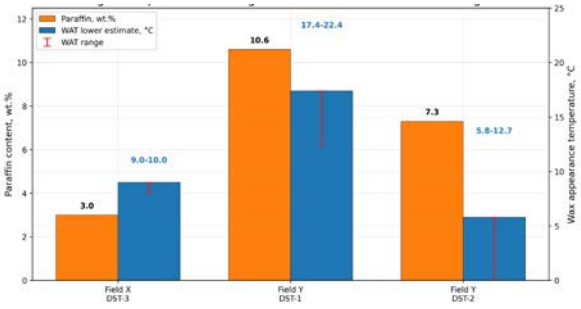

Figure 8 - Organic-deposition constraints across tested oils

Emulsion stability as a produced-fluid handling constraint

Emulsion behavior is a key produced-fluid handling control factor for water-based, chemical, and hybrid EOR methods. Field X artificial emulsions retain up to 70% water, and Field Y DST-1 emulsions retain up to 80% water. Field Y DST-2 behaves differently: a stable emulsion does not form at 60-90% water, indicating a less persistent emulsion structure at high water content. The microscopy results also show different globule-size ranges, with Field Y DST-1 having the broadest range. This result is important because increased water cut, surfactant use, WAG cycling, or produced-water recycling increases separation requirements even when subsurface displacement is favorable. The emulsion-screening results are summarized in Table 7 and Figure 9.

Table 7 - Emulsion-screening results

Oil sample	Maximum retained water, %	Aggregative stability behavior	Globule-size range, μm
Field X DST-3	70	highest stability at 30-50% water; relative decline at 60-70%	19.6-31.7
Field Y DST-1	80	100% aggregative stability at all water contents; maximum stability at 50-70%	17.7-73.9
Field Y DST-2	50	stable emulsion absents at 60-90% water; high stability preserved at 30%	18.0-29.2

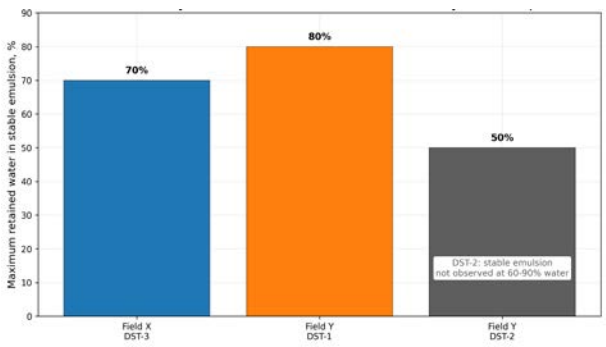

Figure 9 - Maximum retained water in stable artificial emulsions

PVT recombination constraints for gas-based and hybrid EOR

PVT recombination controls the validity of gas-EOR and hybrid-EOR laboratory tests. For Field X, associated gas analogues were used to reconstruct a representative reservoir fluid at 18 MPa and 60.5 °C. The recommended gas-oil ratio for the coreflood-ready recombined fluid is not above 90 m^3/t for the selected analogue, corresponding to a representative viscosity of approximately 1.2 cP. This condition is used as a laboratory boundary to avoid gas breakout during filtration experiments and to ensure that gas-based screening reflects the intended reservoir fluid rather than an unstable experimental mixture. The corresponding PVT recombination constraints are summarized in Table 8.

Table 8 - PVT recombination constraints for gas-EOR screening

Gas analogue	Gas-oil ratio range, m^3/t	Viscosity range, cP	Recommended gas-oil ratio, m^3/t	Decision note
Associated gas analogue A	70-95	1.00-2.11	≤90	Selected for recombined fluid coreflood preparation
Associated gas analogue B	70–95/98	1.05-1.50	95 and below	Recommended due to operationally convenient sampling pressure

Filtration compatibility and injectivity risk

Filtration compatibility provides a link between fluid chemistry and near-wellbore injectivity risk, but it does not constitute an EOR displacement-efficiency test. The tested alternative injection water produced up to 7% permeability decline after interaction with Field X brine and rock. Within the supplied dataset, this endpoint is used only to indicate that no larger permeability loss was observed in the reported compatibility test; qualification of water-based or hybrid EOR still requires method-specific coreflood/injectivity testing under representative saturation, rate, and stress conditions. The filtration-compatibility endpoint and its screening interpretation are summarized in Table 9.

Table 9 - Filtration compatibility indicator

Test system	Permeability response	Screening interpretation
Alternative injection water with Field X brine and rock	up to 7% permeability reduction	compatible/acceptable for further screening

EOR method screening matrix

The laboratory results were integrated into an ordinal integrity-qualification matrix across six domains: corrosion, scale, organic deposition, emulsion, PVT/phase behavior and filtration compatibility. For method j and domain i, a coupling score sij of 1, 2, or 3 was assigned: 1 = low direct dependence on the domain within the available evidence and routine verification only; 2 = moderate or method-specific dependence requiring dedicated qualification before a pilot; and 3 = strong/direct dependence for which mitigation or validation is mandatory before the method advances. Thus, the score represents qualification burden, not predicted recovery, economics, technical success probability or incremental oil. Equal default weights (wi = 1/6) were used because the supplied dataset provides no defensible basis for preferential criterion weighting. The raw score is $S_j = \Sigma s_{ij}$ (range 6–18) and the

normalized index is Rj = Σwi·sij = Sj/6 (range 1–3). Scores of 6–9 are interpreted as lower qualification burden, 10–12 as moderate burden, and 13–18 as high burden. These bands are decision-support categories only and are not field-admissibility thresholds. The resulting integrity-qualification score matrix is presented in Table 10, while the interpretation of the qualification burden and the required next-stage evidence are summarized in Table 11.

A one-at-a-time weight-sensitivity analysis was added to test whether the ranking is an artifact of equal weighting. Each criterion weight was independently increased and decreased by 25%, with all six weights renormalized to sum to unity, giving 12 perturbed weighting cases. WAG retained the highest normalized qualification-burden index in every case (R = 2.44–2.57), and gas injection remained second (R = 1.96–2.04). The other method groups remained within R = 1.61–1.88. This analysis demonstrates the robustness of the burden ordering to moderate weight perturbation; it does not validate EOR recovery performance. The corresponding criterion-weight sensitivity results are shown in Figure 10.

Table 10 - Integrity-constrained EOR screening score matrix for Field X-Field Y

EOR method group	Corrosion	Scale	Organic	Emulsion	PVT	Filtration	Total score
Conventional/modified waterflooding	3	3	1	1	1	1	10
Low-salinity or engineered-water flooding	3	3	1	2	1	1	11
Polymer flooding	2	3	1	2	1	1	10
Surfactant/alkali-surfactant methods	2	3	1	3	1	1	11
Gas injection / miscible or near-miscible gas	3	2	2	1	3	1	12
WAG / hybrid gas-water EOR	3	3	2	3	3	1	15
Thermal stimulation	2	2	3	1	1	1	10
Microbial / biochemical EOR	3	2	1	2	1	1	10

Table 11 - Interpretation of the integrity-qualification matrix and required next-stage evidence

EOR method group	Qualification-burden interpretation and next-stage evidence
Conventional/modified waterflooding	Moderate burden (S=10; R=1.67). Scale/corrosion control must be qualified; displacement performance requires direct coreflood or validated simulation.
Low-salinity or engineered-water flooding	Moderate burden (S=11; R=1.83). Requires brine-rock compatibility, sulfate control, and method-specific wettability/displacement testing.
Polymer flooding	Moderate burden (S=10; R=1.67). Requires polymer stability/rheology in high-salinity/high-hardness brine, retention/injectivity, and displacement corefloods.
Surfactant/alkali-surfactant methods	Moderate burden (S=11; R=1.83). Requires phase behavior, salinity compatibility, adsorption/retention, emulsion/separation, and displacement testing.
Gas injection/miscible or near-miscible gas	Moderate burden (S=12; R=2.00). Requires PVT/miscibility qualification, corrosion/flow-assurance assessment, and direct displacement or compositional-simulation validation.
WAG/hybrid gas-water EOR	High burden (S=15; R=2.50). Couples aqueous scaling/corrosion, emulsion, and gas-phase PVT constraints; requires integrated coreflood, compositional simulation, and pilot validation.
Thermal stimulation	Moderate burden (S=10; R=1.67). WAT/viscosity data support temperature sensitivity, but thermal feasibility, heat loss, well/facility integrity, and displacement response were not tested here.
Microbial/biochemical EOR	Moderate burden (S=10; R=1.67). Requires microbiology/SRB, souring, biocide compatibility, and direct displacement validation before pilot consideration.

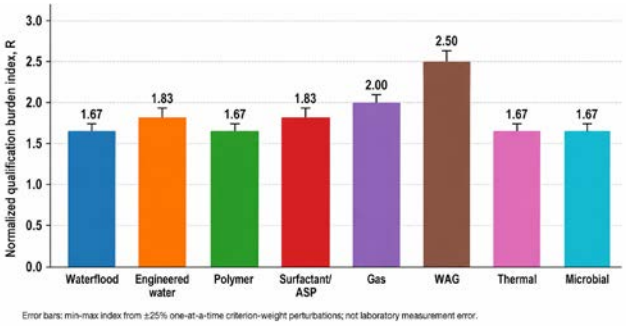

Figure 10 - Normalized EOR qualification-burden index under criterion-weight sensitivity. Error bars indicate the minimum-to-maximum index obtained from ±25% one-at-a-time criterion-weight perturbations and do not represent laboratory measurement uncertainty

Discussion

Implications for water-based methods

Conventional waterflooding and modified water injections remain candidates for further evaluation when BaSO4 scaling and corrosion are controlled. Field X-Field Y formation-water mixtures show zero predicted precipitate at 60 °C in the supplied calculation, whereas cooling increases predicted precipitation. Consequently, any water-based EOR design should include sulfate-barium compatibility, oxygen management and corrosion inhibition, followed by method-specific injectivity and displacement testing. The temperature sensitivity is particularly relevant to offshore systems where reservoir, wellbore and surface temperatures differ substantially.

Implications for chemical EOR

Chemical EOR requires targeted qualifications because polymer, surfactant and alkali-surfactant systems can be affected by salinity, hardness, scale and emulsification. The present matrix does not establish chemical-EOR displacement efficiency. Instead, it defines the minimum follow-up program: polymer viscosity retention in representative brines, surfactant/alkali phase behavior, adsorption and retention, injectivity, emulsion/separation response, scale-inhibitor and corrosion-inhibitor interference, and direct displacement coreflooding before any pilot recommendation.

Implications for gas-based and hybrid methods

Gas injection and WAG remain candidates for subsequent displacement evaluation after integrity qualification. PVT recombination provides a controlled fluid-preparation boundary, while the organic-deposition dataset identifies Field Y DST-1 as the most temperature-sensitive oil among the tested samples. WAG has the highest integrity-

qualification burden in the matrix (S=15; R=2.50) because it simultaneously couples water-phase scaling/corrosion, emulsion behavior and gas-phase PVT constraints. This designation does not mean that WAG has the highest EOR performance or the highest probability of failure; it means that the largest number of integrity domains require method-specific qualification before recovery performance can be evaluated.

Implications for thermal and microbial/biochemical methods

The viscosity-temperature and WAT data show that increasing temperature reduces the measured viscosity of Field X DST-3 and moves the system away from wax-appearance conditions; however, the present dataset does not establish the recovery efficiency of a thermal process. Thermal methods therefore require dedicated heat-loss, well-integrity, surface-facility, and displacement-feasibility studies. Microbial/biochemical EOR likewise requires SRB/biocide, souring-risk and fluid-compatibility qualification followed by direct displacement testing. These method groups are retained as screening candidates rather than declared technically admissible technologies.

Study scope, validation level and limitations

No direct oil-displacement experiments with polymer, surfactant, gas, WAG, thermal, or microbial systems, no reservoir-simulation cases, and no field-pilot data are included in the supplied study dataset. Consequently, the framework cannot quantify recovery factor, incremental oil production, sweep efficiency, miscibility benefit, or field economic value. Its validated output is limited to organizing the available laboratory compatibility evidence and identifying the relative integrity-qualification burden of method groups. The added weight-sensitivity analysis tests robustness of the ordinal decision layer, not physical EOR performance. The appropriate next validation stage is method-specific coreflooding and/or compositional reservoir simulation, followed by a pilot where warranted. A second limitation is incomplete legacy metadata for several laboratory procedures; specimen dimensions, preparation details, instrument models, test duration, replicate counts, standard identifiers, and instrument uncertainties should be recovered from the original laboratory reports before claiming full experimental reproducibility.

Scientific contribution

The contribution of this study is a transparent pre-pilot decision layer that treats corrosion, scaling, organic deposition, emulsion behavior, PVT stability, and filtration compatibility as EOR qualification domains rather than disconnected production-chemistry observations. Unlike reservoir-property screening or data-driven ranking, the framework does not claim to identify the method with the highest recovery. It identifies which candidate methods are most strongly coupled to the documented operational-integrity constraints and therefore require the most extensive qualification before displacement testing. The scoring definitions, equal-weight assumption, burden thresholds, data-type classification, and weight-sensitivity analysis make the decision logic auditable and reduce ambiguity between laboratory compatibility evidence and EOR performance prediction.

Conclusions

An integrity-constrained pre-pilot EOR screening workflow was developed for the Field X-Field Y system using six laboratory domains: corrosion, inorganic scaling, organic deposition, emulsion behavior, PVT/phase stability, and filtration compatibility. The workflow is an operational-qualification gate and is not a displacement-efficiency or recovery-factor model.

Corrosion is the most severe measured infrastructure constraint in the supplied dataset. Untreated rates reach 11.586 mm/year at the ESP outlet and 2.942 mm/year at the wellhead; inhibitor screening reduces the best reported test values to 0.107–0.112 mm/year, demonstrating the need for chemical protection and field validation in any EOR design that increases corrosive exposure.

Formation-water compatibility is temperature sensitive. The supplied precipitation calculations give zero precipitate at 60 °C for all Field X/Field Y ratios but up to 18.849 mg/L at 30 °C for the 75/25 mixture. The broader marine-water case reaches a predicted 58.79 mg/L under the evaluated low-temperature/low-pressure condition.

Organic-deposition and emulsion data identify Field Y DST-1 as the most restrictive tested oil for flow assurance: paraffin content is 10.6 wt.%, WAT evidence spans 17.4–22.4 °C, and artificial emulsions retain up to 80% water. Field X DST-3 emulsions retain up to 70% water.

Gas/hybrid laboratory preparation requires PVT control. For the selected associated-gas analogue, the supplied recombination evidence supports a gas-oil-ratio boundary of ≤90 m^3/t at 18 MPa and 60.5 °C to maintain the intended single-phase preparation condition.

The filtration-compatibility record shows up to 7% permeability decline after interaction of the

alternative injection water with Field X brine and rock. This endpoint supports only compatibility screening; it does not replace method-specific injectivity or displacement coreflooding.

The revised matrix uses a defined 1–3 ordinal method-domain coupling scale and equal criterion weights. WAG has the highest qualification burden (S=15; R=2.50), followed by gas injection (S=12; R=2.00). Under ±25% one-at-a-time criterion-weight perturbations, WAG remains highest (R=2.44–2.57) and gas injection remains second (R=1.96–2.04), indicating robustness of the burden ordering to moderate weighting changes.

The study does not contain direct EOR displacement tests, reservoir simulation, or field-pilot validation; therefore, no conclusion is made regarding incremental oil recovery, recovery factor or economic superiority of the screened methods. The matrix identifies the qualification work required before those performance questions can be answered.

The next technical stage should combine recovered laboratory metadata and replicate-level uncertainty, method-specific displacement corefloods, and–where gas or WAG is considered–compositional reservoir simulation before pilot selection.

Data availability. The laboratory and calculation data supporting the reported numerical results are available from the author upon reasonable request, subject to confidentiality requirements related to anonymized field information. The current compiled archive does not contain complete replicate-level raw records and instrument metadata for every legacy test; these items should be recovered from the originating laboratory reports for full procedural reproducibility.

Acknowledgements. The authors gratefully acknowledge the laboratory teams involved in fluid, water, corrosion, emulsion, PVT, and filtration testing.

CRediT author statement: **A. Niyazbayeva**: Conceptualization, methodology, data interpretation, writing–original draft preparation; **I. M. Saaid:** Supervision, scientific guidance, validation, and writing–review and editing.

Conflicts of interest. The authors declare that there is no conflict of interest.

Cite this article as: Niyazbayeva AB, Ismail M Saaid. Integrity-Constrained Laboratory Screening of EOR Methods for Heavy-Oil Carbonate Reservoirs. Kompleksnoe Ispolzovanie Mineralnogo Syra = Complex Use of Mineral Resources. 2028; 346(3):142-152. https://doi.org/10.31643/2028/6445.34

Ауыр мұнайлы карбонатты коллекторлар үшін пайдалану сенімділігі шектеулерін ескеретін EOR әдістерінің зертханалық скринингі

[1]Ниязбаева А.Б., [2]Ismail M. Saaid

[1]Атырау мұнай және газ университеті, Атырау, Қазақстан
[2]ПЕТРОНАС Технологиялық университеті, Сери Искандар, Малайзия

Мақала келді: *29 маусым 2026*
Сараптамадан өтті: *29 шілде 2026*
Қабылданды: *8 қыркүйек 2026*

ТҮЙІНДЕМЕ

Мұнай өндіруді арттыру (МӨ) әдістерін скринингтеу әдетте қабат пен флюид қасиеттеріне, ығыстыру механизмдеріне және мұнай өндірудің күтілетін әлеуетіне негізделген. Алайда, техникалық тұрғыдан күрделі теңіз жүйелері үшін әдісті таңдау кезінде коррозияны, бейорганикалық тұздардың шөгуі, органикалық шөгінділерді, эмульсия тұрақтылығын, фазалық тұрақсыздықты және ұңғыма маңы аймағының зақымдануын ескеру қажет. Бұл жұмыста X–Y кен орындарының интеграцияланған жүйесі үшін пайдалану сенімділігінің шектеулерін ескеретін пилотқа дейінгі зертханалық скрининг әдістемесі әзірленді. Әдістеме судың химиялық құрамы мен үйлесімділігін талдауды, коррозия мен ингибиторларды сынауды, парафиннің пайда болу температурасы (WAT) мен тұтқырлық деректерін, эмульсия тұрақтылығын, PVT-рекомбинациясын және сүзу үйлесімділігін біріктіреді. Ингибиторсыз коррозия жылдамдығы электрлік батырмалы сорғы шығысында 11,586 мм/жылға, ұңғыма сағасында 2,942 мм/жылға жетті. Қабат сулары 60 °C-та үйлесімді болды, ал 30–50 °C-та негізінен $BaSO_4$ шөгіндісінің болжамды мөлшері артты: 30 °C-та 75/25 қоспасы үшін 18,849 мг/л, ал теңіз суы сценарийінде 58,79 мг/л-ге дейін. Field Y DST-1 органикалық шөгінділер бойынша ең шектеуші мұнай болды: парафин мөлшері 10,6 масс.%, WAT 17,4–22,4 °C. Жасанды эмульсиялар Field X DST-3 үшін 70%-ға, Field Y DST-1 үшін 80%-ға дейін суды ұстап қалды. Таңдалған ілеспе газ аналогы үшін бірфазалы рекомбинация шегі 18 МПа және 60,5 °C-та ≤90 м³/т болды. Алты компонентті матрица мұнай өндірудің ранжирлеу құралы емес, тең салмақты реттік квалификациялық жүктеме индексі ретінде қайта құрылды; ең жоғары

	жүктеме WAG үшін анықталды (S=15; R=2,50) және критерий салмақтарын ±25% кезекпен өзгерткенде де сақталды. Әдістеме coreflood сынақтары, композициялық модельдеу және пилоттық валидация алдында қажетті пайдалану сенімділігі шектеулері мен зертханалық квалификацияны анықтайды, бірақ қосымша мұнай өндіріліуін сандық түрде бағаламайды.
	Түйін сөздер: мұнай өндіруді арттыру, МБА скринингі, коррозия, барий сульфаты шөгіндісі, парафин пайда болу температурасы, PVT тұрақтылығы.
Ниязбаева Айнұр Бауыржанқызы	***Авторлар туралы ақпарат:*** *PhD докторант, Мұнай және газ факультеті, Атырау мұнай және газ университеті, 060000, Атырау Қазақстан. Email: n.aynur22@aogu.edu.kz; ORCID ID: https://orcid.org/0009-0001-4586-7578*
Ismail Mohd Saaid	*Доцент, ПЕТРОНАС Технологиялық университеті, Сери Искандар, Малайзия. Email: ismailsaaid@utp.edu.my; ORCID ID: https://orcid.org/0000-0003-0747-2724*

Лабораторный скрининг методов увеличения нефтеотдачи с учетом ограничений эксплуатационной надежности для тяжелонефтяных карбонатных коллекторов

[1] Ниязбаева А.Б., [2]Ismail M. Saaid

[1] Атырауский университет нефти и газа, Атырау, Казахстан
[2]Технологический университет ПЕТРОНАС, Сери Искандар, Малайзия

Поступила: *29 июня 2026*
Рецензирование: *29 июля 2026*
Принята в печать: *8 сентября 2026*

АННОТАЦИЯ

Скрининг методов увеличения нефтеотдачи (МУН) обычно основан на свойствах пласта и флюидов, механизмах вытеснения и ожидаемом потенциале нефтеотдачи. Однако для технически сложных морских систем выбор метода должен также учитывать коррозию, солеотложение, органические отложения, устойчивость эмульсий, фазовую нестабильность и повреждение призабойной зоны. В работе разработан предпилотный лабораторный скрининг для интегрированной системы месторождений X–Y с учетом ограничений эксплуатационной надежности. Методика объединяет анализ химии и совместимости вод, коррозионные и ингибиторные испытания, данные по температуре появления парафинов (WAT) и вязкости, устойчивости эмульсий, PVT-рекомбинации и фильтрационной совместимости. Скорость коррозии без ингибитора достигала 11,586 мм/год на выходе ЭЦН и 2,942 мм/год на устье. Смешение пластовых вод было совместимым при 60 °C, тогда как при 30–50 °C возрастало прогнозируемое выпадение преимущественно $BaSO_4$: до 18,849 мг/л при 30 °C для смеси 75/25; в сценарии с морской водой — до 58,79 мг/л. Field Y DST-1 характеризовался наибольшим риском органических отложений: 10,6 масс% парафина и WAT 17,4–22,4 °C. Искусственные эмульсии удерживали до 70% воды для Field X DST-3 и 80% для Field Y DST-1. Для выбранного аналога попутного газа граница однофазной рекомбинации составила ≤90 м³/т при 18 МПа и 60,5 °C. Шестикомпонентная матрица представлена как равновзвешенный порядковый индекс квалификационной нагрузки, а не как инструмент ранжирования нефтеотдачи; максимальная нагрузка установлена для WAG (S=15; R=2,50) и сохранялась при ±25% поочередном изменении весов критериев. Методика определяет ограничения эксплуатационной надежности и объем лабораторной квалификации перед coreflood-испытаниями, композиционным моделированием и пилотной валидацией, но не количественно оценивает прирост нефтеотдачи.

Ключевые слова: повышение нефтеотдачи, МУН-скрининг, эксплуатационная надежность, коррозия, сульфат бария, температура появления парафинов, PVT-стабильность.

Ниязбаева Айнур Бауыржановна	***Информация об авторах:*** *PhD докторант, Факультет нефти и газа, Атырауский университет нефти и газа, Атырау 060000, Казахстан. Email: n.aynur22@aogu.edu.kz; ORCID ID: https://orcid.org/0009-0001-4586-7578*
Ismail Mohd Saaid	*Доцент, Технологический университет ПЕТРОНАС, Сери Искандар, Малайзия. Email: ismailsaaid@utp.edu.my; ORCID ID: https://orcid.org/0000-0003-0747-2724*

References

[1] Taber JJ, Martin FD, Seright R.S. EOR screening criteria revisited - Part 1: Introduction to screening criteria and enhanced recovery field projects. SPE Reservoir Engineering. 1997; 12(3):189-198. https://doi.org/10.2118/35385-PA

[2] Taber JJ, Martin FD, Seright RS. EOR screening criteria revisited - Part 2: Applications and impact of oil prices. SPE Reservoir Engineering. 1997; 12(3):199-206. https://doi.org/10.2118/39234-PA

[3] Thomas S. Enhanced oil recovery - An overview. Oil & Gas Science and Technology - Revue de l'IFP. 2008; 63(1):9-19. https://doi.org/10.2516/ogst:2007060

[4] Alvarado V, Manrique E. Enhanced oil recovery: An update review. Energies. 2010; 3(9):1529-1575. https://doi.org/10.3390/en3091529

[5] Muggeridge A, Cockin A, Webb K, Frampton H, Collins I, Moulds T, Salino P. Recovery rates, enhanced oil recovery and technological limits. Philosophical Transactions of the Royal Society A. 2014; 372:20120320. https://doi.org/10.1098/rsta.2012.0320

[6] Al-Shalabi EW, Sepehrnoori K. A comprehensive review of low-salinity water flooding: Theory, mechanisms and experimental evaluations. Journal of Petroleum Science and Engineering. 2016; 139:137-161. https://doi.org/10.1016/j.petrol.2015.11.027

[7] Dang CTQ, Nghiem LX, Chen Z, Nguyen NTB, Nguyen QP. CO_2 low salinity water alternating gas: A new promising approach for enhanced oil recovery. SPE Improved Oil Recovery Symposium. 2014; SPE-169071-MS. https://doi.org/10.2118/169071-MS

[8] Ali M, Jha NK, Pal N, Keshavarz A, Hoteit H, Sarmadivaleh M. Recent advances in carbon dioxide geological storage, experimental procedures, influencing parameters, and outlook. Earth-Science Reviews. 2022; 225:103895. https://doi.org/10.1016/j.earscirev.2021.103895

[9] Oddo JE, Tomson MB. Why scale forms in the oil field and methods to predict it. SPE Production & Facilities. 1994; 9(1):47-54. https://doi.org/10.2118/21710-PA

[10] Igunnu ET, Chen GZ. Produced water treatment technologies. International Journal of Low-Carbon Technologies. 2014; 9(3):157-177. https://doi.org/10.1093/ijlct/cts049

[11] Wei Z, Zhu S, Dai X, Wang X, Yapanto LM, Raupov IR. Multi-criteria decision making approaches to select appropriate enhanced oil recovery techniques in petroleum industries. Energy Reports. 2021; 7:2751-2758. https://doi.org/10.1016/j.egyr.2021.05.002

[12] Foukerdi A, Esmaeili S, Shahrabadi A. A hybrid FAHP-MCGP approach to sustainable assessment of candidate EOR methods for a given oil reservoir. Journal of Petroleum Science and Engineering. 2021; 207:109143. https://doi.org/10.1016/j.petrol.2021.109143

[13] Mahdaviara M, Sharifi M, Ahmadi M. Toward evaluation and screening of the enhanced oil recovery scenarios for low permeability reservoirs using statistical and machine learning techniques. Fuel. 2022; 325:124795. https://doi.org/10.1016/j.fuel.2022.124795

[14] Su S, Zhang N, Wang P, Jia S, Zhang A, Wang H, Zhang M. Investigation and Optimization of EOR Screening by Implementing Machine Learning Algorithms. Applied Sciences. 2023; 13(22):12267. https://doi.org/10.3390/app132212267

[15] Hajinorouz M, Alavi SE. A new approach based on VIKOR and Monte-Carlo algorithms for determining the most efficient enhanced oil recovery methods: EOR screening. Journal of Petroleum Exploration and Production Technology. 2024; 14:623-643. https://doi.org/10.1007/s13202-023-01726-y

[16] Nesic S. Key issues related to modelling of internal corrosion of oil and gas pipelines - A review. Corrosion Science. 2007; 49(12):4308-4338. https://doi.org/10.1016/j.corsci.2007.06.006

[17] Kermani MB, Morshed A. Carbon dioxide corrosion in oil and gas production - A compendium. Corrosion. 2003; 59(8):659-683. https://doi.org/10.5006/1.3277596

[18] De Waard C, Milliams DE. Carbonic acid corrosion of steel. Corrosion. 1975; 31(5):177-181. https://doi.org/10.5006/0010-9312-31.5.177

[19] Popoola LT, Grema AS, Latinwo GK, Gutti B, Balogun AS. Corrosion problems during oil and gas production and its mitigation. International Journal of Industrial Chemistry. 2013; 4:35. https://doi.org/10.1186/2228-5547-4-35

[20] Aiyejina A, Chakrabarti DP, Pilgrim A, Sastry MKS. Wax formation in oil pipelines: A critical review. International Journal of Multiphase Flow. 2011; 37(7):671-694. https://doi.org/10.1016/j.ijmultiphaseflow.2011.02.007

[21] Mullins OC. The modified Yen model. Energy & Fuels. 2010; 24(4):2179-2207. https://doi.org/10.1021/ef900975e

[22] Kokal SL. Crude-oil emulsions: A state-of-the-art review. SPE Production & Facilities. 2005; 20(1):5-13. https://doi.org/10.2118/77497-PA

[23] Kilpatrick PK. Water-in-crude oil emulsion stabilization: Review and unanswered questions. Energy & Fuels. 2012; 26(7):4017-4026. https://doi.org/10.1021/ef3003262

[24] Whitson CH, Torp SB. Evaluating constant-volume depletion data. Journal of Petroleum Technology. 1983; 35(3):610-620. https://doi.org/10.2118/10067-PA

[25] Coats KH. An equation of state compositional model. SPE Journal. 1980; 20(5):363-376. https://doi.org/10.2118/8284-PA

МАЗМҰНЫ
СОДЕРЖАНИЕ
CONTENTS

Техникалық редакторлар:
Г.К. Қасымова, Н.М.Айтжанова, Т.И. Қожахметов

Компьютердегі макет:
Г.К. Қасымова

Дизайнер:*Г.К. Қасымова, Н.М.Айтжанова*

“Металлургия және кен байыту институты” АҚ
050010, Қазақстан Республикасы, Алматы қаласы, Шевченко к-сі, 29/133

Жариялауға 9.09.2026 жылы қол қойылды

Технические редакторы:
Г.К. Касымова, Н.М. Айтжанова, Т.И. Кожахметов

Верстка на компьютере:
Г.К. Касымова

Дизайнер:
Г.К. Касымова, Н.М.Айтжанова

АО “Институт металлургии и обогащения”
050010, г. Алматы, Республика Казахстан. ул. Шевченко, 29/133

Подписано в печать 9.09.2026 г.

Technical editors:
G.K. Kassymova, N.M. Aitzhanova, T.I. Kozhakhmetov

The layout on a computer:
G.K. Kassymova

Designer:
G.K. Kassymova, N.M. Aitzhanova

“Institute of Metallurgy and Ore Beneficiation” JSC
050010, Almaty city, the Republic of Kazakhstan. Shevchenko str., 29/133

Signed for publication on 9.09.2026